Thermal wave testing of ceramics

Morris, J. D.

Award date:
1990

Awarding institution:
University of Bath

THERMAL WAVE TESTING OF CERAMICS

Submitted by: J D Morris

For the degree of PhD of the University of Bath 1990

J D Morris

ProQuest LLC
789 East Eisenhower Parkway
P.O. Box 1346
Ann Arbor, MI 48106-1346

ABSTRACT

Thermal wave interferometry is evaluated for the characterisation of translucent plasma sprayed ceramic thermal barrier coatings. It is shown that thickness can be measured, and that physical properties (such as diffusivity and optical absorption coefficient) can be determined. It is also shown that the performance of the technique is similar to that previously found with opaque metallic and metalloid coatings, subject to the proviso that knowledge of the optical translucency is essential if quantitative results are required.

The potential for incorporating infrared and optically transmitting fibres into the system is considered. It is shown that optical fibres can be incorporated successfully; in contrast, the quality of available infrared fibres is not yet adequate to permit this.

Finally, the technique is shown to be suitable for detecting surface-breaking cracks in both monolithic and plasma-sprayed materials. It is also shown that sensitivity to such flaws can be higher in translucent materials than in opaque media.

CONTENTS

Acknowledgements

Thanks are due to my supervisors, Dr D P Almond and Mr H Reiter of the School of Materials Science at Bath University, for their help and assistance. Particular thanks go to Dr P M Patel for advice and encouragement above and beyond the call of duty.

The financial assistance of the Ministry of Defence and the Science and Engineering Research council is gratefully acknowledged.

1 INTRODUCTION

1 INTRODUCTION

Modern technologies make increasing demands on the performance of materials, to the extent that a single material may not be able to satisfy conflicting needs.

There is much current interest in the possibility of using ceramic components in diesel engines and gas turbines [1,2]. These would allow higher operating temperatures leading to significant improvements in operating efficiency, with consequent reduction in fuel demand, running costs and pollution [3]. This permits a more efficient engine which can reduce fuel costs by up to 20% [4]. In addition to the fuel savings due to higher operating efficiencies, ceramic components can be lighter than metallic ones, and because cooling systems are not required, further savings due to reduced weight are possible. Monolithic ceramics are, however, brittle and difficult to fabricate to the required integrity.

A favoured approach is to apply a ceramic thermal barrier coating to an existing metallic component, thus enabling either a higher operating temperature to be used, or to allow operation of the component at reduced temperature to extend operational life [5]. An advantage of this approach is that it enables the engine design to remain largely constant, with only minor changes required to components to allow spraying, whereas the use of all-ceramic components requires major redesign of parts of the engine.

Bennet claimed [5] that use of insulating ceramic thermal barrier coatings in the combustion chamber and early stages of the turbine in the Rolls Royce RB211 could cut fuel costs by 1-2%.

Ceramic plasma sprayed coatings have many other applications. Alumina is used in the textile industry to give wear resistance to thread guides and heater plates. Chromia and titania are used to protect against erosion by synthetic fibres, and on the facings of rotating seals and glands to increase life. Oxide and carbide coatings are used in power stations to protect pipes and impellors against wear from the abrasive pulverised fuel. They have widespread use in the aerospace industry as thermal barrier coatings, and to reduce wear & erosion of turbine blades. Carbides are generally used for wear resistance, whereas oxides are more commonly used for thermal barrier coatings [6].

Yttria stabilised and partially stabilised zirconia is used as a thermal barrier material, eg in flame cans and on turbine blades, because it has a low thermal conductivity, it is strong, reasonably corrosion resistant, and has a high thermal shock resistance. In diesel engines, zirconia coated exhaust valves & piston crowns are resistant to some of the aggressive contaminants such as vanadates and sodium compounds in low grade fuels.

Thermal barrier coatings applied by plasma spraying (section 2) are in the form of a mass of rapidly cooled lenticular particles with porosity present to an extent determined by spraying conditions, and extensive microcracking. This is excellent for a thermal barrier coating, because the microcracking enhances the thermal resistance of the coating [7], and can also protect against gross failure by thermal shock.

The use of a protective coating on a substrate incapable of withstanding the operating environment demands a high degree of coating integrity. Any failure of the coating will inevitably lead to the failure of the rest of the component, with the possibility of serious economic and human damage as a consequence of this.

In such a case, a reliable means of testing the coating is essential for safe operation of such components. Ideally it should be a non-destructive test so that it can be applied to each and every component, both before and during service.

The structure of the plasma sprayed coating is such that ultrasound is heavily attenuated [8] and cannot readily be used for characterisation. Radiography is potentially hazardous and cannot readily reveal the presence of laminar defects, ie those parallel to the surface, because the change in absorption cross section is very small. Thermal techniques have previously been shown to be effective for characterising plasma sprayed metallic coatings [9-11] , although they have not been thoroughly examined with regard to ceramic coatings.

Thermal wave techniques are a development of photoacoustic techniques, which are themselves derived from photoacoustic spectroscopy which has been in use since the 1930's [12]. In photoacoustics, chopped light falls onto a sample in a gas cell containing a microphone or equivalent transducer. Periodic heating thus occurs as the light is absorbed, leading to expansion of the gas in the cell. The resulting pressure wave registers on the transducer, and the interpretation of the signal can reveal information about the sample.

Photothermal techniques use a similar means of heating, but rely on the monitoring of emitted infrared radiation to provide information about the sample. The heat generated by the absorbed light pulse spreads throughout the sample, and when the source is periodic, the temperature variation is also periodic. It is this periodic temperature variation which leads to the term "thermal wave". If a region of differing thermal character is encountered by the thermal wave, it will undergo a partial reflection, much as light would on encountering a region of different refractive index. The interference between the reflected wave and the incoming wave leads to variations in the surface temperature, and hence in the emitted infrared radiation. Thus the received signal contains information about the subsurface structure.

Analysis of theoretical models of coating systems, with computer modelling to predict the response, can lead to an understanding of the way in which a particular feature will influence the received signal. Thus the reliability of interpretation of the signal is improved.

It is the purpose of this work to explore several aspects of the use of thermal waves in the characterisation of plasma sprayed thermal barrier coatings, and also in some monolithic materials. Initially, the effect of coating translucency on the response is considered, with regard to how it affects the sensitivity of the technique and the interpretation of the results. Secondly, the potential for optical and infrared optical fibres to enhance the operational flexibility of the system is considered, and finally the suitability of the test system for detecting surface breaking cracks is assessed. The latter, in particular, pose a particular hazard to thermal barrier coatings, as they can act as conduits for heat to reach the unprotected substrate. Also, fuel trapped in the crack could lead to catastrophic coating failure if it detonated during the engine's operational cycle.

2 PLASMA SPRAYING

2 PLASMA SPRAYING

Plasma spraying is a process in which a material is melted or partially melted in a gas plasma and then sprayed onto a target workpiece by a carrier gas. The plasma flame is very hot and the heat transfer very efficient, so that the coating material need only stay in the flame for a short time. This allows the use of a high carrier gas speed, which results in a high impact speed of the sprayed material on the target. Thus the coatings are strong and dense. This section will start with a summary of flame spraying techniques, and will then move on to discuss the advantages of plasma spraying and some commonly used test methods.

2.1 Flame Deposition

Flame deposition is a generic term for surface application techniques in which molten or semi-molten particles of a material are sprayed onto a substrate. Almost any material can be applied, provided that it melts without degrading at the operating temperature of the spray system. Coating thickness is limited by factors such as thermal stress build up within the coating, and thermal mismatch between the coating and substrate, but in some systems, such as metal coatings on metal substrates, the thickness is virtually unlimited.

Max Schoop first reported flame spraying in Switzerland in 1910. Metal powder was passed through a combustion flame and driven onto the substrate by compressed air (figure 2.1). Many improvements have since been made, including the use of a continuous wire feed to replace the powder feed, and the use of an electric arc rather than a combustion flame which permits a much higher temperature to be achieved. Plasma spraying and the detonation gun technique are superior versions of the process, which allow better coating quality and the deposition of some materials which cannot be melted in combustion and arc flames.

In general, a superior bond will be achieved with a higher impact velocity as described below. This can be achieved with a higher temperature because the particles need less time in the hot zone to become sufficiently hot for melting to begin. The higher velocity also allows a faster deposition rate because more material can be passed through the flame in a given time. The superior coatings which can be made with plasma spray systems and the detonation gun can be attributed to the higher temperatures and velocities achieved.

2.1.1 Combustion Flame Spraying

A fuel gas such as acetylene (C_2H_2), propane (C_3H_8) or hydrogen (H_2) is burnt with oxygen to melt the coating material [13]. Flame temperatures can reach over 3000 °C. Impact velocities are typically 30m/s but higher velocities can be achieved with special configurations. Porosity levels are typically about 15% and oxide inclusions are common because of the oxidising flame.

In wire fed spraying, a continuous wire, or plastic tube filled with a fine powder, is fed into the combustion region. The flame is directed at the wire tip by compressed gas jets, and these serve to direct the resulting spray of molten material onto the target. Powder spraying involves feeding the powder into a gas stream which carries it into the flame and then to the target.

2.1.2 Flame Jet Spraying

This is an improved version of flame spraying in which the molten or semi-molten particles are accelerated to a higher velocity before striking the target [14] (figure 2.2). The higher velocity, up to 92 m/s, allows superior bonding, and thus improves their mechanical properties.

Tensile tests indicated strengths 1•5 times those of conventional flame sprayed coatings. Rockwell hardness tests also indicated that the flame jet coatings were superior to flame sprayed coatings. Morimoto et al [14] claimed that flame jet sprayed TiO_2 coatings had mechanical properties approaching those of plasma sprayed TiO_2 coatings.

2.1.3 Electric arc spraying

Electric arc spraying uses an electric arc rather than a combustion flame to heat the sprayed material. An arc is struck between wires made of the coating material which are used as consumable electrodes. The arc vaporises the wire and the resultant molten droplets are directed onto the target by a blast of compressed gas (figure 2.3). Temperatures of about 4000 °C can be achieved, which allows an improvement in performance over most combustion processes. The need to strike an arc between the electrodes restricts this technique to conductive materials only. If required, the two wires can be of different materials, so that a coating with combination properties can be put down.

2.2 Plasma Spraying

Plasma spraying uses a gas plasma rather than a combustion flame to heat the spray material.

2.2.1 Plasma Generation

The plasma is typically generated from a mixture of argon and hydrogen, but nitrogen and helium can also be used [15]. An arc is struck between a tungsten anode and a water cooled copper cathode using a dc power supply of up to 160V and 80kW. The resulting discharge is confined by compressed gas jets so that it reaches very high temperatures (up to 20000K [15]). The spray material is then fed into the flame on a carrier gas, again typically argon or an argon hydrogen mix (figure 2.4).

The extremely high temperature allows particles to heat up very quickly, so that they need only spend a small time within the plasma flame. Thus the coating material can be carried through at high speed, which leads to an impact velocity of 250 to 600 m/s depending on plasma gun design [16], and hence to a mechanically sound coating.

2.2.2 Spray Materials

As mentioned above any material that melts without decomposition can be deposited by plasma spraying, and coating thicknesses can be varied over a wide range, subject to thermal stress limitations [15]. Oxide coatings and coatings where oxidation is not a problem can be sprayed in air. Coatings that must have a low oxide content can be sprayed under an argon shroud [15]. Where oxide levels must be low and porosity must be reduced, then low pressure plasma spraying [17] or vacuum plasma spraying [18] can be used. These techniques are less convenient to use, but they can yield excellent coatings.

It is possible, though unusual, to feed wire into the plasma rather than using a powder feed system. Wire feed systems are claimed to have some important economic advantages in some applications [19].

2.2.3 Non-Atmospheric Spraying

In some instances, such as when the material to be sprayed is oxygen sensitive, it is necessary to control the spraying environment. This entails the use of large chambers (up to 3 metres across [16]) within which the required environment can be maintained. Some of the requirements are: excluding oxygen ie spraying under a neutral atmosphere; spraying under vacuum - this allows very high densities to be achieved, since gas entrapment is negligible; spraying under reduced pressure is a less taxing alternative to the above.

The cost of a large airtight or reasonably airtight chamber is very high. It is also technically demanding, since adequate ventilation must be present to remove carrier gas and combustion products, and to avoid overheating. Such a system must be fully automated too, since the environment will be hostile to humans, so that operators cannot remain present during deposition. The need to evacuate the chamber necessarily slows down the process.

2.2.4 Substrate Preparation

Best results are obtained by spraying onto grit blasted substrates which have been subsequently degreased when the preparation has been done just before spraying [13,15]. Shot blasting removes dirt, oxide layers and loose material from the substrate, and also roughens the surface on a scale of about 25 microns which enhances mechanical keying and strengthens the bond by increasing the surface area available. It can also reduce stress build up at the interface [16].

2.2.5 Bond Coats

Not all flame sprayed coatings are deposited directly onto the substrate, as there are some circumstances in which it is advantageous to have an intermediate coating, or bond coat. These are:

i) It can be used to promote (or permit) adhesion between the primary coating and the substrate;

ii) It can reduce thermal, or other mismatch between the primary coating and the substrate if it has intermediate properties;

iii) It can provide protection that the primary coating does not;

iv) It can provide additional protection to the substrate if the main coating fails.

When yttria-stabilised (or partially stabilised) zirconia (YSZ) is used as a thermal barrier coating, on a nickel or iron based superalloy combustion can or turbine blade, a bond coat of MeCoCrAlY (where Me = Fe or Ni) is often used. Where, as here, coating and substrate contain appropriate materials, there is the possibility of diffusion bonding occurring [15,20]. Zirconia is known to exhibit non-stoichiometry, and the transfer of oxygen ions from the YSZ to the oxygen deficient components of the bond coat is a realistic possibility. NiCoCrAlY has thermal properties intermediate to the substrate and primary coating, and thus reduces thermal expansion mismatch on heating. It is oxidation resistant and thus protects the substrate where the primary coating does not, and since it has a relatively low thermal conductivity, it also helps protect the substrate from the high temperature environment.

2.2.6 Formation of Coatings

When a molten or semi-molten particle hits the substrate, it will deform and take on a flattened aspect (figure 2.5). The degree of melting and the impact velocity will both determine the extent of the deformation. The impact will also deform the substrate to some extent, and this improves the mechanical bonding (figure 2.5). Where the substrate has an oxide coating which might interfere with coating adhesion, a high impact velocity will help to penetrate this and so improve adhesion.

Thermal expansion mismatch between the coating and substrate leads to stresses on cooling which can cause the coating to fail prematurely. These stresses can be reduced by reducing the thermal expansion gradient. If a ceramic is being sprayed onto a metallic substrate, then thermal expansion coefficients are likely to be very different. The presence of a bond coat reduces the mismatch but if required it can be reduced further by changing the composition as spraying progresses from pure bond coat through mixed bond coat/ coating to pure coating. Thermal stress can also be reduced by cooling or heating the substrate rear face to reduce differential thermal stresses.

2.2.7 Coating Structure

Plasma sprayed coatings have a characteristic microstructure containing many small (8-25 micron diameter) lenticular particles about 8-15 microns thick that are heavily microcracked. There is porosity, between 2 and 8 percent, and interlaminar microcracking. Other possible features include:

impurities-residual grit from blasting
cracks -vertical cracks, interparticulate microcracks, horizontal delaminations
porosity -large voids or regions of microporosity
interfacial defects-regions of poor adhesion, total delamination, or inclusions

These are shown schematically in figure 2.6. Figure 2.7 shows an optical micrograph of a plasma sprayed yttria stabilised zirconia (YSZ) coating on an aluminium substrate, showing the coating structure and some thickness variation. Figure 2.8 shows a similar coating with less thickness variation but poor interfacial bonding and a substantial void that has significantly reduced the local coating thickness.

Micro-cracking can be beneficial for thermal barrier coatings in that it reduces the thermal conductivity [7]. It can also make the coating more resistant to thermal shock by acting as a crack stopper.

Vertical cracking is generally deleterious to coating properties, although it can improve thermal shock resistance, because it can allow hostile media through protective coatings. In particular, in thermal barrier coatings in combustion chambers, vertical cracks can lead to hot spots, and if fuel infiltrates the crack, then subsequent ignition can lead to catastrophic failure of the coating by explosive spalling.

Where a thermal barrier coating contains a conductive inclusion, local breakdown of insulation leads to hot spot formation and subsequent failure. The situation is similar in electrical barrier coatings. Where a coating is for wear or corrosion resistance, the presence of a non-resistant particle can lead to premature failure. As a final example, lack of adhesion at an interface or in the coating will predispose the sample to mechanical failure, and can lead to a failure by breakdown of protective properties.

Some of these flaws can arise in service, while some will be present in the original coating. In both instances, coating failure is undesirable, and the consequences can be serious both economically and in human terms (e.g. failure of a combustion can thermal barrier in an aircraft engine). Quality control of coatings, both pre-service and in-service, is thus essential.

2.3 Quality Control

Generally, spray conditions are established by past procedure and destructive testing of samples. Once a suitable regime has been determined, quality is assured by strict process control with extensive automation, plus the destructive testing of representative samples to ensure that the coatings produced are suitable for their intended application. A number of destructive tests are described in the following chapter.

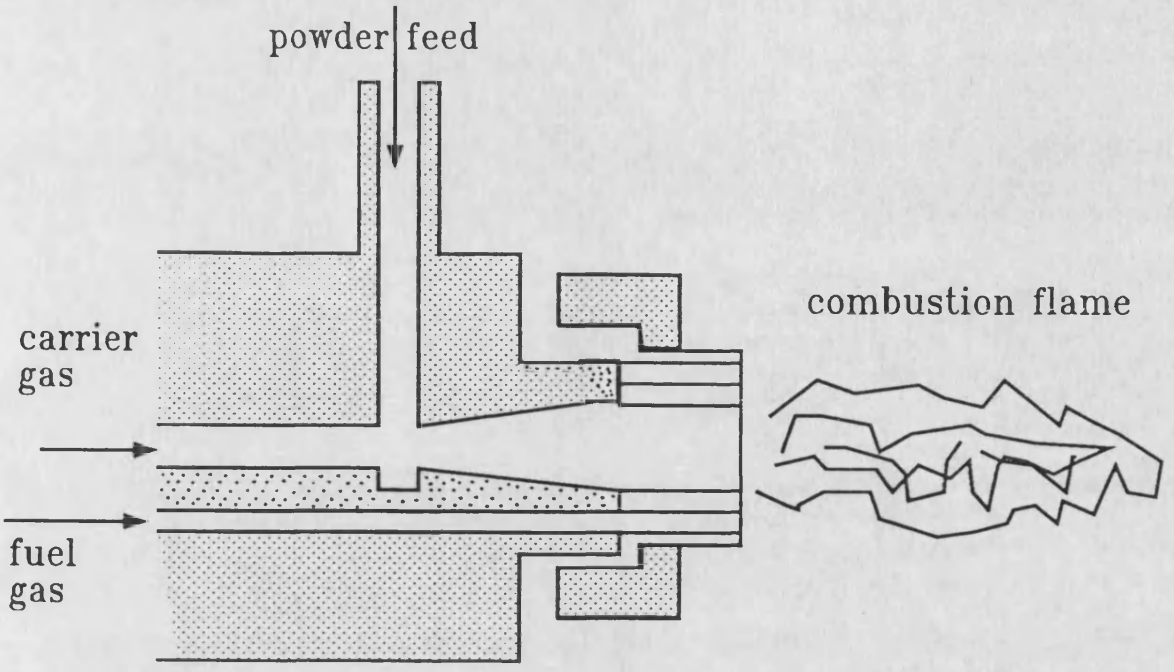

Figure 2.1 Schematic diagram of a combustion torch (after [16])

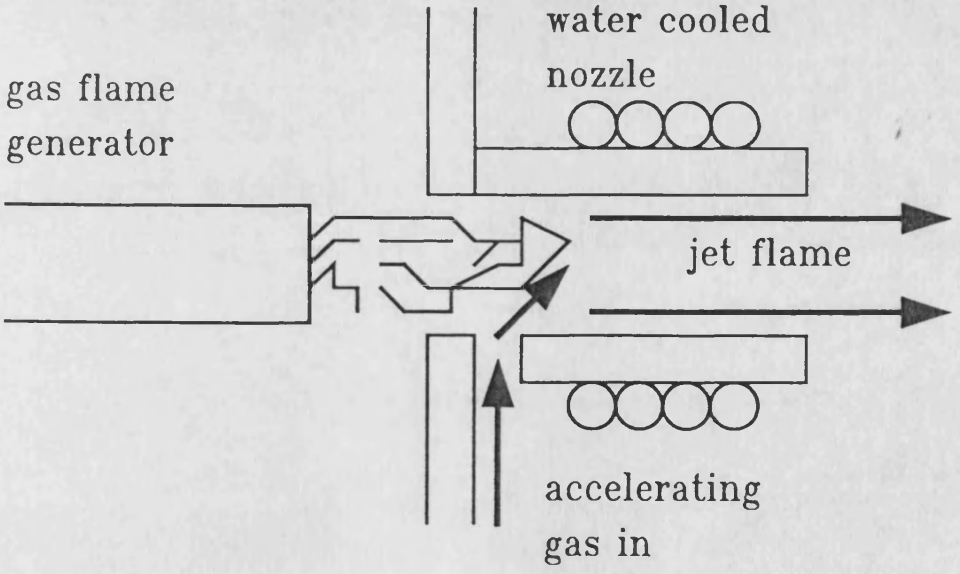

Figure 2.2 Schematic diagram of flame jet gun (after [14])

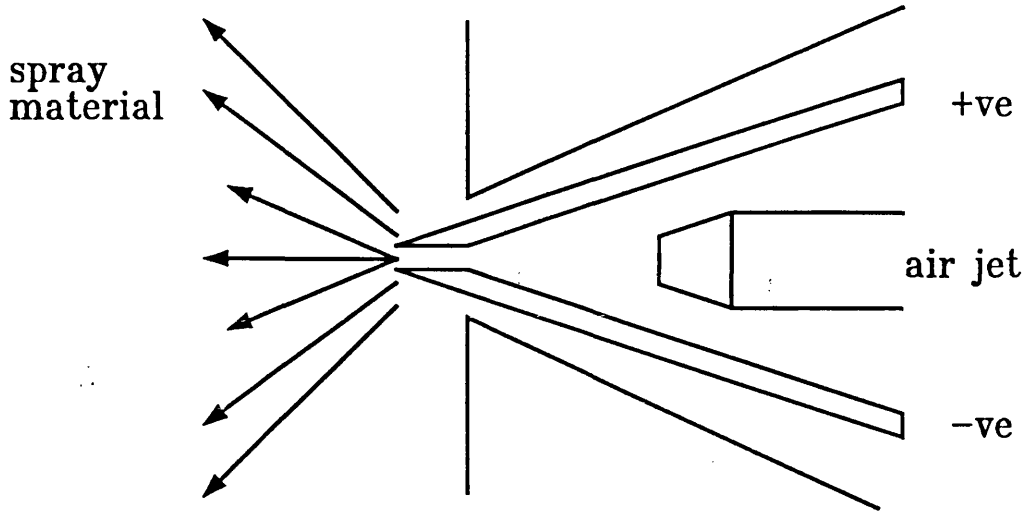

Figure 2.3 Schematic diagram of arc spraying (after [16])

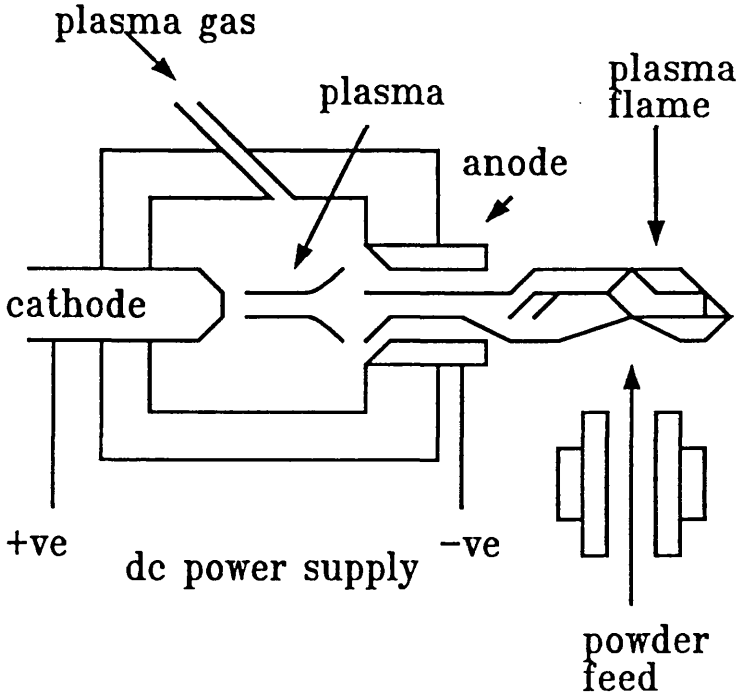

Figure 2.4 Schematic diagram of plasma spray gun

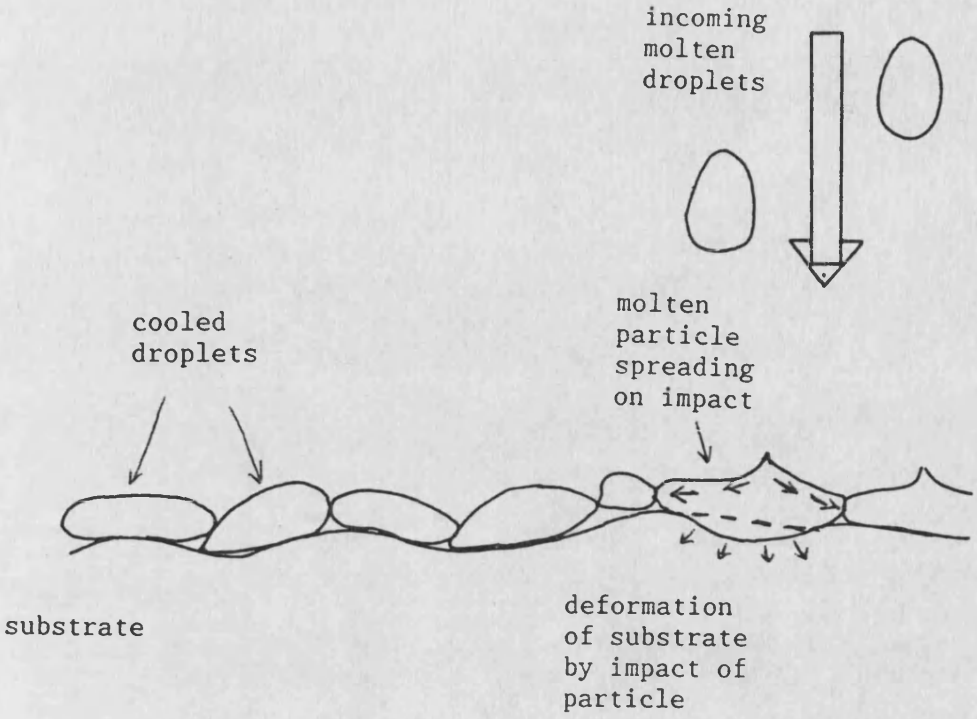

Figure 2.5 : Schematic depiction of molten plasma sprayed droplets striking a substrate

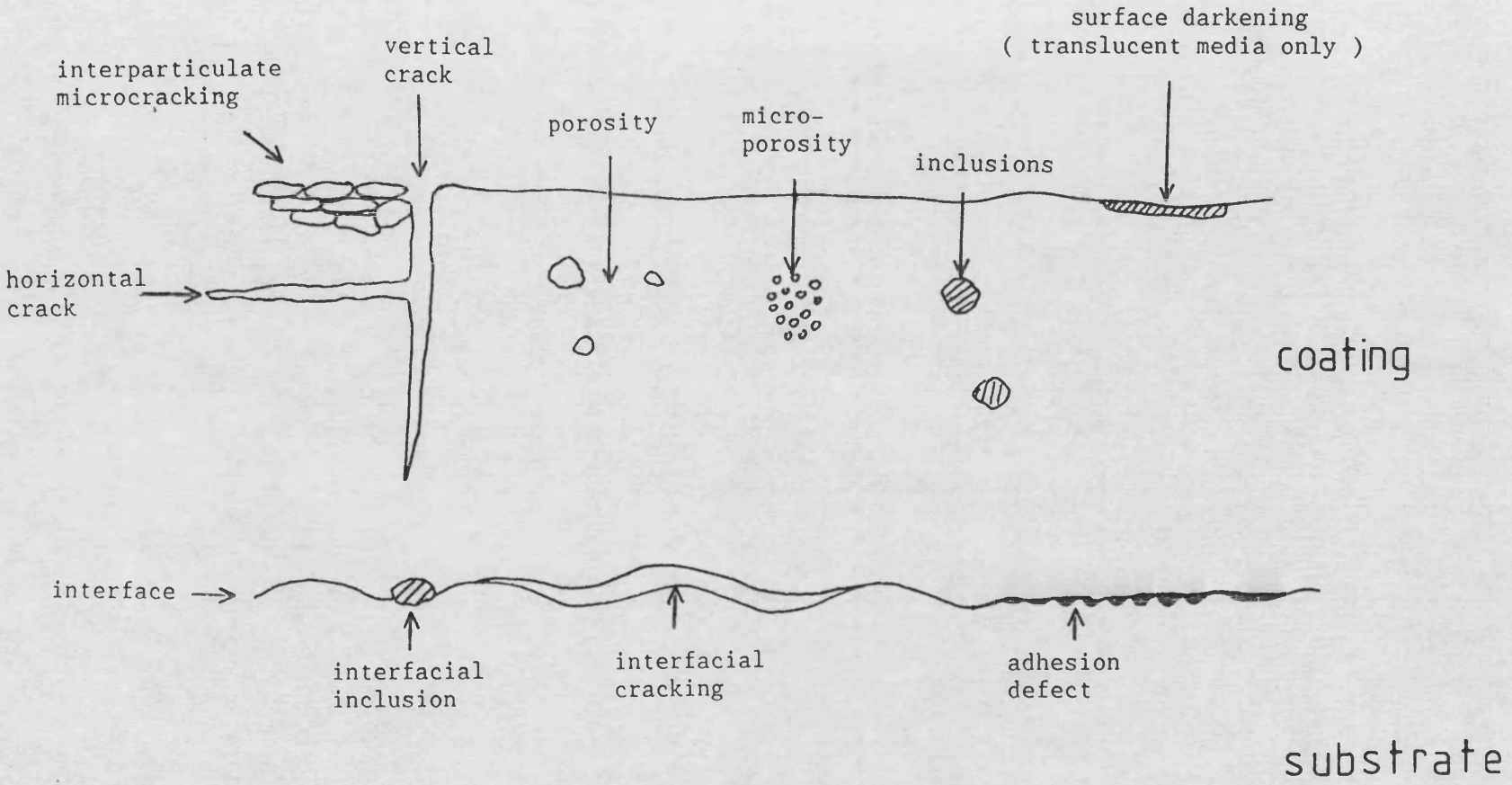

Figure 2.6: Schematic of defects found in plasma-sprayed coatings

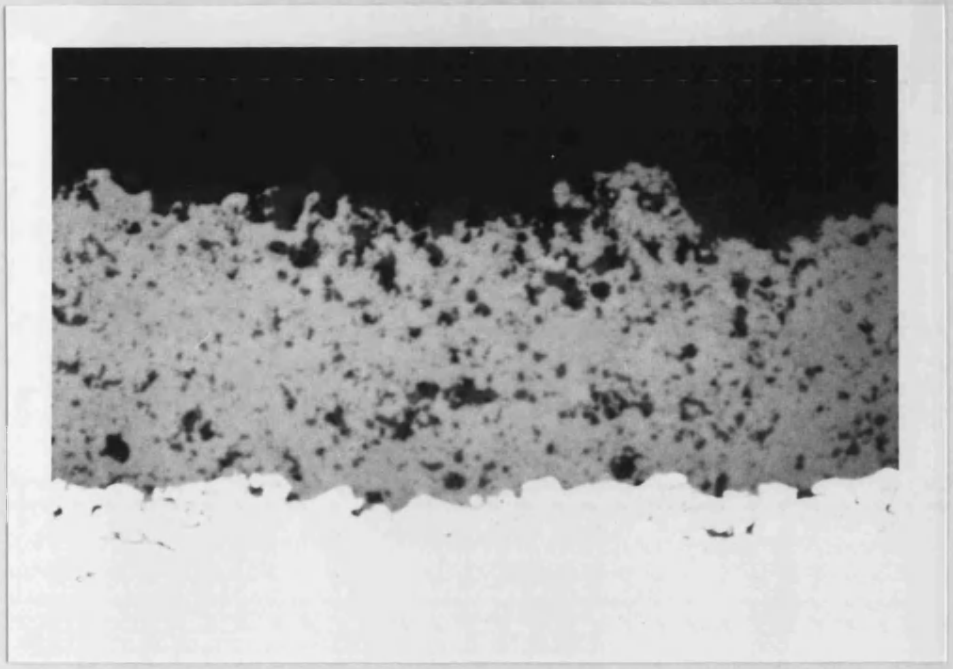

Figure 2.7: Photograph showing 300 micron (nominal) plasma sprayed YSZ coating on aluminium substrate (magnification x128)
YSZ coating - aluminium substrate
Note variation in coating thickness (from 250 to 340 microns)

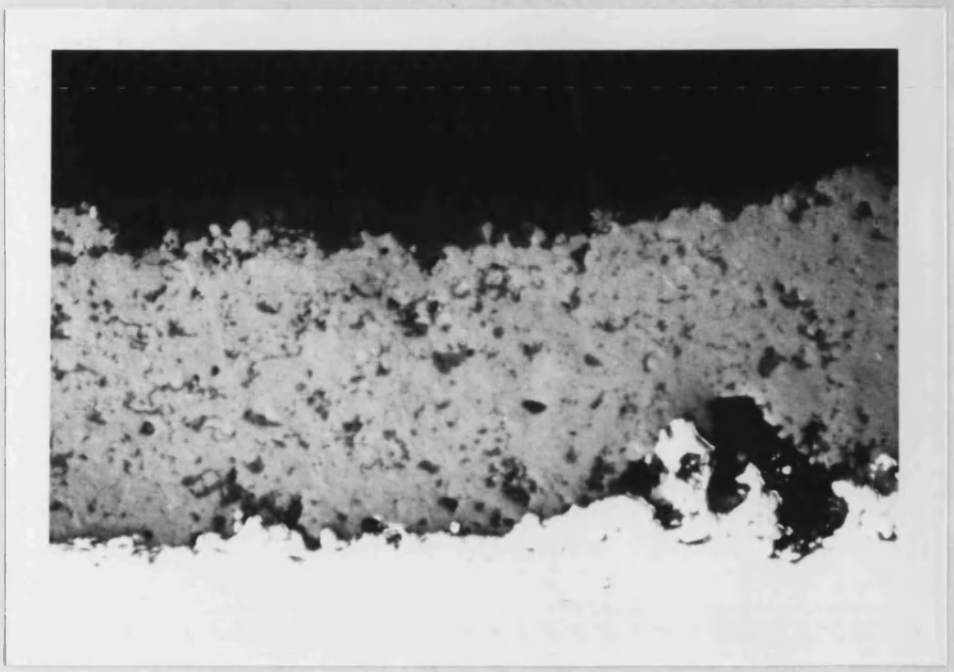

Figure 2.8: Photograph showing 300 micron (nominal) plasma sprayed YSZ coating on aluminium substrate showing interfacial voids and generally poor interfacial adhesion (magnification x128)
YSZ coating - interface - aluminium substrate
Note variation in coating thickness from 290 to 360 microns and down to 195 microns over the large void on the right hand side of the photograph

3 DESTRUCTIVE TESTING OF PLASMA SPRAYED COATINGS

3 DESTRUCTIVE TESTING OF PLASMA SPRAYED COATINGS

Plasma sprayed coating quality control is conventionally achieved by rigid adherence to accepted procedures, and also by the destructive testing of representative samples. Some of the more widely used tests are detailed below (3.1 to 3.4), along with some of the less common tests (3.5).

3.1 Tensile Testing

Tensile strength of coatings is determined by the tensile adhesion test (TAT). The end face of a standard sized rod is sprayed with a coating, and this is then bonded with an epoxy adhesive to an uncoated but otherwise identical rod. The assembly is then pulled apart to determine the load to cause tensile failure. The strength of the coating and the coating/substrate bond determines whether the failure is cohesive or adhesive. This test is easy to do and gives readily interpreted data, but does not simulate typical in service failures. Where the coating strength is high, the adhesive can fail before the coating, so that the test does not apply. It is covered by ASTM standard C633-69.

3.2 Indentation Testing

A diamond pyramid indenter is driven into the coating under a known load. The size of the indent and the size of cracks caused by the indent are related to the strength of the coating. This test gives good comparative information on coating soundness, especially when combined with a Weibull analysis of the data [21]. Two types are available: Rockwell hardness testing, covered by British standards BS4175 and BS891; and Vickers testing covered by BS427.

3.3 Double Cantilever Beam Testing (DCB)

A coated sample is bonded with an adhesive onto an otherwise identical uncoated sample, coated face to prepared but uncoated face. A saw cut or similar notch is induced into the adhesive bond line, extending into the coating, and the sample is subjected to loading. This test is used to find the crack opening displacement load. Both mode I (opening mode) and Mode II (shear mode) can be applied. Mode II is claimed to be superior [22] because it more closely emulates in service failures.

3.4 Metallography

A coated sample is sectioned, mounted and polished for optical or other examination. Study of the coating and interface can reveal soundness, presence of inclusions and thickness. Nicoll et al [23] noted that metallographic preparation is the only part of plasma spraying process control which is not yet fully automated, and they suggested some potential improvements.

3.5 Other Methods

Two cylindrical pieces are butted together end to end, and then coated across the join. The test piece is then subjected to failure in tension, and the load at failure is used to determine the strength of the coating.

Wear resistance is assessed by conventional means, so that the sample need only be sprayed to appropriate dimensions. Similarly, corrosion resistance is assessed by carrying out conventional corrosion tests on the sprayed sample. Erosion testing is again determined by conventional means.

Thermal shock resistance is of particular importance for thermal barrier coatings. At Bath University, coatings are tested on a purpose built rig on which samples are periodically heated and cooled while being monitored for acoustic emissions which are assumed to correlate with cracking events.

Coating stresses can be determined in a number of ways. Hobbs [1] dissolved substrates away from the coatings which then curled due to residual stresses. By measuring the curvature , he was able to determine the stresses. In a similar manner, Hobbs also determined stresses in coatings by bending test coupons. Provided the substrate is sufficiently thin, then the effect of the coating and bond coat can be determined from the overall behaviour of the coupon.

3.6 Shortcomings of the Above and the Need for NDT

All of the above tests yield information about the coating in general terms, and with a sufficiently large sample batch, they can give a statistically useful picture of the soundness of the coating. Nonetheless, it is a feature of destructive tests that they damage or destroy the test piece. Where such tests are being used as a means of quality control, then obviously the components that are actually put into service will be the ones that have not been tested. Additionally, many quality control tests are done on test pieces which have a much simpler geometry than the components intended for service.

In safety critical applications, this may well not be adequate, and each component would need assessment. Thus a suitable non-destructive test is required which is reliable, and, ideally, is easy to use and interpret as well as being fast. The following chapters contain a discussion of non-destructive test systems and their applications.

4 NON DESTRUCTIVE TESTING (NDT)

4 NON DESTRUCTIVE TESTING (NDT)

4.1 The Need For NDT

It has already been mentioned that the integrity of safety critical components is paramount, and thus should not be determined solely by the destructive testing of representative samples. Whenever possible, components should be individually assessed to ensure that specifications are met. In service testing may also be required, and the same standards are needed.

4.2 Types of NDT

There are a number of non-destructive evaluation techniques available, all of which are suitable for different circumstances. The British Institute of Non-Destructive Testing, for example, produces reference lists of which techniques are suitable for locating particular defects [24]. It also suggests suitable techniques according to what material is to be tested. The following is intended as a brief overview of the capabilities of some of the major test techniques illustrating their advantages and drawbacks with particular reference to plasma sprayed coatings. A concise summary in this vein is provided by Reynolds [25].

4.2.1 Visual Inspection

Naked eye inspection is a rapid and inexpensive way to make a preliminary assessment of component quality. Except where the component is transparent or translucent, sub-surface features can only be detected by their effect at the surface such as a bulge over an inclusion or a dip over a void or hole. Whether a surface breaking defect, such as a crack, can be detected depends on the size of the defect, the lighting and surface conditions, and the magnification available.

Visual aids such as microscopes, magnifying endo- and boro-scopes all increase the effectiveness of visual inspection by revealing smaller or otherwise hidden defects. A permanent record of the observation can be made via photographic or video technology, and for inaccessible or hazardous environments, such as radioactive areas, the entire operation can be viewed remotely. If real-time viewing is not required, then image enhancing can be used to improve contrast.

Visual inspection of plasma sprayed coatings will generally only reveal large defects, but the speed of application and the ease of use make it worthwhile. Visual characterisation is a valuable aid to locating suspect regions for further testing.

4.2.2 Mechanical Thickness Measurement

Coating thickness can be determined by measuring the sample dimensions with a micrometer before and after spraying. Results will be less reliable where there is a bond coat, where the substrate is soft, or when the component has a complex geometry. Measuring the coating thickness with a micrometer would clearly give misleading results in this case.

Where the component has a complex geometry, it will be difficult to repeat measurements in the correct position, and it might prove difficult to get the micrometer into some positions, such as turbine roots. This technique involves contact with the sample, so it is not suitable for fragile samples or coatings that need to be free of damage and contamination.

4.2.3 Liquid Penetrant Testing

This is a development of an ancient technique using carbon black to highlight cracks in pottery glazes. A liquid is applied to the clean component and is drawn into any cracks present by capillary action. Excess liquid is then wiped away. The next stage is to apply a fine chalk based powder onto the surface. Dye in flaws is then drawn into the powder thus revealing their presence. The presence of the powder enhances the visibility of the cracks because of lateral dye spreading within the chalk. If a fluorescent dye is used and the sample is illuminated under a suitable uv source, the fluorescence reveals the presence of the defects. Defects as small as 150 nm can be detected [24].

This test is widely used industrially. It is low cost and can be applied to a wide variety of surfaces. Surfaces to be inspected should be clean and non-porous, and can be of any material. The penetrant must be compatible with the test material, however, so that wetting occurs and adverse reactions do not. Only surface breaking defects will be revealed. The application of dye and powder to the sample might be unacceptable in some cases, such as in very high tolerance components.

Plasma sprayed coatings have a rough and porous structure, so that the dye penetrant is absorbed by both defects and harmless features. The structure also makes it difficult to wipe away excess liquid which reduces the effectiveness of this method.

4.2.4 Magnetic Particle Inspection

Magnetic discontinuities in a ferro-magnetic material which are roughly perpendicular to an applied magnetic field will cause leakage fields to form. Finely divided magnetic particles applied to the surface will collect at flux leakages thus revealing the presence of discontinuities. Both surface and near surface defects can be revealed in this way, so long as they are perpendicular to the applied field. It is thus useful to apply the field in two directions to improve the chance of spotting a flaw. Deep defects will not disturb the surface field and thus cannot be detected [26].

This technique can be used on rough or dirty surfaces, but in this case, sensitivity is impaired as the powder accumulates in hollows and at dirty areas. The technique cannot be used on a non-magnetic material. Considering that most plasma sprayed coatings are naturally rough, and that many are non magnetic, this technique is not well suited to their testing.

4.2.5 Radiography

Most types of radiation can be used to inspect samples, but the most commonly used ones are gamma radiation and x-rays [27]. These are absorbed by dense materials, especially by most metals, so that if radiation is passed through a sample, then the denser and thicker parts will absorb most strongly. The image produced on a photographic plate or fluorescent screen will thus indicate the presence of variations in density and thickness. This makes it useful for detecting porosity, cracks parallel to the radiation, thinning and inclusions. It does not readily detect the presence of cracks perpendicular to the radiation path as there is very little variation in thickness.

The image produced can be of real size, or enlarged if required for improved sensitivity. A mini- or micro- focus x-ray source (<100μm) is used, and the film or detector placed a long way from the sample [28]. In x-ray tomography, many x-ray images are taken, and computer imaging techniques are used to build up a complete picture of the sample. The computer screen can then be used to display cross sections of the sample at almost any orientation.

Against the usefulness of the technique are its high cost and the hazards of working with ionising radiations. Some samples might be damaged by the radiation, and low density and weakly absorbing materials such as most polymers and other organic materials, show very little contrast, so sensitivity is low.

It is possible to use other forms of radiation in a similar manner. Beta radiation, alpha particles, positrons and microwaves have some applications, although they tend to be very expensive to use and cannot be made into portable equipment.

4.2.6 Neutron Radiography

Neutrons are neutral charge nuclear particles that, along with protons, form the bulk of the atomic nucleus. Low energy neutrons have very different absorption characteristics to x- and gamma- rays, being absorbed strongly by hydrogen, boron, gadolinium, and indium plus a few other elements excluding the common engineering materials. Thus the technique is complementary to x- and gamma- radiography in which the common engineering materials absorb strongly, but hydrogenous materials do not.

Applications include locating hydrogenous and organic materials, such as cooling fluids, propellants and explosives, and the testing of polymers [24]. They are hazardous, as are x- and gamma- rays, and they are expensive to use and not available in portable equipment, as with alpha- and beta radiation. Neutrons can be detected by suitable films or by an appropriate fluorescent screen. The majority of plasma sprayed coating materials do not absorb neutrons, so this technique is generally inappropriate, except where the objective is to probe behind or within the sample.

4.2.7 Potential Drop Crack Depth Gauging

Two closely spaced electrical contacts are placed in contact with a conductive reference sample and the resistance measured [24]. The gauge is then placed so that the contacts are either side of the crack. The increased path length the current experiences due to having to pass around the crack increases the resistance. The result is compared to a look up table, or the gauge readout can be calibrated to give a direct reading. This is not only contactive, but will only work on conductive materials. If the crack contains a conductive material, then a false reading will result.

4.2.8 Capacitive Roughness Measurement

A rough metallic surface can be considered to consist of a number of conductive peaks with intervening 'valleys' of air. If an electrode plate is placed on the surface, the rough surface acts as a capacitor whose capacitance is a function of the surface roughness. The capacitance is compared with values determined from specimens of known roughness. This is applicable to plasma sprayed coatings provided they are electrically conductive [26].

4.2.9 Acoustic Emission

The propagation and initiation of cracks in materials will generate stress waves which give rise to acoustic events [29]. Acoustic emission testing involves the study of these phenomena. Piezoelectric transducers are attached to the sample or microphones are placed near it during testing. The output is recorded, either on a chart recorder or electronically for subsequent analysis. The distribution of acoustic events and their frequencies are used to determine the nature of the events which caused them.

This is a non-localised technique, in that a probe will pick up an acoustic event which occurs anywhere in the body of the sample. The use of multiple transducers allows the event to be located, because the different distances that the acoustic signal has to travel to each of the transducers will appear as a different time delay in the transducer response.

The microstructure of plasma sprayed coatings will contribute acoustic emission events thus masking the signatures of defects. The exact effect cannot be predicted, but even in the best cases this will complicate the analysis. The structure is also heavily attenuating to sonic energy (see below), and this would also make acoustic emission analysis of plasma sprayed coatings less feasible. Other limitations are that the pulses are very small and that some materials emit only weak acoustic signatures. Moghisi performed an extensive investigation of acoustic emission testing of plasma sprayed coatings [29].

4.2.10 Eddy Currents

If a coil carrying an alternating current is placed near an electrically conductive component, secondary eddy currents will arise within it. These will produce a magnetic field in opposition to that of the coil. The two fields then interact creating a back emf in the coil, thus altering its impedance. In a uniform sample, the emf will be uniform except at edges where field confinement occurs. If there are defects in the component, or other structural irregularities, then the eddy currents, and hence the field will be distorted. The impedance of the coil is thus altered by the presence of a defect or discontinuity within the sample [26,27].

4.2.10.1 Skin Depth

Eddy currents are concentrated in the surface directly under the probe coil, and at large distances below the surface, they are negligible. The skin depth ,S, is the distance in which the magnitude drops by one exponential constant. This is determined by equation 4.1 [153]:

$$S = \sqrt{(2/\mu_r \mu_o \sigma w)} \qquad \text{equation 4.1}$$

where σ is the conductivity, μ_r is the relative magnetic permeability, μ_o is the permeability of free space, and w is the angular frequency $2\pi f$.

Eddy currents induced within a component are dependent on both internal factors (crystal grain size, heat treatment condition, electrical conductivity, magnetic permeability, flaws and physical hardness) and external factors (size and shape of coil, current in coil, coil-sample distance and frequency). If the external factors are known, then the internal values can be inferred.

Both magnitude and phase of the currents can be varied by the presence of discontinuities, and the way in which the two vary can yield information about the nature of the defect. The electrical conductivity of the material affects the generation of eddy currents within the sample. This can be used to determine the conductivity by comparing it with a known standard.

Similarly, sample dimensions must be considered when using eddy current techniques since edge effects will also alter readings. Thus an accurate reading can only be obtained when the sample-probe distance is maintained constant and the sample region is sufficiently remote from edges that edge effects are absent. This may not be possible with small sample dimensions.

4.2.10.2 Lift Off

All eddy current test coils give a reading when switched on even when remote from a conductor. As the probe is brought closer to a conductive sample, the back emf, and hence the impedance, will alter until the probe is in contact with the surface. This effect is known as lift off and imposes a serious limitation on the technique, making it very difficult to measure components with complex geometry. It can be used for determining the thickness of a non conducting coating on a conductive substrate, since the reading will vary according to the distance between the probe and the conductor.

To get best results, it is necessary to back the technique with a sound theoretical knowledge of the affect of the structural/geometrical characteristics of the test piece, as a given response could have a number of potential causes. While insulating materials cannot be directly measured, thin coatings on a conductive substrate can be probed. The roughness of plasma sprayed samples, however, means that they are not ideal test pieces.

4.2.11 Optical Metrology and Holography

4.2.11.1

Laser probes can be used to determine the distance between the laser head and the target by determining the time delay between sending the signal and receiving the reflection. This can be used to determine the thickness of plasma sprayed coatings as they are being sprayed [30]. Very small displacements of the surface can be detected optically, and this is the basis of some optical beam deflection techniques (see later).

Local surface roughness would be a source of error, as would reflections off particles still in flight. The test equipment must operate in close proximity to the plasma flame, and stray radiation from the flame might also cause stray readings. If the sample were translucent, then the apparent distance travelled by the light may not correspond directly with the probe-surface distance.

4.2.11.2

Optical holography involves the use of a split laser beam, one part of which is used as the reference, and the other of which is used to illuminate the sample surface. The combination of these two beams gives rise to an interference pattern - the hologram - which contains information of a three dimensional view of the sample [24]. This reveals only surface-influencing structures. Sub-surface defects which do not affect the surface topography will remain undetected.

4.2.11.3

If a smooth surface is laser illuminated, the surface will appear to be speckled. This speckle is determined by the detailed structure of the surface. Any change in the surface structure will become apparent by the movement of the speckles [24]. The image can, again, be viewed in real time, captured electronically or photographed.

The limitations of this technique are similar to the above. Sample roughness will increase the variability of the signal, and sample translucency will distort the image relative to the sample surface structure.

4.2.12 Thermography

All bodies emit infrared radiation, and the wavelength and intensity of this will depend on the emissivity of the body and its temperature. This infrared radiation can be viewed by an infrared sensitive video camera, or by an infrared viewer. The equipment can be used to monitor the temperature of a body in use, to determine the presence of hot spots and cold spots, or it can be used to monitor the propagation of a heat pulse through the body. Defects in the structure will give rise to local hot or cold regions as the thermal energy propagates at different rates through defective regions.

The required heating for the latter technique can be supplied by a number of methods, and this is described further in the chapter on thermal wave techniques (chapter 5). Thermographic images can be obtained by other means than video imaging. Standard infrared detectors can be used [31], or solid state detectors [32], individually, in linear [33] or area arrays. Also, the sample surface can be painted with heat sensitive cholesteric single crystals which change colour when heated [26].

4.2.13 Ultrasonic Testing

Ultrasonic testing is the most widely used ndt technique at present. It holds this position because it is versatile and has applications in detecting many of the flaws that are industrially undesirable, such as weld defects, and voids. As such, it will be discussed in greater depth than the preceding techniques.

Ultrasonic waves have a frequency greater than the human audio threshhold (20kHz). In fluids, they oscillate in the direction of travel by compression and rarefaction. Two other modes of propagation are observed in solids: transverse or shear waves in which the oscillation occurs perpendicular to the direction travel; and Rayleigh waves which are surface travelling waves whose intensity decays exponentially with distance from the surface. There are other propagation modes, but these are only rarely used for non-destructive testing, and so are not considered here.

The propagation velocity of ultrasonic compression waves is given by equations 4.2 [26]:

$V_C=(B/\rho)^{0.5}$ in a fluid equation 4.2a

$V_C=(E(1-\nu)/(1+\nu)(1-2\nu)\rho)^{0.5}$ in a solid equation 4.2b

where ρ is the density of the medium, ν is the Poisson ratio, E the Young's modulus and B the bulk modulus.

Typical compression wave velocities are 330 m/s in air, about 1500 m/s in fluids, 2-3000 m/s in organic solids and 4-7000 m/s in metallic solids [26]. Shear wave velocity is roughly half the compression wave velocity (equation 4.3).

$$V_s = (G/\rho)^{0.5} \qquad \text{equation 4.3}$$

where G is the shear modulus, and ρ the density.

Rayleigh wave velocity [153] is roughly 90% of shear wave velocity, as given by equation 4.4.

$$V_r/V_s = (.87+1.12\nu)/(1+\nu) \qquad \text{equation 4.4}$$

Features within the medium with dimensions of the order of the wavelength or above will interact with the waves. thus it can be seen that the choice of frequency affects the sensitivity, since a high frequency will give a finer resolution than a low one. Higher frequency waves are, however, attenuated more strongly than low frequency waves, so there must usually be some compromise between the sensitivity and attenuation levels achievable.

4.2.13.2 Generation and Detection of Ultrasound

Ultrasound for ndt is both generated and detected using piezoelectric transducers which exhibit a strain under an applied voltage and yield a voltage when strained. Originally, natural quartz was used, but now a range of synthetic ceramics are used instead. Chief amongst these are barium titanate, lead metaniobate, and lead zirconate titanate (PZT), which is the most widely used. Wave generation is most efficient at the transducer's resonant frequency, which is dictated by the material properties and by the geometry of the transducer. A 5 MHz transducer would thus need to be thicker than a 10 MHz transducer.

Except in the theoretical case of a point source, the ultrasonic emission will emerge from the transducer as a roughly parallel beam before spreading. The distance over which the beam remains parallel or nearly so, is known as the near zone, and is determined by the approximation [26]:

$l \quad d^2/4\lambda$ where d is the transducer diameter

Beyond this, in the far zone, the beam will diverge with an angle α given by equation 4.5

$$\sin(\alpha/2) = 1.12\lambda/d \qquad \text{equation 4.5}$$

As λ tends to d, there is reduced beam propagation, and as $\lambda/d > 1$, the ultrasonic waves will radiate spherically.

Sensitivity increases with distance in the near zone, but falls as the square of the distance in the far zone. For a transducer of given size, a higher frequency will extend the near zone and reduce the extent of beam spreading. It will also give better resolution but the penetrating power is reduced.

These results are for plane plates and unfocussed transducers. Where the sample is not a plane plate, there will be reflections from edges and other surfaces, and the interpretation and analysis will be more complex.

Where a high lateral resolution or localised high intensity is required, ultrasound may be focussed. The relatively large wavelength of ultrasound means that rather than focussing to a point, ultrasonic waves are focussed to a volume with a limiting lower size corresponding to a diameter of one wavelength [34].

Focussing can be achieved either by using an unfocussed transducer and an acoustic lens, or by using a focussed transducers. Acoustic lenses are made of materials whose refractive powers are suitable at the frequencies used. Focussed transducers are made with spherical curvature, and focus to the centre of curvature [34,35]. They are best made from piezoelectric ceramics such as barium titanate, which can be readily ground to the correct geometry, and which can be polarised to oscillate along the radial direction only.

4.2.13.3 Effect of Interfaces

At an interface between two dissimilar media, ultrasonic waves will be partially reflected and partially transmitted. For normal incidence, transmission will be by compression wave. The reflection and transmission coefficients for pressure waves, R and T, can be determined from the acoustic impedance Z of the media where $Z=\rho Vc$:

$$R = (Z2-Z1)/(Z2+Z1) \qquad \text{equation 4.6a}$$

$$T = 2Z2/(Z2+Z1) \qquad \text{equation 4.6b}$$

Z has units of MPa s/m [26].

Reflection at an air /metal interface is near 100% at the frequencies used for ndt. This can be reduced by the use of an intervening layer with intermediate properties - a coupling medium. The use of a coupling fluid (oil/water) reduces the reflection loss for steel to 94%. Transmission efficiency is greatly increased if the thickness of the coupling medium is small, $<<\lambda$. Transmission varies with film thickness, and thus is affected by pressure, so that a probe must be attached with both a high and a constant force or the coupling efficiency will vary and lead to false results.

For non-normal incidence, the transmitted beam will be refracted, and in a solid, both compression and shear waves will be transmitted (Fig 4.1). Similarly, at a solid-solid interface both compression and shear waves will be reflected.

An ultrasonic wave will be reflected from the backface of a thin sample, and by any defects - e.g. cracks, delaminations, porosity, inclusions etc. - which are larger than the wavelength. The test frequency used on materials with a lot of internal features, such as grey cast iron, must be chosen to avoid sensitivity to the internal features. Defects the same size as the graphite flakes or nodules in cast iron will not be distinguished among the response from the graphite particles.

4.2.13.4 Loss Mechanisms

Attenuation of the signal occurs because of scattering at grain boundaries second phase particles and inclusions, and because of internal friction effects. Features within the medium with dimensions of the order of the wavelength or above will interact with the waves. Thus it can be seen that the choice of frequency affects the sensitivity, since a high frequency will give a finer resolution than a low one. Higher frequency waves are, however, attenuated more strongly than low frequency waves. Thus the frequency used will be an optimum for the material under test and the information required from the test. Typical test frequencies are 10-20 MHz for metals, 2-5 MHz for polymers, and 0.5-2.5 MHz for graphite (Table 4.1).

4.2.13.5 C-Scanning

There are a number of ways to produce an image of the test piece from its ultrasonic response. The basis of these techniques is to plot some property relating to the signal as a function of position to give a linear or areal trace. Signal amplitude can be plotted, or more commonly attenuation. A C-scan is an area scan in which attenuation is plotted against position as the sample is raster scanned. The entire test system is immersed in a coupling medium, usually water, and the sample scanned either manually or under computer control via a motor driven x-y stage [36,37].

4.2.13.6 Summary of Ultrasonic NDT

A large amount of data can be gathered by using the three ultrasound propagation modes in solids, and by varying the source/detector configurations (e.g. whether separate probe and detector are used or whether one transducer is used for both functions). The interpretation must, however, be done by a skilled operator to ensure that responses are not attributed to false causes. Choice of operating frequency, probe dimensions, propagation mode and probe positioning also require a skilled operator.

Ultrasound testing involves contact with the sample and is best suited to testing smooth samples. Thick couplant layers can help in some cases, or specially shaped probe heads can be used. Otherwise the sample can be immersed in a tank of coupling fluid e.g. water, although this might not be suitable in all circumstances.

Plasma sprayed ceramic coatings, such as YSZ, attenuate ultrasound very strongly. Patel and Almond [11] showed that losses of 500 dB/cm could be expected. Reflection tests become unattractive because of the extra distance involved over transmission testing. Transmission testing, however, has its own drawbacks in that it is not a single-sided technique as are reflection techniques, and in that there is scope for misalignment between the detector and source probes. Additionally, it is difficult to apply ultrasonic tests to rough components when they have a complex geometry, and it may be undesirable to wet the component due to the possibility that retained water could lead to spalling or other failure in high temperature service.

4.3 Summary of NDT Techniques

There exist many non-destructive test techniques, all of which have a range of benefits and drawbacks. None of those mentioned above is ideally suited to plasma sprayed coatings. While most test requirements could be met from some combination of the above, this would not be convenient, and ideally a single alternative test technique would be found to fulfil all the test requirements of sprayed materials.

In the following section, thermal techniques will be discussed, and will be shown to be an effective method of performing ndt and characterisation of plasma sprayed coatings.

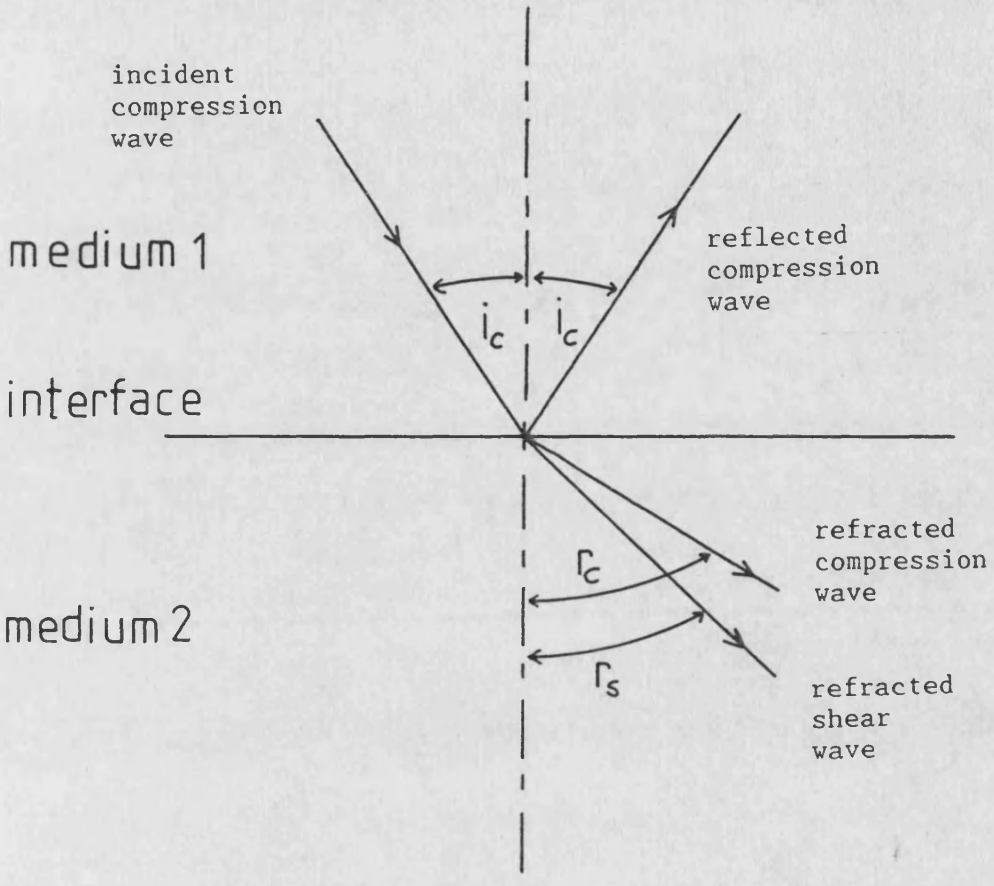

Figure 4.1: Schematic showing refraction and reflection of an incident ultrasonic compression wave at a boundary with a solid medium (after Hull and John [26])

Material	Frequency (MHz)		
	1.25	2.5	5.0
Air	0.26	0.13	0.06
Water	1.14	0.57	0.28
Aluminium	4.95	2.48	1.24
Copper	3.68	1.84	0.92
Steel	4.65	2.32	1.16
Perspex	2.18	1.09	0.55
PGA Graphite			
parallel	2.54 (1 MHz)	1.02	0.51
perpendicular	1.88 (1 MHz)	0.75	0.37

Table 4.1 : Wavelength of ultrasound compression waves (in mm) in some materials (after [26])

5 THERMAL WAVE TECHNIQUES FOR NDT

5 THERMAL WAVE TECHNIQUES FOR NDT

The following chapter outlines the background for thermal ndt techniques, and thermal wave techniques in particular, with an emphasis on photothermal techniques where the sample is heated optically.

5.1 Infrared Emission

All bodies emit electromagnetic radiation in accordance with their temperature as described by the Stefan Boltzmann law.

$$W = \varepsilon\sigma T^4 \qquad \text{equation 5.1}$$

Where W is the total power radiated at all wavelengths, ε is the emissivity of the body, where a perfect emitter has $\varepsilon=1$, and real bodies have $0<\varepsilon<1$, σ is the Stefan Boltzmann constant $5.67*10^{-8}Wm^{-2}K^{-4}$ and T is the absolute temperature of the body. The spectral distribution of this radiation is given by equation 5.2.

$$E_{\lambda-(\lambda-\delta\lambda)} = \frac{8\pi hc}{\lambda^5}\,\frac{1}{(e^{hc/\lambda kT}-1)}\,d\lambda \qquad \text{equation 5.2}$$

where h is Planck's constant, k is Boltzmann's constant, λ is the wavelength, and c is the speed of light. Figure 5.1 shows the spectral distribution of an ideal emitter at a range of temperatures as determined by equation 5.2.

Thus, as the temperature of the body increases, the total amount of radiation emitted increases, and the wavelength of peak emission decreases. The peak emission wavelength is given, to a good approximation, by the Wein law 5.3.

$$\lambda = 2880/T \quad \text{(microns)} \qquad \text{equation 5.3}$$

When the temperature of an emitter varies, the change in emitted power is given by equation 5.4.

$$dW = 4\varepsilon\sigma T^3 dT \qquad \text{equation 5.4}$$

Thus, as T increases, the change in emitted power with temperature rises with T^3 so that techniques relying on the measurement of emitted radiation to determine temperature change (such as the technique used here) should be more sensitive at higher temperatures.

Hence by monitoring the emission of infrared radiation from the sample surface, the surface temperature can be determined. If the monitored signal is passed through a lock-in amplifier and referenced to the modulation signal, then both the phase and amplitude of the signal can be determined.

5.2 Literature Survey on Photoacoustic & Photothermal Phenomena

Photoacoustic and photothermal phenomena are closely related. In the former, the absorption of light by a sample causes heating which leads to the heating of adjacent gas, and thence to the generation of sound via the resultant pressure wave. In the latter, infrared emission results from the surface heating caused by absorption of the incoming radiation.

There follows a brief overview of the history of photoacoustics and its eventual development into the photothermal techniques of the present.

5.2.1 Historical Perspective

The history of photoacoustics dates back to 1880, when Alexander Graham Bell first demonstrated the photophone, a device for transmitting speech via modulated solar radiation [38]. Many theories were proposed to account for its operation, largely centring on the concept that the incoming radiation caused desorption of adsorbed gas on the cell walls [39-41].

There was no sustained interest in the subject, and it was neglected until the 1930's, when the absorption of infrared radiation by gases was used as the basis for the first commercial gas analyser [42]. Photoacoustic spectroscopy is still in use today, as a sensitive test with unique capabilities [43,44].

Further interest in the phenomenon arose in the 1970's when Rosencwaig [45] developed a method of photoacoustic spectroscopy (PAS) applicable to solids and semi-solids,and when Rosencwaig and Gersho [46] and Parker [47] proposed acceptable accounts of the origins of the photoacoustic effect for the simplified case of 1-dimensional heat flow.

One advantage of PAS over other spectroscopic techniques is that it can be used on almost any material. Powders, gels, smears and biological materials can all be studied by PAS [46] along with liquids and gases, for which other techniques can be used. Also, since only the absorbed light is converted to sound, scattered light effects, which cause problems in conventional spectroscopy, are eliminated. It has been shown too that PAS could be used to determine reflectance spectra, even of opaque solids [46].

Other workers considered the limitations of the technique and of the supporting theoretical models. Helander [48] considered the effect of strongly scattering samples, while Aamodt et al [49], McDonald and Wetsel [50], Quimby and Yen [51], and Chow [52] all considered various aspects of the effect of sample cell size on the response, and Kuo and Favro [53] considered the case where the source spot was non-central or had uneven intensity.

In recent years, there has been a number of reviews of photoacoustic and photothermal techniques, covering all aspects of use and equipment [54-56]. A short overview of photothermal techniques is presented below.

5.2.2 Simplifications

Apart from the one-dimensional assumption noted above, other simplifying assumptions are frequently made. The surface is considered to be flat; scattering of incident light is assumed negligible; infrared transparency of the medium is low, so that changes in the emitted radiation can be attributed solely to the surface temperature effects; sinusoidal heating is assumed.

5.2.3 Textual Description of Thermal Waves

Thermal waves are wavelike temperature variations within a body caused by periodic heating [57]. They can be generated in a number of ways, such as electrically, by resistance [58] or induction heating [59], by flames and hot gas jets [60,61], or by irradiation, including ion beams [62], electron beams [56], and electromagnetic radiation [63,64]. Most recent work, however, has been accomplished using modulated laser beams because of the convenience of the spatial and temporal control of the heating they produce [54,56].

The heat then propagates through the medium until equilibrium is achieved. Where the radiation source is constant, this will be a stable equilibrium. Where the light source is modulated the equilibrium will be a dynamic one, with a constant temperature variation superposed upon the background temperature rise.

The variable part of the temperature response has a wavelike character, and it is from this that the term thermal wave arises. It is found that the phase of the temperature cycle lags the illumination by 45 degrees in an opaque, semi-infinite body (appendix A).

Thermal waves describe the way in which the temperature varies within a body with time and distance. Equation 5.5 describes the propagation of a thermal wave with a periodic source term 1/2(1+cos iwt):

$$T = T_o e^{-x/\mu} e^{i(wt-x/\mu)} \qquad \text{equation 5.5}$$

where To is the initial temperature, w is 2π times the modulation frequency, and $\mu=\sqrt{(2k/w\rho C)}$, where k is the thermal conductivity, ρ is the density and C the specific heat capacity of the medium, is the thermal diffusion length in which distance the amplitude decays by one exponential constant, and the phase changes by one radian. This can be written more conveniently as:

$$T = T_o e^{i(wt-\sigma x)} \qquad \text{equation 5.6}$$

where $\sigma=(1+i)/\mu$ is the complex thermal wave number.

This is determined by the physical properties of the medium and by the modulation frequency of the heat source as shown above.

5.2.4 Loss Mechanisms

Thermal waves are heavily damped, losing energy by heating the medium they travel through, so that they interact only over short distances. They thus do not interact over distances greater than 2 or 3 times the thermal diffusion length, because their amplitude becomes negligible at these distances. The thermal thickness, x/μ, is used to describe thickness or distance in terms of this, and where it exceeds these values, then the medium is thermally thick, or the feature thermally distant.

5.2.5 Effect Of Interfaces

When a thermal wave encounters an interface or a region with different thermal properties, there will be a partial reflection and partial transmission of that wave, much as when light encounters a region of different refractive index. The strength of the reflection and the effect it has on the phase of the thermal wave are determined by the degree of thermal mismatch and the relative effusivities of the two media respectively (appendix A).

$$\Gamma_{12} = \frac{1-b}{1+b} \qquad \text{equation 5.7a}$$

$$T_{12} = \frac{2b}{1+b} \qquad \text{equation 5.7b}$$

$$\text{where } b = \frac{[(\rho Ck)_2]^{1/2}}{[(\rho Ck)_1]^{1/2}} \qquad \text{equation 5.8}$$

where the subscripts 1 and 2 refer to the properties of media 1 and 2, and where Γ and T are the reflection and transmission coefficients respectively.

A large thermal mismatch leads to a large reflection coefficient and vice versa. If the wave travels from a high effusivity medium to a low effusivity medium, then the phase remains the same, but when it travels from a low to a high effusivity medium, a phase shift of π radians occurs.

5.2.6 Interference

In a coated sample, where the coating is thermally thin, the reflected component of the thermal wave interferes with the unreflected thermal wave (figure 5.2). By the superposition principle, the resultant wave is the vector sum of the components (figure 5.3). Thus subsurface features which are thermally discontinuous will influence both the magnitude and phase of the resultant surface temperature via this interference. The ac surface temperature can be determined for the simplified 1-dimensional case [46,65,66] by equation 5.9 (appendix A). Here it is assumed that heat flow is one dimensional, the media are homogeneous and isotropic, optical absorption is exponential and infrared transparency is negligible, so that heat transfer is solely by conduction.

$$T_{ac} = \frac{I_o(1-R)n\beta}{2k\sigma(1-\Gamma_{10}\Gamma_{12}e^{-2\sigma l})}\left[\frac{1-e^{-(\beta+\sigma)l}}{\beta+\sigma} + \frac{\Gamma_{12}e^{-2\sigma l}(1-e^{-(\beta-\sigma)l})}{\beta-\sigma}\right]$$

equation 5.9

where I_o is the incident radiation intensity, R is the surface reflectivity, n the optical-thermal conversion efficiency (approximately 1), β is the bulk optical absorption coefficient, k is the thermal conductivity σ the complex thermal wavevector, and l the thickness of the coating, and Γ_{ij} is the reflection coefficient between media i and j.

For an optically opaque coating medium where $\beta l >> 1$, this can be simplified to:

$$T_{ac} = \frac{I_o(1-R)n}{2k\sigma}\left[\frac{1+\Gamma_{12}e^{-2\sigma l}}{1-\Gamma_{10}\Gamma_{12}e^{-2\sigma l}}\right] \qquad \text{equation 5.10}$$

This is illustrated in figure 5.4, which shows how the locus of the phase- and amplitude- thickness plot alters with Γ for an opaque coating medium. As more practical illustrations, figure 5.5 shows the theoretical trace for LC1B, a wear resistant coating on stainless steel, where Γ is negative, and figure 5.6 shows the trace for a coating of WC-Co on mild steel where Γ is positive.

If there is a bond coat, or other intermediate layer, then there will be two interfaces to consider, coating to bond coat, and bond coat to substrate. Thus there will be two reflections to consider. If both interfaces have negative Γ, then the effect will be for both reflections to complement each other, as it would be for both positive. If one were positive and one negative, the relative magnitude of the two coefficients, and the thermal thickness of the coating and bond coats become important.

If the upper interface has large positive Γ, and the lower has negative Γ, then the upper one will dominate, because the extra distance that thermal waves must travel from the lower interface will reduce their amplitude so that their contribution will be less significant than that from the upper one. If, however, the upper boundary had a small negative Γ, and the lower one had a large positive Γ, then which one dominated would depend on the relative magnitudes after considering the extra attenuation incurred by the signal from the lower one in travelling further. In some circumstances, it can be envisaged that the two will combine so as to reduce the reflected contribution to the surface temperature virtually to zero.

$$\Gamma_r = \Gamma_{12} + \Gamma_{23} \exp(-2\sigma_2 l_2) \qquad \text{equation 5.11}$$

where Γ_{ij} is the reflection coefficient between media i & j, and Γ_r is the resultant reflection coefficient. Γ_r determines whether the subsurface structure is visible, and, if so, to what extent.

In some circumstances, where $\Gamma_{23} \exp(-2\sigma_2 l_2) \approx \Gamma_{12}$, then the resultant will be negligible, and no features will be seen. Similarly, when $\Gamma_{23}\exp(-2\sigma_2 l_2) >> \Gamma_{12}$ then the lower interfacial term will be dominant. This requires both a large Γ_{23} and a small value of $\sigma_2 l_2$.

Throughout this work, most of the bond coats were between 50 and 100 microns thick. The thermal diffusion length in the FeCoCrAlY bond coats used was about 700 microns, and that of YSZ about 350 microns at 1 Hz. Here, for a 50 micron bond coat, $\Gamma_{23} \exp(-2\sigma_2 l_2) = -0.24$ and $\Gamma_{12} = -0.50$ so $\Gamma_r = -0.76$. If the bond coat is 100 microns, however, $\Gamma_{23} \exp(-2\sigma_2 l_2) = -0.06$, and $\Gamma_{12} = -0.50$ so Γ_r is -0.56. Thus the bond coat thickness is quite important to the overall effects seen. The effect of bond coat thickness is illustrated in figure 5.7, for a YSZ coating on a stainless steel substrate.

Note that in the above two paragraphs, a simplified picture is presented, in which the effect of multiple thermal wave reflections within the media is ignored.

5.2.7 Imaging and Non-Destructive Evaluation (NDE)

Wong et al [67] were among the first to consider PAS as a means of NDE. Both they, and Kuo et al [68] discussed the detectability of vertical and planar flaws by photoacoustics.

Wong et al [69] and others [70,71] discussed the use of SPAM - scanning photo acoustic microscopy - in which the image is built up by scanning the sample with a tightly focussed laser spot and recording the signal or phase as a function of position. They successfully detected artificial sub-surface flaws in silicon nitride and carbide.

Opsal and Rosencwaig [72,73] considered the use of thermal and plasma waves for depth profiling, and the limitations that applied. Their theoretical explanation was for the simplified case of one dimensional heat transfer within the media.

In a similar manner, Busse [74] examined aluminium test pieces containing sub-surface holes by PA techniques. His work revealed the advantages of using phase sensitive detection to increase the resolution in defect detection, and Aithal et al [75] used photoacoustic methods to characterise sub-surface defects of teflon, alumina and boron nitride in metallic coating - metallic substrate systems.

Von Gutfeld and Melcher [76] were the first to use photoacoustic waves for imaging in 1977. This was still in use much later, when Rosencwaig and Opsal [77] discussed the use of thermoacoustic imaging, a microscopic technique based on thermal waves.

Opsal and Rosencwaig [77] discussed a thermal wave microscope using electron beam heating with a spot size of 0.5 microns. The modulation required for thermal wave imaging was found to allow operation of the sem facility with only a small drop in resolution. They compared the images available with both techniques and used piezoelectric detection of the elastic waves generated by the thermal waves.

Sheard [78] described a thermal wave microscope that worked with infrared detection, rather than the widely used thermo-elastic detection. The spot size used was 2 microns, and the temperature excursions were detected down to 10^{-4}K. The configuration was that the laser heated the sample surface, and the emitted infrared radiation then passed through an infrared filter to be focussed onto the detector.

5.3 Techniques

There are a number of thermal wave based techniques in use for ndt at present. Some of these are discussed briefly below.

5.3.1 Optical Beam deflection (Mirage Effect)

In optical beam deflection (OBD) the heating (pump) laser heats the sample surface which then heats the overlying gas. This changes the refractive index of the gas, and hence deflects a surface skimming probe laser beam (figure 5.8a). The deflection of the probe beam is related to the surface temperature and hence to the sample's thermal structure. A related technique, in which a parallel probe beam is deflected by thermally induced surface distortion (figure 5.8b), was discussed by Murphy and Aamodt [79], and Mandelis et al [80]. This was claimed to be better suited to testing rough and irregular surfaces because of the absence of the surface skimming probe beam.

Other variations have been proposed, Jackson et al [81], for example, discussed photothermal deflection spectroscopy and distinguished it from OBD. They detected the gradient of the refractive index of the overlying gas rather than its curvature, and determined that surface roughness as small as 0.1 microns could be resolved.

The lateral resolution of OBD is determined by the spot diameter or the thermal diffusion length, with a limit of 1-10 microns [79]. The system with parallel pump and probe beams had a similar resolution of a few microns.

5.3.2 Photothermal Radiometry (PTR)

In photothermal radiometry, the infrared radiation emitted by a heated sample is monitored. The interaction of thermal energy, in the form of thermal waves, with the subsurface thermal structure alters the surface temperature response, and hence the emitted infrared radiation.

The basic theory of photothermal radiometry was expounded by Santos and Miranda [82] who interpreted the response with respect to the time and frequency domains and by Kanstad and Nordal [83]. Their conclusions suggested that the capabilities of PTR were similar to photoacoustic (PA) techniques, but the method has the advantage that it is totally non-contacting, and that it could be used in vacuum.

Kanstad and Nordal [83] dated interest in photothermal radiometry to 1978-81, with its uses in spectroscopy and commented "If a general setup is required that is inexpensive, flexible and simple to use, it appears that chopped cw would be the choice". They also recommended the use of a chopper with as few and as large blades as possible to reduce phase noise, which they claimed was always worse than the manufacturers specifications. They noted too that for a very thin alumina layer on polished aluminium, coherent noise contributed 20-30% of the signal.

They [83] said that for translucent media, if the optical absorption coefficient is smaller than the infrared absorption coefficient then the detector looks deeply into the sample and little contrast remains (PTR saturation).

They also referred to a case in which a chopper let through the illuminating source and the emitted signal alternately [84].

Busse [85,86] explored the use of photothermal transmission in comparison to photoacoustics. He considered the response obtained through wedge shaped samples, and concluded that photothermal techniques offered superior resolution to photoacoustics, but that transmission techniques could not be used for determining the depth of thermal features such as defects. This problem was subsequently overcome by Busse's stereoscopic transmission system [87], here used with two sources, but equally applicable with one source and two detectors or a spatially modulated source, which allowed depth to be determined to a high degree of accuracy with only a simple geometrical calculation.

Kaufman et al [88] distinguished between discrete scanning, in which a spot is heated to a quasi static state, in which case both phase and amplitude information can be obtained, and continuous scanning in which only the amplitude can be monitored.

5.3.3 Thermal Wave Interferometry (TWI)

Bennett and Patty [65] gave an introduction to thermal wave interferometry in 1982. Developing the work of Rosencwaig and Gersho, [46], they showed that TWI could be used in PAS, and they verified the effects of thermal thickness (thickness/ thermal diffusion length) on the response by adjusting both the modulation frequency and the sample thickness.

Almond et al [11] claimed 2% sensitivity in thickness measurement due to 0.1° detector limit on phase noise when measuring step coating thickness and locating adhesion defects in NiCrC coatings on 316 steel. While Miller [89] claimed a rather more impressive 1 part in 500 depth resolution with phase detection.

5.3.4 Transient Techniques

When a heating pulse is applied to a semi-infinite sample, the rate at which the temperature decays is determined by the diffusivity of the medium [57]. If a real sample (ie not semi-infinite) contains a thermally different region, then the rate at which the temperature decays in this is also different.

Thus, if the heat pulse encounters such a region, eg a substrate or a defect, the rate at which the surface temperature changes will alter. If the sample temperature is monitored, either in transmission [90] or reflection [91], the presence of the thermally distinct region will be revealed by a change of slope in the temperature-time plot [92]. The depth and diffusivity of the region can be determined by further analysis of the trace [93].

The control of the heating pulse, and the associated synchronisation of the monitoring equipment is achieved electronically, which makes this system more complex and expensive than the chopped continuous wave technique used in this work. There are, however, advantages in the effective penetration depth possible, the higher test speed, especially when testing low diffusivity materials, and higher precision.

5.3.5 Thermography

Cielo et al [94] described the use of infrared thermography on carbon fibre composites. They noted that the detection times required varied with the square of defect depth so that for a 100 micron ceramic coating, the time per reading was 10ms, a 1cm coating would take 100s.

Leung and Tam [95] used pulsed photothermal radiometry (PPTR) to examine thin polycarbonate films epoxied to gold coated copper substrates with the intention of assessing the curing of the resin. They determined the thermal contact resistance of the epoxy to within 1%.

Long and Anderson [96] used the same technique to investigate the response of layered structures, and successfully measured the depth of a sub-skin layer in a volunteer's forearm, thus showing succesfully that noninvasive in vivo examinations were feasible.

They [96] assumed that if the optical absorption coefficient was $>5*10^4/m$, then it could be regarded as infinite. They also considered the possibility of using infrared transmitting fibres in endoscopy, based on the work of Zur and Katzir [97].

Thermography is particularly well suited to rapid measuring of thin samples, eg for detecting disbonds and adhesion defects in laminated structures such as aluminium laminates and composites. They [96] used tungsten halide lamps to heat a 50*50 mm area to +15°C and also used a cold thermal wave by cooling a preheated sample with a gas jet. Two interpretations were described, space domain where an undamaged region is used as a reference to eliminate effects of power variation between flashes, and time domain where the signal from one spot is compared at two different times to eliminate effects of local emissivity variations.

Tam and Sontag [98] used PPTR to determine the thickness of air gaps beneath opaque surface films. The films were heated by about 10°C. They used a 20 micron polycarbonate film filled with carbon black, and the film-substrate distance was controlled by a piezoelectric actuator to within 1 micron. A large uniform spot 200mm^2 was used (15mm diameter) to heat the sample.

For an air gap <1mm, radiation losses were lower than conduction losses, and since all the gaps considered were below 500 microns, radiation effects were neglected. They obtained agreement between theoretical curves and experiment for air gaps between 30 and 500 microns. Below that, the gap thickness is approaching the mean free path of air, and the gas properties alter as the gas approximates a two dimensional fluid [99].

Where there were rough surfaces, the roughness enhanced the apparent air gap width, so that, for example, a 1 micron rough gap appeared to be 10 microns. PPTR was used to determine gap thickness by interpretation of the curves obtained. Since thin air gaps behave much like thermal contact resistances, the same method could be used for determining these.

In similar manner, Kuo et al [100,101] described a system in which a focussed laser was scanned across a sample synchronised with an IR video camera scan. This allowed time resolutions on the sub-millisecond scale, and an entire video scanned vertical line could be acquired at the scan rate. This configuration can be considered as a moving line of point detectors because of the rapid scan rate. The laser spot is a fixed time interval ahead of the detector position, and this can be varied to provide further information. It can be used to detect sub-micron films which would require nanosecond response times with an unfocussed heat source. The computing power required is intensive but gives good results.

5.4 Commercial Systems

There is a small number of commercially available thermal wave test systems. Siemens produce the Aladin system which is moveable, with a mobile probe head attached to the main body by a long umbilical cord [102]. A laser pulse is applied to the sample in a predetermined raster pattern followed by infrared detection at a specific time delay to record the thermal response. This equipment comes with computer facilities to analyse the data, and display and print out the resulting image. This is a versatile system which can be used to measure thickness of coatings and locate cracks on a variety of materials.

Two other systems are known, Laser Inspect 2000 from Vanzetti Inc [103], and the Thermal Wave Impedance Scanner from Hanford Engineering Laboratory [104]. Hartikainen and Luukkala [105] discussed a test system which they claimed to be developing for industrial use.

The recent advances in diode laser technology have raised the available power from a few milliwatts or tens of milliwatts to watt level outputs [106]. The power available from diode lasers is thus now comparable with that of gas lasers, and at a competitive price. The significant reduction in physical bulk and special services requirements, combined with their higher operational lifetimes in comparison with gas tubes, makes the prospect of reasonably priced, truly portable test systems a realistic one.

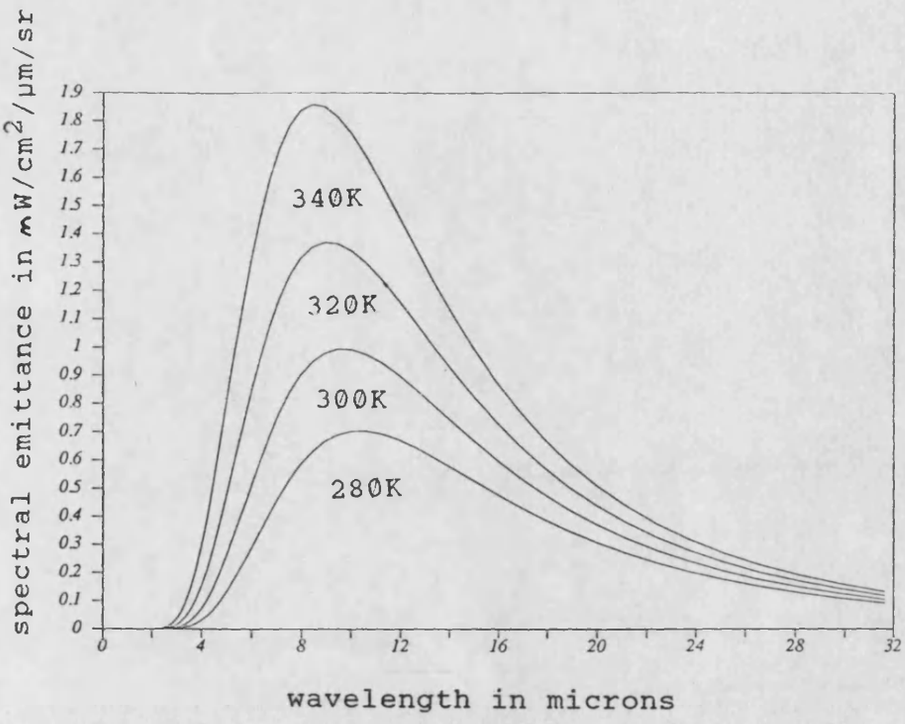

Figure 5.1 : Variation of spectral emittance of a black-body sample with wavelength at four different temperatures

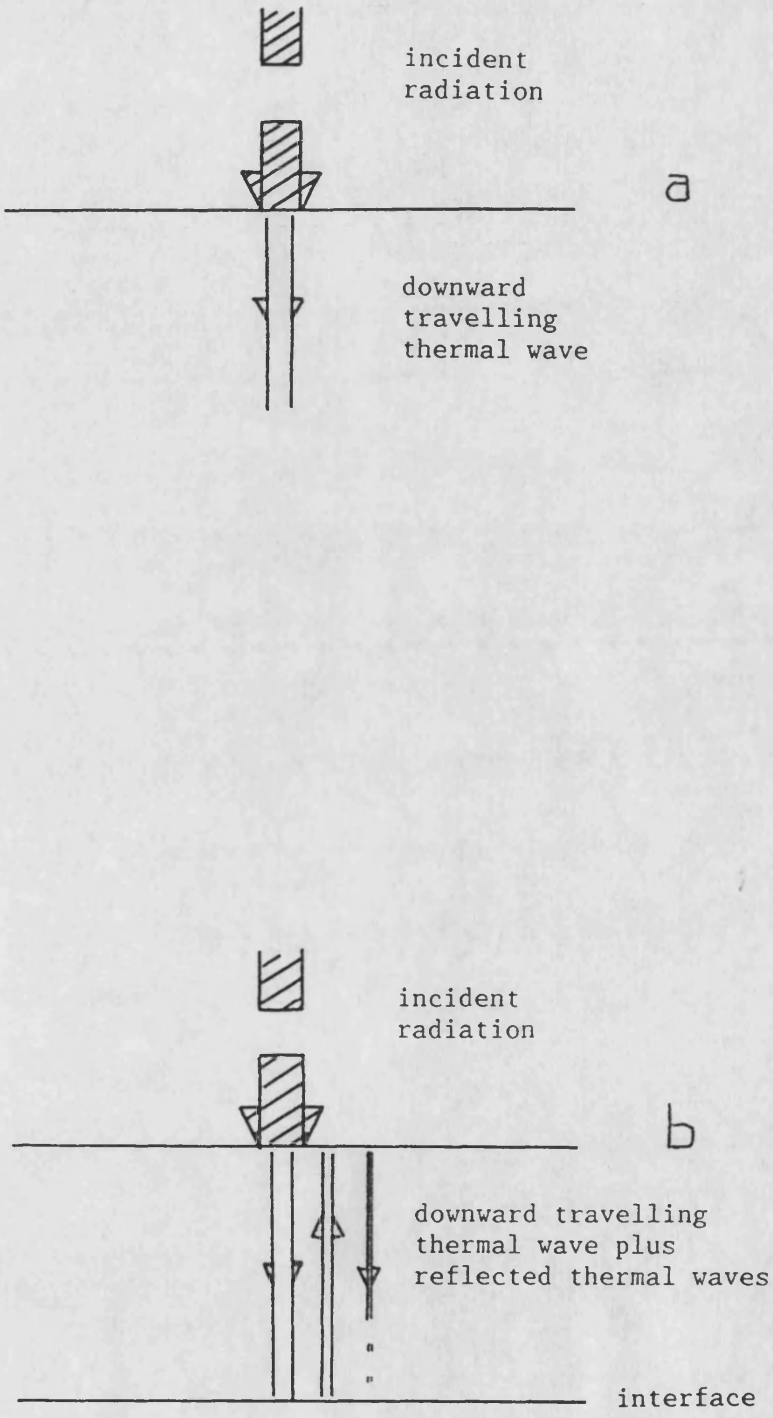

Figure 5.2: Schematic showing reflection of thermal waves in a thermally thin optically opaque medium
a) thermally thick medium - no reflection from thermally distant interface
b) thermally thin medium - reflection of thermal wave leads to interference

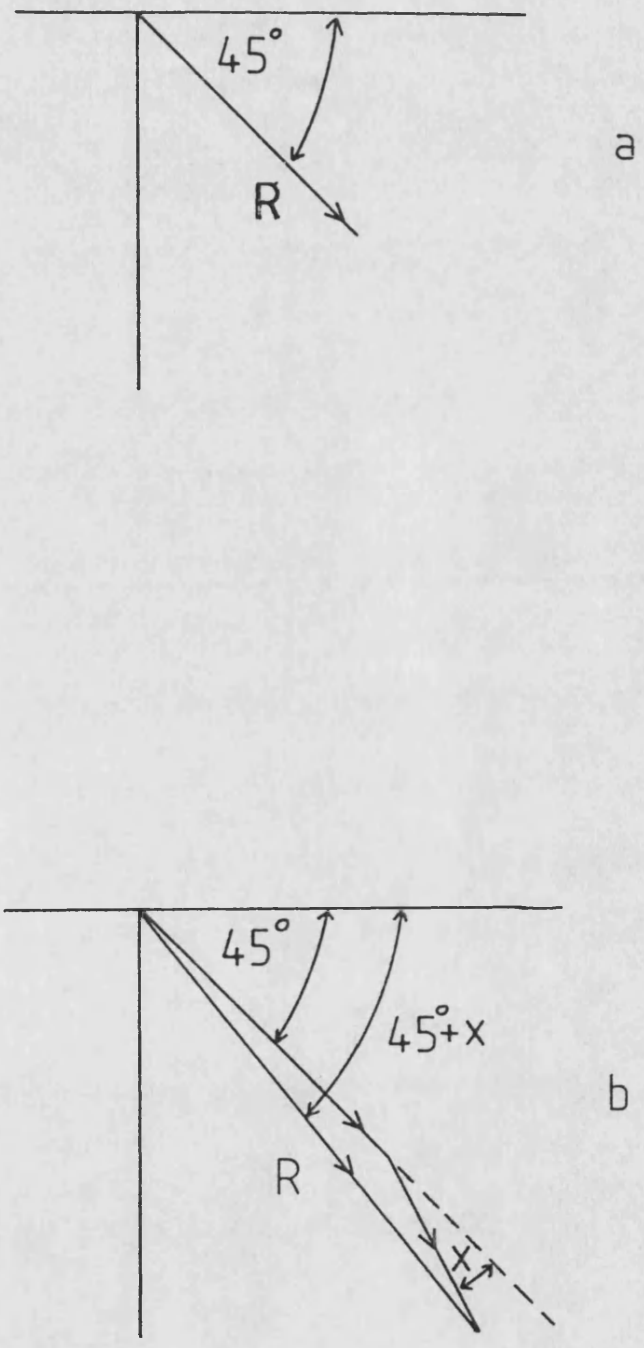

Figure 5.3: Phasor representation of thermal wave in thermally thick and thermally thin opaque media
a) thermally thick: resultant R, phase lag 45°
b) thermally thin : resultant R, phase lag 45° plus interference term x

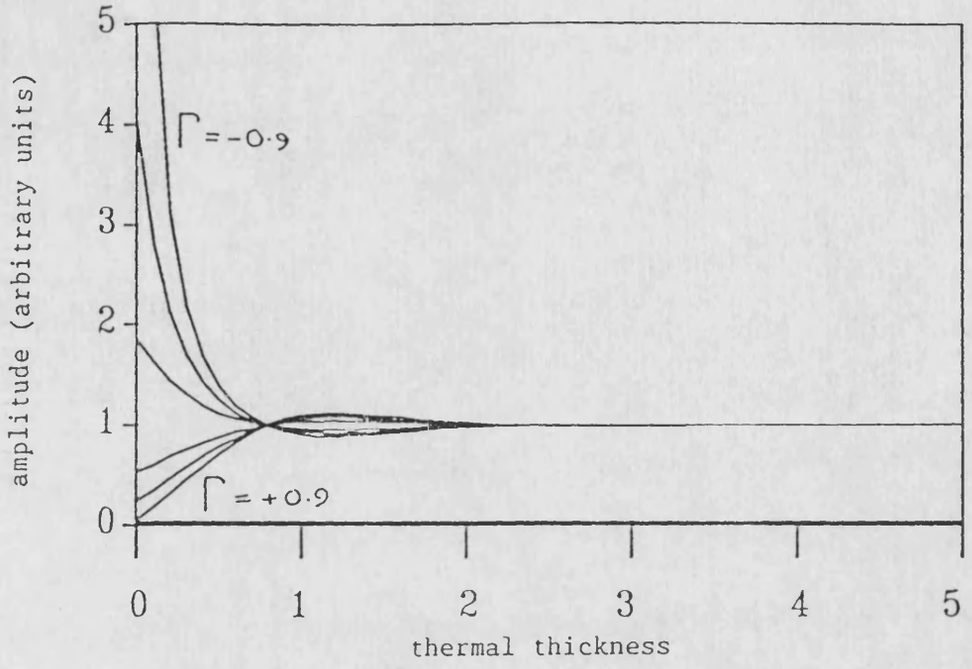

Figure 5.4a : Computer modelled variation of amplitude with thermal thickness at various interfacial reflection coefficient, Γ.
Γ = +0.9,+0.6,+0.3,-0.3,-0.6,-0.9

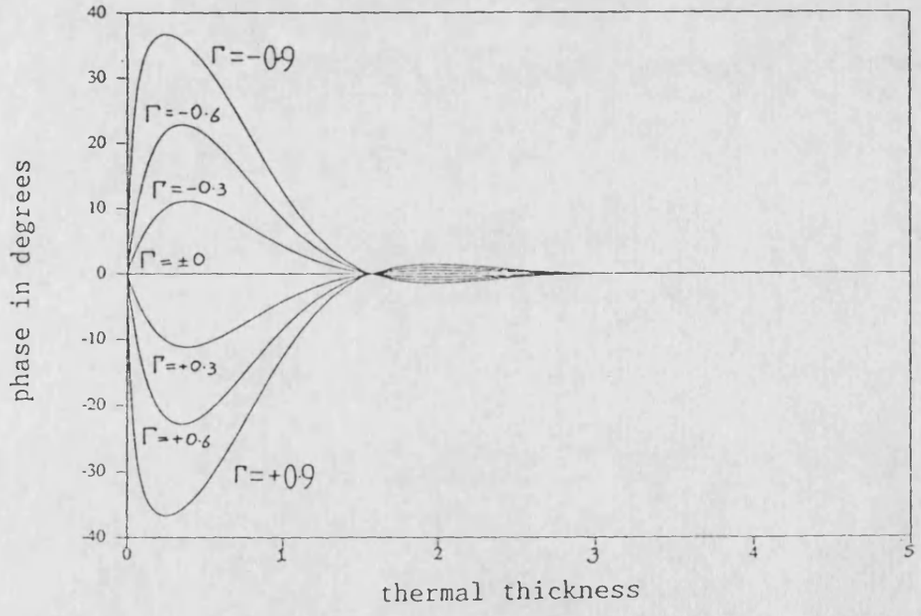

Figure 5.4b : Computer modelled variation of phase with thermal thickness at various interfacial reflection coefficient, Γ.
Γ = +0.9,+0.6,+0.3,-0.3,-0.6,-0.9

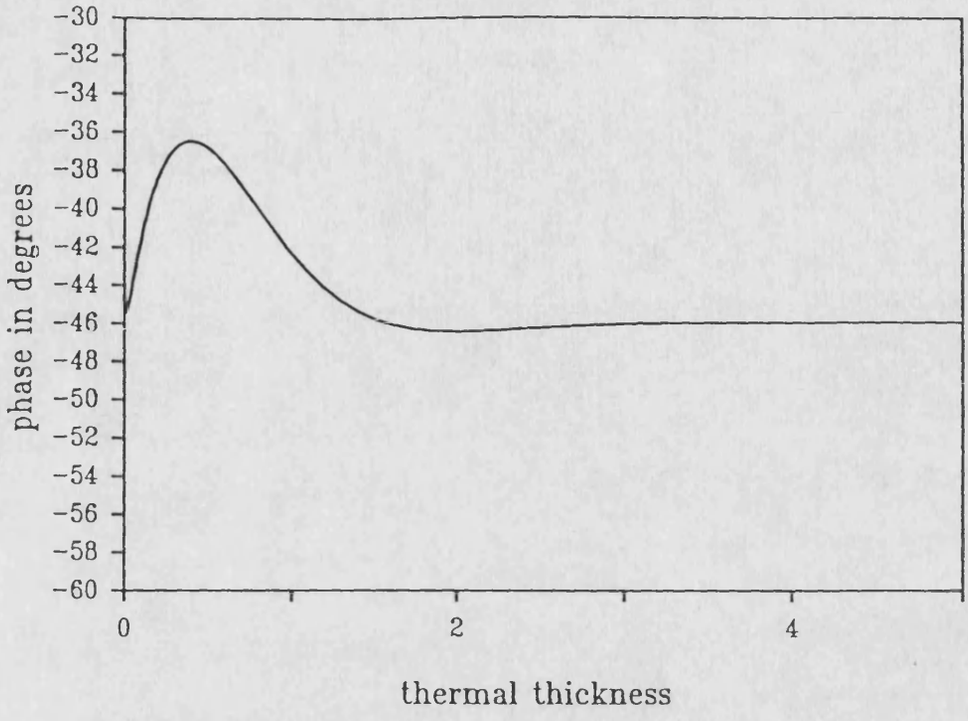

Figure 5.5 Variation of phase with coating thickness for LC1B on stainless steel f = 20 Hz

(modelled using equation A.21)

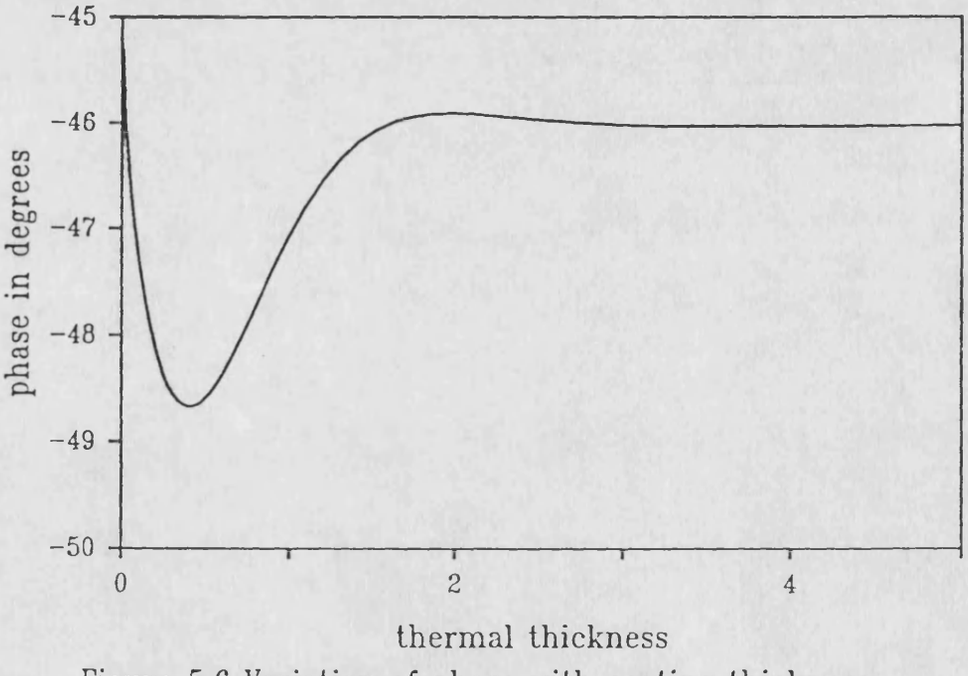

Figure 5.6 Variation of phase with coating thickness for WC/Co on titanium f = 50 Hz

(modelled using equation A.21)

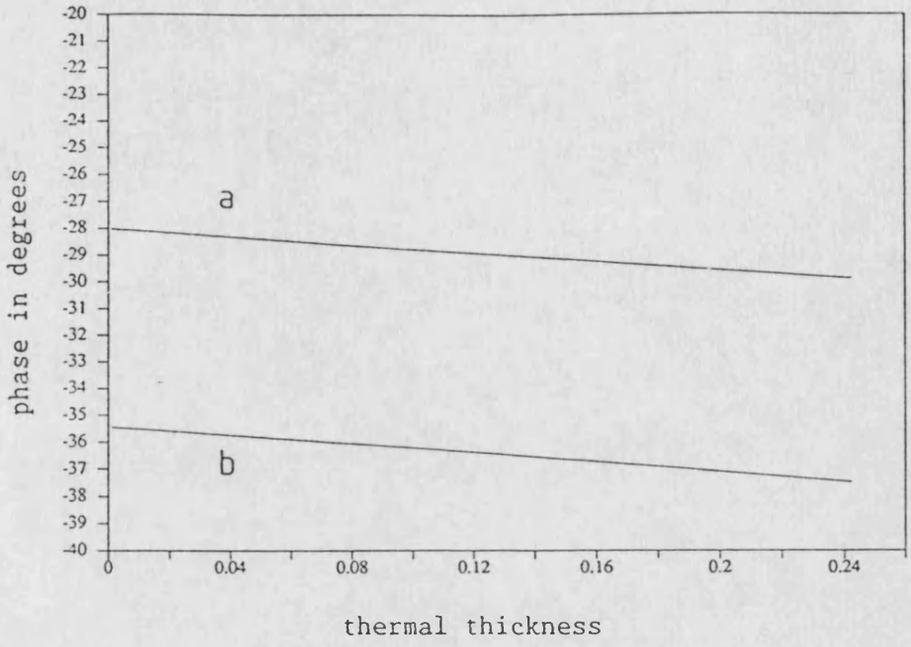

Figure 5.7 : Variation of phase with thermal thickness of a NiCrAlY bond coat between a 250 micron YSZ coating and a 316 steel at different coating optical absorption coefficients
a) β = 10^6/m b) β = 10^4/m

(modelled using equation A.29)

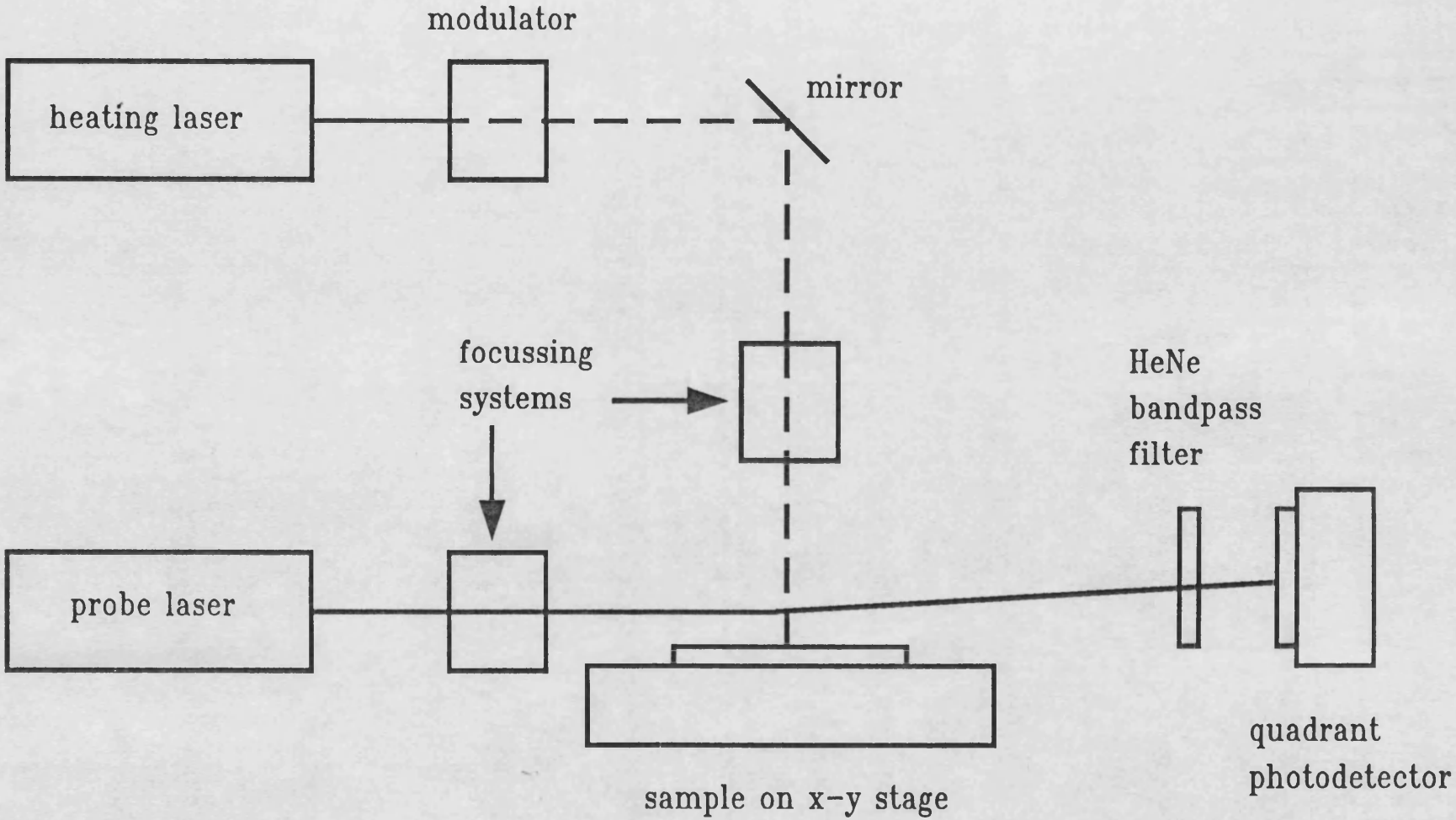

Figure 5.8 Schematic diagram of an optical beam deflection (mirage effect) test system

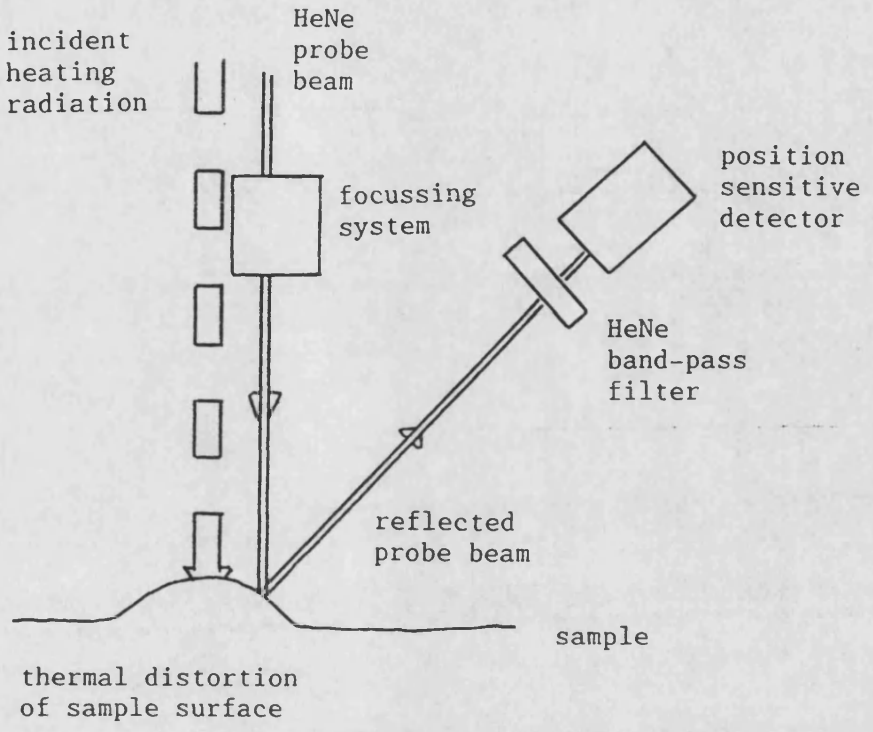

Figure 5.9: Schematic of vertical optical beam deflection system (probe beam shown displaced for clarity)

6 EQUIPMENT

6 EQUIPMENT

Different equipment configurations were used in the course of this work. The layout shown in figure 6.1 was used for the major part of this work with minor variations (figure 6.2). They are described briefly below.

A 5W argon laser [107] was modulated either mechanically with a Brookdeal model 9497 [108] or by a model 304D acousto-optic cell [107]. When required, the light was focussed using either a 50 mm diameter 200mm focal length biconvex lens or a 10 mm diameter asphere [109], and filtered through a water filled quartz cell to remove infrared radiation from the laser output.

The sample was mounted on a motor driven x-y stage [110]. This stage allowed a maximum 300mm horizontal movement, and a maximum 100mm vertical movement. An IBM PC XT computer [111] was used to control the stage movement via an IBM GPIB board [111]. Infrared radiation emitted from the heated sample was received by a TGS pyroelectric detector [112]. Stray optical radiation was eliminated either by placing a dielectric interference filter directly over the detector window [113] or by placing a plastic infrared filter film over the collector mirror opening [114]. The infrared signal was referenced to the modulation signal via a lock-in amplifier [108] and the phase and amplitude data were sent to the PC via the GPIB board.

6.1 Detector

The aniline doped tri-glycine sulphate pyroelectric detector was chosen for a number of reasons, principally that it had a low noise at the low frequencies required for testing (<100Hz); it had a sufficiently fast response so that the received signal followed the modulation; it was sensitive to wavelengths above 3 microns; and it did not require cryogenic cooling. Other detectors available were a Cadmium Mercury Telluride (CMT) semiconductor detector which required cryogenic cooling but had a better high frequency response (>100Hz)[115], and a solid state detector which had a lower sensitivity and a poorer overall response [116].

The amount of radiation received was increased by fitting an ellipsoidal collector mirror [109] to the detector which increased the signal by up to 35 fold [117]. The infrared transmitting filter film was fitted over the opening of this because optical radiation would otherwise be absorbed and generate secondary heat sources. This also kept the collector mirror surface free of contamination, and protected the infrared fibres (section 8).

6.2 Power Meter

A power meter [118] was used to measure optical transmission. The meter used was sensitive to a wide wavelength range, and was position insensitive. Provided that all the emitted/transmitted radiation enters the meter window, the exact alignment is unimportant. This was considered important when measuring divergent sources, where the intensity varied across the beam.

6.3 Infrared Source

A commercial 25 watt soldering iron was used as an infrared source. The tip temperature was controlled by passing the mains power through a variac controller with a range of 0 to 260 volts ac at 13 amps. A bit intended for decorative work was found to give a more even temperature distribution, and a higher peak temperature. This item had a 10 mm diameter and the pattern comprised a number of raised concentric circles.

6.4 Infrared Fibre Testing

Infrared fibres were tested using the 25 watt source mentioned above. The TGS detector was used with the mechanical light chopper modulating the incident infrared radiation. Reference readings were taken with the TGS detector at the collector mirror focus. When the fibres were tested, they were held at the mirror focus within a dummy detector. The real detector was then placed facing away from the infrared source to eliminate direct illumination, and the fibre tip was placed facing the detector element.

6.5 Lock-in Amplifier

The lock-in amplifier gave relative phase values, rather than the absolute phase values required. For much of the work, this was unimportant because phase differences were needed. Where absolute phase values were needed, a reference could be obtained from a thermally thick opaque sample, which would have a thermal wave phase lag of 45 degrees.

6.6 System Performance Limitations

The ultimate performance of the system is limited by the minimum detectable temperature difference, δT, that the system can detect. This is the temperature change that results in a response in the detector which is equal to the noise equivalent power (NEP). This may be expressed by equation 6.1.

$$\delta T = NEP * \frac{1}{4\varepsilon\sigma(T_o)^3 A} * \frac{1}{T_m(\lambda)\sin^2\eta} \qquad \text{equation 6.1}$$

where NEP is a detector dependent term, $1/[4\varepsilon\sigma(T_o)^3 A]$ is a sample emission term, in which T_o is ambient temperature and A is the emitting area, and $1/[T_m(\lambda)\sin^2\eta]$ is a collection efficiency term where $T_m(\lambda)$ is an IR transmission term, and η is the angle of acceptance.

At room temperature, assuming radiation from the laser spot and an acceptance angle of 30 degrees, δT is $2.2*10^{-3}$K. Typically, the periodic sample surface temperature will be 15.2K for a YSZ sample (see appendix A.10), and should thus be readily detected.

If an infrared fibre is used to direct emitted IR radiation to the detector, $T_m(\lambda)$ will decrease, and hence δT increase, by a factor determined by the overall transmission loss of the fibre link (about 14dB at 10.6μm and about 10dB more at other IR wavelengths). Hence δT_{fibre} will be about 1K. The influence of coupling or misalignment losses and geometrical factors is discussed in section 8.

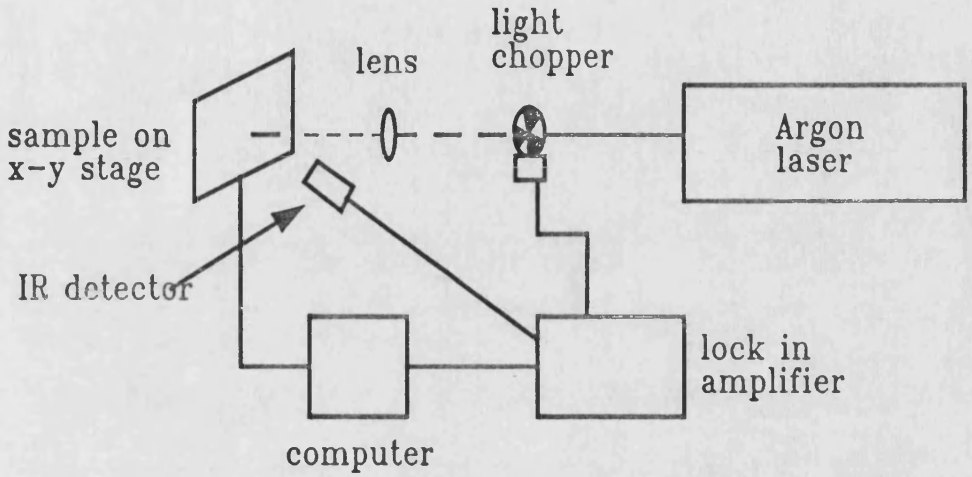

Figure 6.1: Schematic diagram of thermal wave test system

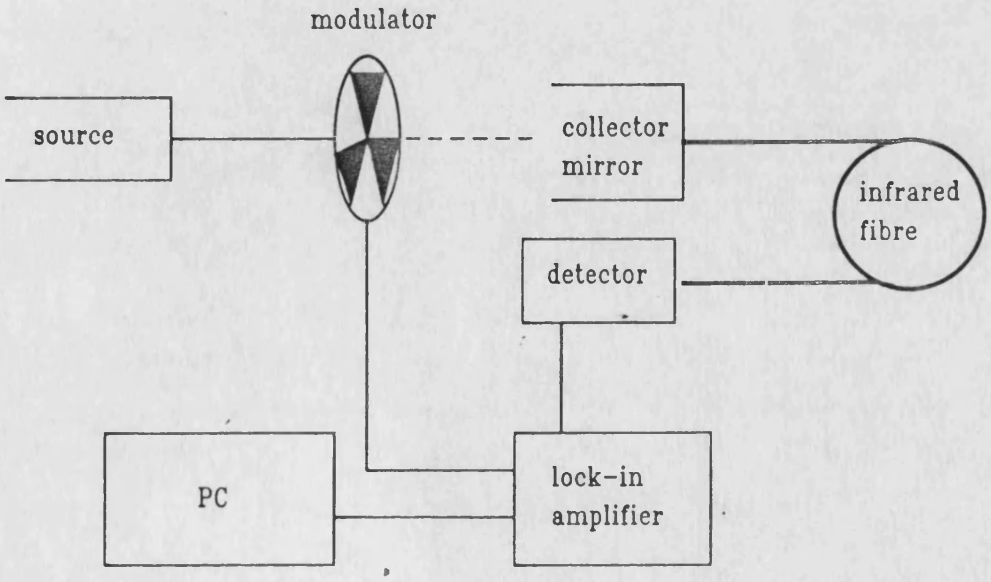

Figure 6.2 Schematic diagram of infrared test rig: with fibre

7 YSZ COATINGS

7 YSZ COATINGS

Yttria stabilised zirconia thermal barrier coatings were sprayed by a number of manufacturers, as well as in-house. All were optically translucent, and had yttria contents between 7% and 20%.

7.1 Thickness Measurement

Thermal barrier coatings, and other protective coatings, need to meet thickness requirements to perform adequately. They also need to have appropriate physical properties, and to be mechanically sound. Thermal waves have properties which suggest that they might be suitable for determining thickness and other properties.

7.1.1 Background

The variation of surface temperature phase with coating thickness is illustrated in figures 5.4 to 5.6, and with thermal conductivity in figure 7.1. The curves have a characteristic shape determined by the sign and magnitude of the reflection coefficient Γ. The phase reaches a maximum at a coating thickness of approximately half the thermal diffusion length μ, and tails off to the thermally thick value at approximately one and a half thermal diffusion lengths. Between these two positions, the slope is roughly linear. Thus if the phase can be determined for an unknown sample, the thickness can be estimated by reference to a previously generated characteristic curve.

The characteristic curve may be obtained in two ways: measuring a number of samples of known thickness (or a single, step-coated sample); and measuring a sample of known thickness at a number of modulation frequencies, so changing its thermal thickness. Both these techniques can be combined if required. The unknown sample is then tested, and the phase obtained compared to the reference curve to determine the coating thickness. Patel and Almond [8] estimated that this could be done to +/- 2% in a nickel-chrome carbide (LC1B) coating. The precision is dependent on the noise of the measurement system, and on the magnitude of the interference effects, which is determined by the reflection coefficient Γ, and on the thickness of the coating.

7.1.2 Experimental Work

Plasma sprayed YSZ coatings on thermally thick stainless steel substrates were tested. One set (A) comprised eight separate test pieces with nominal thicknesses supplied, and the other (B) consisted of two step coated samples with nominal thicknesses between 2 and 20 thousandths of an inch (51-508 microns). These were tested at a number of frequencies, and the results recorded (figure 7.2). The curves have the characteristic shapes predicted by theory. The manufacturer claimed that sample b had a higher density than sample a. It also had a higher optical absorption. Curve a) has a broader phase peak than b) because the thermal diffusion length is determined by $k^{1/2}$, so the optical effect dominates.

7.2 Coating Characterisation

The shape of the phase-thickness trace shown in figures 5.4 to 5.6, is determined in part by the modulation frequency and in part by the physical properties of the materials. It has this effect both through the reflection coefficient, and the thermal diffusion length. The thermal diffusion length effect can be eliminated by plotting thermal thickness rather than actual thickness. It is possible to model the curve from a knowledge of the properties of the coatings and the appropriate equations (equation 5.9). These modelled curves can be used in an iterative process to determine the physical properties of the sample, especially the thermal conductivity whcih is dependent on the geometry of the porosity as well as the absolute void content.

The effect of thermal conductivity on the shape of the characteristic curves is shown in figure 7.1. Note that this is also illustrative of the variations that would be observed if any of the other physical variables affecting the diffusivity (density and specific heat capacity) altered.

One way of characterising the coating is to measure the response of a sample of known thickness, and to generate computer modelled curves to find what values give a close fit. The modulation frequency will be known, and all that is required is to systematically vary the coating properties within reasonable bounds until a fit is obtained. The substrate will generally be monolithic and thermally thick, so that it will be free of the variability found in plasma sprayed coatings.

An alternative and complementary method, is to plot out the phase-thickness curve, and to note the thickness at which the phase peak occurs, and where the trace levels off at thermal thickness. These points can be used to estimate $\mu/2$ and $3\mu/2$ respectively. Where the coating is translucent, the curve is modified by interference between surface- and sub-surface- generated thermal waves. Where the coating is thermally thick, the phase can be used to estimate the optical absorption coefficient β from equation 7.2 (below).

7.3 Optical Translucency

When a coating is not opaque, but radiation only passes a limited way into the medium, so that transmission is small or negligible, then the coating is considered to be translucent.

7.3.1 Background

Much previous work has concentrated on the thermal wave study of plasma sprayed metallic and metalloid coatings, such as nickel chrome carbide anti-wear coatings (LC1B) [11, 115-117]. These are all optically opaque at practical thicknesses, and all have a relatively high thermal conductivity (6 W/m/K or more). As a consequence of their opacity, incoming optical radiation is absorbed, and hence heat is generated, at or near the surface. Thermal waves therefore effectively originate from a single position. This is approximately true for many materials, particularly metallic ones, in which absorption occurs very close to the surface. If the Beer law is followed, then the absorption will take the form:

$$I/I_0 = \beta \exp(-\beta x) \qquad \text{equation 7.1}$$

where I is the intensity at a distance x into the surface, and I_0 is the initial intensity at x = 0.

If the medium is only partially absorbing, ie it is translucent, then it will absorb light over an extended region dictated by the optical absorption coefficient β. The optical absorption length, or optical penetration depth, is defined as $1/\beta$, and is analogous to the thermal diffusion length μ. This is denoted μ_o or μ_{opt}, to distinguish it from $\mu_{thermal}$.

Light absorption over an extended region leads to heat generation over an extended region. Thus thermal waves originate from an extended region in a translucent medium. Thermal waves originating from different depths beneath the surface interfere with each other. This then alters the surface temperature response even in the absence of an interface or defect. Where there is also an interface and/or a defect, then interference will arise between the thermal waves from different origins, and their reflected components as well. This is illustrated in figure 7.3.

Where the optical penetration depth is larger than the thermal diffusion length, energy will be deposited within the sample that cannot reach the surface. The sample is said to be photothermally saturated [83]. Except for weakly absorbing samples, this situation would normally arise only at high frequencies where μ is small.

Throughout this work, the term 'translucent' is used to describe a medium in which significant optical absorption occurs both within and beneath the surface. It is shown in appendix A that the phase lag, ϕ, due to translucency in a thermally thick semi-infinite medium (ie one in which reflected waves can be neglected) is approximated by:

$$\phi = -\tan^{-1}\{(\beta+2\sigma)/\beta\} \qquad \text{equation 7.2}$$

where the minus sign indicates a phase lag, and σ is the complex thermal wave number (see appendix A.12).

It can be seen from equation 7.2, that if β is very large, ie the medium is opaque, then the phase reduces to a lag of 45°. If β is set to 0, ie totally non-absorbing, then it can be seen that the phase will be -90°, which is what would be expected.

Figures 7.4 and 7.5 show how variations in β influence the response of a coated medium. At large β, the response is the same as for an opaque sample. At very low β it is the same as for a transparent medium. At intermediate values, it is seen that the phase peak is slightly shifted to the right, and the peak is reduced. The phase at large thickness is reduced as expected.

It can be seen from figure 7.5 and table 7.1 that the peak to large-thickness phase difference is constant over the range of β. The standards must, however have identical β to the sample and to each other. If this were not the case, then the variation due to changes of β could be more significant than the phase changes due to thickness. This would detract from the overall accuracy and reliability of the technique.

7.3.2 Preparation of Samples for Optical Measurement

Plasma sprayed coatings are macroscopic entities in that they are agglomerations of particles whose individual properties are not necessarily shared by the bulk structure. As such, there is a minimum thickness below which the sample becomes a collection of particles on a substrate, rather than a coating. This minimum will generally be between about two and five times the particle thickness, which corresponds to a coating thickness of 16-75 microns for a typical particle size of 8-15 microns.

Optical absorption coefficients in YSZ were expected to be of the order of 10^4/m, giving optical penetration depths between about 10 and 100 microns. Optical pentration would thus be negligible in any such coating thicker than about 300 microns, and possibly as thin as 30 microns. However, experience with coatings which had been removed from substrates suggested that coatings thinner than about 300 microns were extremely fragile.

The coatings were thus sprayed onto glass microscope slides for support, with 1 to 8 passes, giving a nominal coating thickness of 30-240 microns. Differential thickness measurements made before and after spraying showed significant deviation from the nominal figures (table 7.2).

Initially, this deviation was thought to be due to penetration of the YSZ particles into the relatively soft glass. Subsequent optical microscopy revealed an exceptionally smooth interface (figure 7.6), although one sample showed a feature suggesting that some surface penetration had occured (figure 7.7).

7.3.3 Measurement of Optical Transmission

The laser power transmitted through an uncoated glass microscope slide was measured with a power meter [118]. The plain glass slide was then replaced with the coated samples and the process repeated. The transmitted power was measured and referenced to the blank slide to determine the transmission loss due to the coating. The plain glass slide was used to eliminate the effects of substrate absorption and reflection losses. Surface roughness effects were assumed similar for all coated samples, so that its effect could be neglected.

Two coated samples were tested with the sprayed coating both facing to the laser and away from it. The two transmission figures were found to be within 5% for both samples, which was similar to the repeatability of the values from the same side. The transmission of one single unsupported sample 348 microns thick was also measured in direct comparison with the unobstructed laser beam.

The values of absorption coefficient obtained are shown in table 7.3. The high apparent value of β for some samples might be due to the coating becoming deeply embedded in the substrate. The differential thickness would be reduced by this, so the apparent absorption per unit thickness would be increased. Sample 3 showed no thickness change after spraying, although it was obvious that the coating had been succesfully deposited. The heat distribution on the spraying table could have been uneven, and a higher temperature would lead to a softening of the glass and deeper embedding of the spray particles. Figure 7.6 shows, however, that the YSZ-glass interface is exceptionally smooth, although figure 7.7 contains features that are suggestive of particle embedment.

It can be seen that the measured values of β are all of a similar order, ranging from 18500 to 32000/m, apart from the unsupported sample which could not be securely clamped because of its fragility and small size, which gave a low reading of 14600/m. Visual estimates also tie in with the measured, modelled and photothermally obtained values, although they are generally somewhat lower (table 7.3).

7.4 Infrared Translucency

Just as optical translucency has an effect on the overall thermal wave response, the infrared transparency also has an affect. In this case, if the infrared radiation is transmitted through the sample, then the coating/body temperature is no longer solely determined by thermal conduction. The apparent thermal conductivity therefore increases, and the existing thermal wave model would become progressively less accurate.

7.4.1 Background

Metallic coatings are opaque to both optical and near-infrared radiation. Ceramics, however, can be more transparent in the infrared than optically. An example would be heavy metal fluoride glasses which have theoretical losses at 2.5 microns which are lower than those at optical frequencies [119]. If a test material were to exhibit significant infrared transparency, then radiation heating would occur, and the distributed source would need to be considered, as noted above.

7.4.2 Infrared Transmission of YSZ

YSZ has an infrared transparency to about 6 microns such that it has been proposed as an infrared window material for 2-6 microns [120]. If the YSZ coatings had a high transparency at the peak infrared emission wavelengths of interest here, then the existing modelling assumptions would be invalid as noted above.

The majority of thermal wave testing is done at slightly above room temperature, so that peak emission occurs between 8-13 microns (figure 5.1, equation 5.3). At 200°C, the peak emission wavelength is about 6 microns, so that the YSZ will be weakly absorbing to a significant proportion of the radiation.

Savage [120] presented a spectral transmittance curve for a 1mm thick YSZ window (figure 7.8). This showed a 75% transmittance from 0.3 to 6 microns and virtually zero beyond 7.5 microns. Considering that the optical penetration length in YSZ ranges between about 30 and 125 microns (table 7.3), it can be seen that the infrared penetration depth for wavelengths longer than 7.5 microns will be considerably smaller. Thus the material may be considered as effectively opaque to infrared radiation, provided the sample temperature does not rise significantly above 200°C.

7.5 Comparison of Opaque and Translucent Coatings

A plasma sprayed YSZ step coating on mild steel was darkened with drawing ink over half its surface. Spot measurements were then made at a number of frequencies on each step, on both darkened and undarkened regions.

The phase and amplitude values obtained are shown in table 7.4. The phase values are plotted as a function of coating thickness in figure 7.9. The amplitude is dependent on surface optical properties, such as reflectivity, as well as opacity, so it is not plotted here.

It can be seen that the traces for the opaque and translucent regions are similar in shape, but are phase shifted relative to one another. This is what the theory predicts (see above). At large thickness, where the sample is thermally thick, the phase for an opaque medium will be -45° (equation 7.2). This permits the absolute phase lag to be determined from the phase difference at thermal thickness between the translucent and opaque samples, even where only relative phase values can be obtained.

Where the thermal diffusion length is known, the optical absorption coefficient can be determined. In figure 7.9 the thermal diffusion length can be estimated from the position at which the plot levels off. The values of β obtained from this are shown in table 7.3.

7.6 Defects

When a thermal wave encounters a laminar defect, (one parallel to the surface), it will be partially reflected as at an interface. If the defect is small with respect to the spot size, its effect will be averaged out over the spot area, so that its effect will be small. If it is relatively large, it will show up as a change in the surface temperature profile as a consequence of thermal wave interference. If the defect is vertical, such as a crack, then the effect is similar in that thermal energy will be partially reflected, and it will manifest its presence through the surface temperature (see chapter 9).

There are two major types of defects to consider: those which can be considered to contain an extra layer, such as where there is a large inclusion; and those in which the defect can be considered as a thin air gap or a thermal contact resistance.

7.6.1 Air Gaps

The effect of an air gap can be represented in equation 5.9 by replacing Γ with the reflection coefficient for the air gap, Γ_{gap} (equation 7.3) [10].

$$\Gamma_{gap} = \frac{\Gamma_{21} + \Gamma_{23}\exp(-2\sigma 212)}{1 + \Gamma_{21}\Gamma_{23}\exp(-2\sigma 212)} \qquad \text{equation 7.3}$$

where the subscripts $_{1-3}$ refer to the top layer, defect medium and substrate respectively, and the gap is l_2 wide.

Air and other gases in gaps of the same dimensions or smaller than their mean free path become effectively more insulating [99]. They then behave anisotropically, conducting better parallel to the faces than across the gap (appendix B).

There are thus some thicknesses for any gas filled 'air gap' for which the effective thermal conductivity is reduced, and they are therefore thermally more insulating, so that there will be enhanced reflection. In extreme cases, where the gap is << mean free path, then the gas behaves as a liquid film, and conduction across the gap is enhanced. Figures 7.10 and 7.11 show the effect of air gap thickness on thermal wave phase for two practical systems, YSZ on 316 steel, and LC1B (a wear resistant coating) on mild steel.

If the defect is a discrete intervening layer of some other medium, liquid or solid, then the analysis is best done by considering the intermediate medium as a separate layer, and treating the system as having n+1 layers rather than n layers with a modified reflection coefficient.

The effect of air gap thickness on thermal wave response has been noted previously [121]. It was noted then that sensitivity was lower for ceramic coatings such as YSZ than with metallic coatings such as LC1B. This is because the effusivity of YSZ is nearer that of air than is the effusivity of LC1B.

7.6.2 Thermal Contact Resistance

Where there is imperfect contact between the coating and the substrate, such as would be the case with an adhesion defect, or between two regions of coating, which could be due to partial cracking or microporosity, then this may be modelled as a thermal contact resistance. A partial intervening layer such as a foil mesh, a pierced film or similar can also be considered to act as a thermal contact resistance more conveniently than by considering it as an incomplete layer. For perfect thermal contact between two surfaces, the thermal contact resistance is zero, and where there is no thermal contact, then the thermal contact resistance is infinite. For an intermediate case, the contact resistance may be modelled by replacing Γ with Γ_{tcr} in equation 5.9, where:

$$\Gamma_{tcr} = \frac{1 - b_{21} + Rk_2\sigma_2}{1 + b_{21} + Rk_2\sigma_2} \qquad \text{equation} \quad 7.4$$

where the subscript 1 refers to the covering layer and 2 to the defect medium, and R is the thermal contact resistance [10].

The different responses are shown schematically in figure 7.12, between full contact, no contact and partial contact.

7.6.3 Effect of Translucency

If the coating is translucent, but no significant radiation penetrates to the defect, then the defect representation used for the opaque case can be applied, with an allowance made for light absorption solely within the coating .

Figure 7.13 shows the locus for a defect in two media differing only in optical absorption coefficient, referenced to an otherwise identical defect free medium. Two values of β are used. It can be seen that both opaque and translucent traces change sign at some point. It is also apparent that this point changes with sample translucency.

When the sample is opaque, the defect becomes undetectable (ie delta phase = 0°) at a larger thickness than is the case for translucent media. Thus, a lower modulation frequency is required to detect this point. This is an advantage in locating the defect, since it suggests that the defect can be found at a greater depth than is possible with translucent samples. The problem is then to confirm that the feature seen is a defect.

If a defect is scanned at frequencies near to that required to get zero phase change, then the lower frequencies will show a peak opposed to the peak found at higher frequencies. This dissappearance and reversal of the peak is used to confirm the presence of the defect. If this occurs at higher frequencies, then confirmation is more readily obtained than at lower frequencies. With ceramics in particular, the frequencies required are low, and the need to scan at a range of frequencies could drive the equipment beyond its operational range. In translucent samples, this is less likely to occur, even though the defects are less easily detected in the first place.

7.6.4 Summary of Effects in Translucent Media

Defects can be found in translucent samples, but at smaller depths. However, the ease of confirming that the effects are due to a defect is greater than with opaque samples. Again the optical properties need to be constant throughout to avoid misleading results.

Translucency does not influence sensitivity for coating thickness or property measurement, provided that it is constant for all the samples and standards used. If the standards or samples have variable translucency, then the phase changes due to this will obscure the thicknes effects.

If β can be determined then this is beneficial, and in many cases this is straightforward. If, however, β varies within or across a sample then it is very much harder to determine accurately.

7.6.5 Manufacture of Defective Samples

Defective plasma sprayed coatings are generally made by spraying onto inadequately prepared substrates [29,117]. They may, for example, be left greasy, or be deliberately contaminated with foreign bodies, such as pieces of adhesive tape. Plasma sprayed coating quality control is, however, achieved in the first instance by rigid adherence to previously determined spray conditions. Thus the typical approach to defect manufacture runs the risk that the coating over the defective region will be substandard. If this occurs, then the response attributed to the defect will instead originate both from the coating and from the substandard coating.

To avoid this, an alternative approach was used. Defects were attached to sound coatings which had been removed from their substrates and bond coats, and a replacement substrate was then affixed. Low conductivity defects were made by attaching a strip of pvc insulating tape to the coating. High conductivity defects were simulated by attaching a strip of aluminium foil. The sample was then mounted in either a hot pressed phenolic resin, (for the high conductivity defect), or a copper filled conductive acrylic resin for the low conductivity defect.

Thus two types of sample were produced, one with a low conductivity defect and a conductive substrate, and one with a high conductivity defect and a low conductivity substrate. No evidence was seen of damage to the coatings as a result of this process (see figures 7.16 and 7.19).

7.6.6 Experimental Work

Line scans were made over the ceramic region of the high conductivity defect sample at a range of frequencies between 0.5 and 3 Hz. Phase and amplitude plots were then produced to show the variation with position (figure 7.14). The samples were then darkened with drawing ink and the scans repeated (figure 7.15). It was expected that the defects would show up on the sample scan, and at some frequency undergo a phase reversal.

No evidence was seen of the high conductivity defect at any of the frequencies used apart from a slight rise in the amplitude at 2Hz (figure 7.15b trace b). The sample was then slit lengthwise on a diamond wheel for inspection. The aluminium foil strip was clearly visible (figure 7.16), but was thermally very thin ($1/\mu$ about 0.03).

The low conductivity defect sample was similarly scanned, and showed a phase peak at 0.5Hz, which largely disappeared at 0.6Hz, and which reappeared reversed at 1 Hz and above (figure 7.17a). The amplitude response showed a gradual reduction of the peak as the frequency increased, due to the greater thermal distance of the defect (figure 7.17b). The amplitude peaks in figure 7.17b are shown displaced for clarity.

The sample was then darkened with drawing ink, to eliminate the effects of sample translucency, and rescanned. The phase position plots at 0.5, 1.0,2.0 and 3.0Hz are shown in figure 7.18a. The phase change is clearly visible at the site of the defect. The amplitude peaks in figure 7.18b clearly show the location of the defect, and diminish at higher frequency as the thermal distance of the defect below the surface increases.

The phase reversal occurred at a higher frequency in the opaque sample than in the translucent sample, which corresponds with the theory.

The sample was then slit on the diamond wheel as with the previous sample. The pvc defect is clearly seen (figure 7.19).

7.7 Damaged Samples - Background

Coated samples are likely to suffer various types of damage while in service. This is likely to include surface abrasion, impact damage, cracking, and damage induced by machining. The effects of this type of gross damage on thermal wave response were investigated using deliberately damaged samples. It was intended that this should reveal any responses that could be used to characterise such defects.

7.7.1 Preparation of Samples

The sample was subjected to a number of abuses. It was thermally shocked five times from 500°C to ambient in water, and dropped 1 metre onto a hard surface so that existing cracks would have an opportunity to grow. Two holes were drilled into the substrate from the rear, one blind hole which caused a slight raising of the coating, and one hole was drilled through the sample, leaving swarf around the edges. Another part was struck with a 5mm diameter centre punch, to simulate impact damage, and another part was scored with a scalpel blade and 'burnt' with a tightly focussed laser beam at high power.

Low power optical microscopy revealed fine cracks to the centre of the coating above the blind hole (figure 7.20), and swarf around the through hole. The impacted region was noticeably flatter, and the scalpel cut left a shallow groove on the surface, while the laser burn left a 30 micron wide glossy flat track in the middle of a 250 micron wide path of discoloured coating. It was calculated that the central part of the mark had reached approximately 8000K, and it was concluded that the zirconia had melted and possibly vitrified.

7.7.2 Damaged Sample Results

The 'damaged' sample has been considered region by region, for clarity, considering the two holes, the impacted region, the knife-cut and the laser damaged regions. A small crack was found near the knife-cut, but did not appear to extend across the region scanned, although there is the possibility that its thermal influence might extend further than this [122,123].

7.7.2.1 Blind Hole

Between 2 and 20Hz, this feature, lying between scanning step numbers 40 and 80 on the scan (figure 7.21), shows up as a pair of phase dips with a raised central peak, giving a 'w' shaped profile which diminishes with frequency. This is reasonable, since there will be edge effects at both sides of the hole, which will diminish toward the centre (see also chapter 9 and figure 9.2). The response at 40 Hz includes a large peak not previously seen. The phase response is not clearly distinguished at 0.5 Hz, but can be tentatively identified.

At frequencies between 0.5 and 20Hz, the blind hole causes an increase in amplitude corresponding to the edges with a dip between the peaks (figure 7.21). There is no distinguishable response at 40Hz which suggests that the remaining coating is thermally thick. In comparison, the phase response is still clear, as would be expected after Busse [124].

The darkened sample (figure 7.22) shows a much clearer response at all frequencies. The phase signature is clear at 0.5Hz, and the amplitude response is still present at 40Hz. It should be noted that above about 34Hz, the optical penetration depth μ_o exceeds the thermal diffusion length μ, so that contrast is lost because energy is deposited in the sample that cannot influence the surface temperature. This effect is not present in the darkened sample.

7.7.2.2 Through Hole

This feature had irregular edges, where swarf had been forced up during drilling. The phase response is essentially 'm' shaped, with two shoulders and a dip in the middle (figure 7.21). At lower frequencies, the aluminium surrounding the hole caused a secondary dip around the 'm' of the hole itself. The amplitude peaked near the centre of the hole, but overall gave a less clear signature.

In contrast, the darkened sample showed a much more pronounced amplitude drop over the hole, and the phase response was less well structured above 5Hz, although it was clear at and below 2Hz (figure 7.22).

7.7.2.3 Impacted Region

This area had been struck with a centre punch (between step numbers 200 and 250 on the trace in 7.21 corresponding to 50 and 62.5mm respectively), and visible inspection revealed a faint mark on the surface, with some reduction in the surface roughness. An irregular phase response, mostly comprising phase drops, can be identified at all the test frequencies (figure 7.22). In contrast, the amplitude shows many peaks in this region at up to 10Hz, which become significantly smaller at 20Hz, and are not observed at 40Hz (figure 7.22).

The darkened sample shows large amplitude peaks at up to 40Hz (figure 7.21), and a reduced phase signature at 0.5Hz (figure 7.21). The phase response changes from comprising mostly drops at low frequency to mostly peaks at higher frequencies at about 10Hz (figure 7.21).

7.7.2.4 Scored Region and Laser Burnt Region

There are no features on either the phase or amplitude traces that can be positively associated with either of these two features for both darkened and undarkened samples (figures 7.21-7.22). There are, however, a number of small amplitude peaks which appear to be associated with phase dips. There are no known causes for these features.

7.7.2.5 Summary of Damaged Samples

The damaged sample had features that were detected in this test, but it also had features that went undetected along with responses for features that were not known. It was found that darkening the sample could be beneficial, in that it generally extended the amplitude response to higher frequencies, and permitted lower laser powers to be used. In some cases, the phase response was found to become worse as the amplitude signature improved. While some damage was revealed, it does not appear that these particular flaws could be readily characterised.

Saturation occured in the translucent sample, in that the thermal diffusion length is smaller than the optical diffusion length above about 34Hz. Heat generation thus occured where it could not influence the surface teperature of the sample. This would account for the improved resolution when the samples are darkened.

7.8 Summary on YSZ Testing

The physical properties of a range of YSZ samples were determined, and a number of typical in-service and pre-existing defects were also detected. In the latter case, a novel method of simulating such defects was developed. It proved difficult to associate the visible features on the sample with simulated in-service damage to the thermal signatures of the features. This is attributed to the complex nature of such defects: they generally consist of a number of features that can interact both constructively and destructively. While it might be possible to predict the thermal response from the damage known to be present, it would be impossible to fully characterise the damage from the thermal wave response alone.

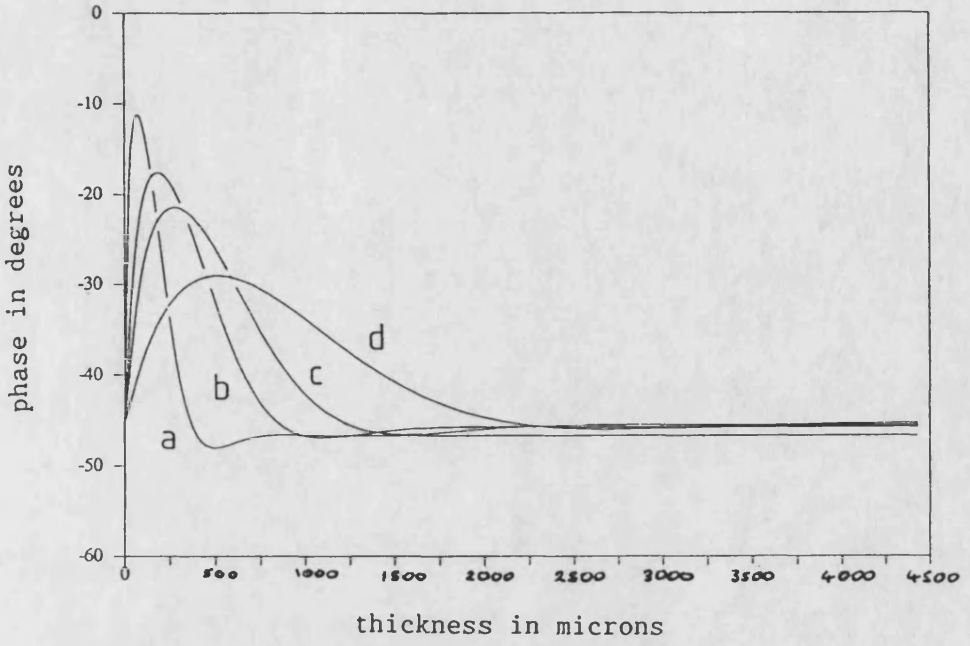

Figure 7.1 : Variation of phase with thickness of opaque YSZ coating on 316 steel for different coating thermal conductivity k
a) k = 0.1 W/m/K b) k = 0.5 W/m/K
c) k = 1.0 W/m/K d) k = 3.0 W/m/K

(modelled using equation A.21)

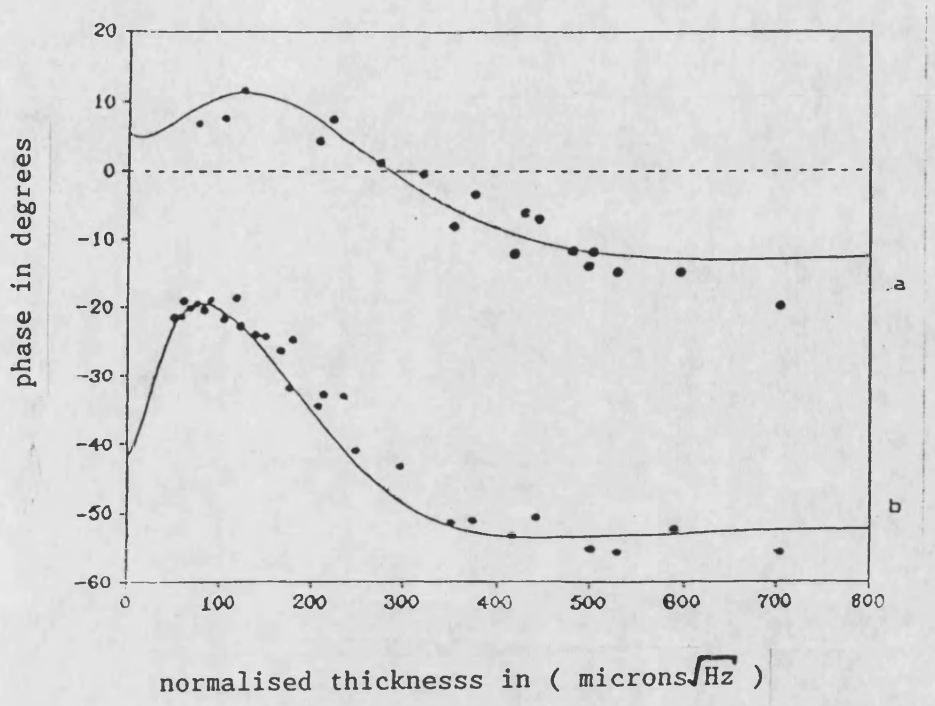

Figure 7.2 : Variation of phase with normalised thickness for two plasma-sprayed YSZ coatings on 316 steel substrates. Thickness normalised to (thickness * $\sqrt{f}$). Continuous curves modelled using equation A.21 , using YSZ properties of:
a) β = 1e4/m ; k = 0.35 W/m/K
b) β = 3e4/m ; k = 1.00 W/m/K
Curve (a) displaced by +45 degrees for clarity

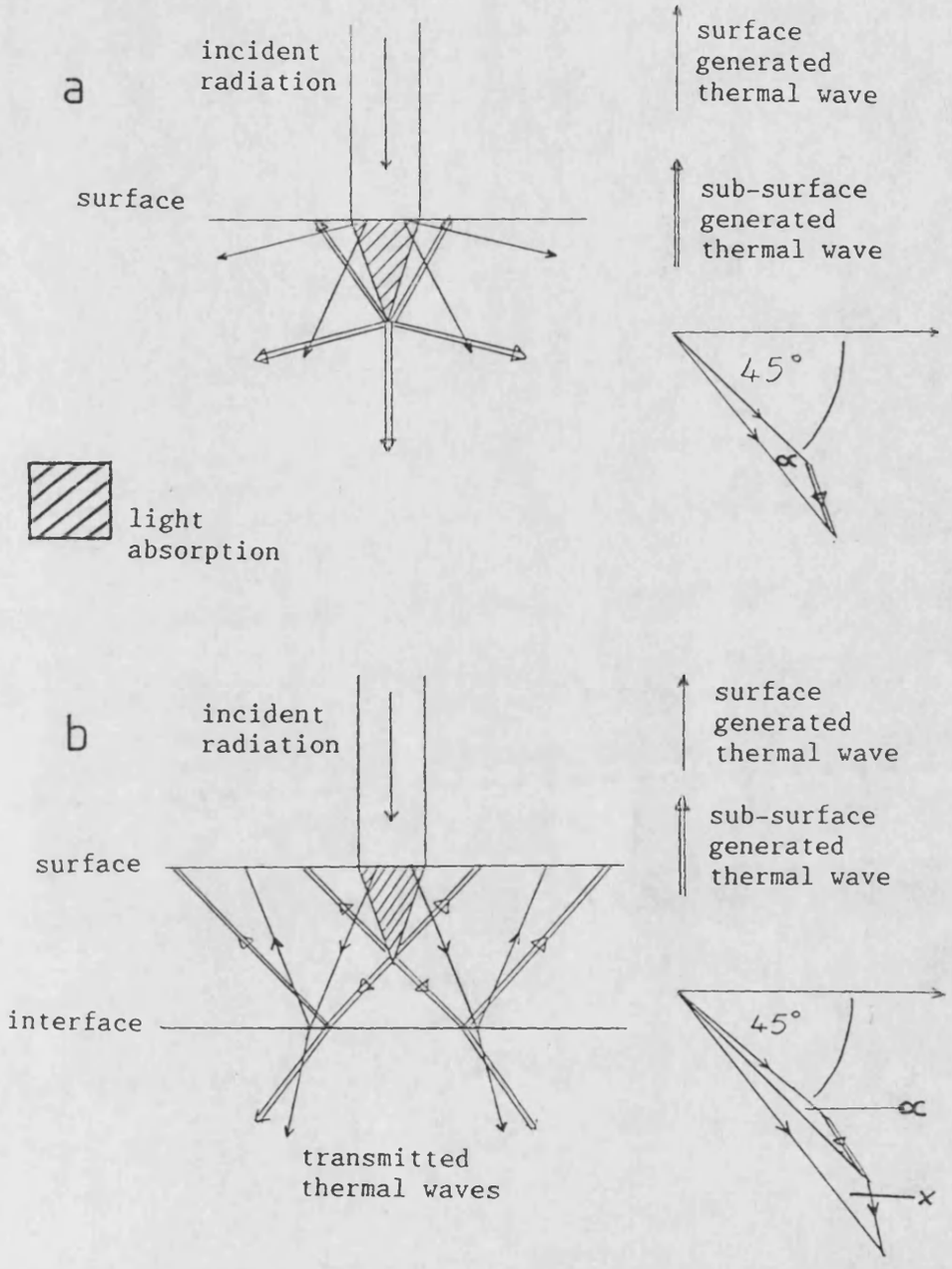

Figure 7.3: Schematic and phasor representation of thermal waves in thermally thick and thermally thin translucent media

a) thermally thick: resultant R, phase lag 45° plus subsurface-surface interference term α

b) thermally thin : resultant R, phase lag 45° plus interference term α plus interface interference term x

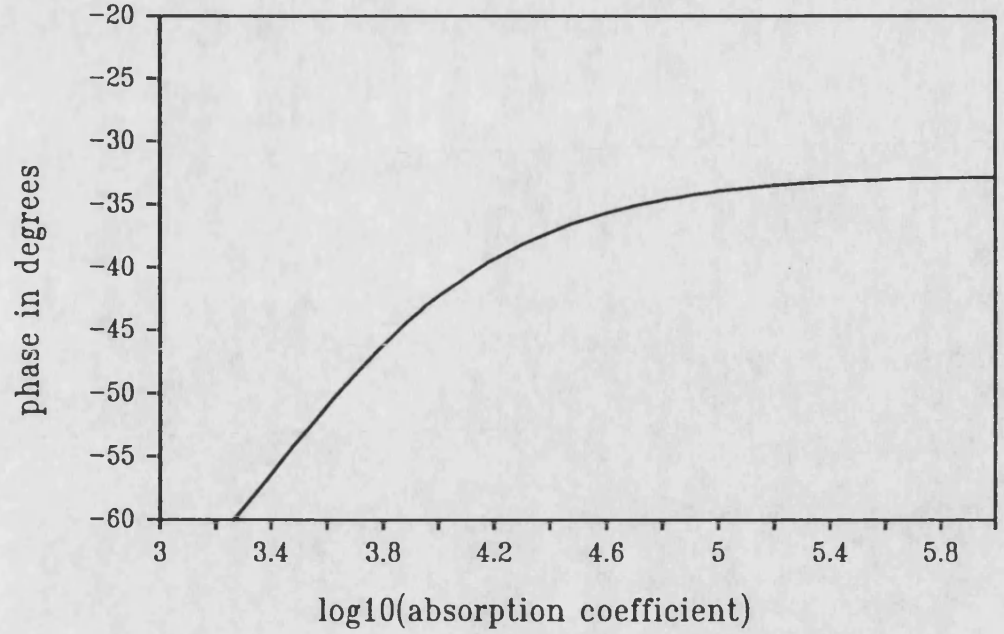

Figure 7.4 Variation of phase with absorption coefficient
250 micron YSZ on stainless steel f = 1 Hz

(modelled using equation A.21)

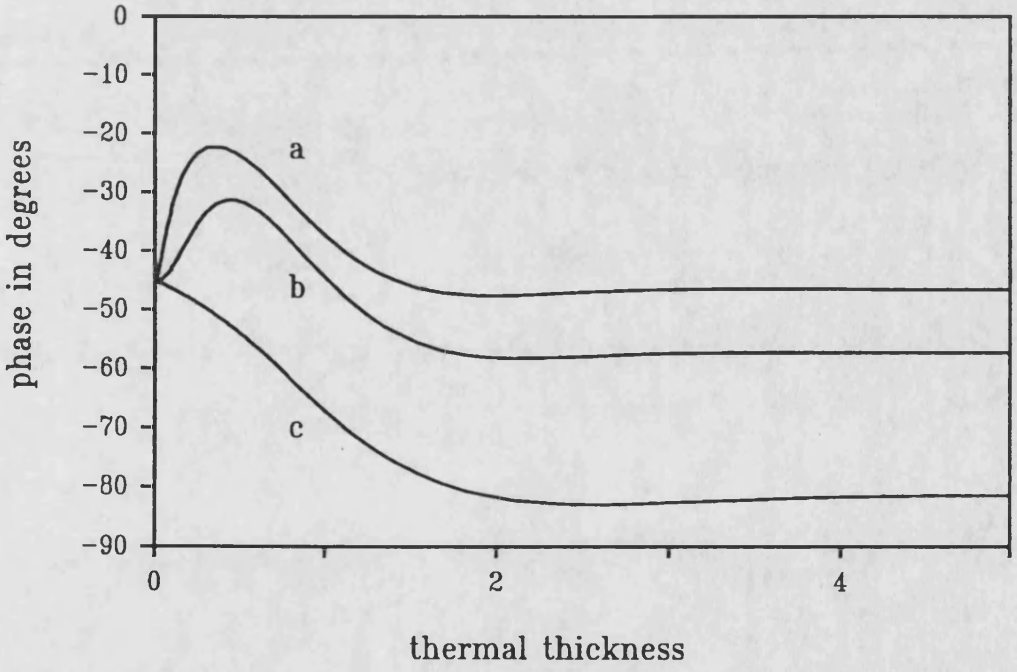

Figure 7.5 Effect of absorption coefficient β on phase–thickness curves for YSZ on stainless steel at 1 Hz
a: β = 1e5/m, b: β = 1e4/m c: β = 1e3/m

(modelled using equation A.21)

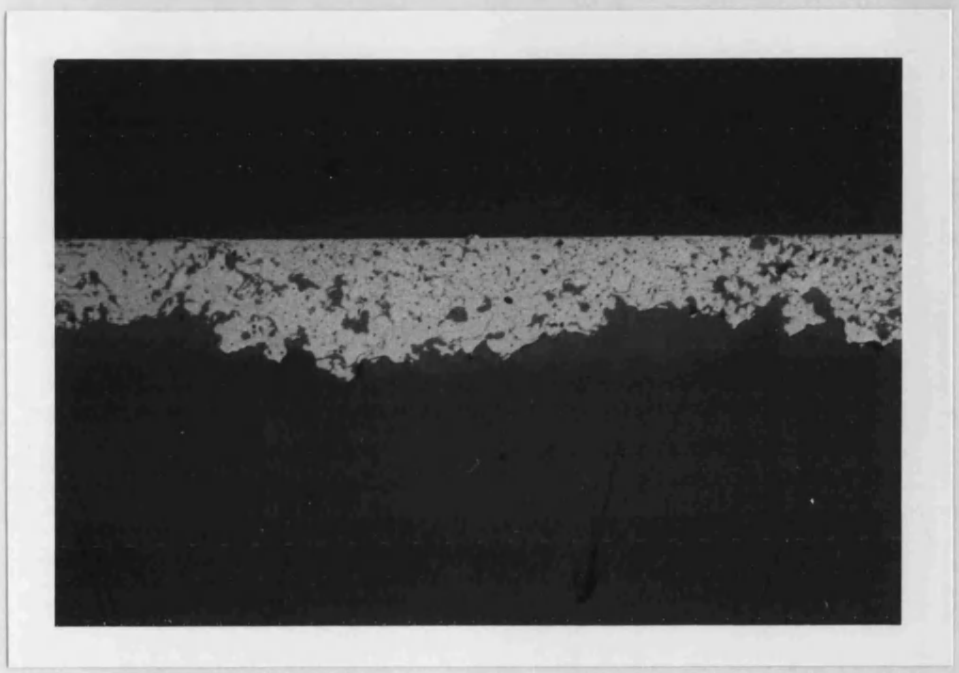

Figure 7.6: Photograph showing plasma-sprayed YSZ coating on annealed borosilicate glass substrate showing flat interface (magnification x128) YSZ coating - glass substrate

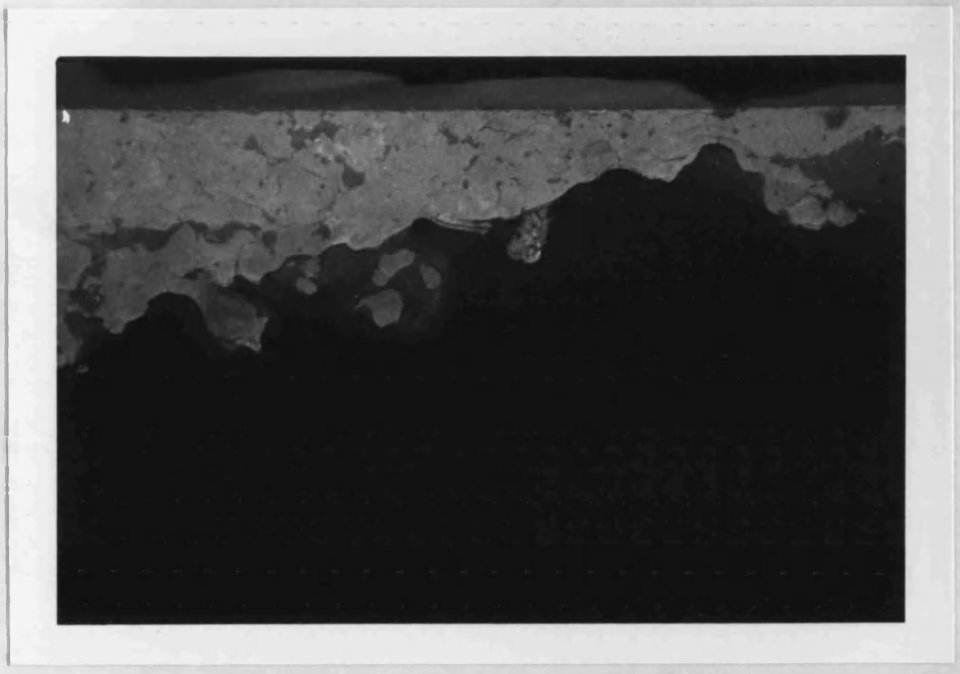

Figure 7.7: Photograph showing plasma-sprayed YSZ coating on annealed borosilicate glass substrate showing flat interface (magnification x320).
Note feature in top of photograph suggesting penetration of YSZ into substrate. glass substrate - possible YSZ penetration - YSZ coating

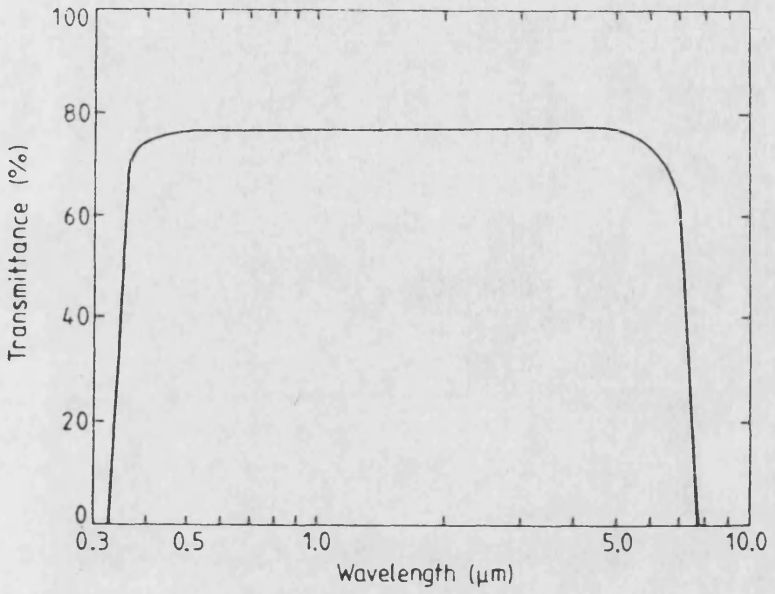

Figure 7.8: Spectral transmittance plot for yttria-12% zirconia window 1mm thick (after Savage [120])

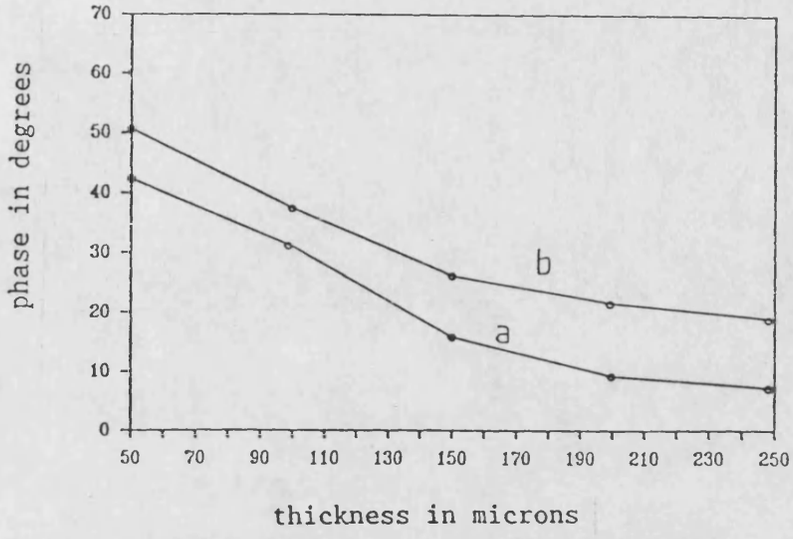

Figure 7.9: Plot of phase angle variation with thickness for plasma sprayed YSZ on mild steel. Laser power 1 watt, modulation frequency 4 Hz.
a) as received b) darkened with ink

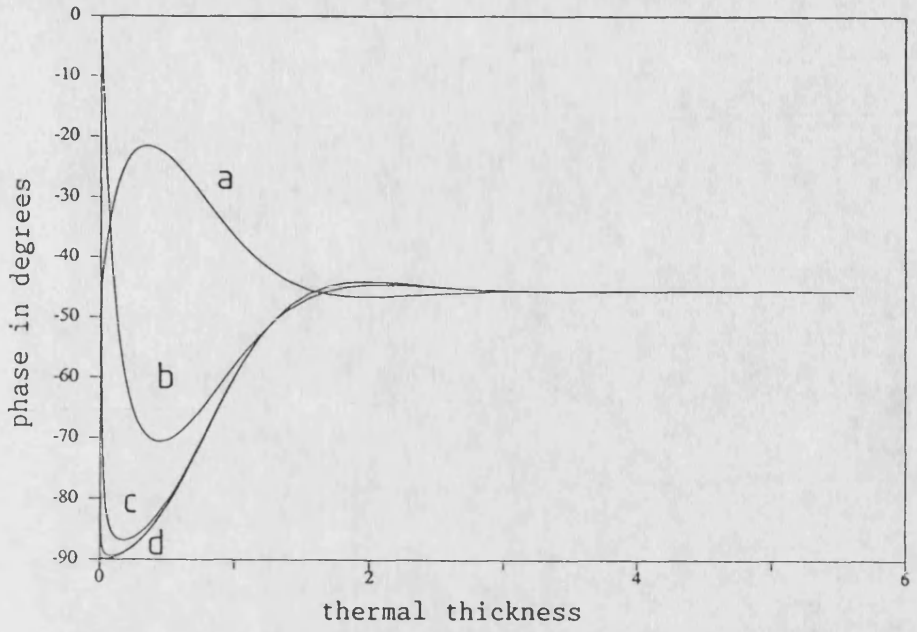

Figure 7.10: Variation of phase with thermal thickness of an opaque YSZ coating on 316 steel at different interfacial air-gap thicknesses, w
a) w = 0 microns b) w = 0.1 microns
c) w = 1 micron d) w = 10 microns
(modelled using equation A.21 plus A.28)

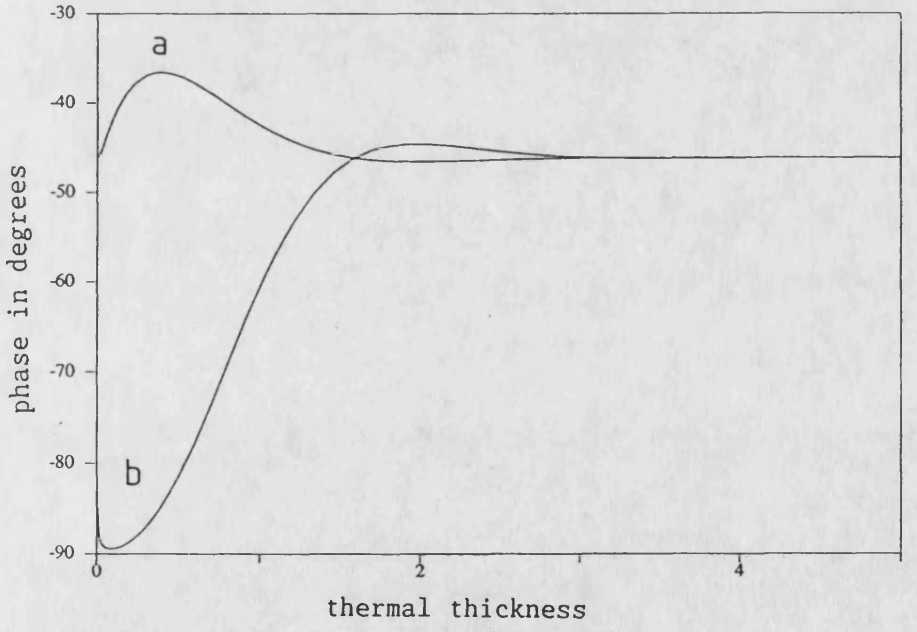

Figure 7.11: Variation of phase with thermal thickness of an opaque LC1B coating on 316 steel at different interfacial air-gap thicknesses, w
a) w = 0 microns b) w = 0.001 microns
(modelled using equation A.21 plus A.28)

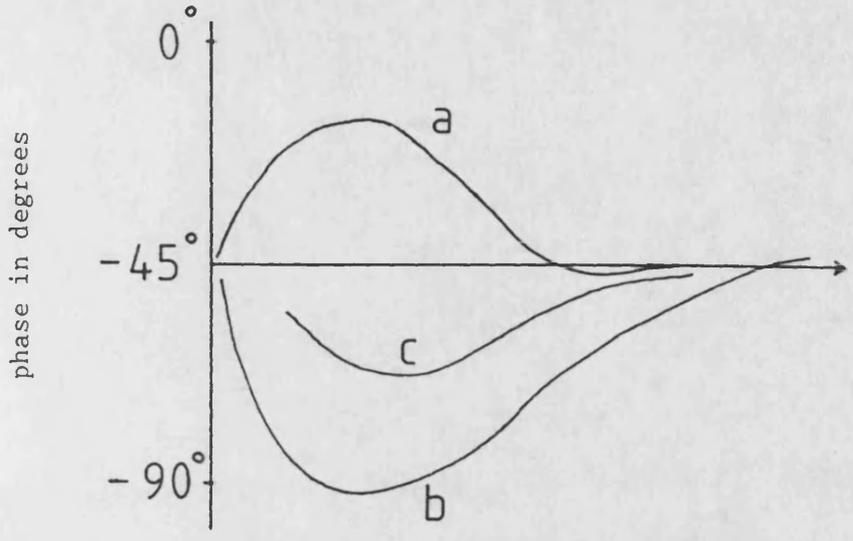

Figure 7.12: Schematic representation of phase - thermal thickness curve for an opaque sample with negative reflection coefficient,
a) no defect - perfect thermal contact between media (TCR = 0)
b) wide air gap - no thermal contact between media (TCR = ∞)
c) partial thermal contact between media (0 < TCR < ∞)

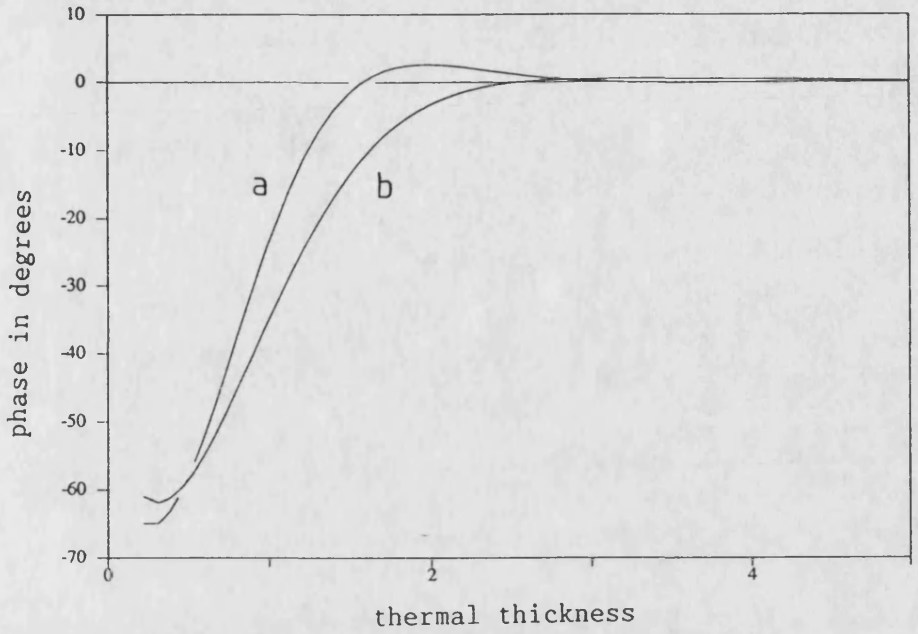

Figure 7.13: Variation of phase change caused by a one micron air-gap with thermal thickness of a YSZ coating on 316 steel at two different optical absorption coefficients,
a) β = 10^4/m b) β = 10^6/m
(modelled using equation A.21 plus A.28)

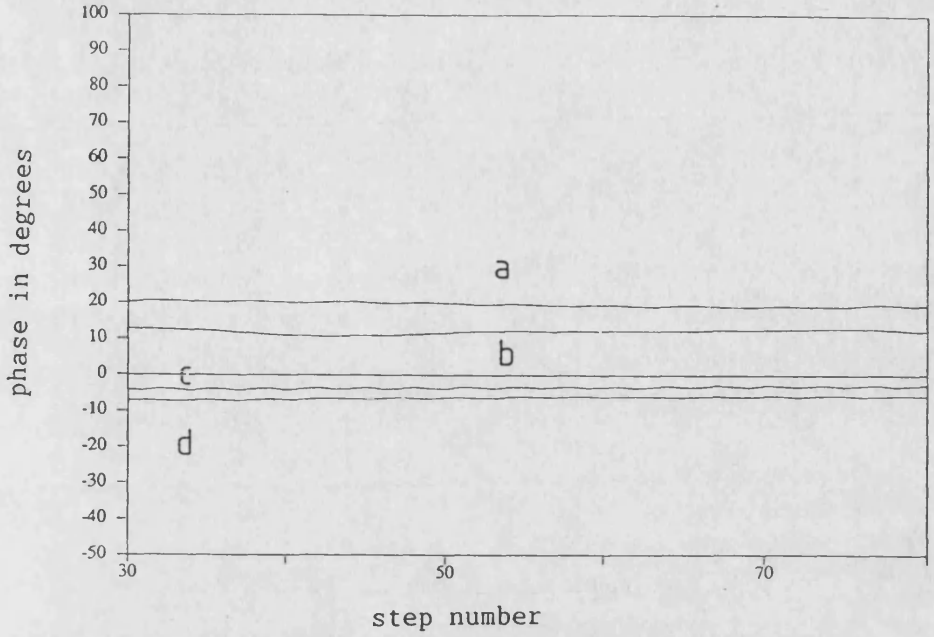

Figure 7.14a: Line scan over a high conductivity defect in an as-received 250 micron plasma sprayed YSZ coating on a low conductivity substrate showing phase variation with position
a) f = 0.5 Hz b) f = 1.0 Hz
c) f = 2.0 Hz d) f = 3.0 Hz

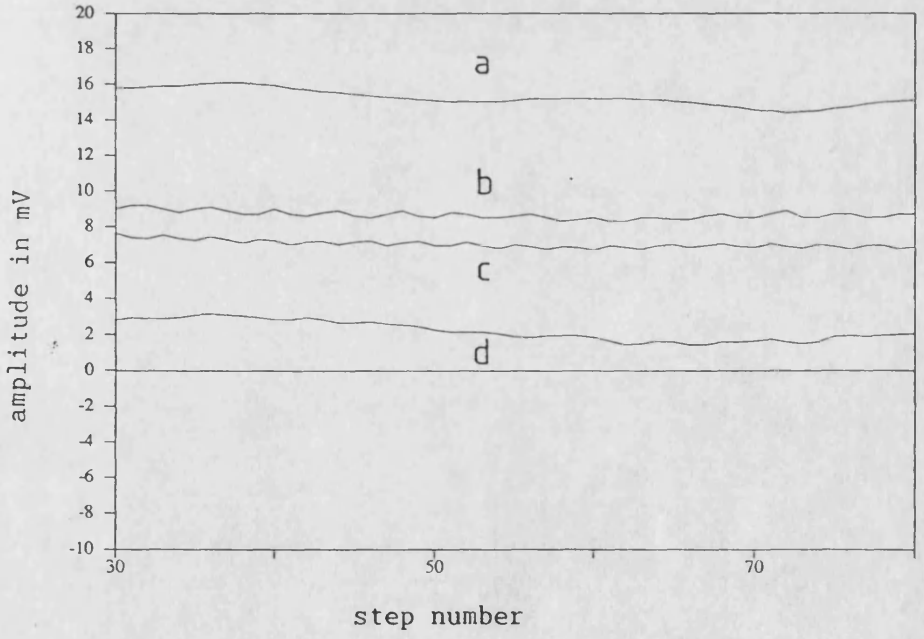

Figure 7.14b: Line scan over a high conductivity defect in an as-received 250 micron plasma sprayed YSZ coating on a low conductivity substrate showing amplitude variation with position
a) f = 0.5 Hz b) f = 1.0 Hz
c) f = 2.0 Hz d) f = 3.0 Hz

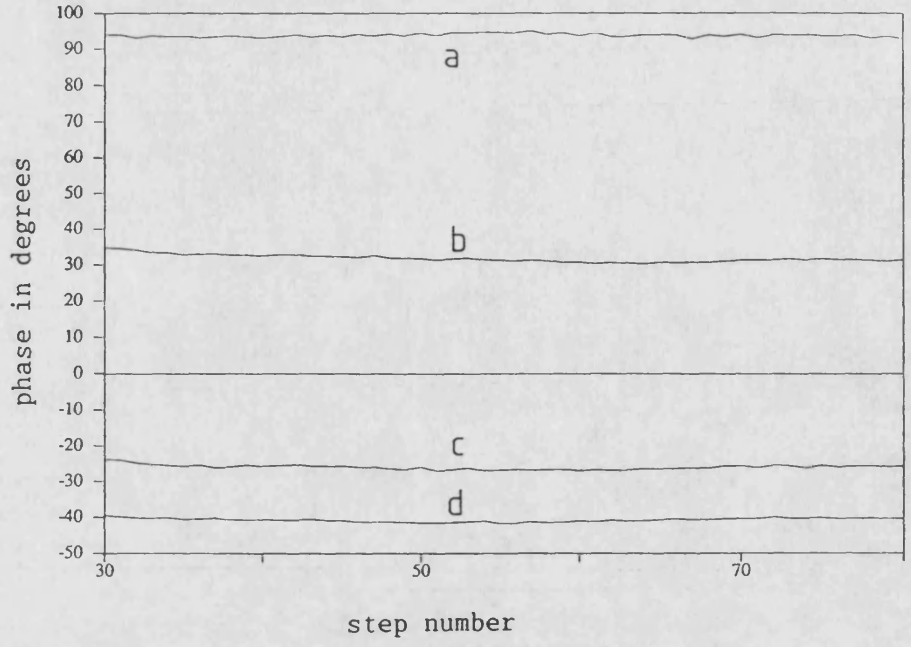

Figure 7.15a: Line scan over a high conductivity defect in an ink-darkened 250 micron plasma sprayed YSZ coating on a low conductivity substrate showing phase variation with position
a) f = 0.5 Hz b) f = 1.0 Hz
c) f = 2.0 Hz d) f = 3.0 Hz

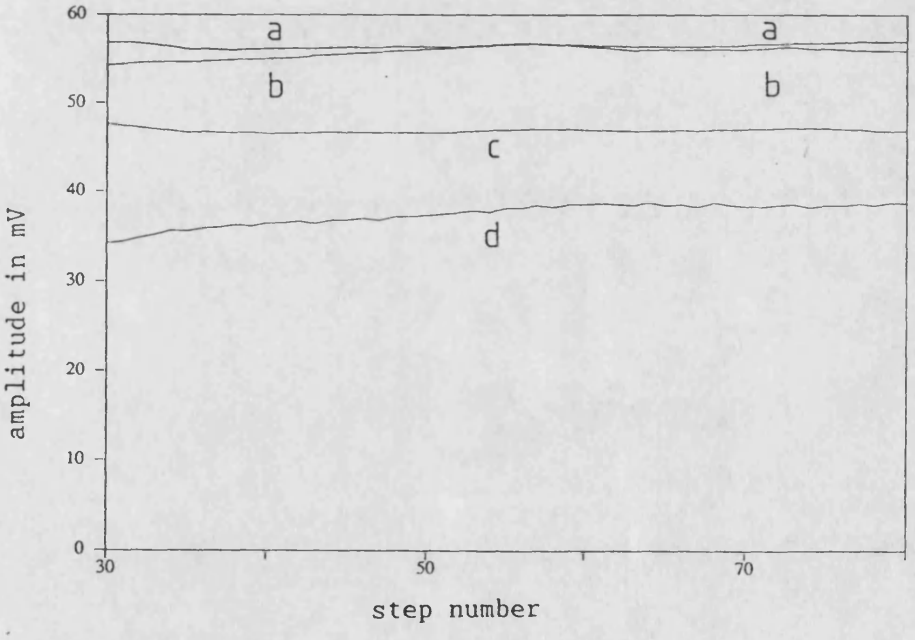

Figure 7.15b: Line scan over a high conductivity defect in an ink-darkened 250 micron plasma sprayed YSZ coating on a low conductivity substrate showing amplitude variation with position
a) f = 0.5 Hz b) f = 1.0 Hz
c) f = 2.0 Hz d) f = 3.0 Hz

Figure 7.16: Photograph showing artificial high conductivity defect in low conductivity substrate (magnification x64)
YSZ coating - Al 'defect' - phenolic resin substrate

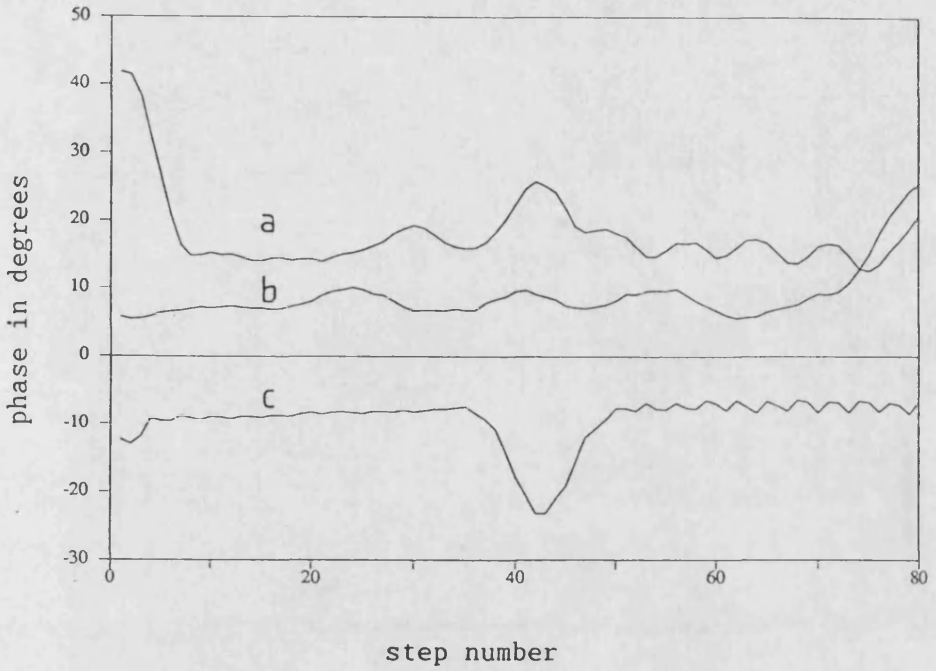

Figure 7.17a: Line scan over a low conductivity defect in an as-received 250 micron plasma sprayed YSZ coating on a high conductivity substrate showing phase variation with position
a) f = 0.5 Hz b) f = 0.6 Hz c) f = 1.0 Hz

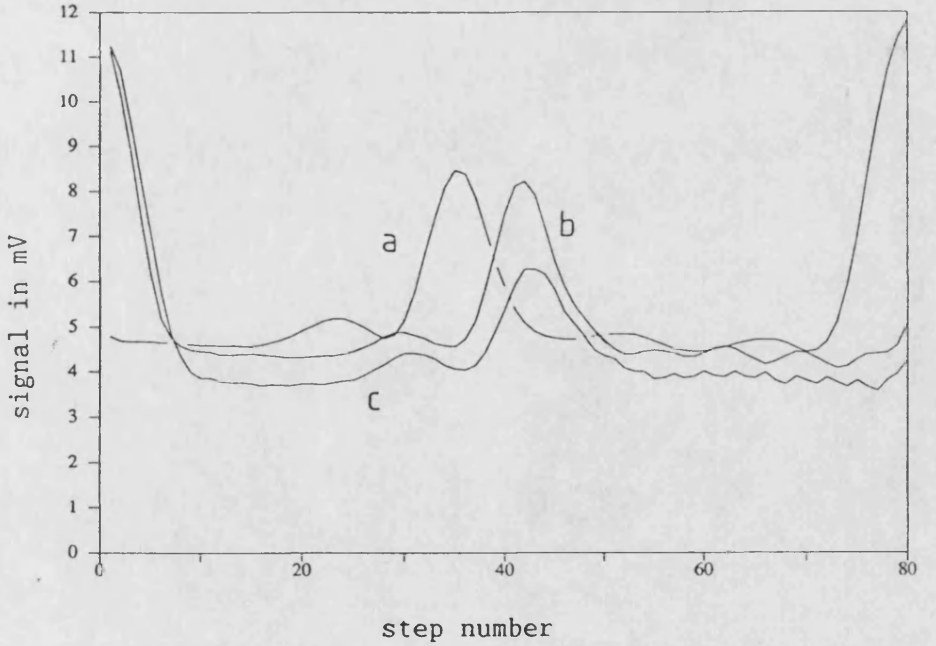

Figure 7.17b: Line scan over a low conductivity defect in an as-received 250 micron plasma sprayed YSZ coating on a high conductivity substrate showing amplitude variation with position
a) f = 0.5 Hz b) f = 0.6 Hz c) f = 1.0 Hz

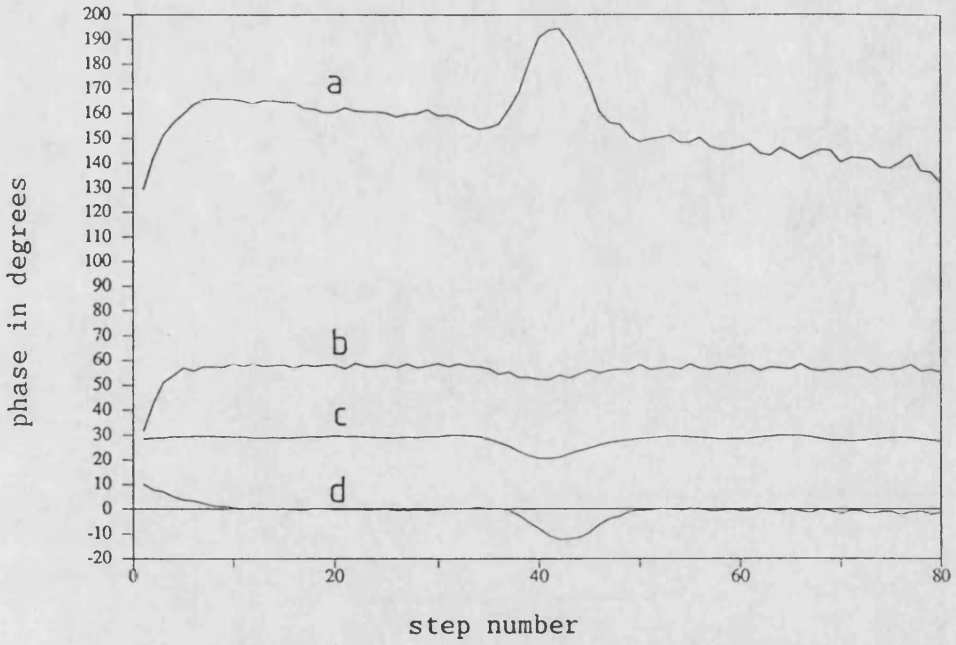

Figure 7.18a: Line scan over a low conductivity defect in an ink darkened 250 micron plasma sprayed YSZ coating on a high conductivity substrate showing phase variation with position
a) f = 0.5 Hz b) f = 1.0 Hz
c) f = 2.0 Hz d) f = 3.0 Hz

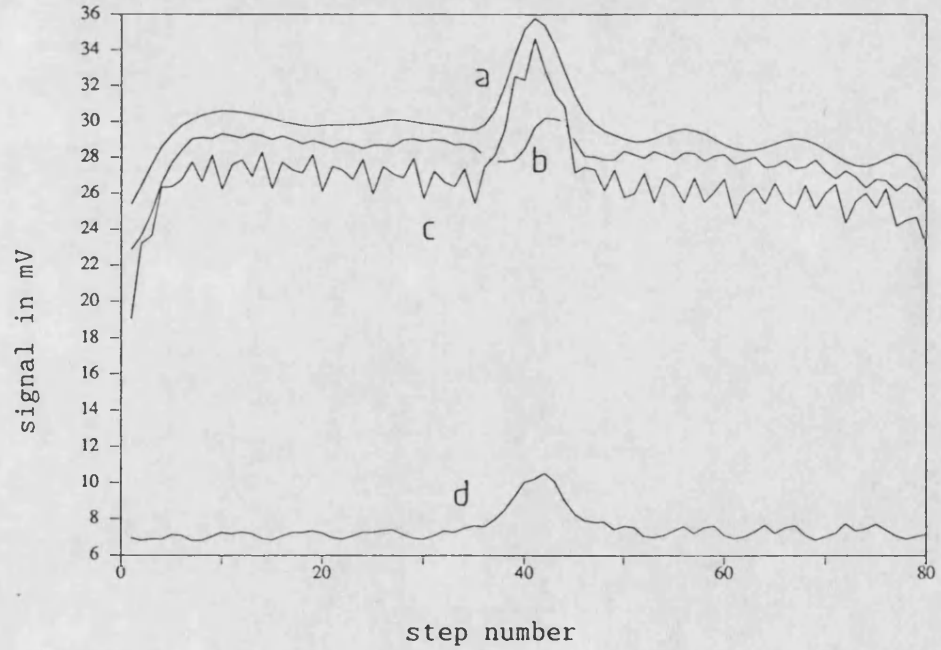

Figure 7.18b: Line scan over a low conductivity defect in an ink darkened 250 micron plasma sprayed YSZ coating on a hgh conductivity substrate showing amplitude variation with position
a) f = 0.5 Hz b) f = 1.0 Hz
c) f = 2.0 Hz d) f = 3.0 Hz

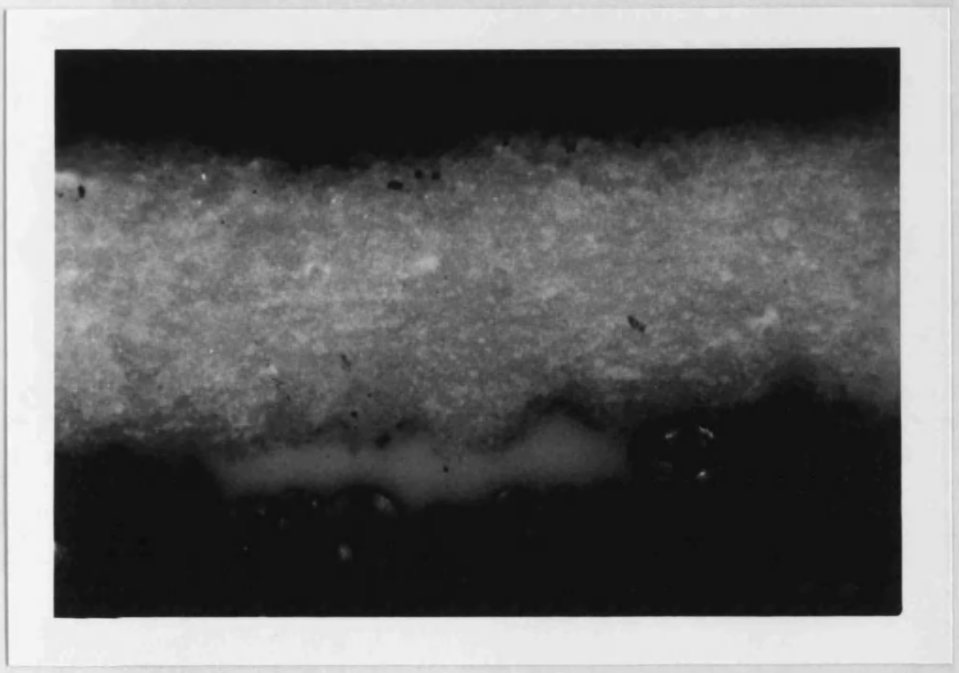

Figure 7.19: Photograph showing artificial low conductivity defect in high conductivity substrate (magnification x64)
YSZ coating - PVC 'defect' - Cu-filled acrylic resin

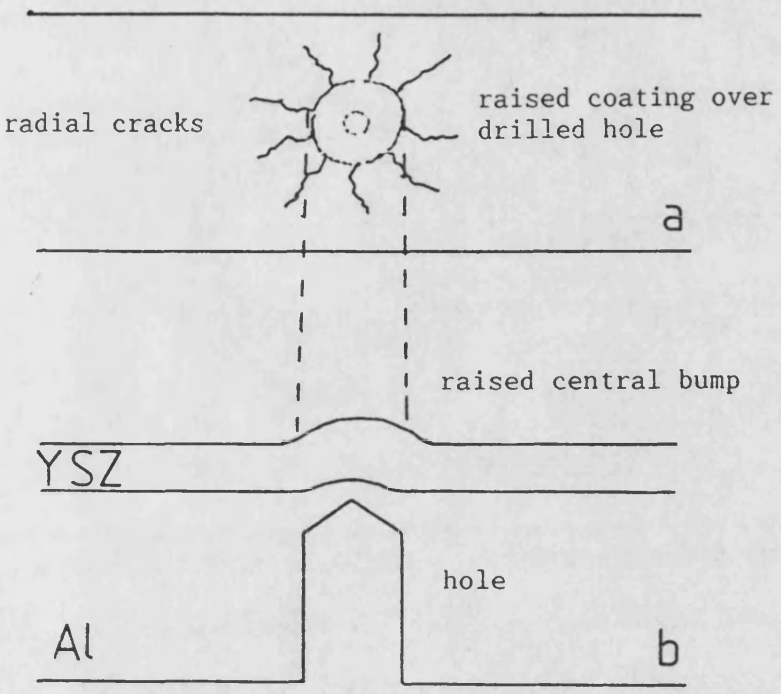

Figure 7.20: Schematic of radial cracking over blind hole in YSZ coated Al

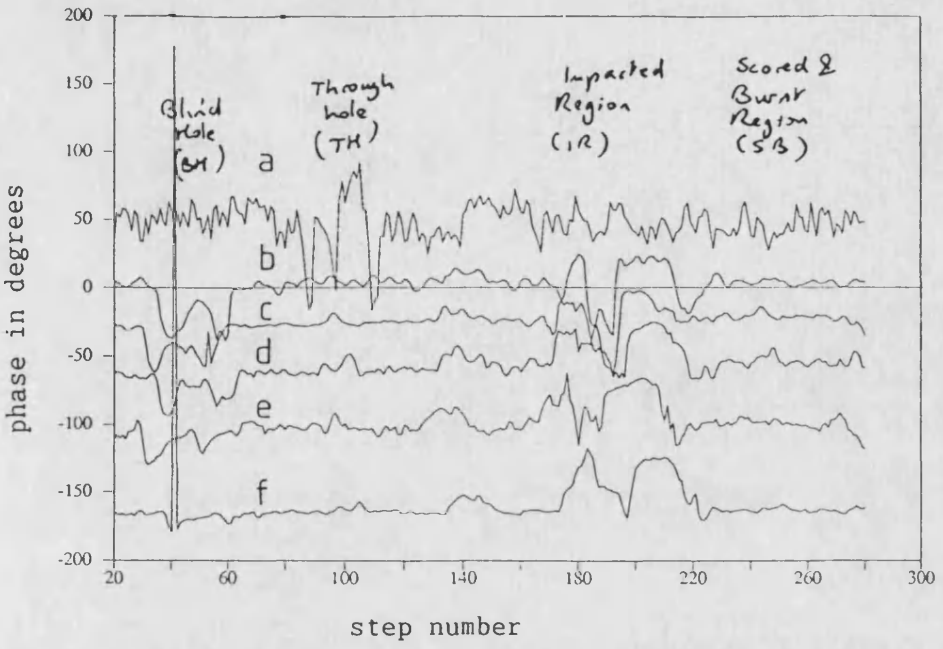

Figure 7.21a: Variation of phase with position for as-received 'damaged' sample of YSZ on aluminium at different modulation frequencies, f. 4 readings/mm
a) f = 0.5 Hz b) f = 2.0 Hz c) f = 4.0 Hz
d) f = 10.0 Hz e) f = 20.0 Hz f) f = 40.0 Hz

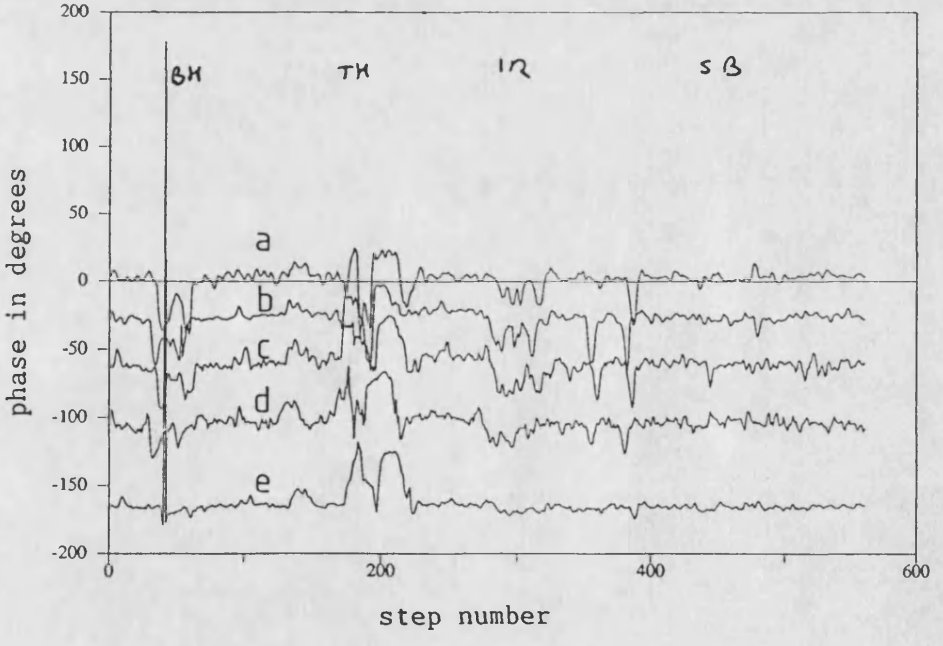

Figure 7.21b: Variation of phase with position for as-received 'damaged' sample of YSZ on aluminium at different modulation frequencies, f. 8 readings/mm
a) f = 2.0 Hz b) f = 4.0 Hz c) f = 10.0 Hz
d) f = 20.0 Hz e) f = 40.0 Hz

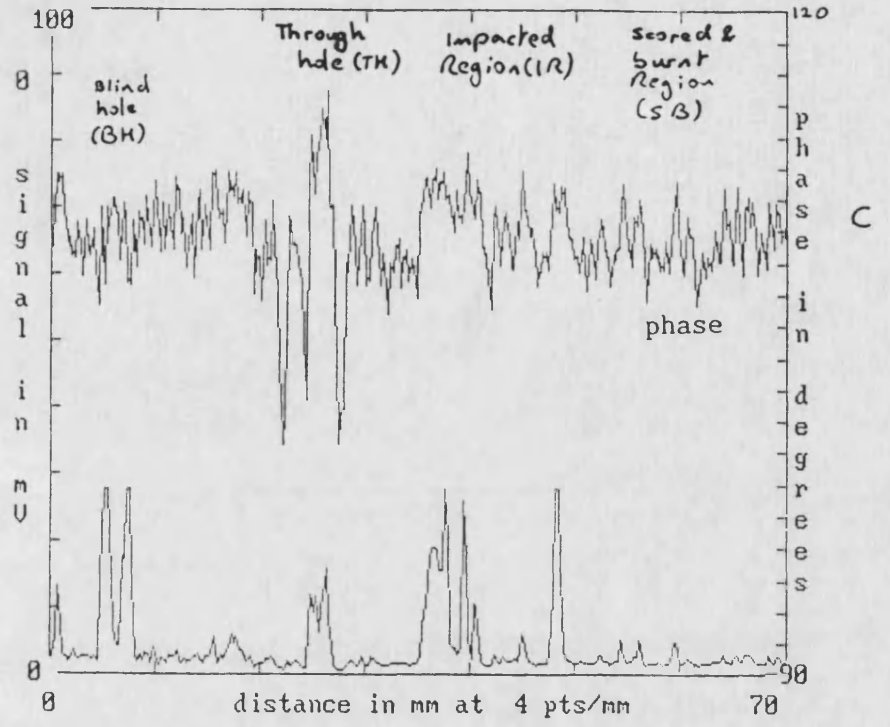

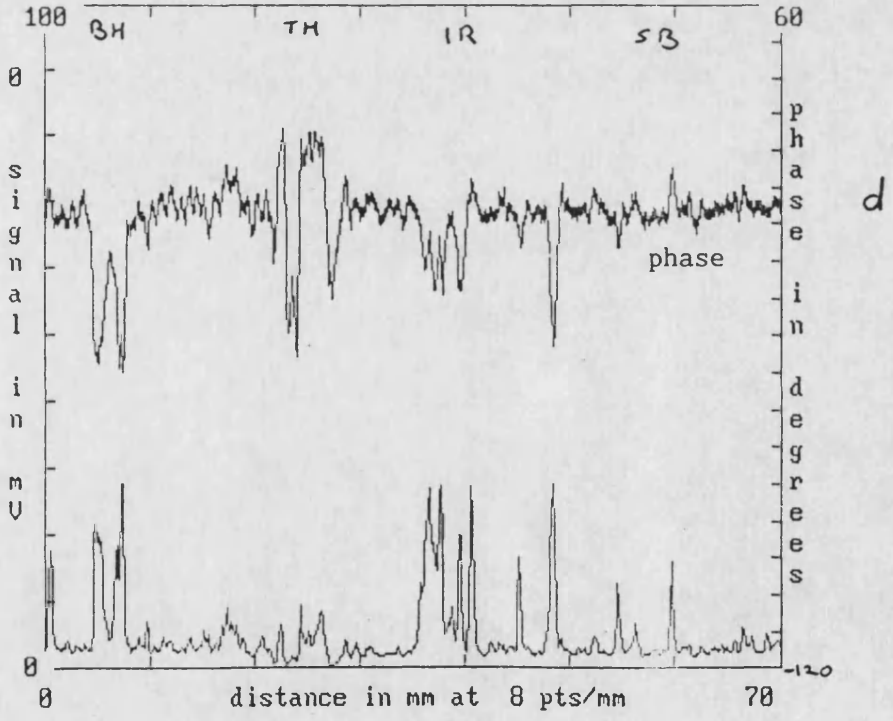

Figure 7.21c: Variation of phase and amplitude with position for as-received 'damaged' sample of plasma sprayed YSZ on aluminium at different modulation frequencies, f.
c) f = 0.5Hz d) f = 2.0Hz e) f = 4.0Hz
f) f = 10Hz g) f = 20Hz h) f = 40Hz

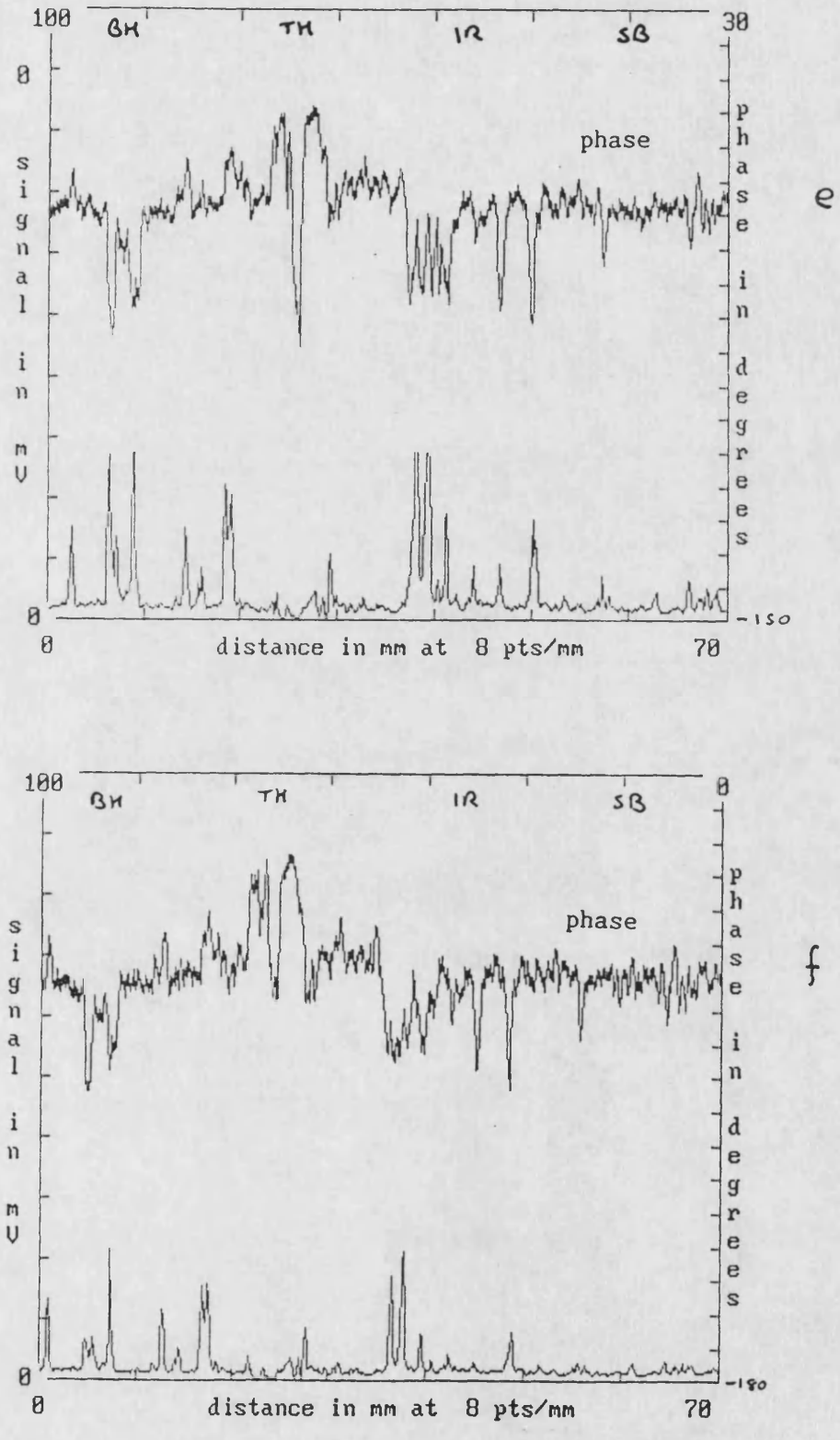

Figure 7.21[9]: Variation of phase and amplitude with position for as-received 'damaged' sample of plasma sprayed YSZ on aluminium at different modulation frequencies, f.
c) f = 0.5Hz d) f = 2.0Hz e) f = 4.0Hz
f) f = 10Hz g) f = 20Hz h) f = 40Hz

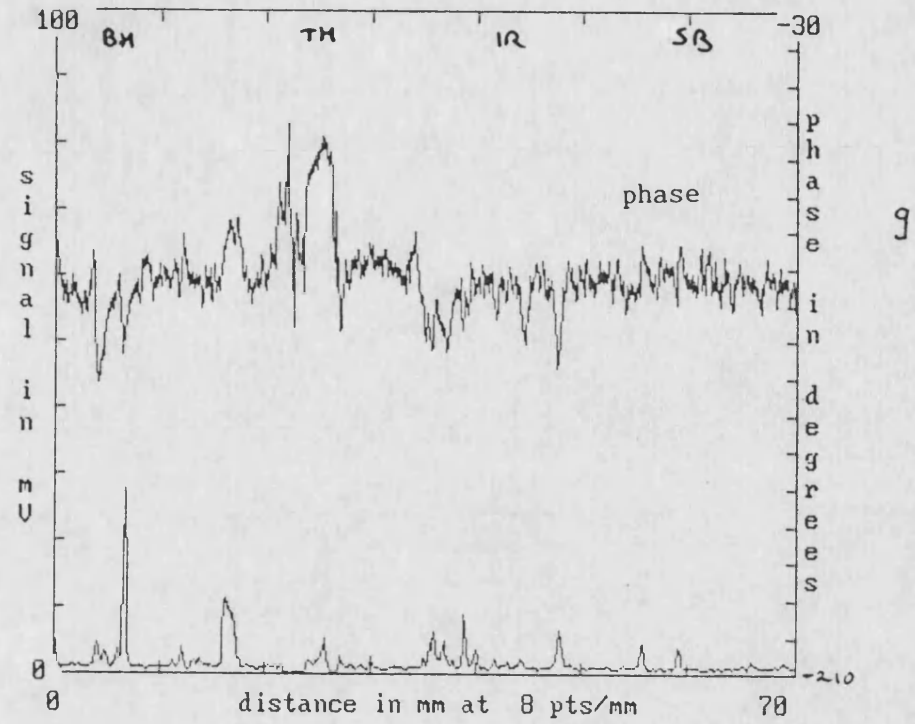

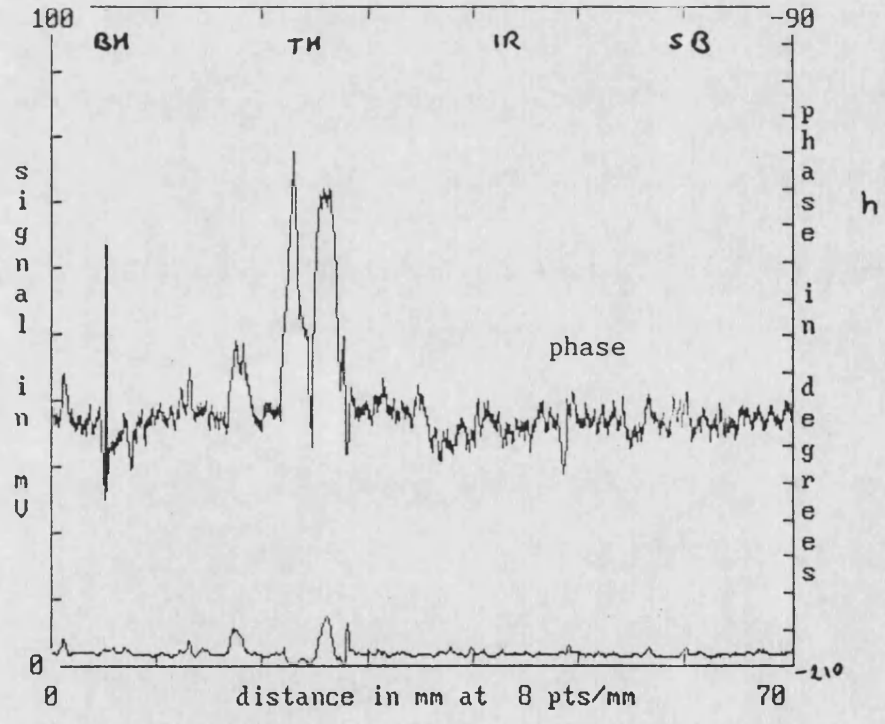

Figure 7.21 : Variation of phase and amplitude with position for as-received 'damaged' sample of plasma sprayed YSZ on aluminium at different modulation frequencies, f.
c) f = 0.5Hz d) f = 2.0Hz e) f = 4.0Hz
f) f = 10Hz g) f = 20Hz h) f = 40Hz

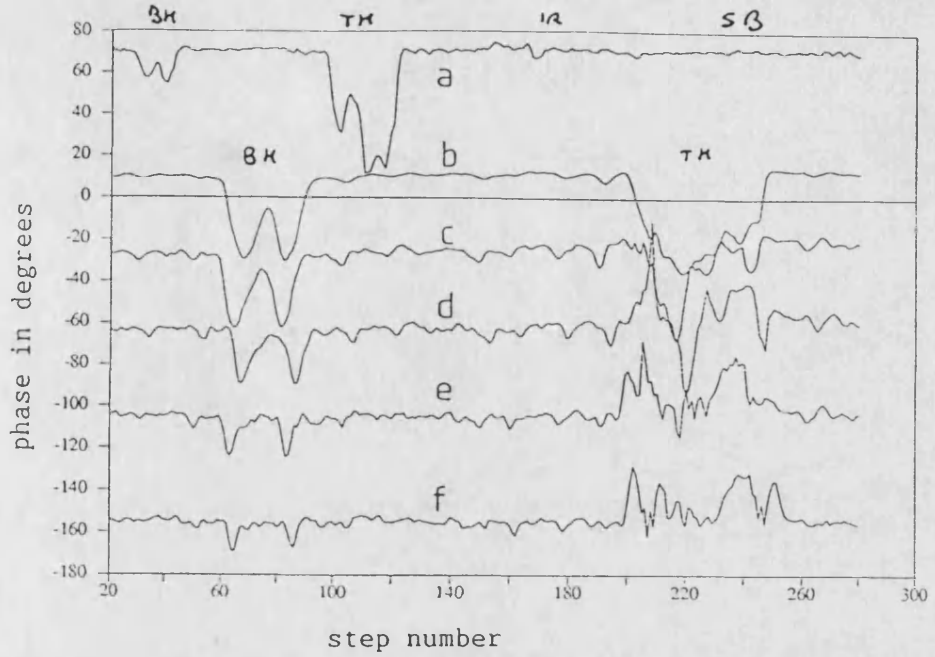

Figure 7.22a: Variation of phase with position for carbon darkened 'damaged' sample of YSZ on aluminium at different modulation frequencies, f. 4 readings/mm
a) f = 0.5 Hz b) f = 2.0 Hz c) f = 4.0 Hz
d) f = 10.0 Hz e) f = 20.0 Hz f) f = 40.0 Hz

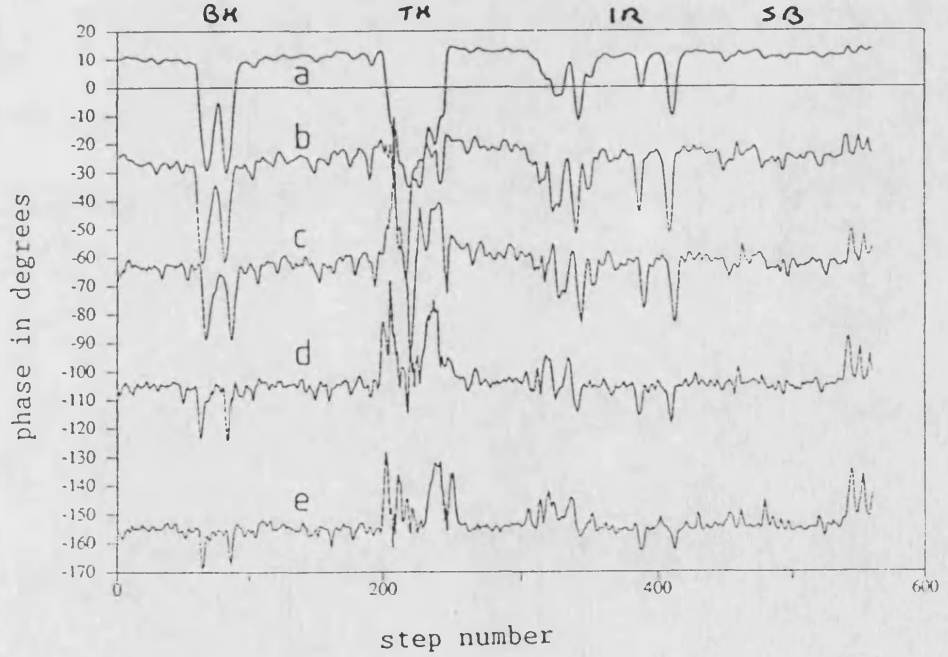

Figure 7.22b: Variation of phase with position for carbon darkened 'damaged' sample of YSZ on aluminium at different modulation frequencies, f. 8 readings/mm
a) f = 2.0 Hz b) f = 4.0 Hz c) f = 10.0 Hz
d) f = 20.0 Hz e) f = 40.0 Hz

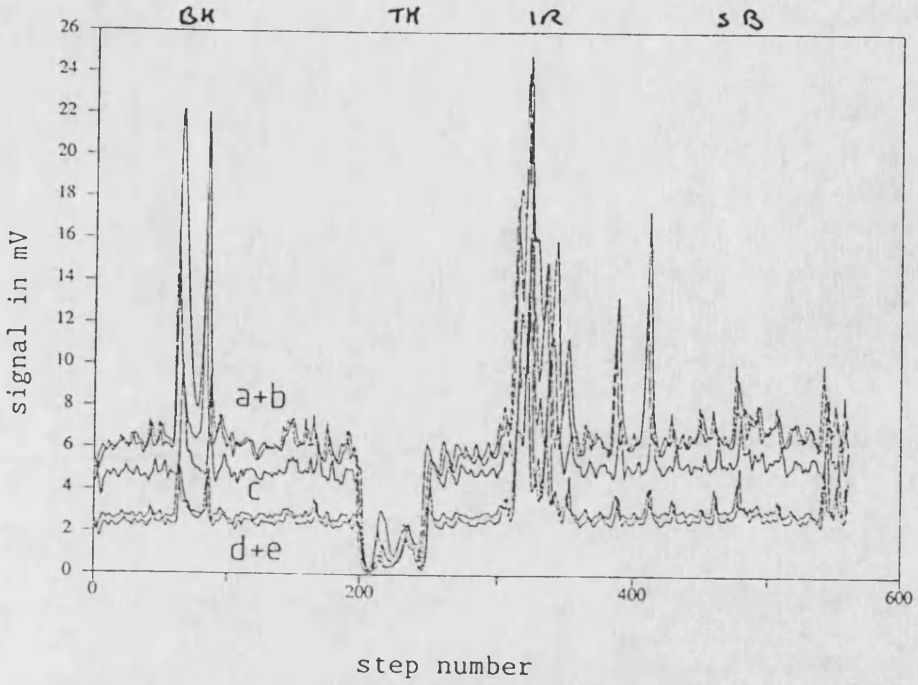

Figure 7.22c: Variation of amplitude with position for carbon darkened 'damaged' sample of YSZ on aluminium at different modulation frequencies, f. 4 readings/mm
a) f = 0.5 Hz b) f = 2.0 Hz c) f = 4.0 Hz
d) f = 10.0 Hz e) f = 20.0 Hz f) f = 40.0 Hz

Optical Absorption Coefficient, β (/m)	Phase Difference in degrees
1e5/m	19°
1e4/m	19°
1e3/m	19°

Table 7.1 : Computer modelled phase differences between peak phase and phase at thermal thickness for a YSZ coating on stainless steel at 1Hz

sample code	number of passes	nominal (*) thickness (microns)	measured (**) thickness (microns)
17	1	30	40
18	1	30	40
21	2	60	50
3	3	90	0(***)
19	3	90	50
15	4	120	90
16	4	120	80
20	5	150	90
13	6	180	100
14	6	180	80
1	7	210	70
5	8	240	70

Table 7.2 : Nominal and measured thickness of plasma sprayed YSZ coatings on borosilicate glass substrates
(*) spraying conditions set to yield 30 microns per pass
(**) coated thickness - uncoated thickness, to 10microns
(***) suggesting YSZ embedded in substrate

Coating Thickness	Optical Absorption Coefficient	Mean Transmission	Method
40 microns	20.2e3/m	15.6%	direct transmission through coating
50 microns	32.0e3/m	2.5%	
70 microns	26.9e3/m	1.3%	
80 microns	22.3e3/m	1.5%	
90 microns	20.3e3/m	1.5%	
100 microns	18.5e3/m	1.4%	
average of above	23.5e3/m		
348 microns (1)	13.6e3/m (2)	0.6% (2)	
sample 1	30.0e3/m		visual estimate
sample 2	10.0e3/m		
sample 1	30.0e3/m		curve fitting to models
sample 2	10.0e3/m		
sample 1	32.0e3/m		comparison of darkened and as-received data
sample 2	8.0e3/m		
sample 2	9.4e3/m		

Table 7.3 : Optical absorption coefficients of plasma sprayed YSZ coatings obtained by different methods.
(1) unsupported coating (2) some uncertainty because received signal was close to system noise level

Nominal Coating Thickness (thou)	Translucent	Opaque	Difference	
2	-0.7	+0.7	8.4	a
4	-21.0	-7.6	13.4	
6	-30.3	-14.1	16.2	
8	-31.4	-13.5	17.9	
10	-29.7	-15.2	14.5	

Nominal Coating Thickness (thou)	Translucent	Opaque	Difference	
2	+18.3	+27.0	8.7	b
4	+1.3	+11.3	10.0	
6	-11.4	+1.3	10.1	
8	-14.8	+0.2	14.6	
10	-13.3	-0.4	12.9	

Nominal Coating Thickness (thou)	Translucent	Opaque	Difference	
2	+42.3	+50.8	8.5	c
4	+31.0	+37.5	6.5	
6	+15.8	+26.3	10.5	
8	+9.3	+21.4	12.1	
10	+7.3	+19.0	11.7	

Table 7.4 : Phase values (in degrees) obtained at different modulation frequencies on ink-darkened (opaque) and as-received (translucent) plasma sprayed YSZ coatings on 316 steel.
Laser power 1 watt (unfocussed)

a) modulation frequency 10Hz b) modulation frequency 7Hz c) modulation frequency 4Hz

8 OPTICAL AND INFRARED OPTICAL FIBRES

8 OPTICAL AND INFRARED OPTICAL FIBRES

Traditional thermal wave test systems rely on line of sight optics for both the delivery of the heating energy and for the reception of the emitted infrared radiation. Modern infrared and optical fibre technology offers the opportunity to eliminate the need for line of sight and improve system flexibility.

8.1 Advantages of Fibres

There are advantages to both delivering the heating radiation to the target by fibre and delivering the infrared radiation from the sample to the detector by fibre, especially if both technologies can be combined in one system. These are:

i) Remote location of electrical components reduces risk in explosive hazard areas;

ii) Flexibility to leave the bulky equipment (lasers, computers etc.) at a remote location improves ease of access to in situ components;

iii) The use of a remote probe head allows inspection of previously inaccessible places such as inside tubes, partially enclosed areas and narrow channels;

iv) Use of different probe configurations can be achieved by merely substituting a different cable.

8.2 Optical Fibres

High quality optically transmitting fibres have become widely available since the advent of optical telecommunications. For telecommunication links, transmission is optimised at near infrared wavelengths, either 1.3 or more recently 1.55 microns, but optical transmission is nevertheless high. Optically transmitting silica fibres can be obtained in a large number of configurations, cabled and bundled, at a reasonable cost and in virtually unlimited lengths. The transmission typically peaks at 0.8 microns, although it is usually considerably below 1dB/m over the whole of the visible spectrum (figure 8.1) [125].

8.2.1 Measurement of Optical fibres

Two optical fibre bundles were obtained, with a nominal length of 2 metres, cabled and with the ends optically polished. One had a nominal bundle diameter of 1.5mm, the other 3mm. Transmission losses were about 0.6 dB/m at 488nm and 0.43 dB/m at 515nm [125] (figure 8.1). The random orientation of the fibres within the bundle was expected to average out the Gaussian profile of the beam, [96].

Transmission losses through the optical fibre cables were determined by comparing the power delivered directly by the laser with the power transmitted through the cable. The configuration used is shown in figure 8.2. The cables were clamped so that the laser beam was central to the fibre. The power meter [118] was position insensitive, so that alignment was not critical. In the second case, an aluminium plate was interposed between the laser and power meter to block stray radiation.

The laser spot overfilled the smaller fibre. The 1/e diameter was 1.2mm [107], and the cable diameter 1.5mm, but the total visible laser spot extended over approximately 2mm. There was no evidence of overfilling with the larger (3mm diameter) cable. Although the emergent beams from both fibres were strongly divergent, the large aperture of the power meter allowed all the emergent beam to be collected.

Results are shown in table 8.1. It is apparent that the measured losses are higher than the nominal losses. There are a number of reasons for this: the loss in the smaller cable would be higher because not all the light entered the fibre; the total number of fibres in the smaller cable was lower, so any failed fibres would contribute a greater loss than in the larger one; the nominal losses were determined from a transmission curve supplied with the cables (figure 8.1), which had a very steep slope in the region of interest, so the losses determined are not exact; the laser operated in 'all lines' mode, so that the light would have been at a number of wavelengths. For a complete picture, the loss contribution at each wavelength would need to be determined.

Despite this, it is clear that a useful power can be delivered to the sample via the fibre. Focussing or collimation would be useful in some applications because of the strong divergence. There was no evidence of damage to the fibre ends, even with an input power density of $420kW/m^2$. Thus incorporation of such a fibre could be achieved with only minor adjustment to the system.

8.2.2 Experimental Incorporation of Optical Fibres

The darkened half of the sample described in section 7.5 was tested with the laser radiation delivered via the 3mm diameter optical fibre bundle described above [125], and with an aluminium plate positioned so that direct illumination of the sample was impossible. The readings obtained are displayed in table 8.2, and the phase values plotted on figure 8.3, along with the equivalent phase for a directly illuminated sample. The phase values from the fibre test have been increased by 10 degrees for clarity.

The presence of the fibre reduced the amount of radiation reaching the sample so that the amplitude has fallen, but the results otherwise correspond well with the results obtained by direct irradiation. A similar experiment carried out by Patel [126] using a diode laser unit was equally successful. The strong divergence of the emergent light is not a problem if the fibre tip can be located close to the sample surface. If precise spatial heating were required, then some form of collimation or focussing would be needed.

8.3 Infrared Fibres

Infrared transmitting optical fibres can be broadly grouped into five categories: silica glass, heavy metal fluoride glasses, chalcogenide glasses, crystalline materials and hollow core fibres.

8.3.1 Silica Fibres

Silica based fibres are used for telecommunications. They can be made with transmission losses close to the theoretical minimum of about 0•2 dB/km at 1.55 microns. While they transmit optical frequencies well, they transmit longer wavelength infrared very poorly, with an effective cut-off at about 2.5 microns [119]. They are mechanically quite strong, with some being made to withstand 2% proof test [127]. They are also physically and chemically durable, and are readily available at reasonable cost.

8.3.2 Heavy Metal Fluoride Glasses

These materials are visibly transparent glasses based on zirconium and barium fluorides. They have theoretical minimum losses as low as 0•01 dB/km at 2.5 microns, and have moderate transmission between about 0.3 and 5 microns [127]. Current minimum transmission losses are typically around 1dB/km at 2.2-2.6 microns because the manufacturing techniques needed to give really low losses cannot be applied at present [119].

Mechanically they are much weaker than silica fibres, principally because the weak bonding required to give low phonon absorption precludes macroscopic high strength. They are subject to water degradation, although cabling reduces this significantly.

8.3.3 Chalcogenide Glasses

Glasses based on Group VI compounds (sulphides, selenides and tellurides) of Group V elements (arsenic and antimony) have transmission windows in the mid-infrared. They have theoretical minimum transmission losses of .01 dB/km at 5 microns (As_2S_3), although lowest reported losses are in practice much higher at 35 dB/km [128].

Chalcogenide fibres transmit between 6 and 12 to 14 microns depending on their composition. The use of the heavier elements selenium and tellurium extends the operational wavelength . Kanamori et al [128] achieved losses below 1dB/m for the following ranges: As_2S_3 0.9 to 6 microns; As-Ge-Se glasses 1.3 to 9 microns; Ge-S glasses, 0.8 to 5 microns. Wehr and le Sargent [129] reported losses of <1dB/m between 5.5 and 10 microns with a minimum of 0.2 dB/m at 6 microns.

Other reported losses are higher 10 dB/m or more at 7-9 microns [130] and the same loss at 10.6 microns [131], (cf Kanamori et al [128] who claimed 6.2 dB/m at 10.6 microns, and Wehr and Le Sargent [129] who claimed 2 to 3 dB/m at 10.6 microns) although this is less of a problem when transmission is required only over a short distance.

Klocek et al [131] reported on the manufacture of chalcogenide glass fibre bundles with transmission losses of less than 10 dB/m in the range 6 to 9 microns. IFS [132] also supply chalcogenide fibre bundles with a reported loss of 8-10 dB/m at 9-11 microns.

The availability of fibres with transmission windows between 8 and 13 microns is desirable because this is the waveband at which objects at ambient temperature emit infrared radiation most strongly. Fibre forming ability is good, and mechanical strength of the fibres is greater than that of the fluorides.

8.3.4 Crystalline Fibres

There are a number of crystalline materials that have theoretical losses low enough to make them attractive as fibre materials for infrared transmission. Silver bromide, zinc selenide, sapphire and sodium chloride all have low intrinsic attenuation. However, the difficulties of growing single crystals suitable for long distance telecommunications fibres are considerable. Not the least of these is the low growth rates of only a few cm per minute, and the difficulty of growing in a core-clad structure.

Polycrystalline fibres show more promise, and were intensively studied in the 1970's by a number of workers [133,134]. Thallium halides were the principal materials studied, with a theoretical transmission loss below 0.01 dB/km at 7 microns. Extrinsic factors such as diameter fluctuations and impurity absorption have limited the transmission figures achieved to between 150 and 400 dB/km. This is, however, retained over a range of between about 6 to 15 microns.

Silver halide fibres are also possible candidates. The Japanese company Matsushita recently exhibited a 2.5 metre fibre with a claimed attenuation of only 0.21 dB/m at 10.6 microns [135]. Other workers have claimed losses of below 1 dB/m at wavelengths greater than 6 microns [99]. Murakami [136] patented an alkali metal halide fibre with a low alkali earth content which had a low but unspecified loss at 10.6 microns.

8.3.5 Hollow Core Fibres

It is possible to make oxide glass tubes with a refractive index of less than unity at 10.6 microns so that the radiation can be guided down the inside of the fibre [137]. Being transparent to visible light, the surrounding tube can be used to deliver a guide laser beam to the target for convenient positioning.

Typical transmission losses are about 1.5 dB/m [138] but bending loses are severe, 1.6 dB for a 1 metre bend radius, which seriously limits their suitability for use as a flexible link.

The fibres are relatively inexpensive, and are similar in mechanical and chemical durability to conventional silica fibres.

8.3.6 Choice of Fibres

In the case of infrared transmitting fibres, the technology is not mature, so conflicting requirements must be balanced when selecting a fibre component. Complete systems such as bundles are less readily available than is the case with optically transmitting fibres, and they are also generally less efficient, more expensive and often mechanically less durable.

Bearing in mind that the technique of interest here was intended to be used at or near room temperature, and striking a balance between cost, availability, mechanical and chemical durability and transmission, it was decided that chalcogenide fibres would be best even though they had a poor transmission record relative to the polycrystalline glasses. The silver halide fibre made by Matsushita of Japan was announced too late for any to be obtained within the lifetime of this work, and was not commercially available [139].

In general, the chalcogenides had a higher overall transmission than the fluorides at expected emission temperatures, but at higher temperatures, the fluorides were superior. When testing ceramics, there might be some circumstances under which it would be appropriate to use fluoride based fibre systems to deliver the emitted infrared radiation to the detector.

This has the drawback that a higher sample temperature must be achieved. In its favour are the greater availability of the fluoride fibres in desirable configurations such as bundles and cables, and the lower cost per metre of fibre.

While there are advantages to be gained from a high sample test temperature, principally that there will be an improvement in sensitivity (equation 5.3), it is generally preferable to keep it low to reduce the risk of misleading readings due to thermal distortions, and of damaging the sample. Thus temperatures are likely to be near ambient, approximately 300-350 K. Peak infrared emission at these temperatures is centred around 8-13 microns.

The incorporation of a fibre reduces the potential signal reaching the detector by at least its transmission and end losses. The minimum detectable temperature therefore rises by this factor, which was approximately fiftyfold for the chalcogenide fibres. Other losses, such as bending losses, misalignment and coupling losses would also contribute if present.

8.4 Infrared Fibre Measurements

The potential advantages of incorporating a flexible lightguide to take the infrared radiation emitted from a heated sample to the detector are described in section 8.1. With the conventional equipment used, a signal amplitude of 50mV or more could be obtained on many samples. Experience with the system suggested that successful results could be obtained with a received signal of 1 or more millivolts (see section 6 for equipment limitations). Thus if a fibre could be obtained with a total system loss of less than 17dB, corresponding to a received signal amplitude of about 1mV, then it would have some potential applications. Where there was a high thermal contrast in the sample, still higher losses could be sustained.

A survey of the literature (see above) revealed that while the theoretical losses in infrared transmitting fibres were very low, the achievable losses were very much higher. Many of the losses quoted were for experimental fibres which were not commercially available. It was considered that a minimum 1 metre length of cable was required because this was just sufficient to demonstrate the flexibility of the system while keeping the transmission loss down to an acceptable level.

8.4.1 Experimental Study

Two infrared transmitting fibres were obtained: one 250 micron diameter unclad fibre with loose ptfe sheathing [127], had a nominal loss of 6.8dB/m at 10.6 microns, although it had been verbally quoted as "about 12dB/m" (fibre A); one 125 micron diameter cabled fibre [130] with optically polished ends, had a nominal loss of 10 dB/m between 7-9 microns, and 0.86dB loss per end (fibre B). The ends of the first fibre were prepared to typical research standard by cleaving them with a diamond bladed knife. It is expected that these would show a greater loss than the optically polished ends. The expected losses for 1 metre lengths were thus >13.7 dB for the first fibre (A), and about 11.7dB for the second (B).

A 25 watt soldering iron was used as an infrared source. It was driven by a variac to allow control of the temperature, and hence the peak emission wavelength (table 8.3,). The emitted radiation was received by the collector mirror [109] and focussed either onto the fibre tip or directly onto the detector element [112]. The focal spot size of the collector mirror was claimed by the manufacturer to be approximately 125 microns - ie of similar size to the fibres. When the fibre was used, the near end was positioned close to the detector element, which faced away from the source.

If the mirror focussed onto a spot that underfilled the fibre, there would be no signal difference due to the different sizes of the fibre end and the detector element (figure 8.4). If the focal spot exceeded the size of the detector element (2 by 1.5mm) [112], then the reduction would be in proportion to the fibre and detector active areas (figure 8.4b) - ie a 61 fold reduction. If the focal spot had an intermediate size then there would be a lesser reduction in the relative signals (figure 8.4c). Since the fibre size and focal spot size were similar [109,130], there would only be a small reduction in signal, if any, unless the fibre and the focal spot were misaligned.

Assuming that the proximal fibre tip was positioned so that all of the emergent radiation cone impinged on the detector, then all the emitted radiation would be received by the detector element, even if this was not fully filled. If the emergent radiation cone overfilled or partially missed the detector element, then there would be a further reduction.

8.4.2 Expected Results

The ellipsoidal collector mirror focussed optical radiation reflected from the sample surface as well as the infrared radiation emitted by the sample. Absorption of this reflected radiation by any of the components would raise their temperatures, so that they would themselves radiate in the infrared, thereby acting as secondary sources. In particular, where optical radiation struck the fibre ends, the fibre itself would heat up. The chalcogenide fibres absorbed strongly at optical and near optical wavelengths, so that at one stage it was found that the fibre ends were ablating. The infrared filter [114] was found to prevent this. Comparative readings taken with and without the filter and with the detector at the mirror focus showed a signal of 2.34 +/- 0.03mV without the filter, and 2.35 +/- 0.02mV with it. The filter thus causes no significant change.

The soldering iron source was set up to give a reading of 2800mV, which was the maximum that could be consistently achieved. The chopping frequency was 40 Hz. The expected signal, after allowing for transmission loss, and assuming correct alignment of all the components would be 120 and 130mV for fibres A and B respectively. If the worst case is assumed, ie that the detector element is fully filled by the focussed radiation, then the expected signals will be 1.96mV for A and 2.08mV for fibre B.

The losses quoted for the fibres are both among the lowest losses in the spectrum. At other wavelengths, the losses will generally be higher. Wehr and le Sargent [129] published traces that suggested losses of > 100dB/m over a wide spectral range. A simple calculation showed that this will cause an extra loss of about 9 fold - so that signals of 0.2mV and 0.23mV could reasonably be expected in the worst case. This would be readily detected, since against a low noise background, signal changes of <0.1mV can be observed. In section 6.6, the minimum detectable temperature is shown to be about 1K with an IR fibre link, compared to 2.2mK with direct irradiation of the detector.

8.4.3 Experimental Results

With both fibres, readings were taken with different source temperatures (table 8.3, figure 8.5). Initially, signals of around 1.5mV were observed. From equations 5.1-5.4, it can be seen that the total amount of radiation emitted increases with temperature, as does the amount of radiation at a given wavelength. Thus the signal amplitude should increase with source temperature. The values observed were all very similar and showed no such trend.

The tests were then repeated with the detector surrounded by screens to block out stray radiation, and no signal was seen above the background noise. The position of the fibre end relative to the detector element was varied, and the position of the fibre end along the mirror axis was varied. No signal was observed in either case. It seems probable that the signals observed initially originated from stray radiation reaching the detector.

If the fibre had broken, it would be apparent in A through the ptfe cladding, although not in B. The fibre alignment within the cable was central; the alignment of the cable within the dummy detector was central, and the detector opening in the collector mirror was central, and the focal spot should be centred along the mirror axis. These observations were confirmed by the ablation of the unclad fibre tip, when it was aligned central to the mirror. One possibility is that the spectral losses are so high outside the quoted wavebands that the total energy delivered is negligible. Thus the absence of observed transmission remains unexplained.

8.4.4 Potential For Improvement

Improvements in the fibre energy collection could be made. The fibre end was slightly recessed within the ferrule of the end connector. This was because the softer chalcogenide suffers greater wear than the ferrule during polishing. When the fibre was mounted in the holder and positioned at the focus of the collector mirror, the fibre end was partially shielded from the collected radiation. If the fibre could be prepared with an end that was not recessed, then an improvement could be expected.

A larger fibre area would increase the likelihood of the focussed radiation entering the fibre. Where the fibre is small, a small misalignment could result in some or all of the radiation missing the fibre. If the diameter becomes too great, then the fibre loses its flexibility, but this can be overcome by grouping fibres into bundles. In the case of the chalcogenide fibres currently available, which are resin coated, the packing fraction in bundles is low, around 39% [132].

The transmission losses of the fibres could, in principle, be significantly reduced. The theoretical losses are much lower than those achieved in present fibre manufacture by several orders of magnitude - 10dB/km rather than 10dB/m for chalcogenide fibres [140]. There are, however, significant technological barriers to be overcome before this can be achieved.

Alternatively, the sample could be heated so that most of the radiation was emitted at shorter wavelengths, which would then permit the use of fluoride fibres. From the Wein law, the sample temperature would need to be 1170°C for peak emission at 2 microns, and 145°C for peak emission at 5 microns. At these high temperatures, there is an increased risk of thermal damage to the sample, and also of local thermal distortion which would give misleading results. In the case of YSZ coatings, the infrared transparency of the coatings is higher to shorter wavelength infrared radiation (figure 7.8), so that radiation heating of the coating would become more significant.

8.5 Summary

The poor showing of the infrared fibres prevented one proposed part of the work, in which a remote probe head was to be developed. A summary of the possibilities is included in appendix B, outlining the opportunities for fibre incorporation, both with current technology, and imminent technology.

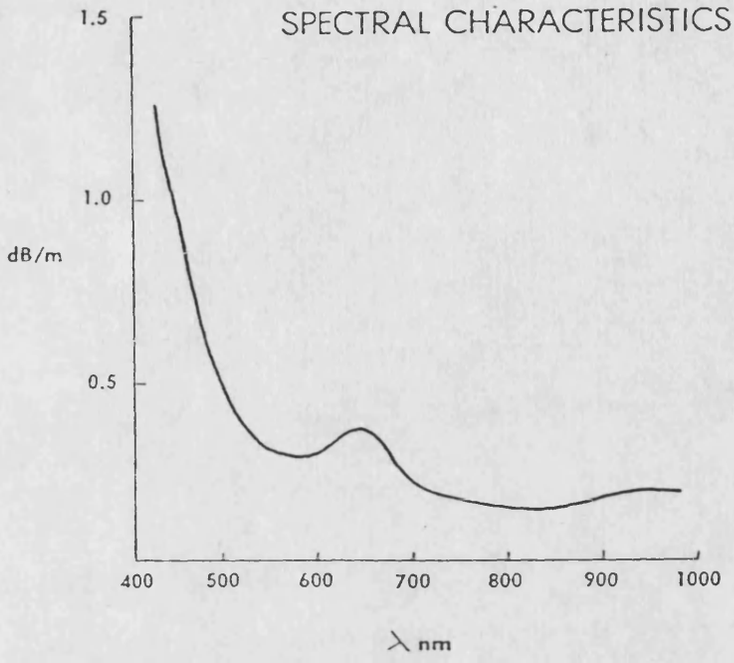

Figure 8.1 : Transmission loss versus wavelength for TBL [125] optical fibres used in this work.

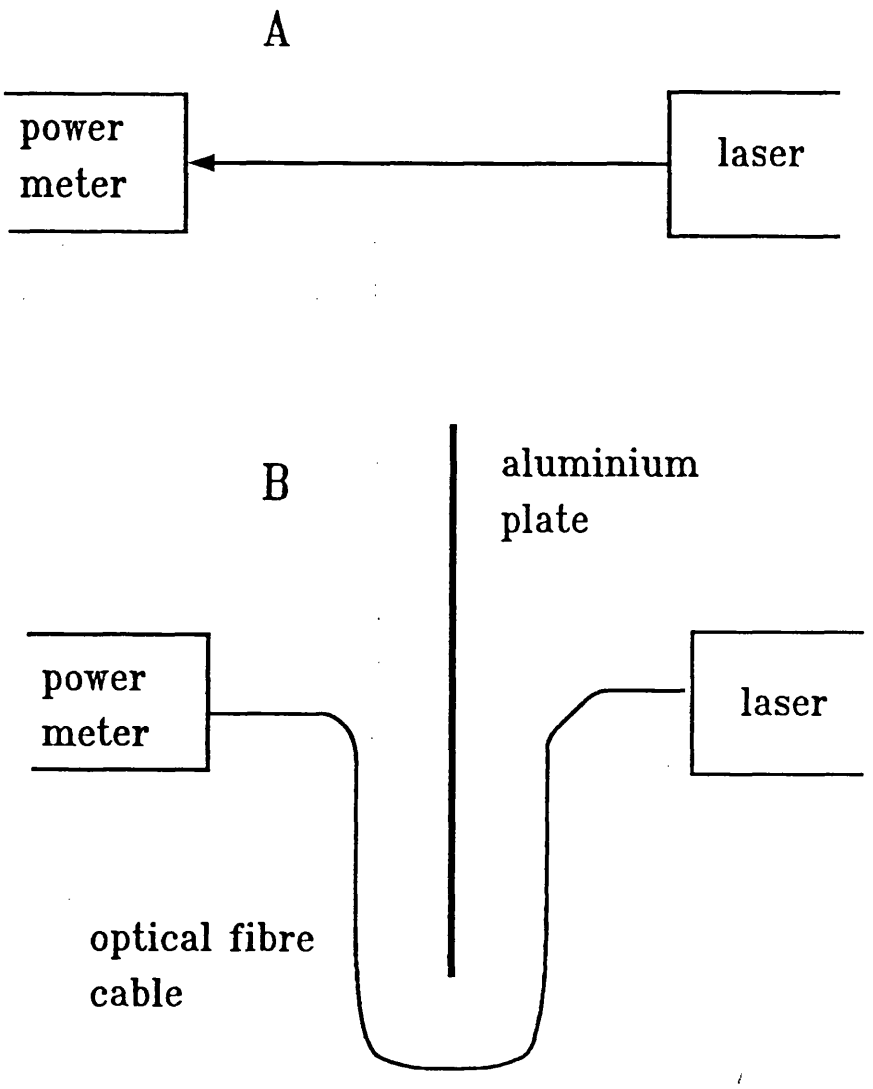

Figure 8.2 test rig for optical fibre bundle
a: without fibre (reference)
b: with fibre and light-proof baffle

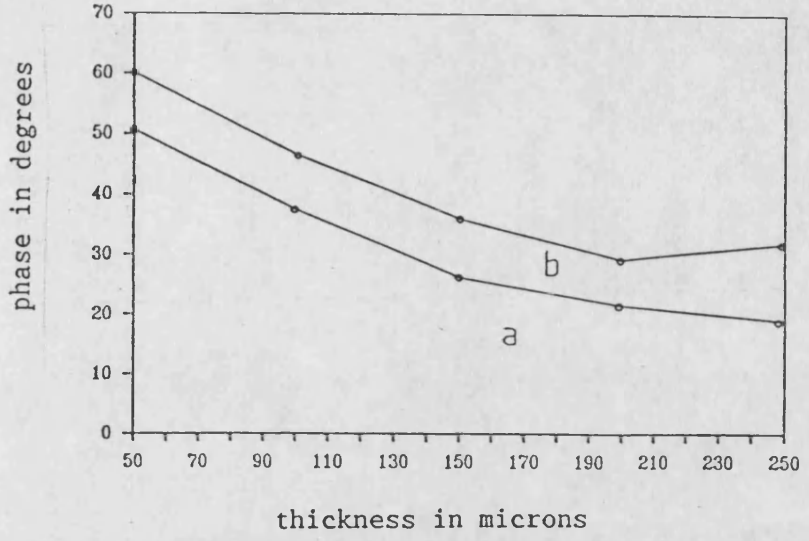

Figure 8.3 : Plot of phase angle variation with thickness for plasma-sprayed YSZ on mild steel.
Laser power 1W, modulation frequency 4Hz
a) darkened with ink; direct illumination
b) darkened with ink; illuminated via optical fibre
(phase shifted by +10 degrees for clarity)

a

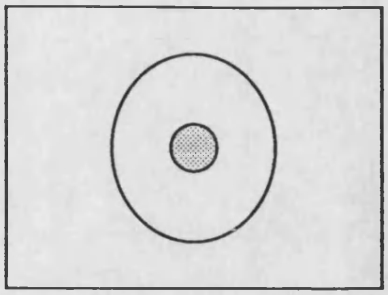

spot < fibre < element

signal collected by fibre

= signal collected by

detector element

b

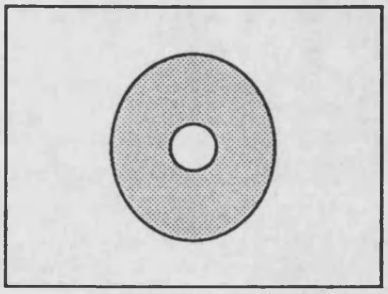

element > spot > fibre

signal collected by fibre

= y x signal collected

by detector element (*)

c

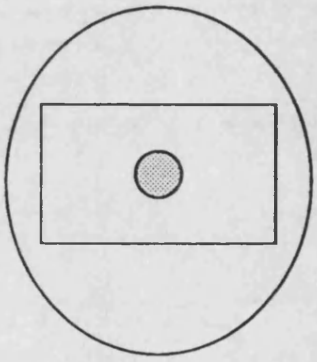

spot > element > fibre

signal collected by fibre

= z x signal collected by

detector element (*)

Figure 8.4 Schematic illustration of the affect of relative sizes of fibre, focussed spot and detector element (fibre end shown shaded for clarity)

* : y = (area of fibre / area of detector element)

: 1 > z > (area of fibre / area of detector element)

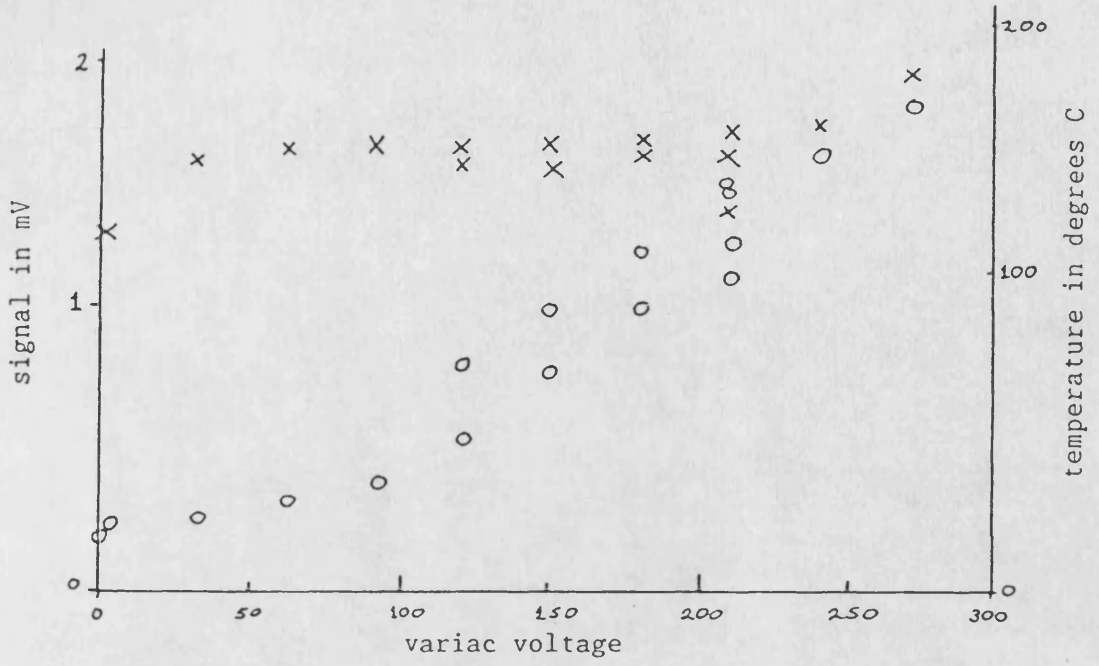

Figure 8.5a : Variation of signal received via unclad chalcogenide glass fibre [127], (x) and source temperature (o) with variac voltage.

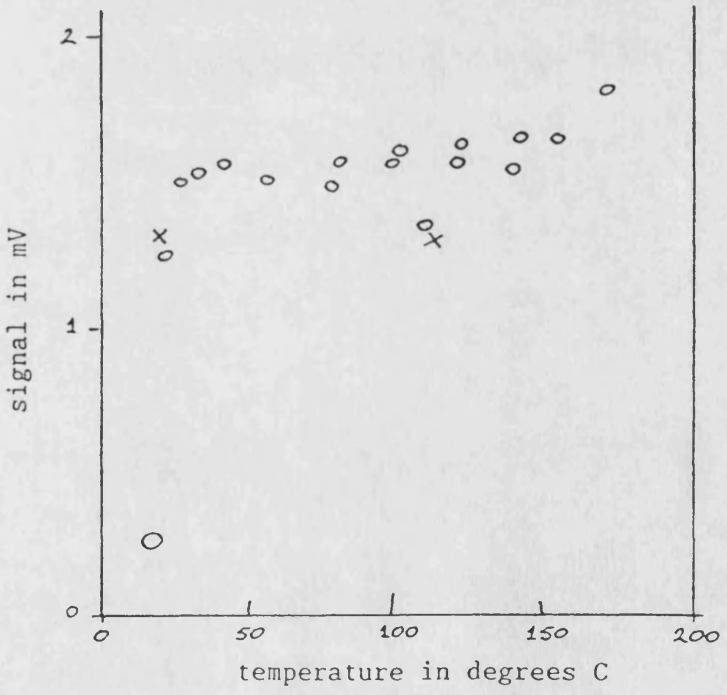

Figure 8.5b : Variation of signal received via unclad chalcogenide glass fibre [127] with source temperature (o). Points marked (x) were taken with an infrared transmitting filter between the source and fibre end.

Cable (1)	% Transmission	loss	predicted loss (2)
A	28.7 +/- 8.4 (3)	5.42dB	1dB (4)
B	42.7 +/- 8.8 (5)	3.69dB	1dB

Table 8.1 : Transmission of optical fibre cables [125]
(1) active diameter A = 1.5mm, B = 3mm
(2) bending losses and losses from fibre breaks not considered
(3) mean & standard deviation of 10 readings at 4 input powers
(4) does not allow for laser spot overfilling fibre
(5) mean & standard deviation of 12 readings at 4 input powers

Nominal Thickness	Sample Illumination Direct	Via Fibre	Phase Difference
2 thou	+50.8°	+50.1°	0.7°
4 thou	+37.5°	+36.7°	0.8°
6 thou	+26.3°	+26.1°	0.2°
8 thou	+21.4°	+22.0°	0.6°
10 thou	+19.0°	+19.2°	0.2°

Table 8.2 : Effect of light transmission via 2m long 3mm diameter optical fibre on phase variation with thickness on a step-coated YSZ sample on 316 steel.
Sample darkened with drawing ink.
Laser power 1W, modulation frequency 4Hz

Variac Voltage	Source Temperature (°C)	Received Signal (mV)
0	21.3	1.24 +/- 0.04
30	26.3	1.49 +/- 0.03
60	33.0	1.52 +/- 0.04
90	41.0	1.55 +/- 0.04
120	56.0	1.50 +/- 0.03
150	79.0	1.48 +/- 0.03
180	100.0	1.58 +/- 0.04
210	122.0	1.61 +/- 0.03
240	154.0	1.65 +/- 0.03
260	172.0	1.82 +/- 0.06

Table 8.3 : Variation in signal received via a nominal 1metre long 250 micron diameter unclad chalcogenide glass fibre and source temperature with variac voltage.

9 CRACK DETECTION

9 CRACK DETECTION

Vertical surface breaking cracks are a potentially serious hazard in thermal barrier coatings and in monolithic components. In the case of protective coatings, they can allow environmental access to the substrate; if the coating is part of an engine component, a crack could trap fuel which would subsequently detonate and damage the coating; in monolithic bodies, cracks are a source of failure if they are above the critical length (typically around 100 microns for ceramics).

The ability to detect such cracks is thus important. While thermal crack detection techniques techniques do exist [141], there are no established rapid tests that can be carried out on irregular and unprepared surfaces. In the following section, the term 'crack' is used to indicate a crack which is predominantly vertical, or which has a significant vertical component.

9.1 Background

It was shown in chapter 5, and in appendix A, that when an opaque semi-infinite body is illuminated by a modulated light source, the thermal wave phase lags the light source by 45 degrees. It was also shown that the presence of a horizontal interface causes reflection of the thermal waves, and that subsequent interference alters both the phase and amplitude of the resultant surface thermal wave according to the sign and magnitude of the reflection coefficient.

If instead of a horizontal interface, there is a vertical interface, such as a surface breaking crack, or an edge, there will also be a reflection from this, and subsequent interference will alter the resultant surface thermal wave phase and amplitude.

The thermal wave response to an edge, corner and mesa was considered by Aamodt and Murphy [131] for the three dimensional case. They used the method of images [57] to account for the effect of thermal wave reflection at the edges. In the method of images, the effect of the reflector (crack) is represented by positioning a mirror image source on the opposite side of the crack from the real source (figure 9.1). In the case of a single interface, it can be seen that there will be an enhancement due to the crack, E_{crack} which is determined by equation 9.1:

$$E_{crack} = 1 + \Gamma_c \exp(-2\sigma x) \qquad \text{equation 9.1}$$

Where the reflection coefficient Γ_c is 1 for perfect reflection (approximated by an air-filled gap), x is the distance from the source to the crack, and σ is the complex thermal wave number.

In general, the one dimensional case is sufficient to demonstrate the principles involved, and will be used throughout where possible. In the simplest analysis, the signal amplitude will increase, as the spot approaches the interface, finally reaching a maximum immediately adjacent to the crack. In the images model, this corresponds to there being two superimposed sources virtually at the same position, and the correspondinmg amplitude is thus twice that without the reflector.

Where the crack is wide, it can be viewed as comprising two distinct edges with an intervening gap. In the theoretical case with a point source and detector, the two peaks observed (one from each edge) would move closer together as the crack width narrowed, but the two peaks would never quite overlap. As the crack width became very small, the peaks would diminish, and ultimately, the crack itself would vanish and the peaks disappear altogether.

In all real cases, the souce and detector spots have finite size, rather than being points. The peaks observed in real cases, will thus experience some averaging, and will therefore be smoother than theoretical ones. As the spots move over a wide crack, two distinct peaks will be seen (figure 9.2a). With a progressively narrower crack, the peaks will be seen to move closer together, and will eventually overlap, so that a single major feature will be seen that has twin peaks (figure 9.2b). Where the crack is extremely narrow, or is closed, only one peak will be observed.

When the crack is very narrow, it can behave as a black-body source, so that rather than the signal amplitude decreasing over the crack, as is commonly seen, it actually increases because of the locally higher emissivity [88]. Kaufman et al [88] exploited this when detecting small cracks in rotating steel shafts: they were able to detect these because they had a significantly higher emissivity than the relatively bright steel background.

Kaufman et al [88] noted that the detector area affected the observed amplitude and phase at a crack. With a larger area detector, they found that the amplitude peak was broader and shallower, as was the phase peak, and both were slightly distorted. These changes are consistent with signal averaging occurring, which would tend to smooth out the response over a larger area (figure 9.2). The distortion seen might have been because the detector spot would, at some time, have 'looked' at regions on both sides of the crack.

They [88] also found that when a crack was angled away from the detector, the response was altered, because the source-crack distance varied through the detected region. The detected region also contained a different heat distribution than when the crack was perpendicular to the source-detector. They found that the phase peak was slightly lower and broader, and the amplitude peak slightly higher and broader than for a perpendicular crack, although neither was strongly affected.

Where the source and detector were not collinear, then the symmetry of the phase and amplitude traces was lost. The amplitude peaks were not significantly affected, but the phase peaks seen were up to double those observed with collinear source and detector spots. It was in this part of the work that they noted the absence of the expected dip in amplitude between the peaks, and they attributed this to the crack absorbing as a black body, and thus also reradiating a stronger signal (see section 9.3.8).

9.2 Theoretical Analysis

In an opaque monolithic medium such as vitreous carbon, the presence of a vertical crack serves as a thermal obstruction. The local temperature increases leading to a rise in the thermal wave amplitude. For a planar vertical crack, in an opaque semi-infinite homogeneous medium, with collinear source and detector spots, the enhancement due to a crack is given by:

$$E_{crack} = 1 + \Gamma_c \exp(-2\sigma x) \qquad \text{equation 9.1}$$

Where Γ_c is the reflection coefficient of the crack, approximately 1, σ is the complex thermal wave number, and x is the distance from the spot to the crack. Equation 9.1 applies equally to an edge if Γ_c is replaced by the edge reflection coefficient Γ_e. The maximum enhancement is, therefore, two fold immediately adjacent to the crack.

9.2.1 Effect of Multiple Interfaces

Where there is another interface present in a cracked medium, such as when two or more cracks intersect, or where there is a horizontal interface such as in a cracked coating, then there will be thermal wave reflections from both interfaces. The resulting interference will lead to a resultant thermal wave which is influenced by both (or all) interfaces.

Considering a two dimensional case, and assuming coincident point source and detector spots, the enhancement term for a right angled corner will be given by :

$$Ecrack = 1 + \Gamma_1\Gamma_2 exp(-\sigma x) exp(-\sigma y) + \Gamma_1 exp(-\sigma x) + \Gamma_2 exp(-\sigma y) \qquad \text{equation 9.2}$$

where Γ_1 and Γ_2 are the reflection coefficients at each interface, σ is the complex thermal wave number, and x and y are the distances to interfaces 1 and 2 respectively (figure 9.1b).

It is apparent here that the maximum amplitude enhancement will be twice that of a single interface, and that it will thus be up to four times the expected amplitude without any interfaces when the source and detector spots are adjacent to the corner. This is because the first interface (A-A) generates one image of the source (I1), and the second interface (B-B) generates one image of the source (I2) plus an image of I1 (I3) (figure 9.1b).

In a coating, the situation is similar to that in a mesa, and the resultant is the summation of the terms due to multiple reflection between the (nominally) parallel faces, and the reflection due to the third face (figure 9.3). It is obvious that the maximum enhancement will occur in the case where the parallel sides of the mesa are very close, or where the coating is very thin. In general, however, the maximum enhancement will not be achieved in this case because the mesa or coating will retain a finite width, and the exact enhancement will depend on the relative position of the source and detector spots between the parallel faces (figure 9.1c). In simple terms, the more edges that are present, then the stronger will be the amplitude enhancement.

A natural crack can be expected to be more variable than an ideal planar vertical crack, such as those used in theoretical models. In a plasma-sprayed coating in particular, the crack profile can be expected to follow an inter-particulate path, and therefore will be locally rough. There will thus be regions which are bounded by multiple edges where enhancement will be increased. This suggests that a natural crack will contain regions which have a more pronounced amplitude 'signature' than will idealised cracks.

9.2.2 Optical Effects

In a translucent medium, light absorption occurs over an extended region, so thermal waves will be generated throughout the optical volume and mutual interference will occur. Energy density will be reduced, so amplitude will be expected to be reduced too. Phase will be shifted downwards, as with uncracked coatings (chapter 7). If the optical penetration depth exceeds the crack depth, then saturation occurs, and energy will be lost within the sample (figure 9.4).

9.3 Factors Affecting Crack Detection Sensitivity

The principal influences on the sensitivity of thermal wave interferometry to the presence of cracks are noted below. The causes include geometrical and physical conditions, and they originate from both the heating/detecting system and from the sample itself.

9.3.1 Scanning Step Size

To ensure that the amplitude and phase features are not missed, it is important to choose an appropriate step size. If it is too large, the chance of missing the crack signature is increased. If the step size is too small, then the scanning operation becomes prolonged.

The maximum step size that can be used where the source and detector are collinear is equal to twice the thermal diffusion length. It is then no more than two thermal diffusion lengths from the spot to the defect and back. Beyond that, attenuation of the thermal wave is such that the feature can be considered "thermally distant", and it will not be observed.

9.3.2 Thermal Diffusion Length

The larger is the thermal diffusion length, the lower will be the energy density within the medium. There will also be a lower energy build up at the defect because the thermal thickness across the gap will be less. The thermal wavelength is controlled here by the modulation frequency, since the material properties are constant.

The expected response to a crack when using a low modulation frequency would be a broad and shallow maximum in amplitude centred on the flaw. As the frequency was increased, the thermal diffusion length would fall, the thermal thickness of the crack would increase, and the energy density would rise. Thus one would expect a sharper and higher peak than at lower modulation frequencies.

9.3.3 Source and Detector Spot Size

If the detector has a large spot size there will be some degree of signal averaging over the spot size [88]. Thus the amplitude near the crack, where it will be high, will be averaged with many regions further from the crack where the amplitude is low. In this instance, some increase in the signal would be expected, but it would be a generalised increase rather than a highly localised one (figure 9.2).

The source spot size to be used is limited by both optical and material considerations. The minimum size is determined by the optics available, and ultimately by the wavelength of the light itself. Since a smaller spot generates a higher power density, and hence a higher sample temperature, the thermal characteristics of the material also effectively limit the spot size. If a high melting point material is tested, then tighter focussing is possible than with a low melting point material at a given power, so a higher intensity and hence a higher signal amplitude can be achieved.

Where either or both of the detector and source spot sizes are finite, and the rms size is large, then lateral thermal diffusion will be negligible, and the downward thermal wave can be assumed to be one dimensional. But if the rms size is small, then lateral spreading effectively reduces the thermal diffusion length of the downward component [144]. This can be an advantage if probing thin samples, as the risk of backface reflections confusing the response is reduced.

Similarly, if the source size was large, then there would be parts of the spot near to the flaw which caused a local increase in amplitude, and parts of the spot which heated sound regions. The temperature at any one point would be a composite of the contributions from all the heated regions, and this would tend to average out the effects of a flaw.

Thus it is apparent that a high resolution will be obtained with a localised heat source and a localised detector. This situation is considered by Aamodt and Murphy [145], wherein the effects of relative spot radius, thermal diffusion length and optical penetration depth are assessed.

9.3.4 Nature of the Defect

If the defect is a large air- or similar gas-filled crack, then it should be readily detected. The reflection coefficient will be large (close to 1), and it will act as an effective thermal barrier so that heat build up will also be large.

If the defect is angled, there will be a reduction in the signal amplitude [145] relative to that of a vertical planar defect. When the crack is irregular and narrow, there may be partial contact across the width which will reduce its insulating properties. Thus $\Gamma_{effective} < \Gamma_{crack}$, and the defect will be less readily detected.

Also, if the crack has become filled with some material with lower thermal contrast than air or any other gas, then the defect will be less readily detected.

9.3.5 Optical Penetration Depth

If the optical penetration depth μ_o is smaller than the thermal diffusion length μ, then all the energy deposited in the sample will be able to influence the surface temperature. If the situation is reversed, then there will be energy deposited within the sample that cannot influence the surface temperature, so that the peak amplitude will be reduced ie saturation has occurred. Similarly, if $\mu_o >$ the crack depth, d_{crack}, then energy will be deposited in the sample that will not encounter the crack, and so thermal contrast will be reduced (figure 9.4).

9.3.6 Crack Depth

If the crack is shallow, ie d_{crack} is small in comparison to μ, then thermal energy will propagate past the base of the crack, and will not add to the energy build up at the obstacle. If the crack is deep ($d_{crack} > \mu$) then all the thermal energy will encounter the thermal barrier it offers and will raise the peak amplitude. If $d_{crack} > 2\mu$, then it can be considered to be infinitely deep [145], (figure 9.5).

If the crack is not surface breaking, then its depth beneath the surface determines its detectability. A crack near the surface will be more thermally significant than an equivalent crack further into the sample, both because thermal energy will 'pass over' the crack (figure 9.6), and because thermal waves have further to travel.

9.3.7 Source-Detector Alignment

If the source and detector spots are separated by a distance z, and x is the distance from the source spot to the crack, then the enhancement term is given by:

$$E_{crack} = 1 + \Gamma_c \exp(-\sigma(2x-z)) \qquad \text{equation 9.3}$$

If the detector is closer to the crack, then 'z' is positive, and if the source spot is closer, then 'z' is negative. Where the crack lies between the source and detector spots, the enhancement will tend to zero because very little energy will cross the crack (figure 9.7).

As the system is scanned over a defective sample, with the source spot leading, the enhancement will be determined by $\exp(-\sigma(2x-z))$ which will yield a maximum value of $\exp(\sigma z)$. The amplitude will then fall as the two spots span the crack, and then the maximum enhancement will again be $\exp(\sigma z)$.

9.3.8 Crack Width

A narrow crack, whether closed or open, will obstruct the passage of thermal waves. The width of the crack has some bearing on the crack signature. If the crack width is near to the mean free path of the gas then the effective thermal conductivity of the gas will be reduced (see section 7.6 & appendix B). Where the crack is very wide, it will behave as two separate edges with no interaction, and two separate amplitude peaks will be observed. As the crack width narrows, there will still be two peaks, but the dip between them will be reduced (figure 9.2). Eventually, only one peak will be observed. Where the crack is very thin, it will be less of an obstruction to the passage of heat. The crack therefore reflects less energy, and so the enhancement will be reduced (subject to the above comments).

The amplitude drop between the two maxima, ie when the source is directly over the crack, may be less than expected. A crack can act as a black body source, [88], so that although the signal drops, the increased emission compensates for this. The emitted power is determined from equation 5.1, $W = \varepsilon\sigma T^4$. Where ε is the emissivity, generally < 1. Thus when the crack acts as a black body, there will be an increase in the emitted power because $\varepsilon_{crack}/\varepsilon_{medium} > 1$.

9.3.9 Interaction With Other Defects and Interfaces

If the crack is near an interface, as would be the case with a thermally thin cracked coating, thermal waves will be reflected from both interfaces. Where the lateral discontinuity is of finite size and close to the vertical crack, then the response may be misleading, especially when the reflection coefficient of the lateral defect is opposite in sign to that of the vertical crack. This is because the amplitude increase due to the vertical crack will be balanced to some extent by the amplitude decrease due to the defect.

Where the coating is of even thickness, the crack response will be superimposed on the response from the coating-substrate interface, so that it will still be apparent. Thermal contrast is likely to be reduced, since the signal amplitude overall will be higher than in a thermally thick sample.

Plasma sprayed coatings have a particulate structure, and since the individual particles are strong, failure is most likely to occur between the particles. Thus the surface may well be irregular (figure 9.8). Heat will be concentrated where there are projections, and so the local temperature will increase, as will the amplitude.

9.3.10 Effect of Translucency

When the medium is translucent, there will be additional factors to consider. The change in surface reflection between the medium and the crack may be significant, and the emissivity difference between the medium and the crack may be much larger. In either case, the signal amplitude will be increased or reduced in a manner that could obscure the expected increase in the presence of the crack. For example, carbon has an emissivity, ε 0.85 [146], while for zirconium oxide, ε lies between 0.18 and 0.61 [146-148]. Thus $\varepsilon_{crack}/\varepsilon_{carbon} = 1.18$, while $\varepsilon_{crack}/\varepsilon_{YSZ} = 1.64$ to 5.56 (depending on the value of ε_{YSZ} taken). This assumes that the crack acts as a black body and has an emissivity of 1.

If the medium is optically scattering, and the crack is optically near to the light source, light will be reflected at the interface, and thus the effective intensity will increase. This then leads to a higher temperature in the body and a larger amplitude. This can be interpreted as $\beta_{effective}$ increasing.

Thus in most cases, a crack will be detected more readily in a translucent medium than in an opaque one. This is shown to be the case in the experimental results section. Table 9.1 shows some possible values for the effects noted above, and indicates the likely effect they would have on the amplitude.

9.3.11 Summary

It is apparent that the interaction of all these factors will determine the ease with which a crack may be detected. For maximum effect, a highly localised heating source and detector are required, the thermal diffusion length should be small, and μ should be larger than or equal to μ_o. The most readily detected cracks will be deeper than both μ and μ_o, and will be smooth, wide, planar, vertical and filled with a highly thermally contrasting medium relative to a solid, such as air or some other gas.

9.4 Equipment

Samples containing either simulated or natural cracks were mounted on the thermal wave test system described in chapter 6, and tested by linear scanning perpendicular to the crack or simulated crack. A number of different materials were tested, including monolithic metallic and ceramic samples, and opaque and translucent ceramic sprayed coatings.

The equipment was the same as that used in the testing of YSZ coatings, (described in chapters 6 and 7). Where the samples were small, they were attached to a large metallic or similar block by doubled sided adhesive tape. This block was then itself mounted on the scanning stage. Where they were larger and more robust, they were mounted directly onto the scanning stage. The delaminated YSZ coating was an exception. This was held in position with a specially made collar, which was a push fit onto a suitable mounting block.

9.5 Experimental Work

Results are grouped by sample material type.

9.5.1 Aluminium Samples

Two blocks of a commercial aluminium alloy were milled to shape, approximately 40*25*15mm, and sprayed with matt black heat proof paint. They were then mounted on a holder as shown in figure 9.9. The holder allowed the block separation to be adjusted, so that different crack openings could be measured on one sample.

Linear scans were then made across a 2mm gap at different detector-source displacements. Figure 9.10 shows the amplitude variation with scan position. The position of the gap is clearly visible in all the traces, and amplitude falls nearly to zero over the gap itself on all the samples. The greatest source-detector displacement used was 5mm (upper curve-a), and the smallest was 0mm (lowest curve-h).

The differences in amplitude between the two sides of the traces were attributed to slight variations in the paint coating, since one was noticeably more reflective than the other. The rounded edge to the traces near the site of the gap was attributed to a slight rounding off of the edges of the blocks themselves. This occurred because the soft aluminium deformed during machining and in subsequent handling. Thickness effects were thought to be unlikely, since the thermal thickness had been determined to be at least 12.

Several unsuccessful attempts were made to eliminate the variation in the paint coating. Black anodised blocks were also used, but the coating could be made opaque without becoming thermally significant, and thus distorting the results.

The phase responses were less consistent than the amplitude responses and have been plotted individually for clarity (figure 9.11 a-h). In all cases, the position of the gap is indicated clearly by a phase peak.

Figure 9.11a shows a double peak with an intervening trough over the gap, consistent with interference peaks arising from thermal wave reflections at the interfaces. However, comparison of the phase plots with the amplitude plots reveals that these peaks fall within the boundaries of the gap. It was observed that in some areas of the base plate, the paint coating had been burnt off by the laser, and it was concluded that this generated most if not all of the observed signal. There is a very small phase dip visible at scan position 9mm on all the phase plots, and it is thought that this is actually caused by the thermal wave edge reflection. The peaks are artifacts seen due to structure on the base-plate within the gap. At maximum displacement (figure 9.11.h), there is a small phase peak rather than a dip at scan position 9mm. This could be caused by minor variations in the starting position of each scan, or possibly by the displacement changes.

9.5.2 Vitreous Carbon (Simulated Cracks)

Carbon was selected as a test material because it is opaque, has convenient thermal properties for thermal wave testing, it is thermally stable, and it was readily available with natural cracks. Trial scans on reactor grade graphite bars which had been broken in mechanical tests showed an uneven thermal wave response, and very unclear crack signatures. This was thought to be because of its thermal anisotropy and pronounced grain structure. Vitreous carbon was then used because it is isotropic and homgeneous, and has the other advantages of graphite, while also being more resistant to handling because it is harder.

9.5.2.1 Sample Preparation

The end faces of two vitreous carbon blocks approximately 20*10*3mm were polished to a 6 micron finish on a diamond wheel. The blocks were then mounted on a base plate with their polished faces butted together to give a narrow simulated crack. These were then linearly scanned across the gap. Phase and amplitude traces are shown in figure 9.12. The amplitude traces show a distinct peak on the left hand side, followed by a marked dip, and a small peak on the right hand side. The phase trace shows a very distinct dip, but no apparent peak. Variations in amplitude suggested that the surface conditions differed, so they were ground flat on a 600 grit silicon carbide wheel for further work.

9.5.2.2 Effect of Scanning Step Size

Two scans were made in which only the scanning step size was changed (figure 9.13). At 8 steps/mm (step size of 125 microns), the amplitude peak is distinct, and a number of other features are seen. When the step size is decreased to 30 microns (32 steps/mm), the peak is sharper and higher. With a larger step size, there is an increased risk of 'stepping over' small features, or in the case of a peak, taking a reading on the edge of a peak rather than at the central highest point.

9.5.2.3 Effect of Focussing

The samples were linearly scanned with a different laser spot size, but otherwise identical conditions (figure 9.14). In figure 9.14a, made with an unfocussed laser spot, there is a slight step approximately 10mm into the scan, and a slight dip in the phase trace in the same position. Figure 9.14b shows a scan made with the laser spot focussed to about 250 microns diameter. The step at 10mm on the amplitude trace has been resolved into a distinct peak, and although the phase dip is clearer, there is less change. The focussed spot reduces signal averaging, and reveals local variations more clearly.

9.5.2.4 Effect of Source-Detector Displacement

The detector was mounted on an x-y-z stage. The majority of readings were taken with the detector position adjusted to give the maximum amplitude at a sound thermally thick region of the sample, ie ideally with collinear source and detector spots. The detector was displaced right and left in 100 micron steps to determine the effects of source-detector alignment. No difference was detected in either the shape or size of the amplitude and phase peaks, even between the maximum displacements of 600 microns right and left (figure 9.15). The system could not be moved any further than that without a major redesign of the system.

It had been expected that the asymmetry of the amplitude peaks would have been reversed at some displacement. this effect was, however, later observed when scanning in the reverse direction, so that the detector led the spot in one direction and lagged in the other.

9.5.3 Vitreous Carbon (Natural Cracks)

A cracked bar of vitreous carbon approximately 100*10*3mm in its undamaged form had been broken mechanically to reveal a conchoidal fracture surface. The fractured surfaces fitted together very closely, and the break was very close to one end of the bar. Optical microscopy revealed that, when placed in contact, a crack less than 2 microns across could be seen at the surface. The curvature of the fracture surfaces made it impossible to determine the exact separation across the whole of the crack, so the width has been quoted as '<2 microns'.

The top surface was ground flat with 600 grit silicon carbide paper, and the sample scanned linearly across the crack at two different modulation frequencies, 20Hz and 40Hz (figure 9.16).

9.5.3.1 Results

At 40Hz modulation frequency, there is a small but clearly defined double amplitude peak about 2mm into the scan (figure 9.16b), which corresponds to the crack position. The peak is about 0.5mV above a background of 2.5mV, a peak:background ratio of 1.2:1. The phase peak is less clearly defined.

At a modulation frequency of 20Hz, the amplitude peaks are significantly smaller and less well defined than at 40Hz, and the phase feature is barely detectable (figure 9.16a). Calculation from equation 7.3 , shows that the reflection coefficient of such a crack is about 0.06, while at 40Hz, it is 0.17. The enhanced peak seen at a modulation frequency of 40Hz is caused by the reduced signal averaging that results from a smaller thermal diffusion length.

9.5.4 YSZ Coatings (Simulated Crack)

Plasma sprayed YSZ coatings with a nominal thickness of 400 microns had been deposited onto aluminium substrates. Sample bars approximately 10*100mm were available. A diamond bladed microtome blade was used to cut notches into the coatings to simulate wide cracks. One cut was made down to the substrate, and the other was cut only part way into the YSZ coating. Because the microtome blade was curved, the cuts varied in depth across the sample. Line scans were thus made across the centre where the cracks had maximum depth. The samples were scanned both as-received, with a translucent YSZ coating, and with the coating rendered artificially opaque by painting it with drawing ink.

9.5.4.1 Results - Translucent Samples

The traces in figure 9.17 show the response of the sawn sample as the chopping frequency increased. The initial reading was taken at 0.5 Hz (figure 9.17a, trace a) and shows a small phase peak over the shallow cut and a dip plus a peak at the site of the large cut. At this frequency, the substrate is thermally thin ($\mu/l < 1$) so interference occurs between incoming thermal waves and backface reflections. At higher modulation frequencies (figure 9.17a, traces b-f), the peak is seen at the shallow cut up to 5 Hz, and then becomes indistinguishable against the background noise. At the same time, the dip at the deep saw cut vanishes as the substrate becomes thermally thick, and the peak is seen to split into a doublet, consistent with the cut appearing as two edges symmetrical about the crack centre.

There is a dip in signal amplitude over both cuts, with that of the shallow cut becoming indistinguishable above a 5Hz chopping frequency (figure 9.17b, traces c-f). Only one peak is seen, and the response is asymmetrical. This could be due either to a misalignment between the detector and source, which would, however, be expected to manifest on the phase trace, or it would suggest that the two edges are not identical. Despite the lack of matching phase response, the former is considered more likely, since this effect has been observed previously in this system, and edge asymmetry would also be likely to influence the phase. The amplitude peak is a maximum at 40 Hz, which is attributable to the greater input power used. The peak:baseline ratio is, however, also greater than at the other frequencies used (table 9.2).

The amplitude traces show a less distinct structure, and there is more 'noise' on the trace. On the large saw cut, there is a very substantial dip over the crack, with a large peak at one edge (step number 200). Peak:background ratios are roughly 2:1 or better throughout. This is quite clear, despite the overlap in the traces.

9.5.4.2 Results - Opaque Samples

With the ink-darkened sample, the phase response is similar (figure 9.18a), except that the peak does not split into a doublet over the large cut, and the peak over the shallow cut is seen at all frequencies.

The amplitude trace shows a drop at all frequencies when over the large cut, and there is no significant peak at the edge unlike with the undarkened sample (figure 9.17b). There is very little amplitude change at the shallow cut, with a very small peak barely visible at 5 Hz and above, and a slight dip at 2 Hz and below. The fall in amplitude can be related to the increased reflectance of the sample where it has been cut, which would reduce the total energy absorbed.

Peak:background ratios are lower than on the translucent sample, between 1 and 2:1, generally on the lower side. The repeatability is low on these scans because of the relatively coarse scanning step size (1/4mm).

9.5.5 YSZ Coatings (Natural Crack)

A naturally cracked plasma sprayed YSZ coating was obtained which had delaminated totally. It was thus in the form of a fragile 50mm diameter disk, with an uneven thickness, generally a few hundred microns (nominal 1000 microns). It contained a long crack stretching almost the whole diameter of the sample, which varied between about 500 microns at one end to below 50 microns at the other. Because the crack followed an intergranular path, the local width varied considerably over short sections (between about 50 microns to below 20 within 1 or 2mm). The crack width was thus quoted as 'below 50 microns'.

The sample was held in a specially made holder, onto which reference marks were made. The crack width between the marks was measured by optical microscopy, and any features seen optically were compared with the thermal wave scan in an attempt to relate the two.

9.5.5.1 Effect of Focussing

Scans were made under similar conditions but with modulation frequency and laser spot size varied. The laser spot was either left unfocussed (1/e diameter 1.2mm) or focussed to 250μm diameter. Modulation frequencies of 5 and 8Hz were used. The traces are shown in figure 9.19.

On figure 9.19, there is a noticeable phase peak between 6 and 8mm on the scan, with a corresponding dip and surrounding double peak on the amplitude trace. This feature is prominent at both 5 and 8Hz modulation frequency. Both phase and amplitude traces obtained with the laser spot unfocussed, however, show little evidence of the same feature at either frequency.

9.5.5.2 Optical - Thermal Wave Comparison

A similar set of measurements was taken over a region known to contain a crack (figure 9.20). After thermal testing, an optical scan was made, and the features noted (figure 9.20, overlay). These are denoted on the overlay as follows:

C = crack; I = (metallic) inclusion; P = pit; R = ridge.

It can be seen that there is some limited correlation between optically detected features and thermally detected features. Some discrepancy in positioning will have occurred due to minor misalignment of the sample when transferring it between the thermal and optical measurement equipment. The natural roughness of the plasma sprayed coating would also distort the response. There are amplitude peaks corresponding to cracks, and the pit and inclusions both appear to be associated with amplitude dips. There was no feature on the thermal trace that could readily be associated with the observed ridge.

In addition to the thermal features noted above that corresponded to observed surface structures, there were also many observed features that had no thermal counterpart, and many thermal features that had no apparent physical cause. An ideal sample or set of samples would have been smooth surfaced, and would have contained only one well characterised physical feature.

9.5.5.3 Effect of Modulation Frequency

The cracked, delaminated sample was scanned at modulation frequencies between 10 and 80Hz at 8 steps per millimetre. Results are shown in figure 9.21.

In figure 9.21a, the modulation frequency was 10Hz, and two distinct peaks are visible, at scan positions of roughly 3 and 13mm, and there are also phase dips of similar magnitude to the noise. The amplitude peaks are 9mV over a background of about 6mV - a peak:background ratio of 1.5:1.

At 20Hz modulation frequency (figure 9.21b), the peaks are more prominent, and the traces generally show more features because there is less signal averaging because of the smaller thermal diffusion length. The peak to background ratios are about 2:1 at 3mm and 3:1 at 13mm, but the phase dips are similar to those seen at 10Hz. The asymmetry in the peaks is attributed to slight movements of the sample between scans.

At 80Hz modulation frequency, and at a higher laser power, the phase dips are again similar to the general phase noise, but the amplitude peaks are very much higher (figure 9.21c), at almost 7:1 peak:background ratio (28mV:4mV and 17mV:4mV). This suggests that signal averaging is very much reduced because of the significant reduction in the area probed (see figure 9.2).

The 7:1 enhancement observed is significantly above that expected by a simple consideration of the images model. It is, however, within the range expected from table 9.1 and section 9.3.8, where other factors are considered.

9.5.6 Unidentified Carbonaceous Pipe Deposit

An unidentified carbonaceous deposit from a pipe in a chemical plant was removed, and two of its surfaces cut with a scalpel to form a right angled corner. The sample was then mounted on a holder so that one cut surface faced upwards, and the other formed an edge. This assembly was then mounted onto the scanning stage. Linear scans were made across the sample, so that they scanned over the prepared edge. As a result of this, the first 1.5mm of the traces in figure 9.22 are of the mounting plate and should be ignored.

The sample was black and opaque, and had an appearance much like ashed wood, with an anisotropic macrostructure, and little mechanical strength. The apparent visual reflectivity varied across the natural surface, but was reasonably constant over the cut surface. At high laser intensities, the material would ignite.

Two modulation frequencies were used, 20Hz and 40Hz. The amplitude enhancement due to thermal wave reflection at the edge is clearly seen in the scan made at 40Hz, while it is not at 20Hz. The change in the amplitude away from the edge is because the sample surface varies outside the cut area, so that thickness, surface texture, and local reflectivity are different. The phase trace is not clear enough to positively identify any feature associated with the edge.

9.6 Summary

Both natural and simulated cracks were detected in a wide range of materials. Crack and/or edge detection was demonstrated in monolithic metallic samples (aluminium), in monolithic opaque ceramic samples (vitreous carbon), in a particulate translucent and opaque ceramic (plasma sprayed YSZ), and in an opaque particulate carbonaceous material.

Cracks as small as 2 microns were detected in vitreous carbon, and as small as 50 microns in YSZ. In this latter case, the response was very strong, which suggests that very much smaller cracks could readily be detected.

It was not found possible to identify any of the features on the thermal trace without prior knowledge of their presence. There are many conflicting influences on the final thermal wave response, and it was not possible to distinguish the causes just from the response. It was, however, possible to identify that there was a feature present on the sample that might warrant further investigation, its location and in some cases, its approximate size.

On a more positive note, the cracks remained detectable under a wide range of operating conditions: laser spot size; scanning step size; sample optical properties; crack width, and little sample pre-processing was needed.

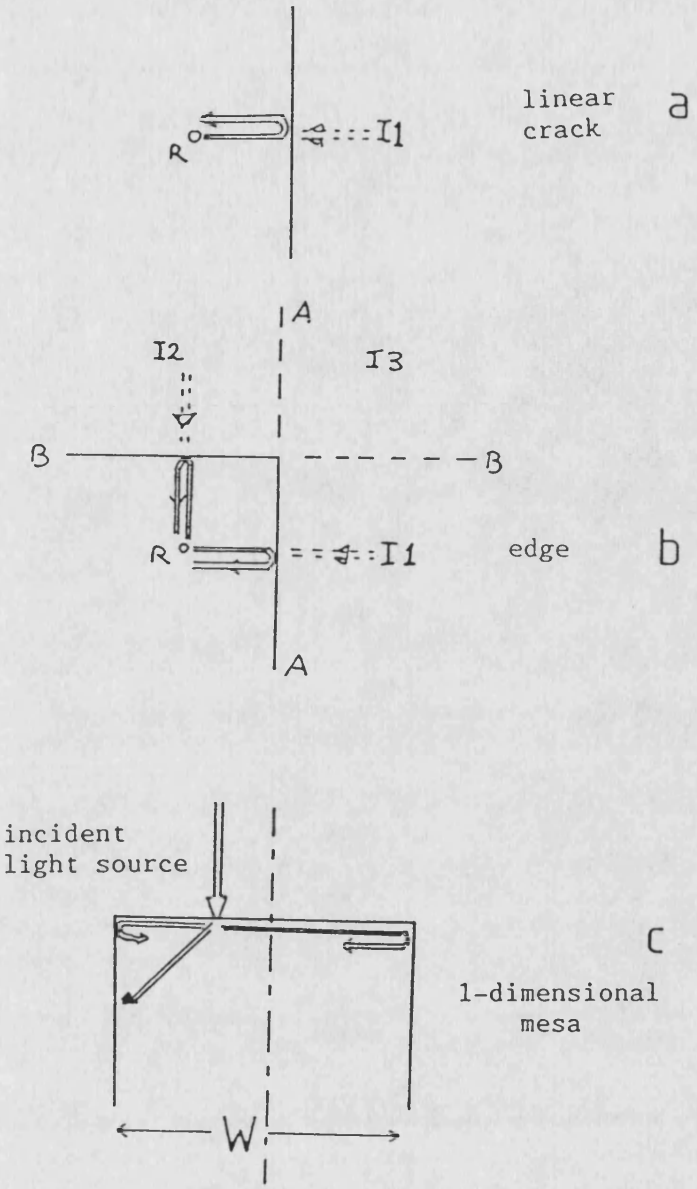

Figure 9.1 : Schematic illustration of thermal barriers with image heat sources. Solid arrows represent real heat flows, broken arrows represent image heat flows. Solid lines represent real boundaries, broken lines indicate planes of image reflection.
R = real heat source; Ix = image heat source number x
Images have been omitted in (c) for clarity

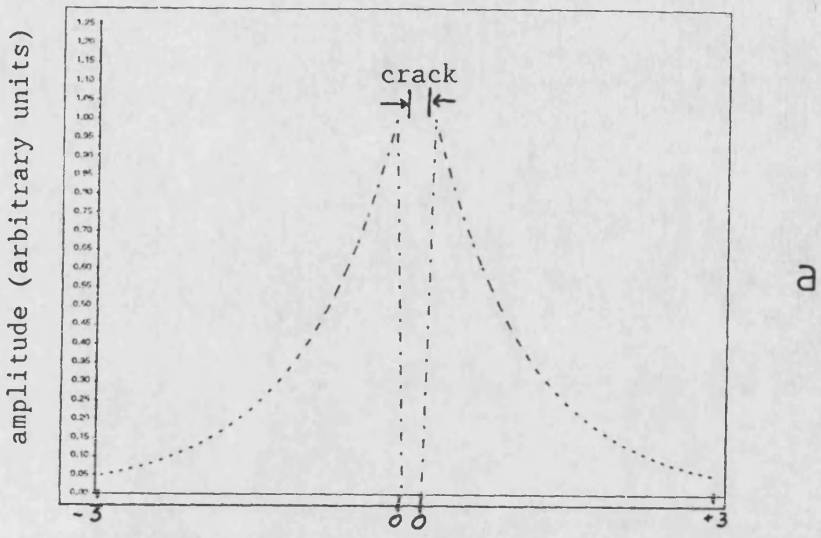

a

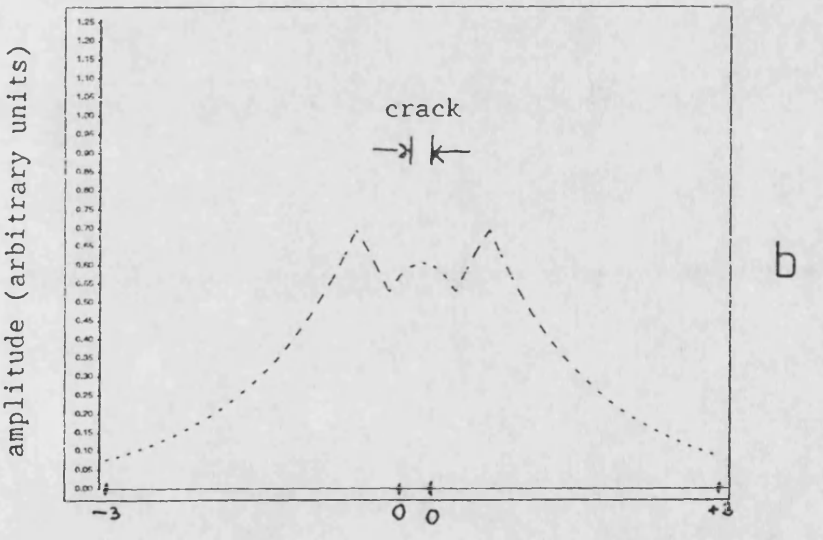

b

Figure 9.2 : Effect of signal averaging on thermal wave amplitude response near a crack.
Crack width 0.3μ , reflection coefficient = 1 .
a) unaveraged signal
b) signal averaged over 0.9μ

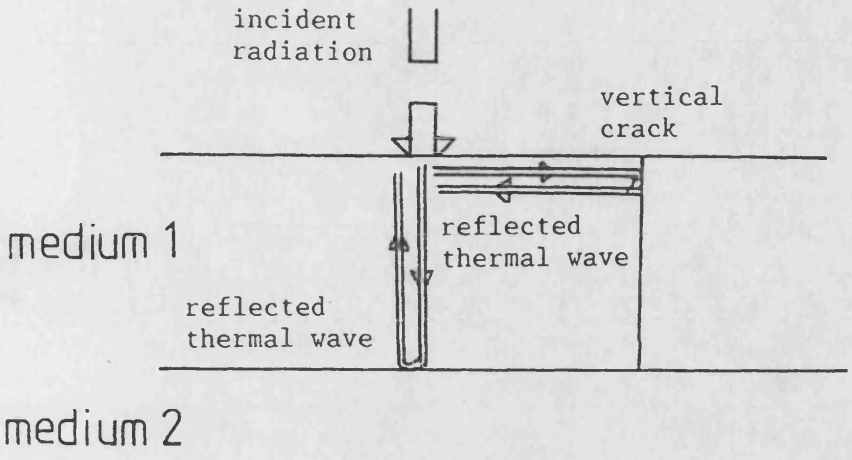

Figure 9.3a: Schematic showing combined reflection of thermal waves at vertical crack and horizontal interface in thermally thin opaque medium

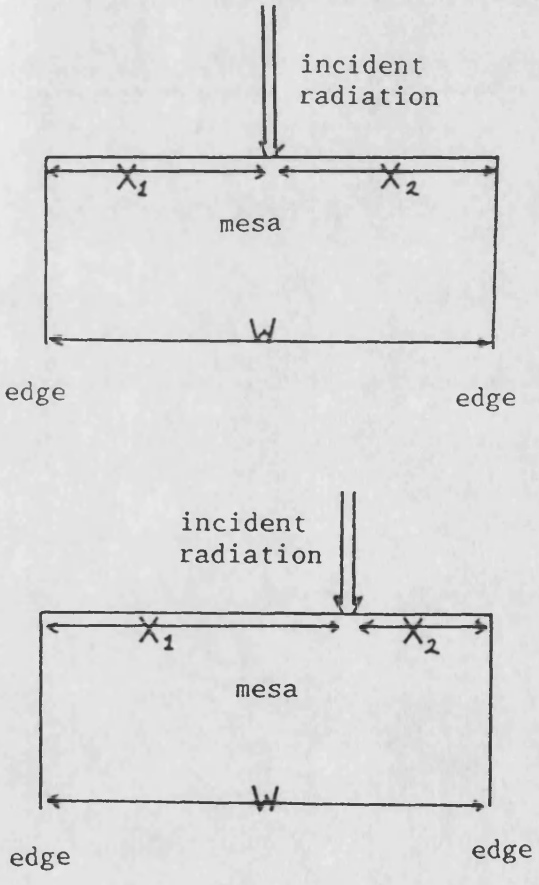

Figure 9.3b : Schematic illustration of illumination of a mesa
i) central illumination, x1 = x2 = w/2,
symmetrical temperature enhancement
ii) off-centre illumination, x1 ≠ x2 = w-x2
asymmetrical temperature enhancement

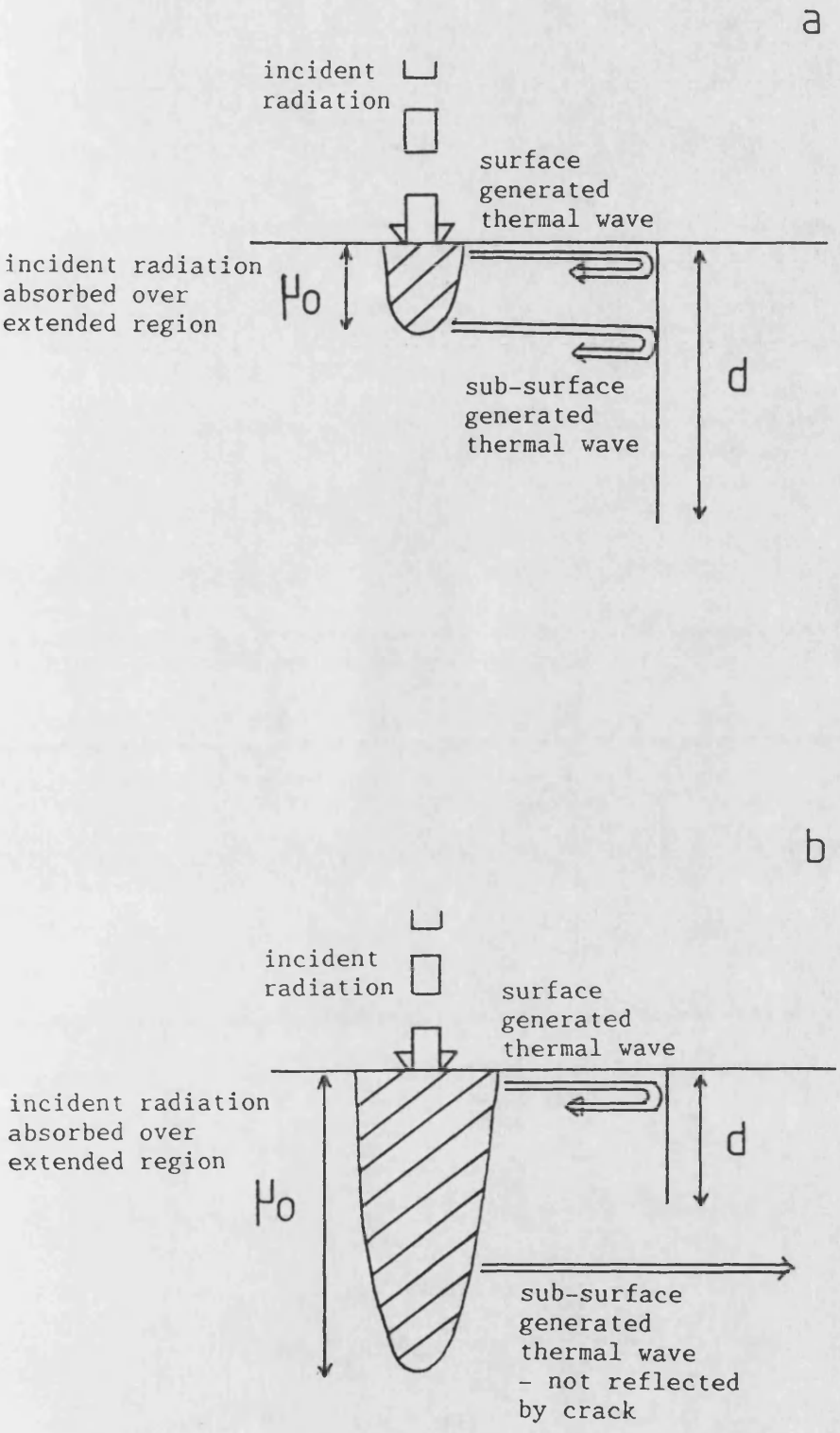

Figure 9.4: Schematic of effect of optical penetration depth μ_o and crack depth d on sensitivity
a) $d > \mu_o$, effective reflection coefficient unmodified
b) $\mu_o > d$, thermal waves generated below the crack, effective reflection coefficient reduced

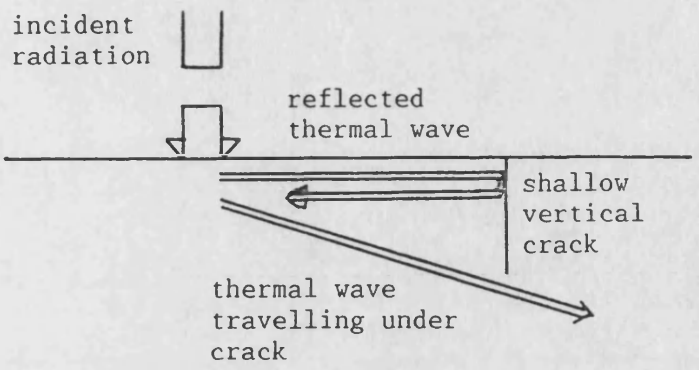

Figure 9.5a: Schematic showing thermal wave 'passing under' a shallow crack - effective reflection coefficient reduced

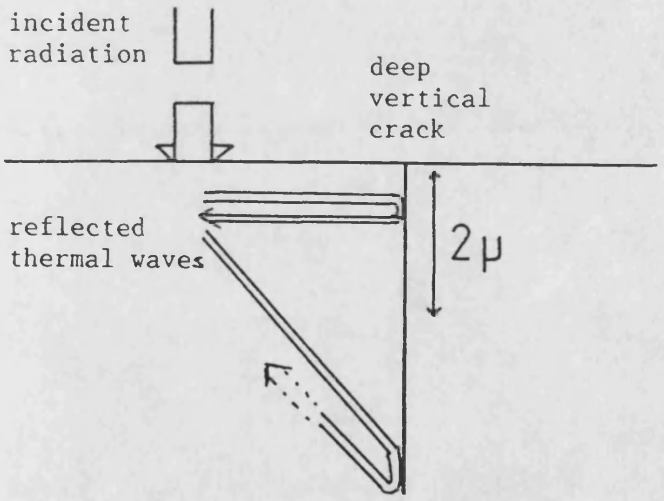

Figure 9.5b: Schematic showing thermal wave reflected by deep vertical crack - effective reflection coefficient unmodified

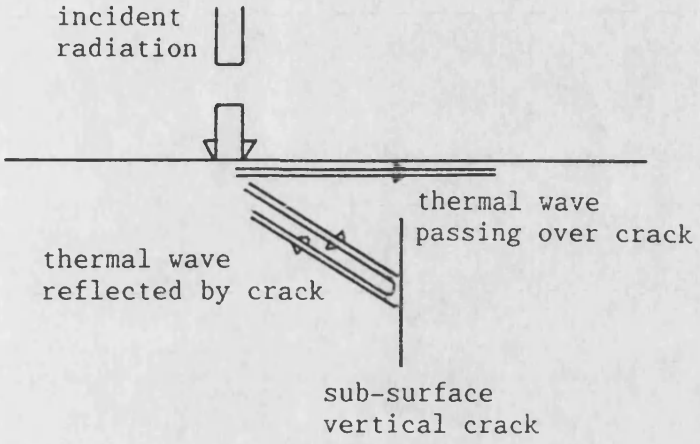

Figure 9.6: Schematic showing thermal wave 'passing over' a sub-surface crack - effective reflection coefficient reduced

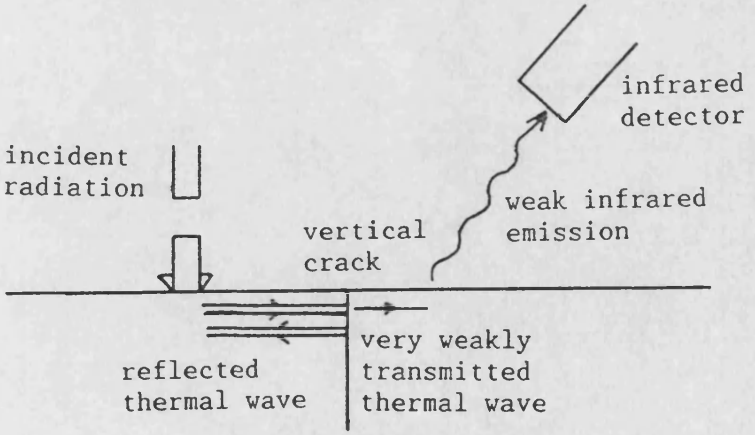

Figure 9.7: Schematic showing source and detector on opposite sides of vertical crack and illustrating the resulting very weak emission

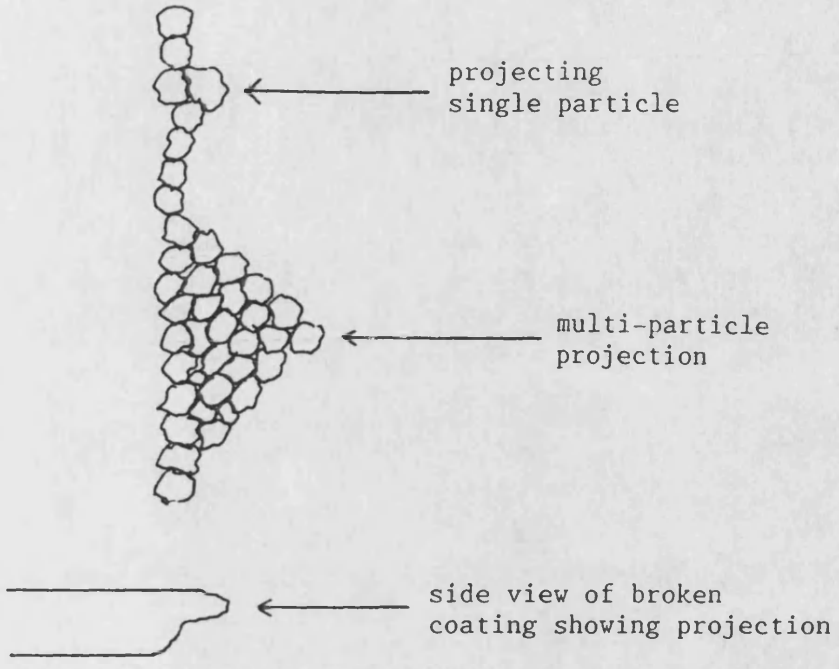

Figure 9.8: Schematic of projections formed by broken particulate coatings
(eg plasma sprayed YSZ)

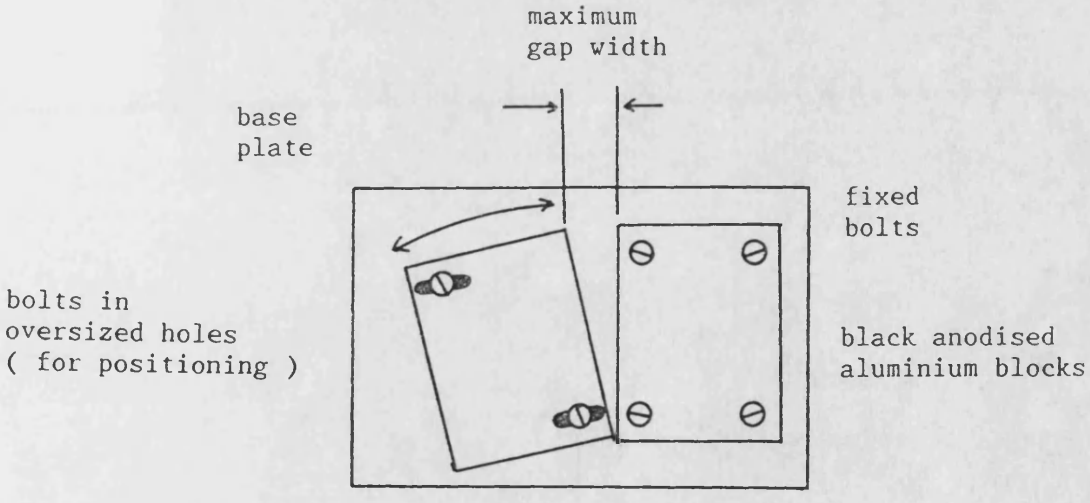

Figure 9.9: Schematic of aluminium test block mounting used to give variable gap width

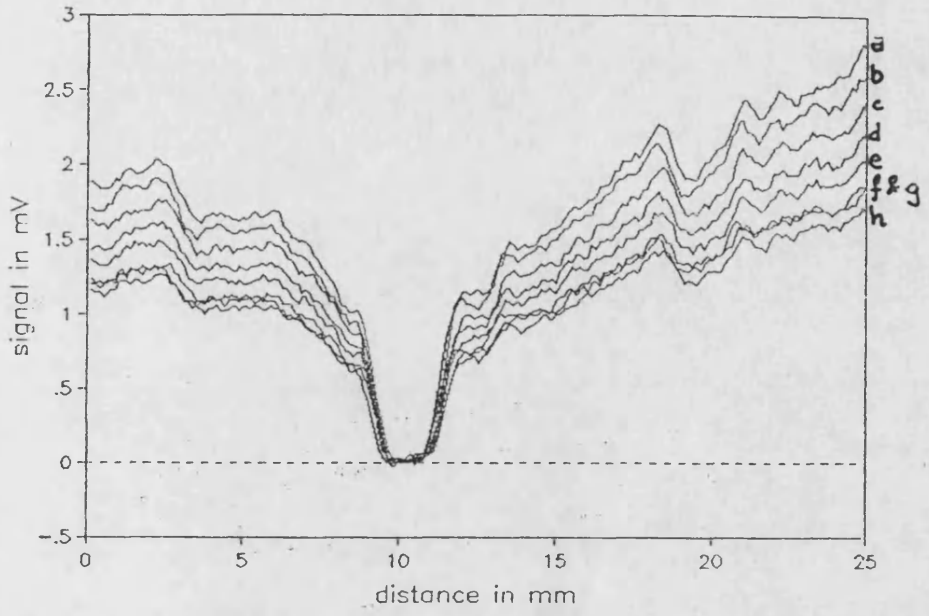

Figure 9.10 : Variation of amplitude with position on black painted aluminium at 10Hz modulation frequency and 8 steps/mm
Detector displacement: a) 0mm b) 0.5mm c) 1mm d) 1.5mm
e) 2mm f) 3mm g) 4mm h) 5mm

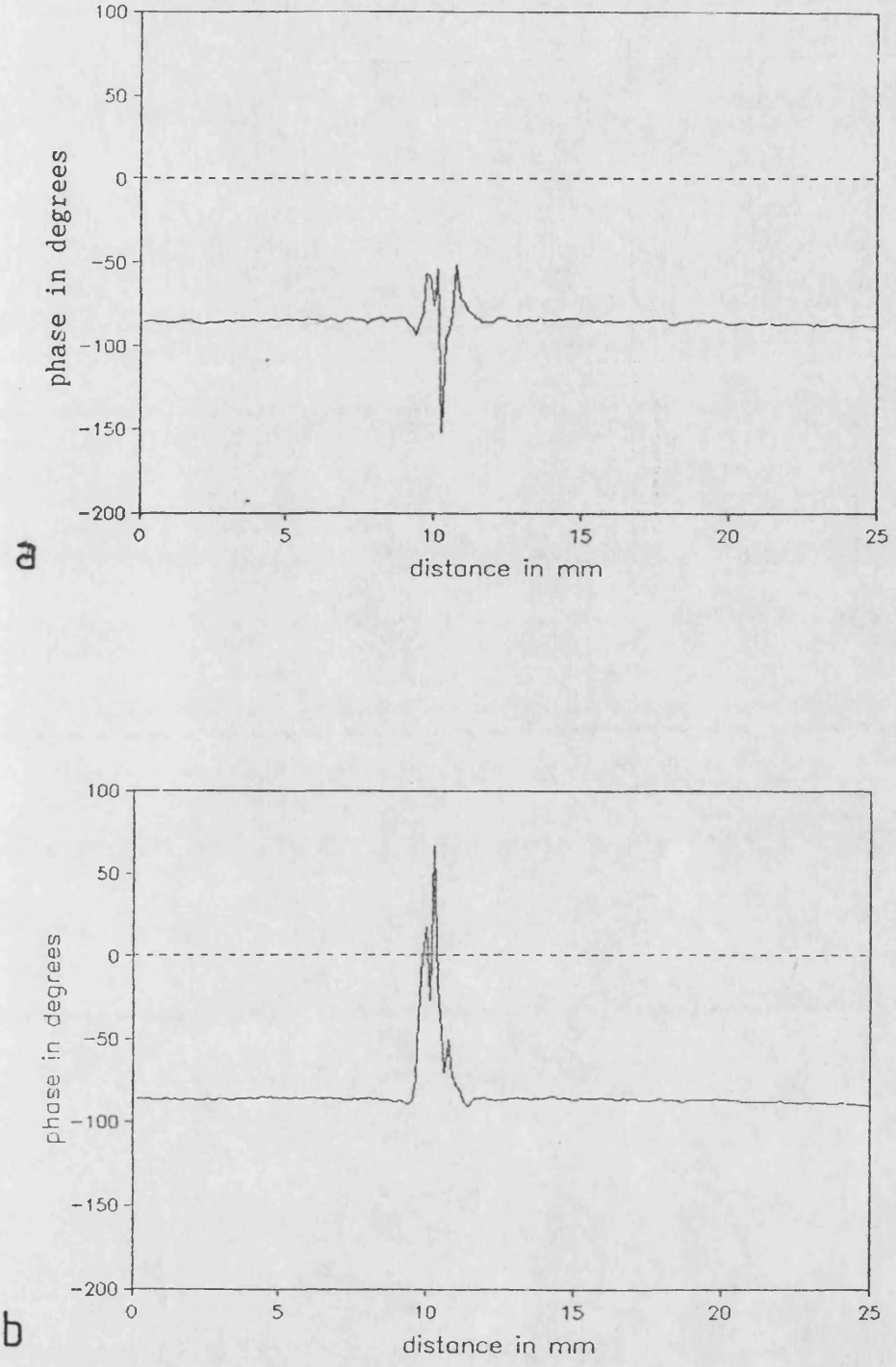

Figure 9.11 : Variation of phase with position on black-painted aluminium at 10Hz modulation frequency and 8 steps/mm
Detector displacement: a) 0mm b) 0.5mm c) 1mm d) 1.5mm
e) 2mm f) 3mm g) 4mm h) 5mm

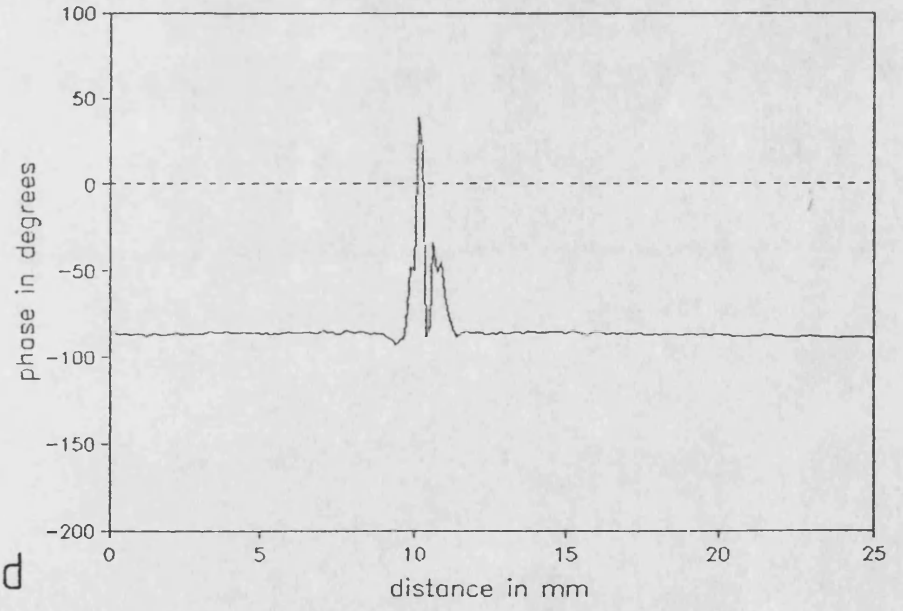

Figure 9.11[A]: Variation of phase with position on black-painted aluminium at 10Hz modulation frequency and 8 steps/mm
Detector displacement: a) 0mm b) 0.5mm c) 1mm d) 1.5mm
e) 2mm f) 3mm g) 4mm h) 5mm

e

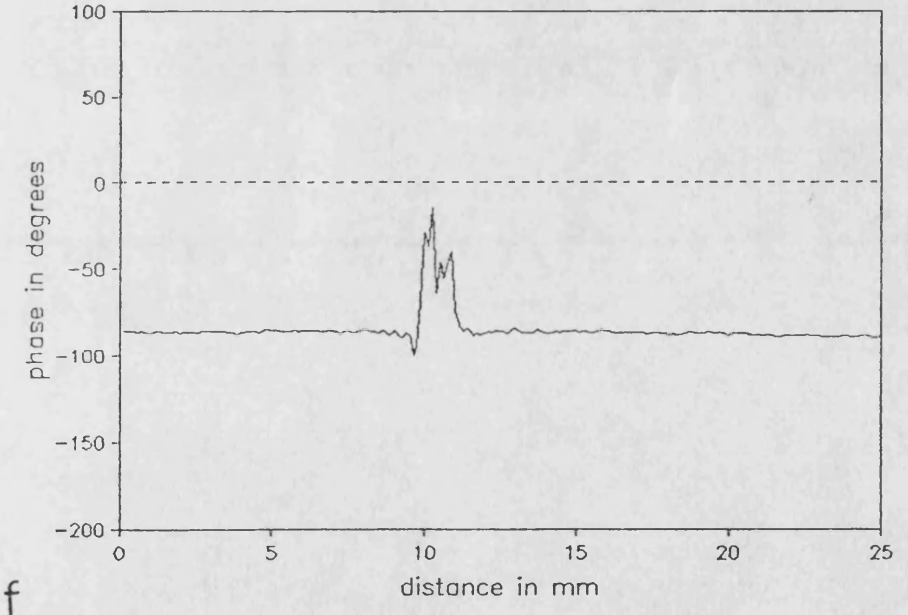

f

Figure 9.11 : Variation of phase with position on black-painted aluminium at 10Hz modulation frequency and 8 steps/mm
Detector displacement: a) 0mm b) 0.5mm c) 1mm d) 1.5mm
e) 2mm f) 3mm g) 4mm h) 5mm

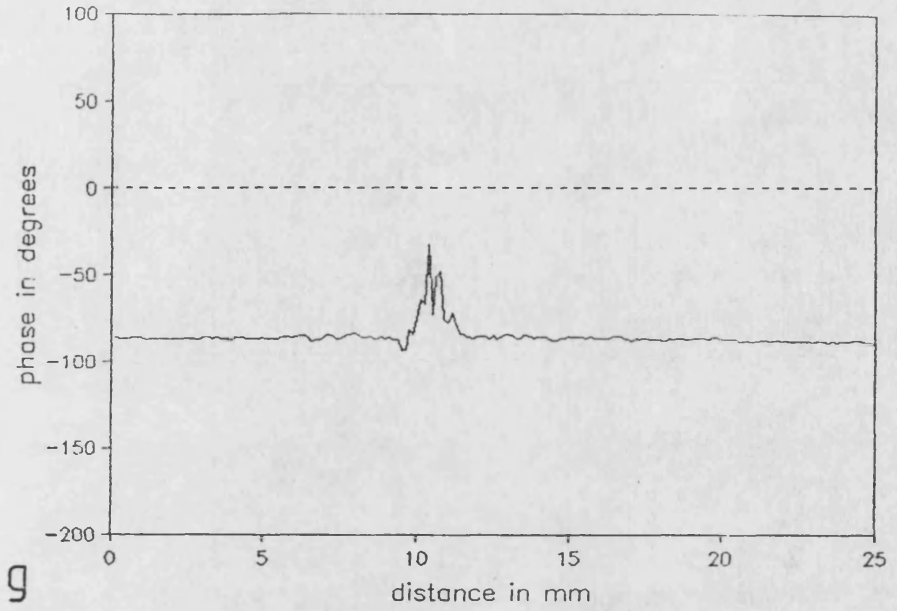

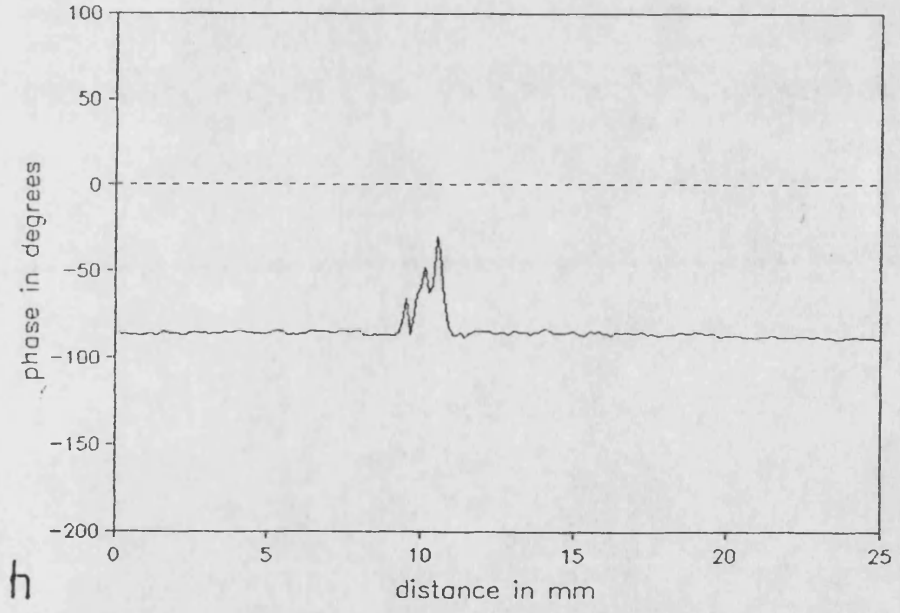

Figure 9.11[c] : Variation of phase with position on black-painted aluminium at 10Hz modulation frequency and 8 steps/mm
Detector displacement: a) 0mm b) 0.5mm c) 1mm d) 1.5mm
e) 2mm f) 3mm g) 4mm h) 5mm

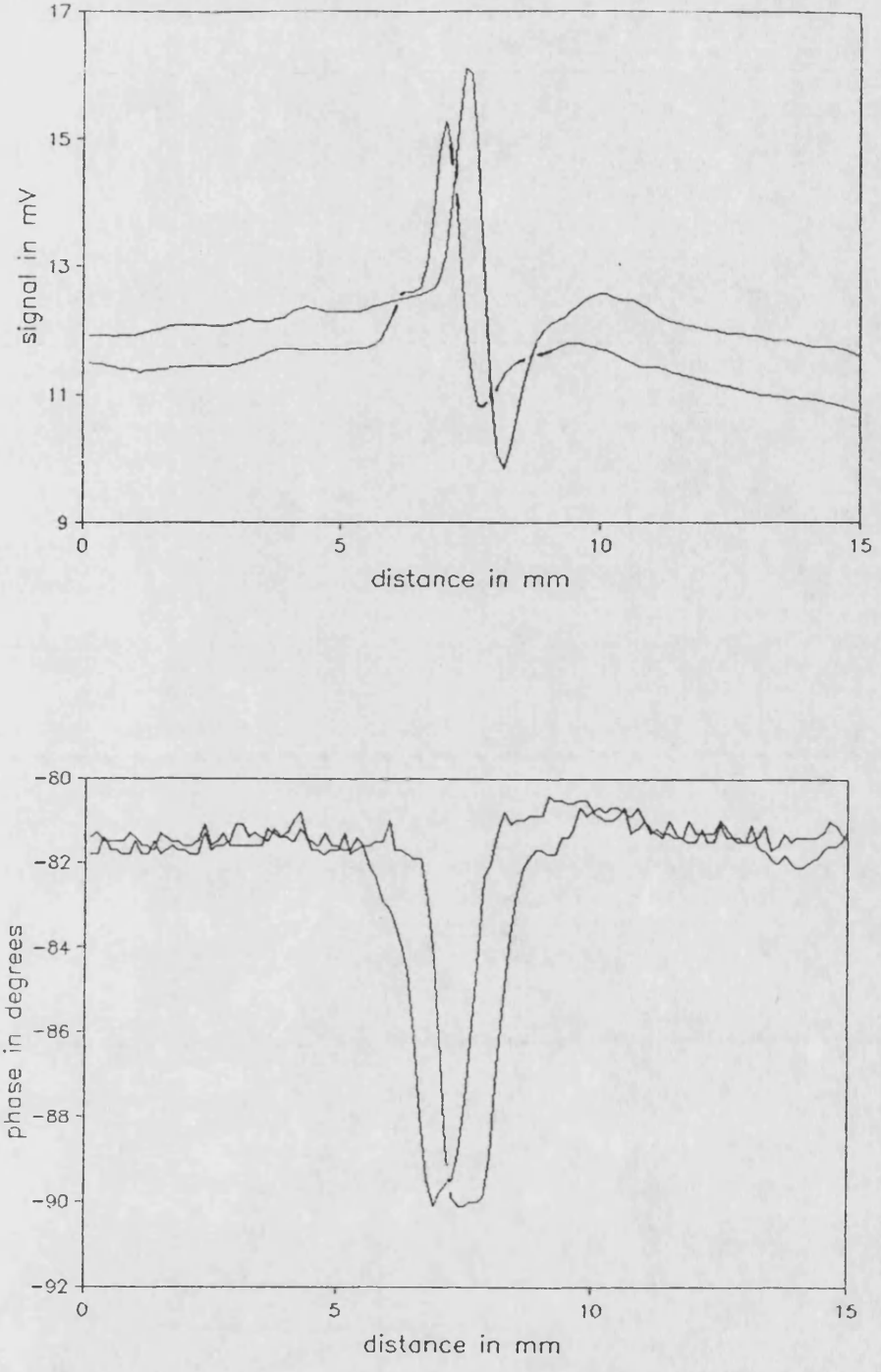

Figure 9.12 : Two plots of phase and amplitude variation with position on vitreous carbon at 20Hz modulation frequency. Laser spot unfocussed (1.2mm); 8 steps/mm

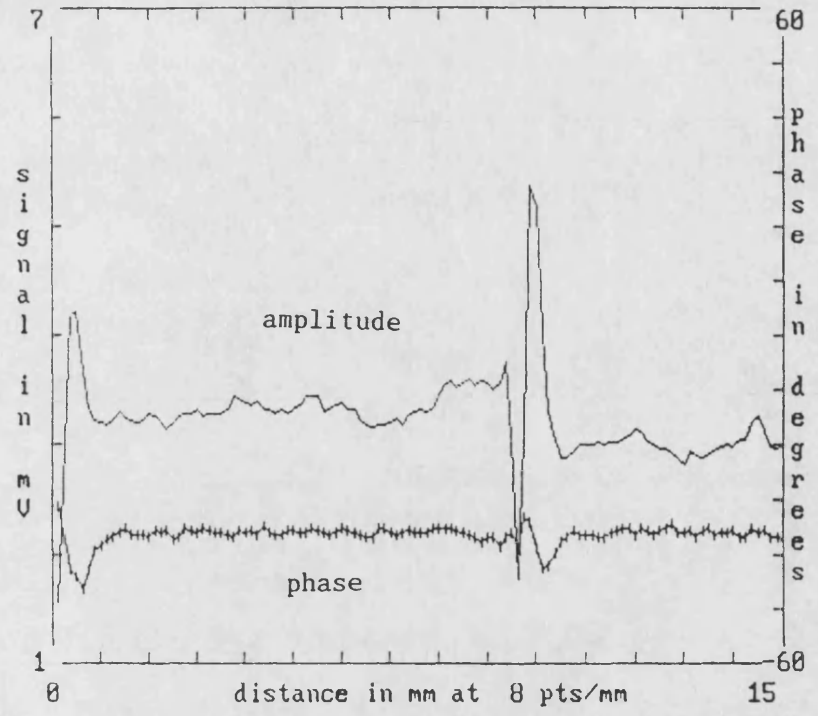

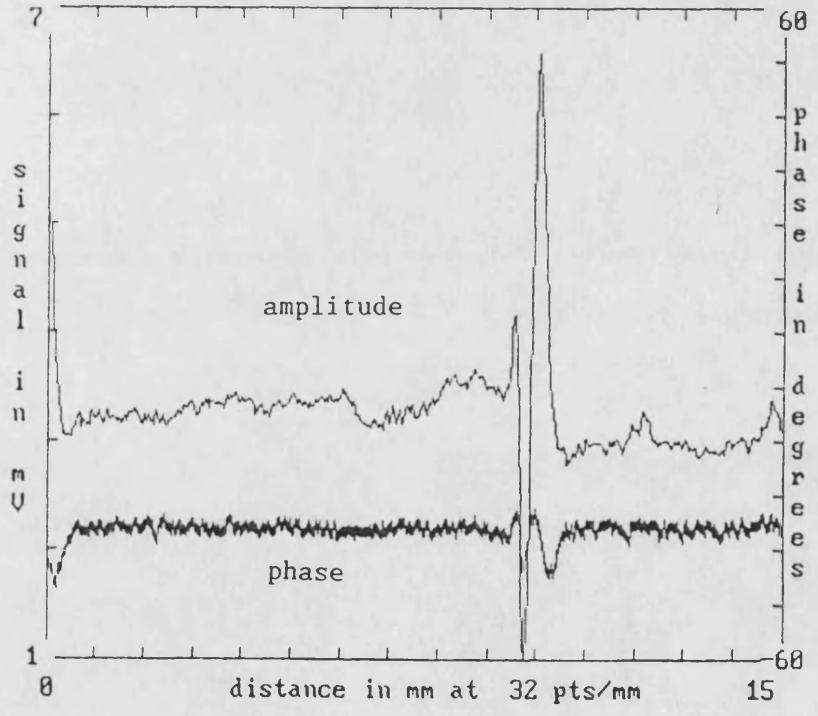

Figure 9.13 : Effect of scanning step size on phase and amplitude variation with position on vitreous carbon with 53 micron simulated crack.
Laser spot 250 microns; modulation frequency 20Hz

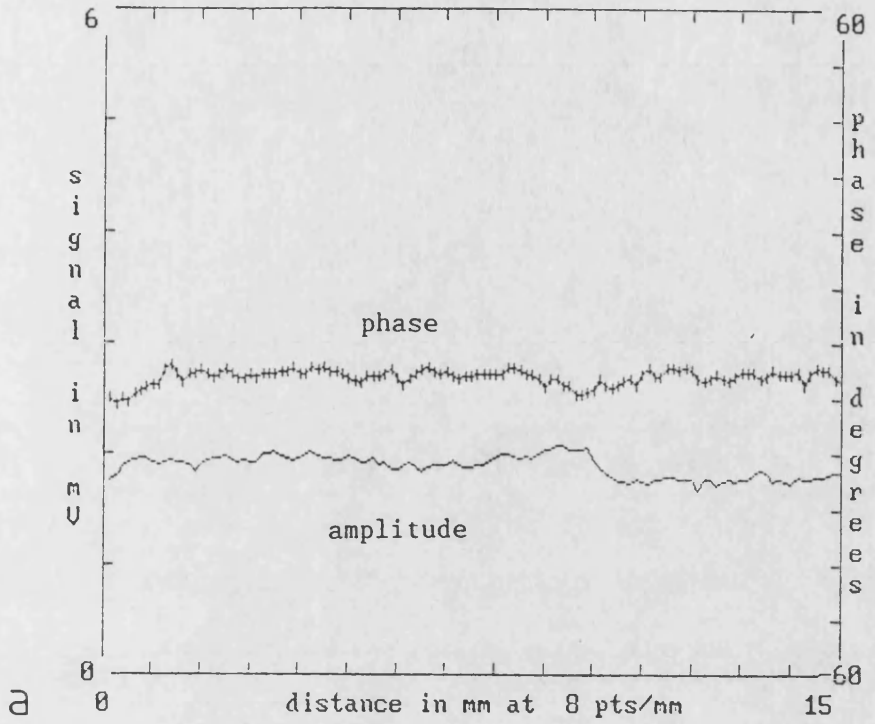

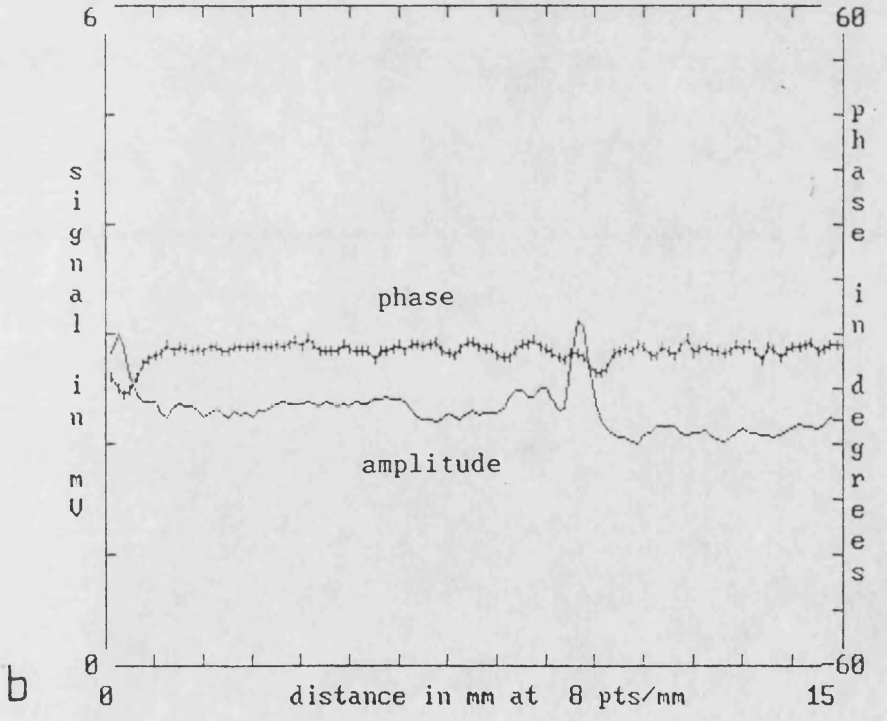

Figure 9.14 : Effect of laser spot focussing on phase and amplitude variation with position on vitreous carbon with a 30 micron simulated crack. Modulation frequency 30Hz
a) laser spot unfocussed (1.2mm diameter)
b) laser spot focussed to 500 microns

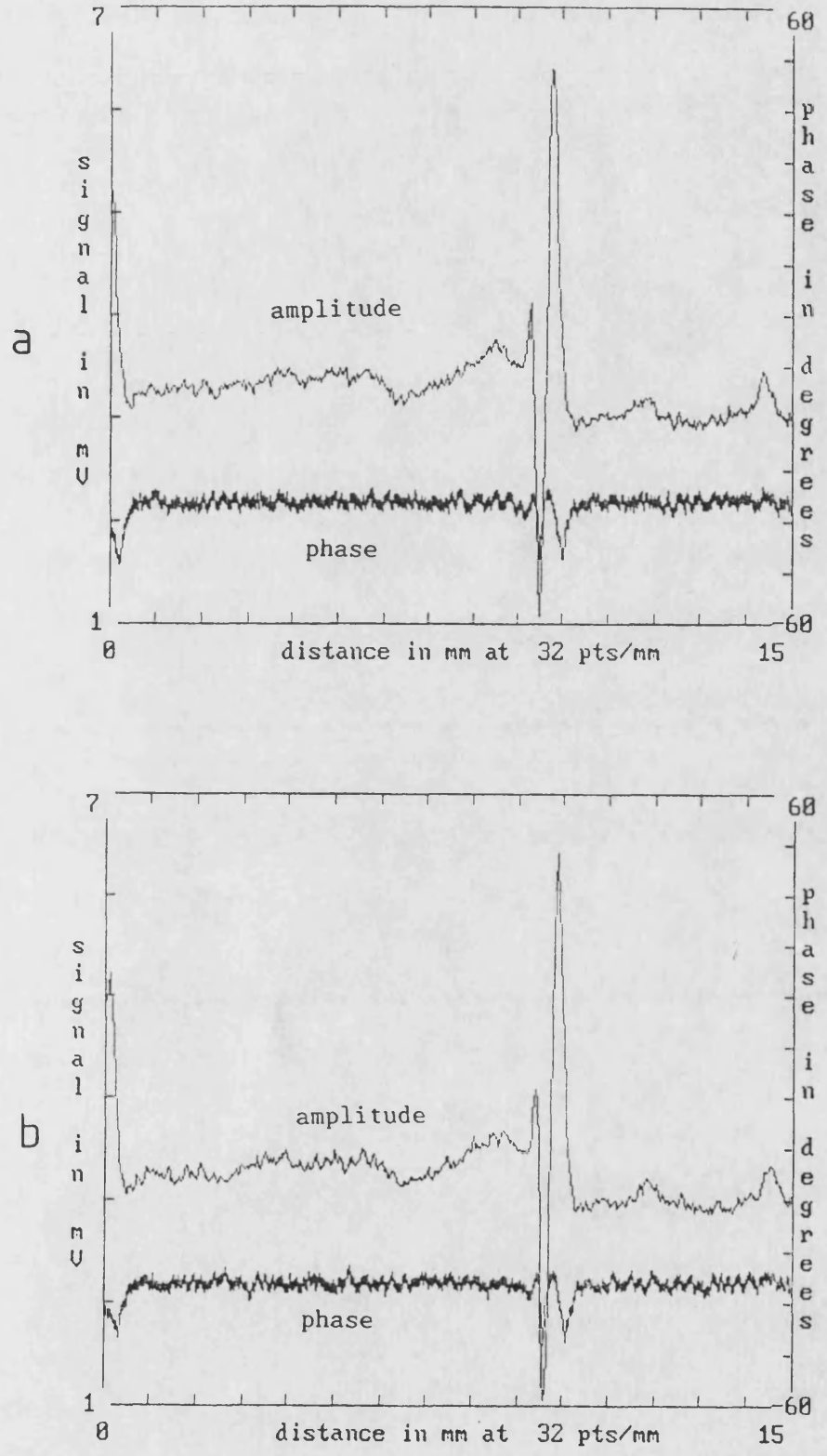

Figure 9.15 : Effect of detector displacement on the variation of phase and amplitude with position on vitreous carbon with a 53 micron simulated crack.
Laser spot 250 microns; modulation frequency 20Hz
a) detector displaced 0.6mm right
b) detector displaced 0.6mm left

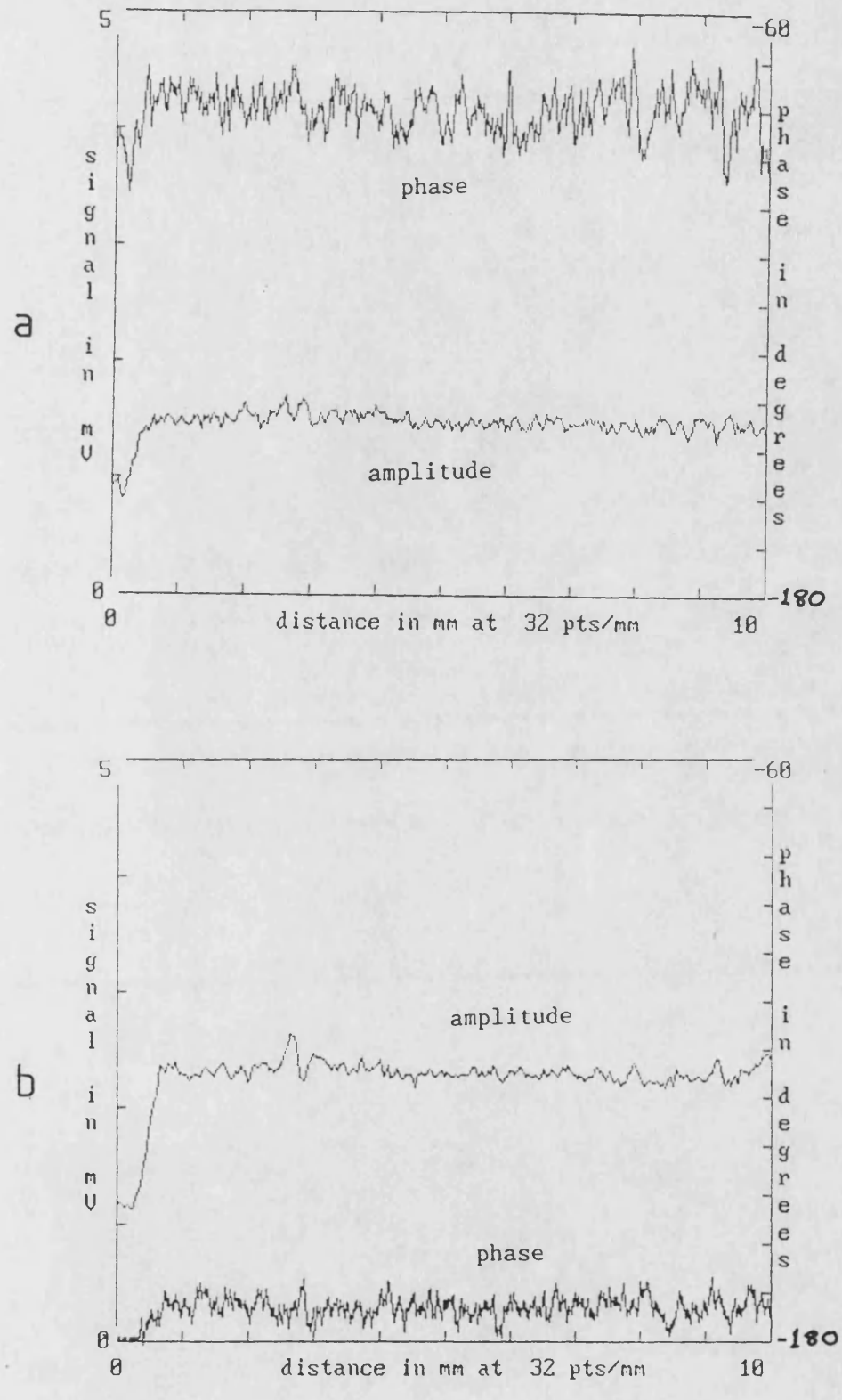

Figure 9.16 : Effect of modulation frequency on phase and amplitude variation with position on vitreous carbon with <2 micron natural crack. Laser spot 250 microns
a) modulation frequency 20Hz
b) modulation frequency 40Hz

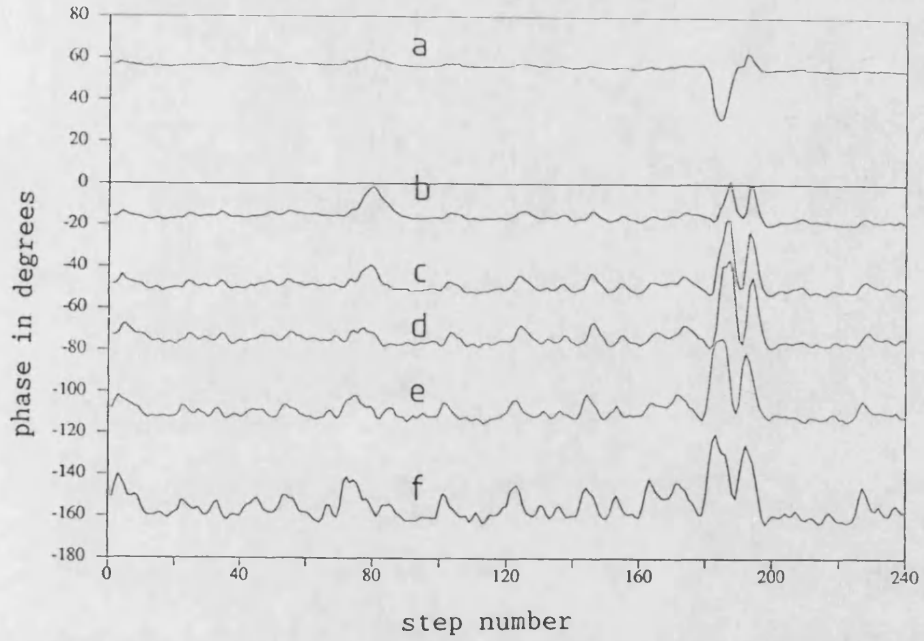

Figure 9.17a: Variation of phase with position for as-received saw-cut sample of YSZ on aluminium at different modulation frequencies, f. 4 readings/mm
a) f = 0.5 Hz b) f = 2.0 Hz c) f = 4.0 Hz
d) f = 10.0 Hz e) f = 20.0 Hz f) f = 40.0 Hz

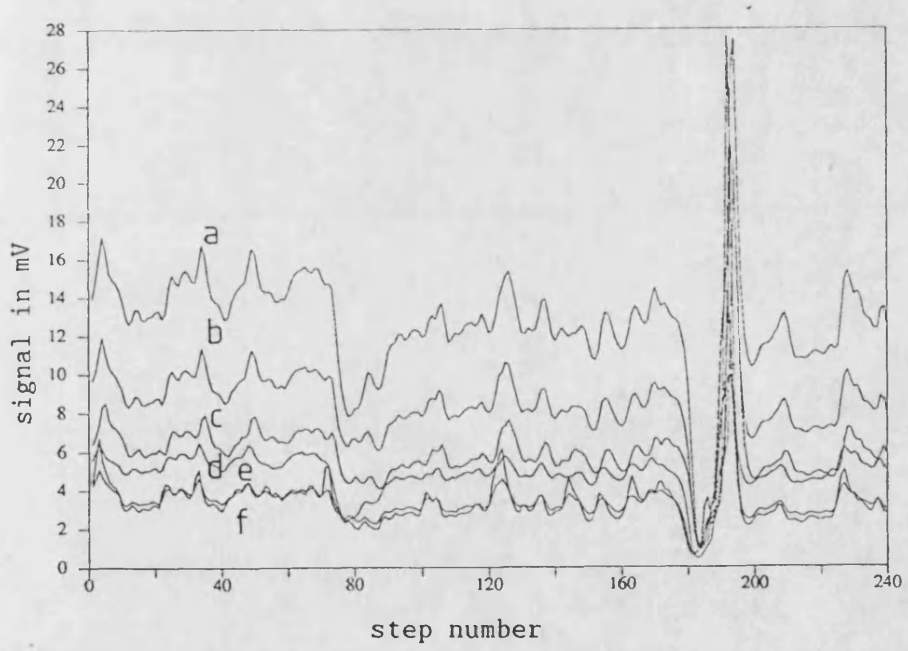

Figure 9.17b: Variation of amplitude with position for as-received saw-cut sample of YSZ on aluminium at different modulation frequencies, f. 4 readings/mm
a) f = 0.5 Hz b) f = 2.0 Hz c) f = 4.0 Hz
d) f = 10.0 Hz e) f = 20.0 Hz f) f = 40.0 Hz

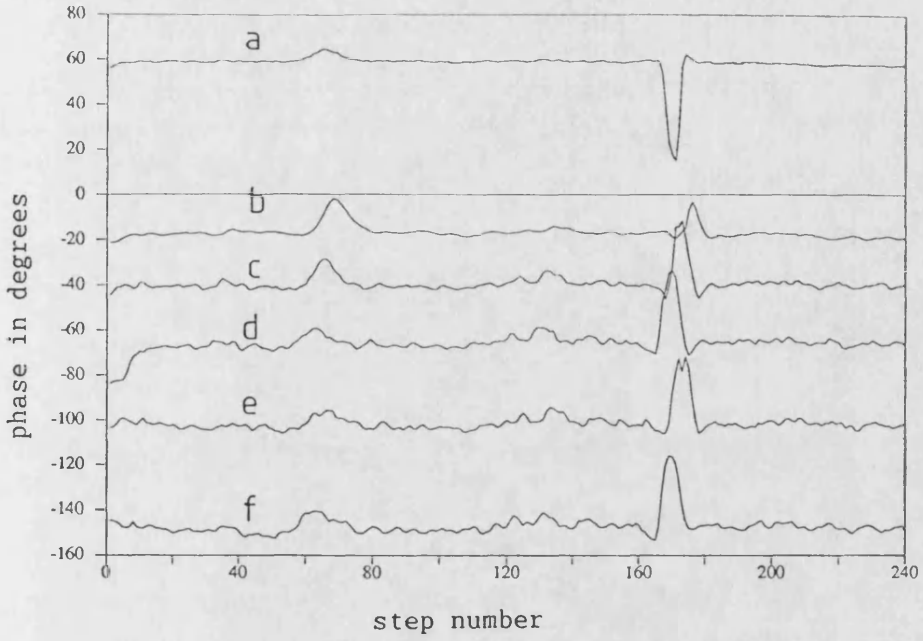

Figure 9.18a: Variation of phase with position for ink-darkened saw-cut sample of YSZ on aluminium at different modulation frequencies, f. 4 readings/mm
a) f = 0.5 Hz b) f = 2.0 Hz c) f = 4.0 Hz
d) f = 10.0 Hz e) f = 20.0 Hz f) f = 40.0 Hz

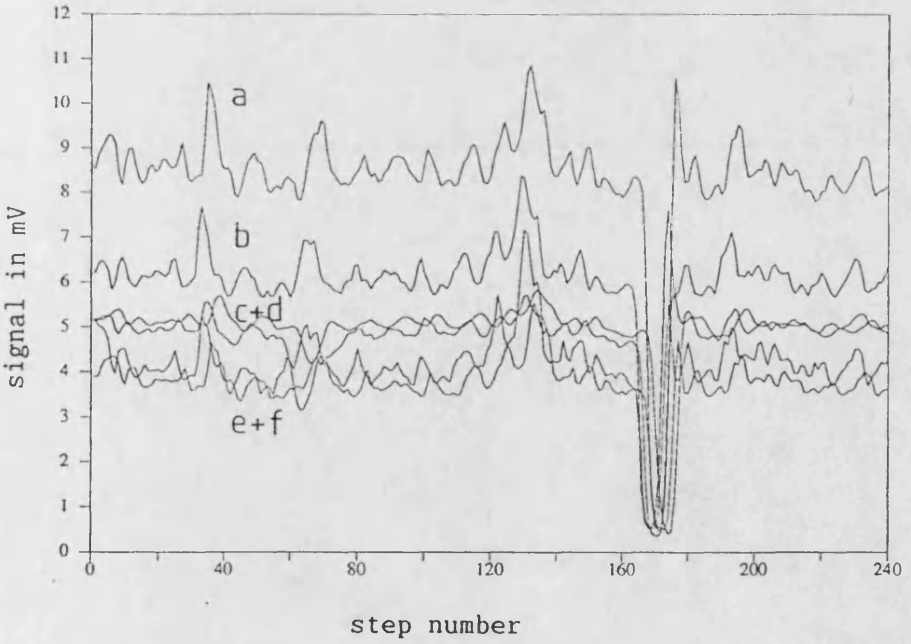

Figure 9.18b: Variation of amplitude with position for ink-darkened saw-cut sample of YSZ on aluminium at different modulation frequencies, f. 4 readings/mm
a) f = 0.5 Hz b) f = 2.0 Hz c) f = 4.0 Hz
d) f = 10.0 Hz e) f = 20.0 Hz f) f = 40.0 Hz

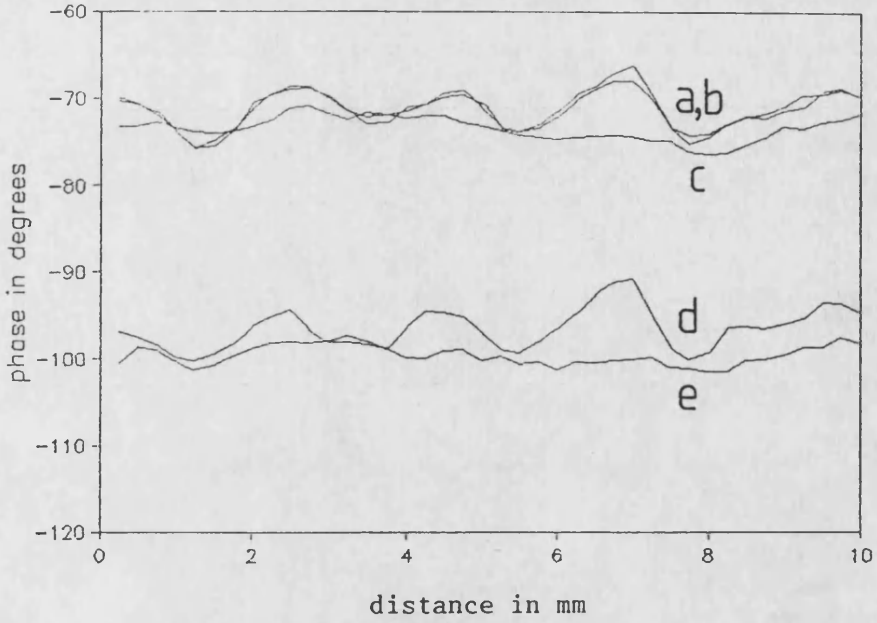

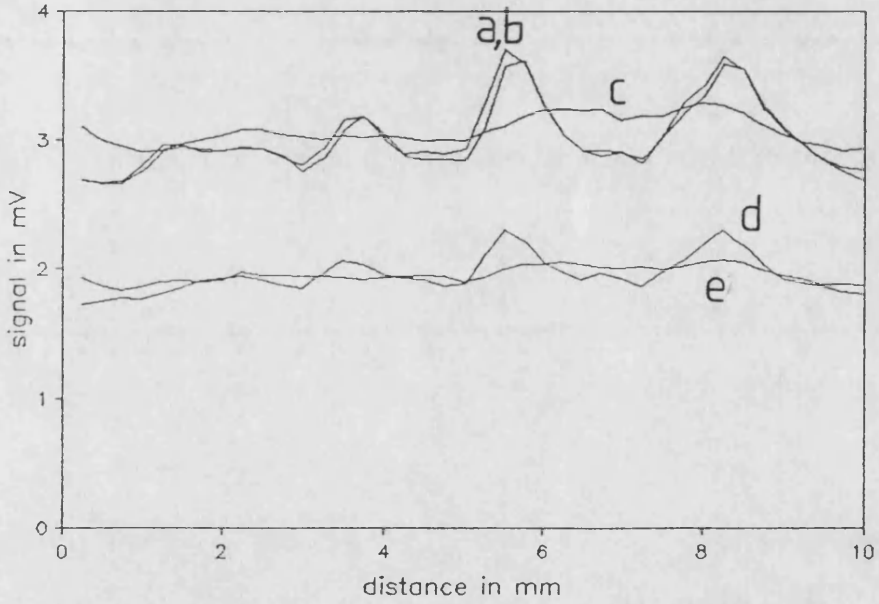

Figure 9.19: Effect of laser spot size on phase and amplitude variation with position on YSZ at different modulation frequencies
a) & b) f = 5Hz; laser spot 250 microns
c) f = 5Hz; laser spot unfocussed (1.2mm)
d) f = 8Hz; laser spot 250 microns
e) f = 8Hz; laser spot unfocussed (1.2mm)

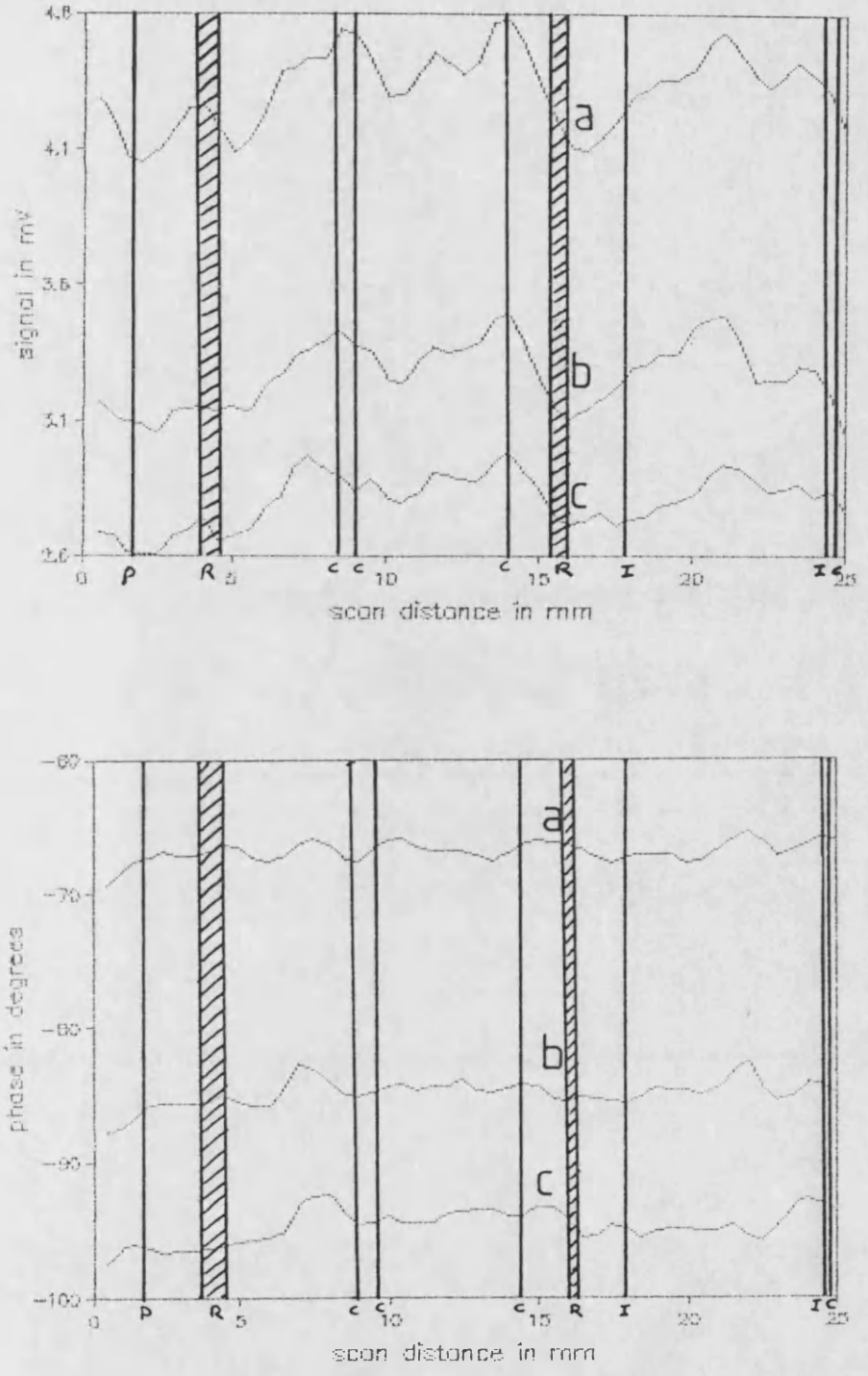

Figure 9.20: Variation of phase and amplitude with position on YSZ at different frequencies.
a) f = 5Hz b) f = 8Hz c) f = 10Hz
Overlay shows position of features noted by optical microscopy
C = crack R = ridge P = pit I = inclusion

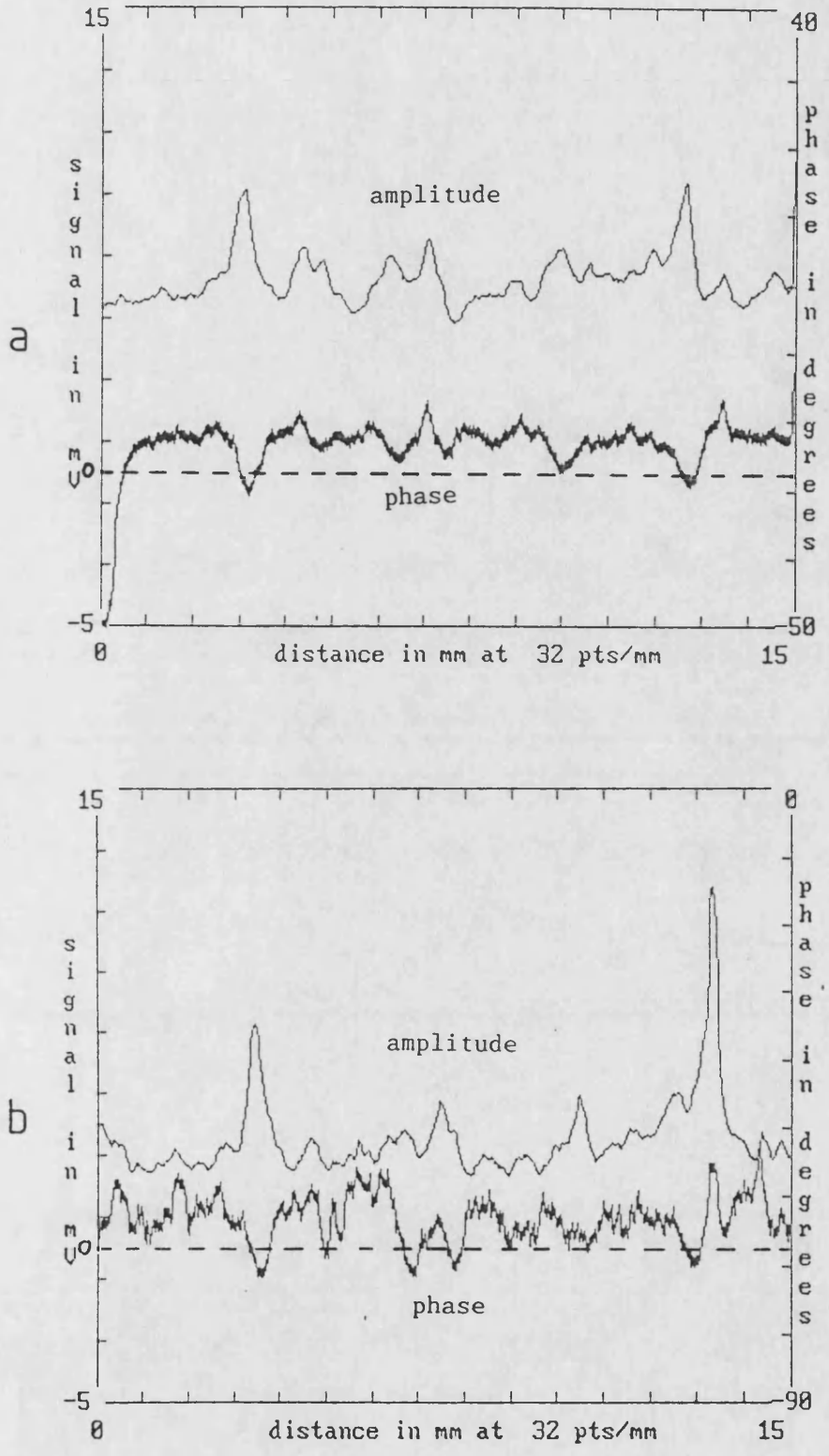

Figure 9.21 : Effect of modulation frequency on phase and amplitude variation on YSZ with <5 micron natural crack.
Laser spot focussed to 250 microns
a) modulation frequency 10Hz; laser power 2.5W
b) modulation frequency 20Hz; laser power 2.5W
c) modulation frequency 80Hz; laser power 4.0W

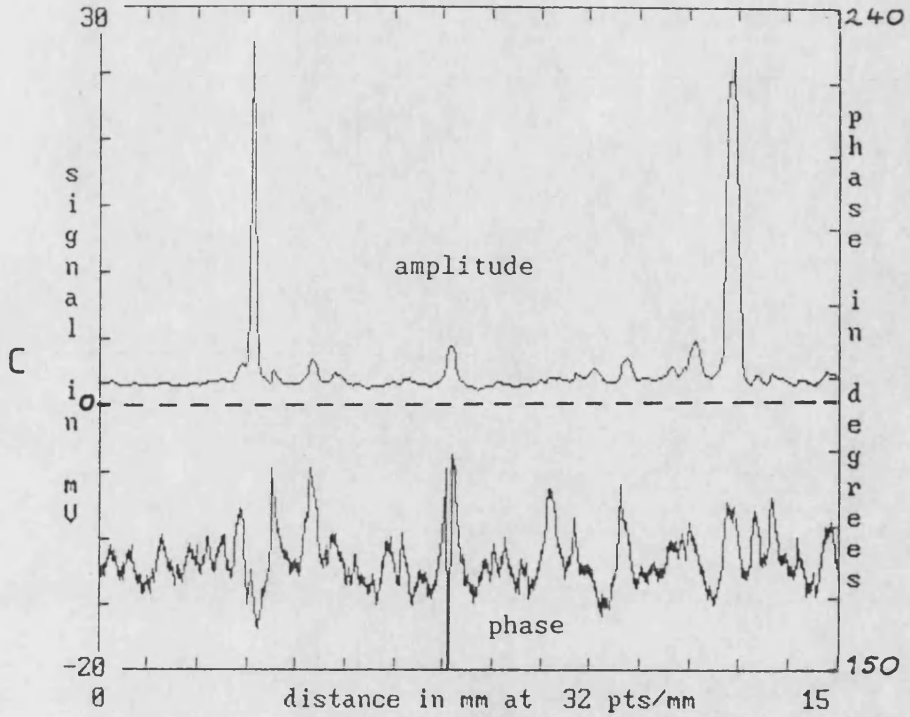

Figure 9.21: Effect of modulation frequency on phase and amplitude variation on YSZ with <5 micron natural crack.
Laser spot focussed to 250 microns
a) modulation frequency 10Hz; laser power 2.5W
b) modulation frequency 20Hz; laser power 2.5W
c) modulation frequency 80Hz; laser power 4.0W

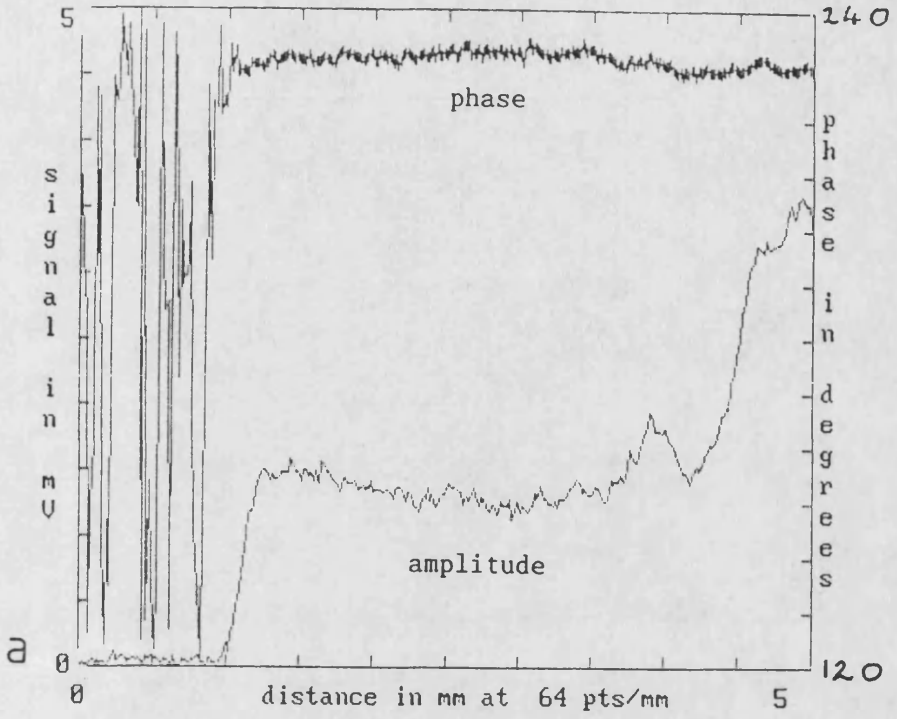

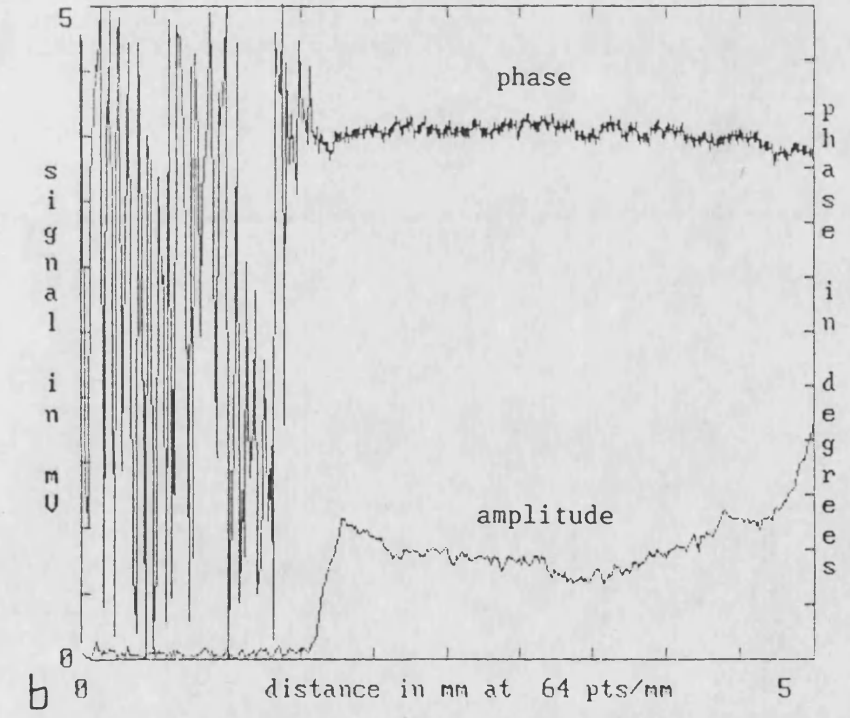

Figure 9.22 : Effect of frequency on variation of phase and amplitude with position for unidentified carbonaceous pipe deposit. laser focussed to 250 microns.

Sample edge is 1.5mm into the plot

a) modulation frequency 20Hz

b) modulation frequency 40Hz

	vitreous carbon	YSZ
increase in temperature due to simple crack	2	2
emissivity of crack > medium	1.18	3.6(*)
increase in effective β due to optical reflection at interface(**)	--	1.07
Reduction due to partial contact	1	0.9
Total Enhancement	2.36	7.2 (***)

Table 9.1 : Amplitude enhancement due to crack in YSZ and vitreous carbon
(*) = mean
(**) = assumes $\beta_{scattering} = \beta_{absorption}$, and n(YSZ) = 2.2
(***) = mean

As received (translucent)

f	background	peak	peak:background
0.5Hz	11mV	20mV	1.8:1
2.0Hz	13mV	27mV	2.1:1
4.0Hz	8mV	22mV	2.8:1
10.0Hz	6mV	20mV	3.3:1
20.0Hz	4mV	14mV	3.5:1
40.0Hz	4mV	28mV	7.0:1

Ink-darkened (opaque)

f	background	peak	peak:background
0.5Hz	5mV	5.5mV	1.1:1
2.0Hz	5mV	5.0mV	1.0:1
4.0Hz	9mV	11.0mV	1.2:1
10.0Hz	6mV	8.0mV	1.3:1
20.0Hz	4mV	5.0mV	1.3:1
40.0Hz	4mV	5.5mV	1.4:1

Table 9.2: Variation of amplitude peak:background ratio with modulation frequency on opaque and translucent saw-cut plasma sprayed YSZ coating on aluminium.

10 CONCLUSIONS

10 CONCLUSIONS

Conclusions have been presented in three groups, corresponding to the work discussed in chapters 7, 8 and 9.

10.1 YSZ Coatings

10.1.1 Thermal wave interferometry has been shown suitable for thickness determination, and physical property determination on plasma sprayed ceramic coatings, as it is on metallic plasma-sprayed coatings

10.1.2 Lower modulation frequencies are needed to test ceramics, which limits the maximum practical thickness that can be tested

10.1.3 Thermal wave interferometry has been shown to be suitable for thickness and property determination of translucent as well as opaque media

10.1.4 Thermal wave phase changes due to optical effects are of similar order of magnitude to those arising from geometrical and thermal changes

10.1.5 Accurate characterisation of translucent media requires that the optical contribution be known

10.1.6 Thermal wave interferometry can be used to detect the presence of both high- and low- thermal conductivity sub-surface defects in ceramic coatings

10.1.7 Detection of surface breaking cracks by thermal wave interferometry can be enhanced in translucent media with respect to otherwise identical opaque media

10.1.8 Many typical in-service defects can be detected by thermal wave interferometry

10.1.9 Typical in-service defects cannot generally be fully characterised by thermal wave interferometry

10.2 Optical and Infrared Optical Fibres

10.2.1 Commercially available optically transmitting silica fibre bundles can be used to deliver light from the laser to the sample with acceptable losses

10.2.2 The above fibres can be readily incorporated into conventional thermal wave test systems

10.2.3 Speciality chalcogenide glass fibres cannot, currently, be succesfully used to transmit emitted infrared radiation from the sample to the detector

10.2.4 Commercially available fluoride glass fibres offer an improved performance over the chalcogenide fibres, provided that sample temperatures can be increased sufficiently

10.2.5 Commercially unavailable silver halide crystalline fibres offer the possibility of succesful radiation transmission between the sample and the detector

10.3 Crack Detection

10.3.1 Thermal wave interferometry can be used to detect vertical surface breaking cracks in a variaty of materials:- bulk metals; bulk ceramics; plasmasprayed ceramics; loosely bound carbonaceous materials

10.3.2 Thermal wave interferometry can be used to detect vertical surface breaking cracks in both translucent and opaque media

10.3.3 There can be an enhanced sensitivity of thermal wave interferometry to surface breaking cracks in optically translucent media with respect to otherwise identical opaque media

10.3.4 Natural cracks as small as 2 microns can be detected in vitreous carbon

10.3.5 Natural cracks as small as 50 microns can be readily detected in plasma sprayed translucent YSZ

10.3.6 Thermal wave response of cracks is influenced by too many variables to allow full characterisation by thermal wave interferometry alone

10.3.7 Sensitivity to cracks is highest under conditions of high energy density: - small thermal diffusion lengths and small spot sizes

11 RECOMMENDATIONS

11 RECOMMENDATIONS

11.1 Portable thermal wave interferometry can, and should, be developed and built using currently available technology at reasonable cost (appendix C).

11.2 Alternative infrared transmitting fibres should be examined. In particular, efforts should be made to obtain commercially unavailable silver halide fibres for research purposes. In addition to this, high sample temperature testing should be done to evaluate the potential of fluoride glass fibres.

11.3 Optical fibre bundles should be obtained in assorted configurations such as with a linear output from a standard round input end, with a view to using a linear light source to speed up testing, by needing only one-dimensional scanning.

11.4 Linear and area arrays of solid state infrared detectors should be obtained and used in conjunction with the above to improve scanning rates.

11.5 Extensive testing on practical components should be done, with particular regard to whether the practically achievable performance will be useful in engineering practice.

11.6 The effect of optical properties could be more thoroughly explored by incorporating different concentrations of absorbing ions into coating materials.

APPENDIX A

DERIVATION OF EQUATIONS

APPENDIX A: DERIVATION OF EQUATIONS

The response of a body to periodic heating, such as by a modulated light source, can be predicted with equations derived from the heat diffusion equation. In-depth studies of these matters can be found in references 46,57,65 and 83. One dimensional heating and heat flow is considered throughout for clarity, but the general principles apply equally to 2- or 3- dimensional cases.

A.1 The Heat Diffusion Equation

Consider a block of unit area and thickness δx, subject to a thermal gradient. At equilibrium, the rate of energy input will equal the sum of the energy output plus the energy used to heat the body, figure A.1.

Heat flow into an element of thickness δx:

$$Q_1 = - k \left.\frac{\partial T}{\partial x}\right|_x \qquad \text{equation A.1a}$$

Heat flow out of an element of thickness δx:

$$Q_2 = - k \left.\frac{\partial T}{\partial x}\right|_{x+\delta x} \qquad \text{equation A.1b}$$

Heat dissipated in raising temperature of element:

$$Q_1 - Q_2 = \frac{\partial T}{\partial t} \delta x . C\varrho \qquad \text{equation A.2a}$$

where C is the specific heat of the medium, and ϱ is the density. A.2a is, then:

$$-k \left[\frac{\partial T}{\partial x} - \frac{\partial T}{\partial x} - \frac{\partial^2 T}{\partial x^2} \delta x \right] = \frac{\partial T}{\partial t} \delta x C\varrho \qquad \text{equation A.2b}$$

Hence we arrive at:

$$\frac{\partial^2 T}{\partial x^2} = \frac{1}{\alpha}\frac{\partial T}{\partial t}$$ equation A.3

where $\alpha = k/(\rho * C)$.

Equation A.3 is known as the Fourier equation.

A.2 Thermal Waves

A thermal wave is a periodic temperature fluctuation within a body with wavelike character that is a solution to the diffusion equation rather than the wave equation. As it propagates, it heats the medium it travels through, and thus decays in amplitude exponentially. The decay length of thermal wave is known as the thermal diffusion length, denoted μ or μ_{th}.

If an element such as that described in A.1 above is subjected to heating by a periodic source $H = H_0 \exp i(wt)$, where H_0 is the initial (maximum) value of H and $i=(-1)^{1/2}$, we seek a solution to the thermal wave equation of the form:

$T = T_0 \exp i(cx - wt)$ equation A.4

By differentiating with respect to time and position, we find:

$$\frac{\partial T}{\partial t} = -i\omega T_0 \exp i(cx-\omega t) \quad \ldots -i\omega T$$ equation A.5a

$$\frac{\partial^2 T}{\partial x^2} = i^2 c^2 T_0 \exp i(cx-\omega t) \quad \ldots i^2 c^2 T$$ equation A.5b

and hence, $c^2 = iw/\alpha$ equation A.6a

from which is obtained the value of c:

$$c = \sqrt{-i}\ \sqrt{\omega/\alpha}$$ equation A.6b

$$c = (1-i)\sqrt{\frac{\omega}{2\alpha}}$$ equation A.6c

The constant c is generally referred to as the complex thermal wavenumber, denoted σ, where $\sigma = (1 + i)*[w/2\alpha]^{1/2}$. The expression for a thermal wave is thus given by:

$$T = T_0 \exp\left(-\sqrt{\frac{\omega}{2\alpha}} \cdot x\right) \exp i\left(\sqrt{\frac{\omega}{2\alpha}} \cdot x - \omega t\right) \qquad \text{equation A.7a}$$

and by setting $\mu = (2\alpha/w)^{1/2}$, we obtain the more concise form:

$$T = T_0 \exp\left(-\frac{x}{\mu}\right) \exp i\left(\frac{x}{\mu} - \omega t\right) \qquad \text{equation A.7b}$$

There are several features of note in this expression. The thermal wave is heavily damped, decaying by one exponential constant for each thermal diffusion length travelled. Thermal waves are thus only short range phenomena. The complex part denotes the phase of the wave, and shows that this is dependent on both the time and on the thermal distance. The thermal distance is the physical distance, x, normalised with respect to the thermal diffusion length μ.

A.3: The Wave Equation

The general one dimensional wave equation may be expressed:

$$\frac{\partial^2 P}{\partial x^2} = c \frac{\partial^2 P}{\partial t^2} \qquad \text{equation A.8}$$

where P is the property that varies in time and space, x and t are coordinates of space and time respectively, and c is a constant. It can readily be seen that the equation is similar to that for heat diffusion, and indeed, for diffusion generally, apart from the first order time differential in the diffusion equation.

A general solution to A. is:

$$P = P_0 \cos(kx - wt) \qquad \text{equation A.9a}$$

or $$P = P_0 \exp i(kx - wt) \qquad \text{equation A.9b}$$

where P_0 is the initial value of the property, w is the angular frequency, $2\pi f$, and k is the wavenumber of the wave.

A.4 Damped Waves

If the wave is damped, ie energy is dissipated as the wave propagates, such as by thermal energy heating up the medium as a temperature wave propagates, then the decay term exp(-ax) must be incorporated to give:

$$P = P_0 \exp i(kx - \omega t) \exp(-ax) \qquad \text{equation A.10}$$

where a is the decay length of the wave, in which the amplitude falls by one exponential constant, e. Within the wave length, the amplitude will fall by $\exp(-2\pi)$ and the amplitude will be negligible. Such waves therefore only interact over short distances.

The above shows the wavelike nature of some solutions to the diffusion equation, and hence justifies the use of the term 'thermal waves' to describe what are, strictly, diffusional phenomena.

A classic example of a damped wave is an electromagnetic wave in a conducting metallic solid, which propagates as:

$$A = A_0 \exp i(x/s - wt) \exp(-x/s) \qquad \text{equation A.10a}$$

where s is the skin depth as defined on page 45, and A is the amplitude of the wave.

A.5 Optical Generation of Thermal Waves

Thermal Waves can be conveniently generated by optical irradiation, such as modulated laser illumination. Absorbed optical energy is converted to heat near instantaneously by non-radiative de-excitation processes. Lasers are often used as optical sources because they allow convenient spatial and temporal control of sample illumination. While square wave modulation is often used (eg mechanical chopping), a sinusoidal waveform is often assumed for mathematical convenience when modelling thermal waves. The errors introduced by this are generally not significant.

A sinusoidally modulated light source may be modelled by:

$$I = I_0 \, 1/2 \, [1 + \cos(wt)] \qquad \text{equation A.11}$$

where I_0 is the peak optical intensity.

Such a light source gives rise to a periodic temperature which has the form:

$$T = I_0 \, (1-R) n\beta \exp(-\beta x) \, [1 + \cos(wt)] \, 1/2k \qquad \text{equation A.12}$$

where R is the surface optical reflection, n is the optical-thermal conversion efficiency, usually taken to be 1 and hence omitted hereafter, β is the optical absorption coefficient, where $1/\beta$ or μ_o is the optical penetration depth, analogous to the thermal diffusion length μ, k is the thermal conductivity and x is the position within the coating.

A.6 Interaction of Thermal Waves With Interfaces

If two thermally distinct media denoted 1 & 2 are separated by a boundary with perfect thermal contact at position x=0, and incident, reflected and transmitted plane thermal waves make angles of α_i, α_r, and α_t respectively with the interface (figure A.2), then the incident, reflected and transmitted thermal waves may be expressed:

$T_i = A \exp(-\sigma_1 x \cos\alpha_i - \sigma_1 y \sin\alpha_i + iwt)$ equation A.13a

$T_r = AR \exp(\sigma_1 x \cos\alpha_r - \sigma_1 y \sin\alpha_r + iwt)$ equation A.13b

$T_i = AT \exp(-\sigma_2 x \cos\alpha_t - \sigma_2 y \sin\alpha_t + iwt)$ equation A.13c

where A is the amplitude of the incident thermal wave and R and T are the reflection coefficients.

For continuity of temperature across the interface,

$A \exp(-\sigma_1 y \sin\alpha_i) = AR \exp(-\sigma_1 y \sin\alpha_r) + AT \exp(-\sigma_2 y \sin\alpha_t)$ equation A.14

Since this must be true for all y positions, the exponents in A.14 must all be equal. Hence:

$-\sigma_1 y \sin\alpha_i = \sigma_1 y \sin\alpha_r = \sigma_2 y \sin\alpha_t$ equation A.15

and we obtain:

$\alpha_i = \alpha_r$ - the Law of Reflection equation A.16a

and $\sigma_1 y \sin\alpha_i = \sigma_2 y \sin\alpha_t$ - Snell's Law equation A.16b

For continuity of heat flux at the interface, we obtain:

$k_1\sigma_1 \cos\alpha_i - R\, k_1\sigma_1 \cos\alpha_r = T\, k_2\sigma_2 \cos\alpha_t$ equation A.17

since $\alpha_i = \alpha_r$, and T = 1-R, R & T may be expressed:

$$R = \frac{k_1\sigma_1 \cos\alpha_i - k_2\sigma_2 \cos\alpha_t}{k_1\sigma_1 \cos\alpha_i + k_2\sigma_2 \cos\alpha_t}$$ equation A.18a

$$T = \frac{2\, k_2\sigma_2 \cos\alpha_t}{k_1\sigma_1 \cos\alpha_i + k_2\sigma_2 \cos\alpha_t}$$ equation A.18b

which may be more conveniently expressed:

$$R = \frac{\cos\alpha_i - b\cos\alpha_t}{\cos\alpha_i + b\cos\alpha_t} \qquad \text{equation A.19a}$$

$$T = \frac{2b\cos\alpha_t}{\cos\alpha_i - b\cos\alpha_t} \qquad \text{equation A.19b}$$

where $b = k_2\sigma_2/k_1\sigma_1$.

For normal incidence, $\alpha_i = 0$, and A.19 reduce to:

$$\Gamma = \frac{1 - b}{1 + b} \qquad \text{equation A.20a}$$

$$T = \frac{2b}{1 + b} \qquad \text{equation A.20b}$$

Γ is used hereafter for the reflection coefficient to avoid confusion with the surface optical reflection term R.

A.7 Coated Substrate (I)

There are many possible combinations of geometrical, thermal and optical properties that can significantly alter the thermal wave behaviour in a sample. The thermal wave equation for one particular case will be illustrated here.

Several simplifications are made. It is assumed that the thermal waves are one dimensional. This will be approximately true if the thermal waves originate from a region whose lateral dimensions are large relative to the thermal diffusion length at the modulation frequency used. This will be so if the incident light spot is large, or if the light is scattered primarily in the horizontal plane, so that the thermal energy is spread over a relatively large area. The light absorption is assumed to be exponential, as is the thermal dissipation. These two are implied by the assumption that the media are homogeneous and isotropic. Their boundaries are assumed to be smooth, planar and with perfect thermal contact. Light intensity is assumed to be sinusoidally varying. The coating layer is assumed to be optically thick and absorbing.

Figure A.3 shows, schematically, a thermally thin layer on a semi-infinite substrate, in which a thermal source is considered to be present at a depth x beneath the surface. The thermal reflection coefficient from the coating to the overlying layer is Γ_0, and that between the coating and the substrate is taken to be Γ_1. The coating thickness is l, complex thermal wave number is σ.

Two thermal wave components can be identified in the one dimensional case, one initially travelling downwards to the substrate, and the other travelling upwards to the surface.

The upward component undergoes attenuation and phase change when travelling, and reaches the surface with a temperature contribution dependent on $\exp(-\sigma x)$. It is then multiply reflected, first at the surface, then at the substrate, the surface and so on. The final contribution to the surface thermal wave will be the sum of all these reflected and direct components, as given by:

$$\exp(-\sigma x) + \exp(-\sigma x)*\Gamma_0\Gamma_1(\exp-2\sigma l) + \exp(-\sigma x)*\Gamma_0\Gamma_1(\exp-2\sigma l)$$
$$*\Gamma_0\Gamma_1(\exp-2\sigma l) + \ldots + \exp(-\sigma x)*(\Gamma_0\Gamma_1)^n*(\exp(-2n\sigma l)$$

This is a geometric series of initial term $\exp(-\sigma x)$, and common term $\Gamma_0\Gamma_1\exp(-2\sigma l)$. Its sum is given by:

$$\frac{\exp(-\sigma x)}{(1-\Gamma_0\Gamma_1\exp(-2\sigma l))}$$

Similarly, the downward term can be represented as a series, with an initial term $\exp(-\sigma(l-x))*\Gamma_1*\exp(-\sigma l)$ and a common term of $\Gamma_0\Gamma_1\exp(-2\sigma l)$. This series sums to:

$$\frac{\exp(\sigma x)\Gamma_1\exp(-2\sigma l)}{[1-\Gamma_0\Gamma_1\exp(-2\sigma l)]}$$

The total contribution is thus given by the sum of these :

$$\frac{[\exp(-\sigma x) + \exp(\sigma x)*\Gamma_1\exp(-2\sigma l)]}{[1-\Gamma_0\Gamma_1\exp(-2\sigma l)]}$$

If the sample is absorbing, the light intensity will determine the thermal energy available at a distance l below the surface. The term is then dependent on:

$$\frac{[\exp(-\beta x)\exp(-\sigma x) + \exp(\sigma x)*\Gamma_1\exp(-2\sigma l)]}{[1-\Gamma_0\Gamma_1\exp(-2\sigma l)]}$$

To determine the total contribution for all depths x, this expression is integrated between the limits x=0, the surface, and x=l, the interface, which gives:

$$\int_{x=0}^{x=l} \frac{\exp(-(\beta+\sigma)) + \exp(\sigma x)\ \Gamma_1\exp(-2\sigma l)}{1-\Gamma_0\Gamma_1\exp(-2\sigma l)}\ dx$$

$$\frac{1}{1-\Gamma_0\Gamma_1\exp(-2\sigma l)} \int_{x=0}^{x=l} \exp(-(\beta+\sigma)) + \exp(\sigma x)\ \Gamma_1\exp(-2\sigma l)\ dx$$

The full equation is thus:

$$T_{ac} = \frac{I_o(1-R)n\beta}{2k\sigma(1-\Gamma_{10}\Gamma_{12}e^{-2\sigma l})}\left[\frac{1-e^{-(\beta+\sigma)l}}{\beta+\sigma} + \frac{\Gamma_{12}e^{-2\sigma l}[1-e^{-(\beta-\sigma)l}]}{\beta-\sigma}\right]$$

equation A.21

A.8 Coated Substrate (II)

In this section, a different approach is used to arrive at the same expression for the surface temperature of a coated substrate. The same assumptions are assumed.

Assume that a plane periodic sinusoidally modulated light source is incident on a flat thermally thin optically absorbing coating on a non-absorbing semi-infinite substrate. Assume further that optical absorption is exponential within the coating (Beer Law) and that all media are isotropic and homogeneous (figure A.4). The heat diffusions take the form:

$$\frac{\partial^2 T_0(x,\omega)}{\partial x^2} - \left(\frac{i\omega}{\alpha_0}\right) T_0(x,\omega) = 0 \quad \text{for } x > 0 \qquad \text{equation A.22a}$$

$$\frac{\partial^2 T_1(x,\omega)}{\partial x^2} - \left(\frac{i\omega}{\alpha_1}\right) T_1(x,\omega) = \frac{I_0 \beta_1 \exp(\beta_1 x)}{2k_1} \quad \text{for } x = 0 \text{ to } -l \qquad \text{equation A.22b}$$

$$\frac{\partial^2 T_2(x,\omega)}{\partial x^2} - \left(\frac{i\omega}{\alpha_2}\right) T_2(x,\omega) = 0 \quad \text{for } x < -l \qquad \text{equation A.22c}$$

where α_i = diffusivity of medium i, and medium 0 is that above the coating, medium 1 is the coating, and medium 2 is the substrate. The boundary conditions are that heat flux and temperature must be equal across the boundaries. Thus:

$$T_0 = T_1 \quad \& \quad -k_0 \frac{\partial T_0}{\partial x} = -k_1 \frac{\partial T_1}{\partial x} \quad \text{at} \quad x = 0$$

$$\& \; T_1 = T_2 \quad \& \quad -k_1 \frac{\partial T_1}{\partial x} = -k_2 \frac{\partial T_2}{\partial x} \quad \text{at} \quad x = -l$$

The solutions should have the form:

$$T_{0(x,w)} = c_1 \exp(-\sigma_0 x) \qquad \text{equation A.23a}$$

$$T_{1(x,w)} = \frac{I_0 \beta_1 \exp(\beta_1 x)}{2k_1[(\sigma_1)^2 - (\beta_1)^2]} + c_2 \exp(\sigma_1 x) + c_3 \exp(-\sigma_1 x) \qquad \text{equation A.23b}$$

$$T_{2(x,w)} = c_4 \exp(\sigma_2 x) \qquad \text{equation A.23c}$$

This may be expressed in matrix form:

$$\begin{bmatrix} 1 & -1 & -1 & 0 \\ 1 & b_o & -b_o & 0 \\ 0 & X^{-1} & X & -Y^{-1} \\ 0 & X^{-1} & -X & -b_1 Y^{-1} \end{bmatrix} \begin{bmatrix} C_1 \\ C_2 \\ C_3 \\ C_4 \end{bmatrix} = \begin{bmatrix} -E \\ b_o \Gamma_1 E \\ EB \\ \Gamma_1 EB \end{bmatrix}$$

concisely, $[A]\ [C] = [B]$ equation A.24b

where: $b_i = k_i\sigma_i / k_j\sigma_j$ where $j = i - 1$

$X = \exp(\sigma_1 l_1)$ $X^{-1} = \exp(-\sigma_1 l_1)$

$Y = \exp(\sigma_2 l_1)$ $Y^{-1} = \exp(-\sigma_2 l_1)$

$$E = \frac{(1-R) I_0 \beta_1}{2k_1 [(\sigma_1)^2 - (\beta_1)^2]} \qquad EB = E \exp(-\beta_1 l_1)$$

and Γ_i is the interfacial thermal wave reflection coefficient from medium i to medium j.

The solution to A.24 is:

$[C] = [A]^{-1}\ [B]$ equation A.25

The periodic surface temperature, T_{ac}, may be determined by evaluating the coefficient C_1. Hence:

$$T_{ac} = \frac{I_o (1-R) n \beta}{2k\sigma (1 - \Gamma_{10}\Gamma_{12} e^{-2\sigma l})} \left[\frac{1 - e^{-(\beta+\sigma)l}}{\beta + \sigma} + \frac{\Gamma_{12} e^{-2\sigma l} [1 - e^{-(\beta-\sigma)l}]}{\beta - \sigma} \right]$$

equation A.26

which can be seen to be the identical to equation A.21.

In an opaque coating, where βl is very large,

$$T_{ac} = \frac{(1-R) I_0}{2k_1\sigma_1} \frac{[1 - \Gamma_1 \exp(-2\sigma_1 l_1)]}{[1 + \Gamma_1 \exp(-2\sigma_1 l_1)]}$$ equation A.26a

and where the coating is semi-infinite (where l_1 is infinitely thick):

$$T_{ac} = \frac{(1-R) I_0}{2k_1\sigma_1}$$ equation A.26b

It might be argued that assuming zero absorption within the substrate is unrealistic. In practical translucent coatings, such as YSZ, and opaque coatings such as LC1B, the coatings are generally optically thick so that very little light reaches the substrate. In this case, the value of β_2 is unimportant, and a value of zero may safely be assumed for mathematical simplicity.

A.9 Thermal Wave Interferometry

Equation A.26a may be rewritten as:

$$T_{ac} = \frac{(1-R)I_0}{2k\sigma}\left[1 + \frac{2\Gamma_1 \exp(-2\sigma l)}{1 - \Gamma_0\Gamma_1 \exp(-2\sigma l)}\right] \qquad \text{equation A.27a}$$

this, in turn, may be expressed as a series summation:

$$T_{ac} = \frac{(1-R)I_0}{2k\sigma}\ 1 + 2\sum_{n=0}^{n=\infty}(\Gamma_0\Gamma_1)^n \exp(-2n\sigma l) \qquad \text{equation A.27a}$$

which is analogous to optical interference within a thin film. Thus equations A.21, A.26 and A.27 physically represent thermal wave interferometry in a thermally thin coating.

A.10 Effect Of Defects

If the coated sample contains some form of defect, such as an air gap or a region of poor interfacial adhesion which acts as some form of thermal contact resistance, then this can be simply incorporated into equation A.21 by replacing Γ_1 with $\Gamma_{air\ gap}$ or Γ_{tcr} as required. The derivation of the defect reflection coefficients has been explored in detail by Patel and others [10,117].

$$\Gamma_{gap} = \frac{\Gamma_1 + \Gamma_2 \exp(-2\sigma_2 l_2)}{1 + \Gamma_1\Gamma_2 \exp(-2\sigma_2 l_2)} \qquad \text{equation A.28a}$$

where $\Gamma_1 = [1 - b_{21}]/[1 + b_{21}]$

and $\Gamma_2 = [1 - b_{32}]/[1 + b_{32}]$

for medium 1 = coating, 2 = air (gap), 3 = substrate.

$$\Gamma_{tcr} = \frac{1 - b_{21} + Rk_2\sigma_2}{1 + b_{21} + Rk_2\sigma_2} \qquad \text{equation A.28b}$$

where medium 2 is the substrate, and R is the thermal contact resistance between the coating and substrate.

A.11 Multiple Coatings

Where there are two or more coatings present, the situation is obviously made more complicated, since multiple thermal wave reflections can occur within all the coatings. Further, each of the coatings may have different optical properties as well as thermal properties. It is possible to obtain the expression for the surface temperature either by matrix techniques, or by assuming that multiple thermal wave reflections will occur and performing series summations much as for the two-layer system discussed in A.6 and A.7.

Both methods, though straightforward, are lengthy and tedious, and will not be illustrated here. The periodic temperature obtained may be expressed:

$$T_{ac} = \frac{I_0 \eta_1 (1-R)\beta_1}{2K_1\sigma_1}\left[A_{1+}\left[1+\Gamma_1\Gamma_2 e^{-2\sigma_2 l_2}\right] + A_{1-}\left[\Gamma_1 + \Gamma_2 e^{-2\sigma_2 l_2} e^{-2\sigma_1 l_1}\right]\right] + \frac{I_0 \eta_2 \beta_2}{2K_2\sigma_2}\left[\left[1+\Gamma_2 e^{-2\sigma_2 l_2}\right] T_{21} \frac{e^{-2(\beta_1+\sigma_1)l_1}}{\beta_2+\sigma_2}\right]$$

$$\left[1+\Gamma_1\Gamma_2 e^{-2\sigma_2 l_2}\right] - \left[\Gamma_1 + \Gamma_2 e^{-2\sigma_2 l_2}\right] . e^{-2\sigma_1 l_1}$$

equation A.29

where the subscripts 1 & 2 refer to the properties of coatings 1 & 2, G_1 is the thermal wave reflection coefficient between media 1 and 2, and G_2 is that between media 2 and 3; G_0 is assumed equal to 1 and omitted.

$$A_{1+/-} = \frac{[1 - \exp(-(\beta_1 +/- \sigma_1) l_1)]}{\beta_1 +/- \sigma_1}$$

A.12 Phase and Amplitude

In the expressions above for the surface temperature, the term σ that appears in all cases is complex. Thus all the expressions are themselves complex. The phase and amplitude can be readily determined, since for a complex number $Z = a + ib$, the phase is given by :

$$\phi = \tan^{-1} (-b/a) \qquad \text{equation A.30a}$$

and the amplitude is:

$$|Z| = (a^2 + b^2)^{1/2} \qquad \text{equation A.30b}$$

As an example, the phase of the surface temperature expressed in equation A.21 will be:

$$\phi = \tan^{-1} \frac{[\ \mathrm{Im(A.21)}\ ]}{[\ \mathrm{Re(A.21)}\ ]} \qquad \text{equation A.31}$$

where Im(Z) denotes the imaginary part if Z, and Re(Z) denotes the real part of Z.

Consider the case where the coating is thermally thick, where l is large, so that equation A.21 approximates A.32:

$$T_{ac} = \frac{(1-R) I_0 \beta}{2k\sigma} \left[\frac{1}{\beta + \sigma} \right] \qquad \text{equation A.32}$$

Hence the phase will be given by:

$$\phi = \tan^{-1} [-(\beta + 2\sigma)/\beta] \qquad \text{equation A.33}$$

Where the coating is opaque, $\beta >> \sigma$, and the argument of A.28 tends to 1, ie ϕ tends to -45, ie a 45 degree phase lag. Where the coating is non-absorbing, $\beta = 0$, and the argument tends to infinity, ie ϕ tends to -90, a 90 degree phase lag.

A.13 Surface Temperature

The overall temperature of a body heated by a periodic source, such as a modulated laser beam, will consist of three components:

$$T = T_0 + T_{ac} + T_{dc} \qquad \text{equation A.34}$$

where T_0 is the original (ambient) temperature, T_{ac} is the periodic temperature, and T_{dc} is the steady state temperature rise. For an opaque thermally thick coating, these can readily be shown to be:

$$T_{ac} = \frac{I_0(1-R)n\mu}{2k} \qquad \text{equation A.35a}$$

$$T_{dc} = \frac{I_0(1-R)nl}{2k} \qquad \text{equation A.35b}$$

where μ is the thermal diffusion length, and l is the thickness of the coating.

For a typical 400 micron thick YSZ coating with a thermal conductivity of 1, μ = 356 microns, R = 0.4, and n = 1, where the laser intensity is 1 watt over a spot size of 0.6mm radius:

T_{ac} = 15.2 K

T_{dc} = 38.2 K

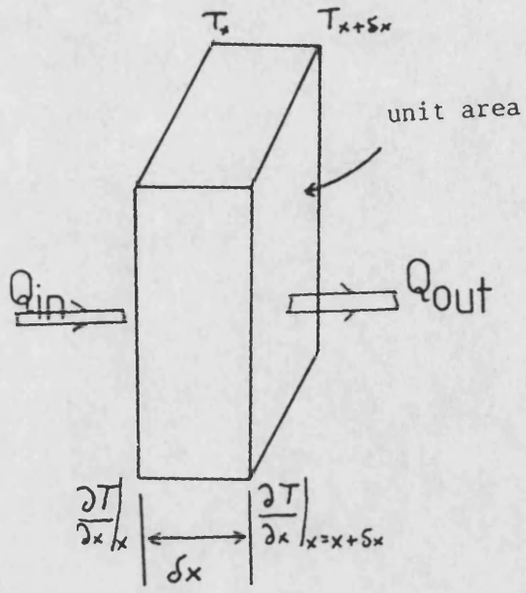

Figure A.1 : Schematic diagram of a representative volume at thermal equilibrium in a temperature gradient dT/dx

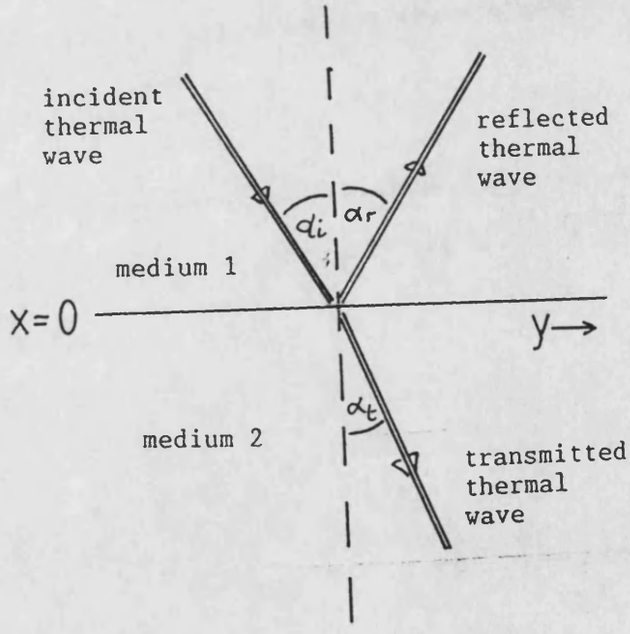

Figure A.2 : Schematic illustration of reflection and transmission of a plane thermal wave at an interface

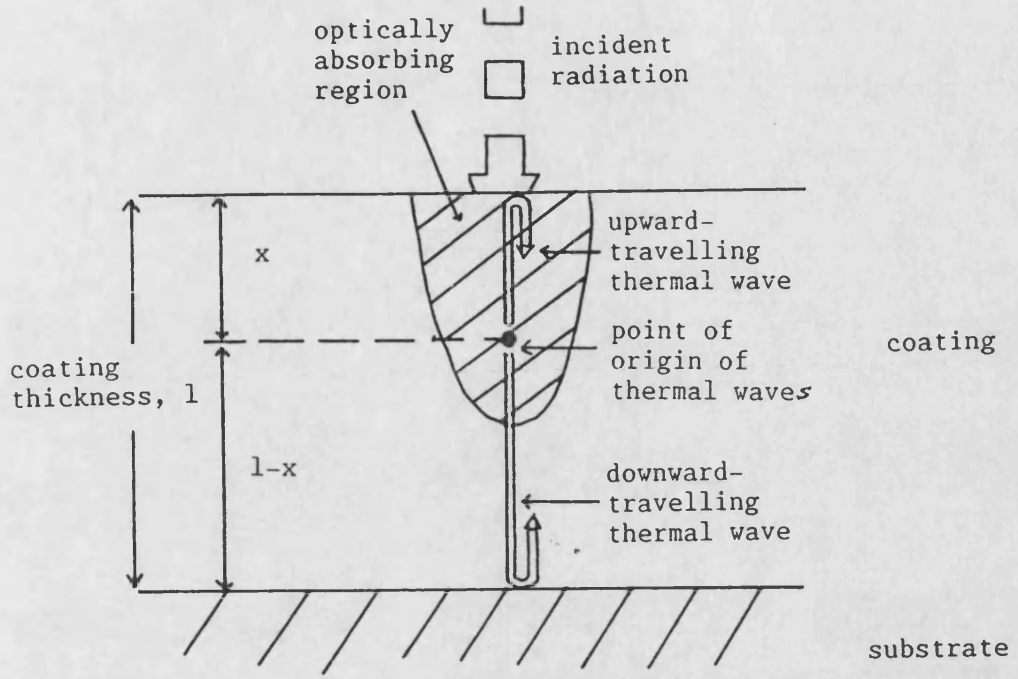

Figure A.3 : Schematic diagram of an optically absorbing thermally thin coating on a semi-infinite substrate showing generation of upward- and downward- travelling thermal waves at a point within the coating.

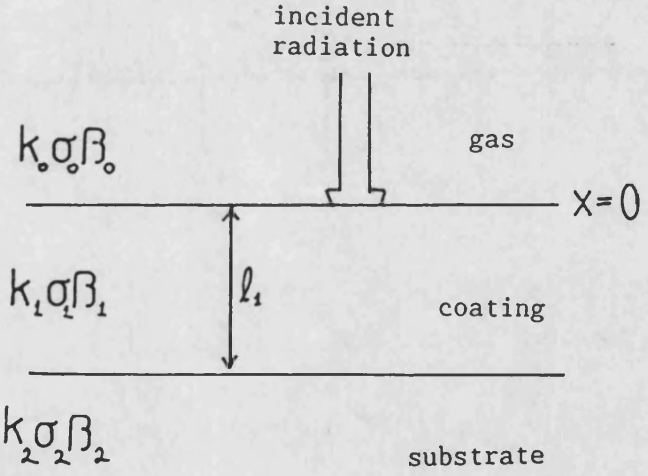

Figure A.4 : Schematic diagram of coating on a substrate

Material	Density Kg m^{-3}	Specific Heat Capacity J $Kg^{-1}K^{-1}$	Thermal Conductivity W $m^{-1}K^{-1}$	Optical Absorption Coefficient m^{-1}
Aluminium	2702	903	201	opaque
LC1B(*)	7000	400	6	opaque
Mild Steel	7960	480	60	opaque
Titanium	4500	400	22	opaque
Tungsten-Carbide/ Cobalt(*)	13500	250	12	opaque
Vitreous Carbon	2000	600	1.6	opaque
YSZ(*)	5000	500	1	10^4
316 Steel	8000	400	12	opaque

Table A.1 : Default values of thermal and optical properties of materials used in computer simulations.
* = plasma-sprayed coating, others are monolithic

APPENDIX B EFFECTIVE THERMAL CONDUCTIVITY OF A GAS BETWEEN PARALLEL PLATES

APPENDIX B

EFFECTIVE THERMAL CONDUCTIVITY OF A GAS BETWEEN PARALLEL PLATES.

There are two main types of heat conduction: continuum heat transfer, in which thermal conductivity is at a maximum; molecular heat transfer, where thermal conductivity is below the maximum.

In the molecular regime, collisions between molecules are less common than collisions between the molecules and either of the two surfaces. The thermal conduction is determined by the gas pressure, which it is directly proportional to, and also by the accommodation coefficient α. The accommodation coefficient is a measure of the energy exchange between a molecule and a surface in comparison to the maximum possible.

In the continuum regime, thermal conductivity is at a maximum, and is relatively pressure independent.

The basic thermal conductivity of a gas is given by:

$$K_g = \varepsilon n C_v$$

$$e = (9\delta - 5)/4$$

$$n = \rho v \lambda / 2$$

$$C_v = R_0 / M(\gamma - 1)$$

where ε is a constant, n is the viscosity coefficient, C_v is the specific heat at constant volume, γ is the specific heat ratio, ρ is the density, v is the mean velocity. [149]

λ is the mean free path

R_0 is the universal gas constant

M is the molecular mass

Hence $K_g = \varepsilon \rho C_v v \lambda / 2$

If the mean free path is defined as

$$\lambda = 1/[(1/\lambda_p) + (1/L)]$$

where λ_p is the inter-particle spacing (= kT/ $(2\sigma P)$), and k is the Boltzmann constant, σ is the collision cross section, and L is the system characteristic dimension, defined as volume/area (ie plate separation).

Thus $K_g = \varepsilon \rho C v v / [2 (1/\lambda + 1/L)]$

where the accommodation coefficient α is 1.

This then allows calculation of the thermal conductivity of the gas over both the molecular and continuum regimes. In general, α has a value between 0 and 1, so the factor F is used to accommodate this.

$$K_g = \varepsilon \rho C v \nu \; / \; [2(1/\lambda + F/L)]$$

Where F is a factor that resembles the emissivity factor in radiative heat transfer. For parallel surfaces of equal size, F is given by:

$$F = 1/\alpha_1 + 1/\alpha_2 - 1$$

It is apparent from equations 4 and 5 that when the plate separation L is large, the thermal conductivity approaches the maximum, bulk value. When the separation approaches the mean free path of the gas, then the thermal conductivity of the gas can be significantly reduced.

For air trapped between two identical plates, and assuming an accommodation coefficient of 0.5, the gas thermal conductivity is reduced to 75% of its bulk value.

$$K_{effective} = K_{bulk} \; / (1+(F\lambda)/L)$$

APPENDIX C

MOVEABLE THERMAL WAVE SYSTEMS

APPENDIX C

MOVEABLE THERMAL WAVE SYSTEMS

High power gas lasers are inherently bulky and commonly require high voltage power supplies and water cooling. As such they are physically immobile. Aditionally, the radiation hazard posed by high power lasers must be considered, so they cannot be used in open environments.

In comparison to the laser, the other components, with the possible exception of the scanning stage, are relatively portable. The lock-in amplifier, modulator, and detector are all man-portable, even though not ideally suited to this.

Thus the major obstacle to devising a portable system is the laser system itself. There are several ways around this. Firstly, the sample can brought to the test system. This is the common situation. Secondly, all but the laser system can be moved to the sample, and the laser radiation brought to the sample via a light guide. Thirdly, a smaller and more portable laser can be used.

C.1 Immobile Systems

The first of these is the typical situation. The laser and associated equipment can be permanently located within a suitable safety area, and samples brought to it. This obviously restricts testing to those samples which can be transported to the test area, and which can be fitted into the safe area. While many samples are small enough for this to be done, such as turbine blades or pistons, large components like power generation equipment are not. The system itself benefits by having a permanent site with enhanced operational safety, and does not suffer from constant movement which could cause damage or misalignment.

C.2 Immobile Laser Plus Flexible Light Guide

The second depends on there being a suitable light guide available to take power from the laser to the test area. If the laser operates at optical or near infrared wavelengths, then current silica fibres are likely to be suitable. Modulation can be carried out near the laser head, so that only the detection, collection and scanning stages need to be moved near the sample. These parts, however, can contain bulky and fragile components.

If scanning is not required, then the operation is simplified. The lock-in amplifier must, however, be referenced to the modulation frequency. Where scanning is not required, the computer requirements are reduced to gathering data from the lock-in amplifier, performing some basic preprocessing, and storing the data.

If scanning is required, then the computer can control these too, but the incorporation of the scanning stage increases the complexity of the system. Not the least of the problems is how to ensure a good light-proof seal between the laser head while allowing either the probe head to move over the sample, or allowing the sample to move beneath the probe head.

Consideration must be given to the safety aspects of laser use. Laser radiation poses a serious hazard, particularly at high powers, so that operators and other personnel must be protected from both direct and reflected radiation. Sensitive equipment must also be protected from the laser, as well as flammable materials. In general, high power laser work should be done in an enclosed light-proof area conforming both to British Standard regulations [150], and relevant local regulations [eg 151].

C.3 High Power Diode Lasers

For the third option, the gas laser can be replaced by a high power diode laser. These devices have recently become available with output levels of half a watt at near infrared wavelengths, and a number of leading suppliers have expressed the view that diodes with output powers of several watts will be available in the near future. They will thus be competing directly with gas lasers in performance.

Diode lasers are small devices, and even when packaged with power supplies and modulation units, they are significantly smaller than an equivalent power gas laser. They do not need special services, and can be operated from standard power outlets. Output is typically through an optical fibre pigtail.

Patel [117] showed that a diode laser operating at 500mW at 1040nm could be used to measure coating thickness steps on a plasma sprayed LC1B wear resistant coating. The trace is reproduced in figure C.1 to illustrate the close agreement between the phase response to irradiation by the diode and gas lasers. The amplitude traces were not similar because of the different laser power densities caused by the different spot sizes and the different incident laser powers.

In addition to their much reduced bulk with respect to gas lasers, and their more convenient service needs, diode lasers have a higher reliability than gas lasers. The design lives of high power diode lasers are typically in ten thousands of hours of service, while the lives of gas laser tubes are typically quoted in hundreds or (rarely) thousands of hours. The cost per milliwatt is higher than for gas lasers, but is likely to drop more in the short term than the cost per milliwatt for gas lasers.

If the laser plus modulator can be made portable, then the entire test system can be made portable, even if in some limited form, such as without scanning capacity. The lock-in amplifier can be mounted on a plug-in board for an IBM compatible personal computer [152], which can itself be used for data collection and preprocessing. The TGS detector unit itself is compact (25.4mm diameter and 76.2mm long), and needs no cryogenic cooling. There is no requirement for scanning for such tests as spot measurements for local coating thickness determination.

While the laser hazard is somewhat reduced because the radiation is in the near infrared rather than at optical wavelengths, it is still serious. Safety precautions must, therefore, be taken during testing. This could be done easily if an ellipsoidal collector mirror were used to enhance the received infrared signal, by extending its casing to form a barrier around the sample area (figure C.2). Light delivery to the sample would then be achieved by introducing the optical fibre into the collector mirror assembly through a small hole in the casing.

C.4 Infrared Transmitting Fibres

Infrared transmitting fibres could improve system flexibility by allowing the detector to remain remote. The minimum probe head dimensions would then be reduced from those required to incorporate the detector (approximately 25mm x 75mm) to those required to incorporate the optical light guide and the infrared guide (approximately 5 or 6mm). This would allow inspection of small cavities, internal bores and many other regions otherwise inaccesible to this test system. For this to be feasible, it would be necessary to have infrared transmission at a comparable level to current optical transmission levels. Such technology is currently unavailable, although there have been isolated reports of a suitable fibre [135,139].

The incorporation of infrared transmitting fibres into a probe head would not be problem-free, however. The presence of intense optical radiation near optically opaque fibres has been shown to cause ablation of the fibre ends (section 8.4.2). If the fibre were both optically and infrared transmitting, such as might be the case with fluoride glass fibres, then it would be possible in principle to deliver the optical power down the same fibre that transmitted the infrared radiation back to the detector. This might require a form of shuttering, so that the detector is shielded from direct illumination, but is uncovered during the "off" part of the modulation cycle.

Table C.1 shows the approximate cost, at current prices, to set up a moveable chopped cw thermal wave test system suitable for taking spot measurements on a reasonably flat surface.

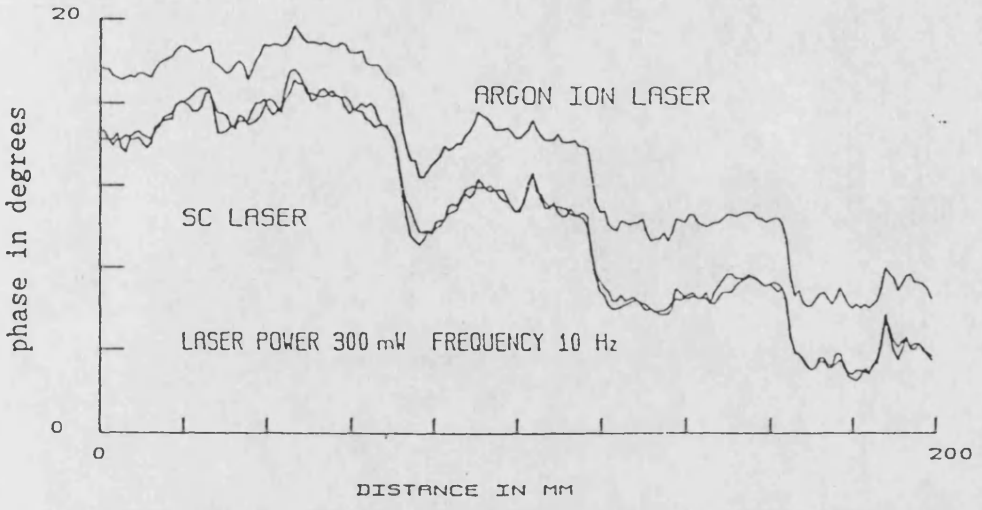

Figure C.1 : Effect of laser type on variation of phase angle with position on a step thicknesss LC1B coating on 316 steel. Modulation frequency 10Hz, laser power 300mW (after Patel [117])

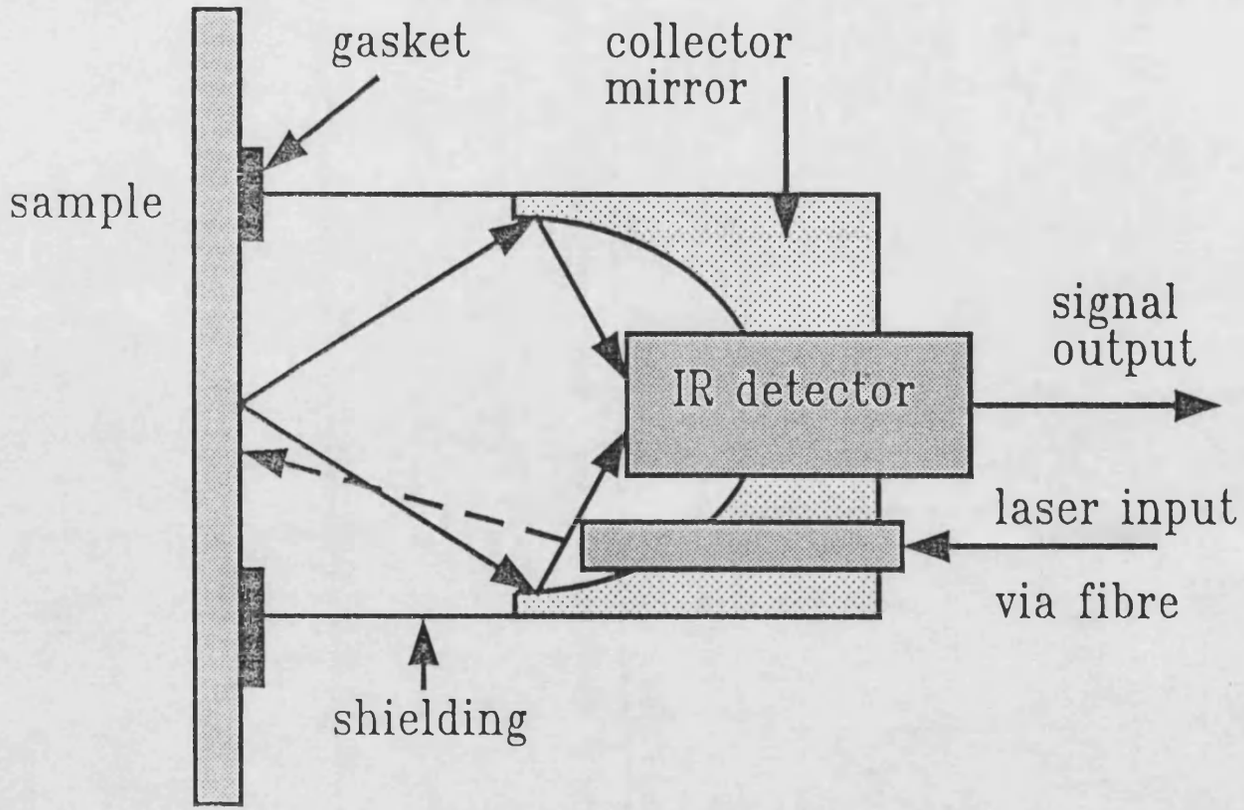

Figure C.2: Schematic diagram of proposed probe head

Components	Cost in Pounds
500mW diode laser plus modulator unit	15000
Optical components (detector, optical cable, collector mirror etc.)	1500
Lock-in amplifier board for PC	1500
IBM compatible PC	1000
Total component cost	19000

Table C.1: Approximate costs (at 1989 prices) of components needed for a portable thermal wave test system

REFERENCES

REFERENCES

1 M K Hobbs, PhD Thesis (1989)

2 "Ceramics Applications in Reciprocating Engines" Scheme, Department of Trade and Industry UK

3 M K Hobbs, Surfacing Journal v16/4 (1985) p101

4 H E Helms, P W Heitman, L C Lindgren and S R Thrasher, "Ceramic Applications in Turbine Engines" Noyes Publications New Jersey USA (1986)

5 A Bennet, Proc Brit Ceram Soc No34 (August 1984)

6 K T Scott, Proc Brit Ceram Soc No34 (August 1984)

7 A Redondo and J G Beery, J Appl Phys v60/11 (1 Dec 1986) p3882

8 P M Patel and D P Almond, J Mat Sci v20 (1985) p955

9 D P Almond, P M Patel and H Reiter, Mater Eval (April 1987) p1986

10 P M Patel, D P Almond and H Reiter, Appl Phys B v42 (1987)

11 D P Almond, P M Patel, I M Pickup and H Reiter, NDT International v18/1 (1985) p17

12 M L Veingorov, Dokl Akad Nauk SSSR v19 (1938) p687

13 H S Ingham and A P Shepard, "Metco Flame Spray Handbook" v2 Metco Ltd Chobham UK (1967)

14 J Morimoto, A Yamaguchi, K Yamada, Y Arata and A Ohmori, Preprints 12th International Thermal Spray Conference, London UK (4th-9th June 1989) vol 2

15 R F Smart and J A Catherall, "Plasma Spraying" Mills and Boon Ltd. London UK (1972)

16 B Towler, "Flame Deposition" Engineering Design Guide no25 Oxford University Press (1978)

17 Proc 11th International Thermal Spray Conference, Montreal, Canada (8-12 Sept 1986) p49-98

18 Proc 11th International Thermal Spray Conference, Montreal, Canada (8-12 Sept 1986) p73

19 W Elgar, A Grubowski, J Herbstritt & S Travis, Preprints 12th International Thermal Spray Conference, London UK 4th-9th June 1989 vol 1 paper 67

20 P E Chandler and M B C Quigley, Proc 11th International Thermal Spray Conference, Montreal Canada (8-12 Sept 1986) p27

21 P Ostojic & R McPherson, Preprints 12th International Thermal Spray Conference, London UK (4th-9th June 1989) vol 1 paper 9

22 P J Callus & C Coddet, Preprints 12th International Thermal Spray Conference, London UK (4th-9th June 1989) vol 1 paper 103

23 A R Nicoll, J Hochstrasser and B Meier, Preprints 12th International Thermal Spray Conference, London UK (4th-9th June 1989) vol 1 paper 81

24 The NDT Yearbook: The Official Yearbook of the British Institute of Non-Destructive Testing (1989)

25 W N Reynolds, NDT International V20/3 June 1987 p153-156

26 B Hull and V John, "Non-Destructive Testing" McMillan, London UK (1988)

27 C A Hogarth and J Blitz, "Techniques of Non-Destructive Testing" Butterworths, London UK(1960)

28 P Gebureck, D Petermann and D Stegemann, Proc 12th World Conference on NDT, Amsterdam, The Netherlands (23-28 April 1989) p42

29 M Moghisi, PhD Thesis (1984)

30 S Kuroda, T Fukishima and S Kitihara, J Vac Sci Tech A5/1 (Jan/Feb 1987) p82

31 P M Patel and D P Almond, J Mat Sci v20 (1985) p955

32 A Tebo "IR Detector Technology Part II: Arrays" Laser Focus/Electro Optics (July 1984) p68

33 F Charbonnier, D Fournier and A C Boccara, "Photoacoustic and Photothermal Phenomena" Springer Optical Series v58, P Hess and J Pelzl eds. (1988) p478

34 J Szilard (Ed) "Ultrasonic Testing" J Wiley and Sons, New York USA (1982)

35 D Ensminger, "Ultrasonics" 2ed Marcel Dekker Inc., New York USA (1988)

36 R Cox, MSc Thesis (1979)

37 M Moghisi and D P Almond, NDT Intl (Feb 1983) p9

38 A G Bell, Am J Sci v20 (1880) p305

39 J Tyndall, Proc R Soc London v31 (1881) p307

40 W C Roentgen, Phil Mag v11 (1881) p308

41 A G Bell, Phil Mag v11 (1881) p510

42 K F Luft, Z Tech Phys v24 (1943) p97

43 A Hadni, J Phys v24 (1963) p694

44 C K N Patel, E G Burkhardt and C A Lambert, Science v184 (1974)

45 A Rosencwaig, Science v181 (1973) p657

46 A Rosencwaig and A Gersho, J Appl Phys V47/1 (January 1976) p64

47 J G Parker, Appl Opt v12 (1973) p2974

48 P Helander, J Appl Phys v54/6 (June 1983) p3410

49 L C Aamodt, J C Murphy and J G Parker, J Appl Phys V48/3 (March 1977) p927

50 F A McDonald and J C Wetsel jr, J Appl Phys v49/9 (April 1978) p2313

51 R C Quimby and W M Yen, Appl Phys Lett v35/1 (1 July 1979) p43

52 H C Chow, J Appl Phys v51/8 (August 1980) p4053

53 P K Kuo and L D Favro, Appl Phys Lett v40/12 (15 June 1982) p1012

54 G Birnbaum and G S White, in "Research Techniques in Nondestructive Testing" v7, R S Sharpe ed., Academic Press New York USA (1984)

55 G Busse, IEEE Trans Son Ultrason SU32(1985)2

56 A Rosencwaig, Ann Rev Mater Sci v15 (1985) p103

57 H S Carslaw and J C Jaeger, "Conduction of Heat in Solids" Clarendon Press Oxford (1959)

58 D R Green, J Appl Phys, 37/8 (1966) p3095-3099

59 J Sanile, M Luukkala, A Lehto and R Rajala, Electron Lett 18/15 (1982) p651-653

60 D R Green, Applied Optics v7 (1968) p1779-89

61 E J Kubiak, Applied Optics v7 (1968) p1743-47

62 D N Rose, H Turner and K O Legg, Can J Phys, v64/9 (1986), p1284-1286

63 A L Tronconi, M A Amato, P C Morais and K S Neto, J Appl Phys, 56/5 (1984) p1462-1464

64 P Cielo and S Dallaire, ASM Metals Congress, Toronto Canada (1985)

65 C A Bennett and R R Patty, Applied Optics v21/1 (1st Jan 1982) p49

66 J Opsal and A Rosencwaig, J Appl Phys v53/6 June (1982) p4240

67 Y H Wong,R L Thomas and G F Hawkins, Appl Phys Lett v32/9 (1978) p538

68 P K Kuo, L D Favro, L J Inglehart, R L Thomas and M Srinivasan, J Appl Phys v53/2 (Feb 1982) p1258

69 Y H Wong, R L Thomas and J J Pouch, Appl Phys Lett v35/5 (1979) p368

70 B Hoffman, H Peukert and W Arnold, "Photoacoustic and Photothermal Phenomena" Springer Optical Series v58, ed. P Hess and J Pelzl

71 B Hoffman and W Arnold, 12th WCNDT (23-28th April 1989) Amsterdam The Netherlands

72 J Opsal and A Rosencwaig, Appl Phys Lett v47/5 (1 Sept 1985) p498

73 J Opsal and A Rosencwaig, J Appl Phys v53/6 (June 1982) p4240

74 G Busse, Appl Phys Lett, v35/10 (15 Nov 1985) p759

75 J Aithal, G Rousset, L C Bertrand, P Cielo and S Dallaire, Thin Solid Films v119 (1984) p153

76 R J von Gutfeld and R L Melcher, Appl Phys Lett v30 p257 (1977)

77 A Rosencwaig and J Opsal, IEEE Trans on Ultrasonics UFFC-33/5 (Sept 1986) p516

78 S J Sheard, IEEE Ultrasonic Symposium (1986)

79 J C Murphy and L C Aamodt, Appl Phys Lett v38/4 (15 Feb 1981) p196

80 A Mandelis, A Williams and E K M Siu, J Appl Phys v63/1 (1 Jan 1982) p92

81 W B Jackson, N M Amer, A C Boccara and D Fournier, Appl Optics v20/8 (15 April 1981) p1333

82 R Santos and L C M Miranda, J Appl Phys v52/6 (June 1981) p4194

83 S O Kanstad and P-E Nordal, Can J Phys v64 (1986) p1155

84 Hendler, Crosbie and Hardy, Appl Physiology v12 (1958) p177

85 G Busse, Applied Optics v21/1 (1 Jan 1982) p109

86 G Busse, Infrared Physics v20 (1980) p419

87 G Busse, Appl Phys Lett v42/4 (15 Feb 1983) p366

88 I Kaufman, P T Chang, H S Hsu, W Y Huang and D Y Shyong, JNDE v6/2 (1987) p887

89 R M Miller, SPIE v917 "Recent Developments of Infrared Analytical Instrumentation" (1988) p56

90 P Cielo, J C Krapez and X Maldague, "Photoacoustic and Photothermal Phenomena" Springer Optical Series v58, P Hess and J Pelzl eds. (1988) p404

91 W P Leung and A C Tam, Appl Phys Lett v51/25 (21 December 1987) p2085

92 S J Sheard, private communication, (1988)

93 S K Lau, MPhil Thesis (1988) Bath

94 P Cielo, X Maldague, A A Deom and R Lewak, Mater Eval v45 (April 1987) p452

95 W P Leung and A C Tam, Appl Phys Lett v51/25 (21 Dec 1987) p2085

96 F H Long, R R Anderson and T F Deutsch, Appl Phys Lett v51/26 (29 Dec 1987) p2076

97 A Zur and A Katzir, Applied Physics Letters v48 (1986) p499

98 A C Tam and K Sontag, Appl Phys Lett v49/26 (29 Dec 1986) p1761

99 S Duschman, "Scientific Foundations of Vacuum Technology", Wiley, New York USA (1949) p320

100 P K Kuo, I C Oppenheim, L D Favro, Z J Feng, R L Thomas, J Hartikainen and L J Inglehart "Photoacoustic and Photothermal Phenomena" Springer Optical Series v58 (1987)

101 P K Kuo, Z J Feng, T Ahmed, L D Favro, R L Thomas and J Hartikainen, "Photoacoustic and Photothermal Phenomena", Springer Optical Series v58 (1987)

102 "Aladin" Test System, Siemens A G, UB KWU, UZQ32, Hammerbacherstrasse 12+14, P O Box 3220, D-8520 Erlanger, FRG

103 R Vanzetti, A C Traub and A A Richard, Brazing and Soldering v2 (1982) p34-37

104 D R Green, M D Schmeller and R A Sulit, Proc IEEE Oceans (1982) pub:Marine Technology Society

105 J Hartikainen and M Luukkala, Rev Prog QNDE 7 (1989) USA

106 Spectra Diode Labs, 80 Rose, Orchard Way, San Jose CA 95134 USA

107 Coherent (UK) Ltd, Cambridge Science Park, Cambridge UK

108 EG & G Instruments Ltd, Doncastle House, Bracknell, Berks UK

109 Melles Griot Ltd, Culdrose House, Aldershot UK

110 Ealing Electro Optics PLC, Greycaine Road, Watford, Herts UK

111 IBM Ltd., Bristol UK

112 Mullards Southampton, Millbrook Industrial Estate, Southampton UK

113 OCLI Optical Coatings Ltd, Hilend Industrial Park, Dunfermline UK

114 Chartland Electronics Ltd., PO Box 83, Cobham, Surrey KT11 2QB UK

115 CEGB report no2620

116 CEGB Report no3071 (April 1984)

117 P M Patel, PhD Thesis (1988)

118 Model 25 Photon Control, Greenfield Works, Broad Lane, Cottenham, Cambridge CB4 4SW

119 M G Drexhage and C T Moynihan, Scientific American (November 1988) p76-81

120 J A Savage, "Infrared Optical Materials and Antireflection Coatings", Adam Hilger Ltd. UK (1985)

121 J D Morris, P M Patel, D P Almond and H Reiter, ASM Congress (14th-17th September 1987) Orlando FA USA

122 F A McDonald, G C Wetsel jr and G E Jameson Can J Phys v64/9 (Sept 1986) p1265

123 L C Aamodt and J C Murphy, Applied Optics v21/1 (Jan 1982) p111

124 G Busse, Appl Phys Lett v35/10 (15 Nov 1979) p759

125 TBL Fibre Optics Group Ltd., Torbay Works, Hunslet Road, Leeds LS10 1AT UK

126 P M Patel, D P Almond and H Reiter, 6th Intl Topical Meeting (July -August 1989) Baltimore USA

127 STL ltd, Old London Road, Old Harlow, Essex CM17 9NA

128 T Kanamori, Y Terunama, S Takahashi and T Miyashita, J Lightwave Tech vLT-2/5 (Oct 1984) p 607-613

129 M Wehr and C Le Sargent, SPIE V618 Infrared Optical Materials and Fibres IV (1986) p130-134

130 IRIS Fibre Optics Ltd, 40 Nagog Park, Acton MA 01720 USA

131 P Klocek, M Roth and R D Rock, Optical Engineering V26/2 (Feb 1987) p88-95

132 Infrared Fibre Systems Inc, 2301-A Broadbirch Drive, Silver Spring MD 20904 USA

133 A L Gentile, M Braunstein, D A Pinnow, J A Harrington, D M Henderson and L M Holbruck from "Fibre Optics Advances in Research and Development" ed. B Bendow and S S Mitra, Plenum Publishing (1979) p105

134 D A Pinnow, A L Gentile, A G Standlee, A J Timper and L M Holbruck, Appl Phys Lett v33/1 (1 July 1978) p28

135 Laser Focus World, July 1989, p133

136 K Murakami, Patent number 4721360, assigned to Sumitomo Electric Company, Japan

137 T Hidaka, K Kumada, J Shimoda and T Morikawa, J Appl Phys v53 (1982) p5484

138 3M EOTec Corporation, 420 Frontage Road, West Haven, Connecticut 06516 USA

139 A Nagano, International Publicity, Matsushita Electrical Industrial Co ltd, 1006 Kadoma, Osaka 571, Japan (PO Box 51 Osaka Central 630-91) (1989)

140 P Klocek and L Colombo, J Non Cryst Solids v93 (1987) p1

141 Z A Yasa, W B Jackson and N M Amer, Applied Optics v21/1 (1 Jan 1982) p21

142 J Rantala, J Hartikainen, R Lehtiniemi, R Vuohelainen, J Jaarinen and M Luukkala, Abstracts of Rev Prog QNDE, Brunswick, Maine USA (23-27 July 1989) p235

143 J Rantala, J Hartikainen, R Lehtiniemi, R Vuohelainen and M Luukala, Abstracts of Rev Prog QNDE, Brunswick, Maine USA (23-27 July 1989)

144 S J Sheard, PhD Thesis (1988)

145 L C Aamodt and J C Murphy, J Appl Phys v54/2 (Feb 1983) p581

146 "Handbook of Physics and Chemistry", Chemical Rubber Corporation v69 (1988-89)

147 American Inst Phys Handbook, ed. D E Gray, pub. McGraw Hill (1972)

148 Smithsonian Physical Tables, 9th edn (1969)

149 N V Tsederberg, "Thermal Conductivity of Gases and Liquids" MIT press (1965) chapter IV

150 British Standard Institute BS4803 Pts 1 & 3 (1983)

151 "Safety Standards and Guidance" The University of Bath, School of Materials Science Handbook, (March 1986)

152 Bentham Instruments Ltd., 2 Boulton Road, Reading, Berks RG2 0NH UK

153 R V Sharman, "Vibrations and Waves" Butterworths, London, UK (1963)